Dynamics of the Solar System Meteoroid Population

A thesis submitted in partial fulfilment of the
requirements for the Degree of Doctor of Philosophy in Physics
at the University of Canterbury

by

Rachel H. Soja

Department of Physics and Astronomy
University of Canterbury
2010

Abstract

The purpose of this study is to develop an understanding of the observability of small-scale dynamical Solar System features in meteor orbit radar data, particularly with reference to mean motion resonance effects. Particular focus is placed on the presence of 'resonant swarms' in meteoroid streams: the resonant swarm at the 7:2 Jovian mean-motion resonance is used as an example, as it best satisfies radar observability criterion. Furthermore, evidence for this structure exists in visual meteor data. The radar dataset used for this study is that of the Canadian Meteor Orbit Radar (CMOR) as this dataset contains the largest number of meteoroid stream particles. The aim here is to determine whether the Taurid resonant swarm is observable in datasets produced by radars such as CMOR, or what improvements in individual orbital uncertainties are necessary for positive detection to be possible.

The observability of the Taurid swarm in radar data depends on the limitations of the radar data (in terms of the individual measurement uncertainties); and on the properties of the resonance itself. Both aspects are investigated in this thesis. A statistical study is first conducted to assess whether evidence for the swarm exists in a dataset containing CMOR Northern and Southern Taurids from the years 2002 to 2007. It is found that the level of variations present is consistent with that expected due to random fluctuations: there is no evidence for a statistically significant resonant feature at the location of the 7:2 Jovian resonance. Additionally, the observability of various sizes of resonant peak for different sizes of dataset and for different levels of measurement uncertainties is investigated by addition of a modelled resonant feature to the data, followed by replacement of individual meteors by Gaussian profiles to simulate the effect of orbital uncertainties. It is clear that the level of broadening resulting from the uncertainties of the CMOR data used will not allow the observation of a resonant peak of the expected size. Detection is expected to be more likely in a 'swarm encounter year' (a year in which the geometry between the resonant swarm and Earth is favourable to detection). The velocity uncertainties of a meteor orbit radar (similar to CMOR) need to be improved by a factor of 5 to 10 (relative to the CMOR uncertainties) in order to detect a resonant swarm that is composed of $\sim 30\%$ to $\sim 5\%$ (respectively) of the total number of observed Taurids in a swarm encounter year. An improvement significantly greater than a factor of ~ 10 is unlikely to result in a significant improvement in the ability to detect the resonant swarm. It is expected that a factor of 10 improvement in radar measurement uncertainties is achievable with the current techniques of radar systems and signal processing.

These statistical tests require knowledge of the resonant width of the 7:2 Jovian

resonance in semi-major axis, as this provides the size of the resonant feature of interest. Such resonant or libration widths can be determined analytically for orbits with low eccentricities. As Taurid orbits have high eccentricities ($e \sim 0.83$), a hierarchical N-body integrator is used to examine the dynamics in the region of the 7:2 resonance, and determine a resonant width of (0.047 ± 0.005) AU. To verify this method the standard analytic equations and a semi-analytic method are compared (at low eccentricities) with the numerical resonant width values: the agreement is within 10% for eccentricities below 0.4.

It is important to know what proportion of radar Taurids are expected to be resonant in a swarm year in order to evaluate the observability of the swarm in radar data. One important factor that may affect this is the mass distribution of particles in the swarm. This is investigated by ejecting particles in multiple directions from three model comets: the first with a mass and orbit in agreement with those of the current 2P/Encke; the second with 2P/Encke mass and an orbit matching that of the proposed proto-Encke object; and a third with the mass and orbit of proto-Encke. The resulting orbits are examined to determine what proportion will land within the 7:2 resonance, for a range of particle masses and densities. The instantaneous effect of radiation pressure on the orbits of ejected particles is also considered. However, it is difficult to determine accurate capture percentage values due to the uncertainty surrounding cometary ejection mechanisms. Nevertheless, it is found that capture of Taurids into the 7:2 resonance by all comets is possible. Using comparisons between the percentages of visual-sized and radar-sized particles captured, it is determined that in weak swarm years (in which only $\sim 20\%$ of visual meteoroids detected are resonant) only 4% to 5% of observed visual Taurids are expected to be resonant. Such a swarm would be on the edge of observability. However, in stronger swarm years (such as 2005), the resonant proportion will exceed that required for detection with a reduction in CMOR measurement uncertainties of a factor of ten.

Acknowledgements

I would like to sincerely thank Prof. Jack Baggaley, for his supervision, guidance and endless patience throughout the course of this study.

Thank you to Dr. Adrian McDonald for invaluable assistance, particularly concerning statistical methods.

Prof. Doug Hamilton of the University of Maryland deserves great thanks for his assistance and guidance as I navigated a new field.

Prof. Peter Brown and Prof. Margaret Campbell-Brown of the University of Western Ontario are gratefully thanked for the access to the CMOR dataset, extraction programs, and advice.

A TEC Top Achiever Doctoral Scholarship was essential to the completion of this thesis, as was support from the Department of Physics and Astronomy, University of Canterbury (including for various conference attendances).

The efforts of various proofreaders - including Kathryn Fitzgerald, Sam Willyams and family - are greatly appreciated.

Finally, thank you to my family and to Sam for supporting me throughout.

Contents

List of Figures

List of Tables

Chapter 1

Introduction

This thesis involves a study of the dynamical structure of the meteoroid population of the Solar System, as sensed by meteor orbit radar systems, and in particular reference to resonance effects. In context, such a study is useful because knowledge of this dynamical structure is necessary to develop an understanding of the formation and evolution of the Solar System that encompasses the observed meteoroid population. By understanding the evolutionary processes of our own Solar System, it is then possible to apply this knowledge to studies of planetary systems forming in debris disks around other stars (Krivov, 2007). The dynamical effects of interest here are largely gravitational resonance effects on the Solar System dust population, but include also non-gravitational effects. In addition, understanding meteoroid dynamics is important for studying the probabilities and effects of meteoroid impacts on spacecraft, man-made satellites, and Earth itself.

1.1 Meteoroids, Meteors, and Meteorites

The Solar System has $\sim 3 \times 10^{17}$ kg of dust particles of mass less than 0.1 kg: such objects are known as meteoroids (Hughes, 1996). This definition is generally assigned to objects of size from a few microns to a few metres - below the observation limit of telescopes. Smaller particles exist, but are ejected from the Solar System by the radiation force of the Sun and must be constantly replenished; larger object are classified as asteroids, comet nuclei, satellites, or planets depending on their origins, properties and orbital characteristics. Small particles in the Solar System are usually termed 'meteoroids' or 'dust particles', depending partially on their size and observation techniques: these terms are used interchangeably in this thesis to describe the micron to centimeter-sized dust of interest. Solar System meteoroids are concentrated close to the ecliptic plane, with most orbits having inclinations less than $\sim 20^\circ$ (Baggaley, 1999). In general, the orbits of such particles around the Sun are prograde, though $\sim 5\%$ are retrograde (Baggaley, 2001). Four sources for these particles exist: ejecta from planetary and satellite surfaces, cometary dust, asteroidal fragments, and interstellar sources.

1.2 History of Meteor Observation

For thousands of years meteors (more precisely, the heated and thus luminous head and train of a meteoroid) have been observed visually by the naked eye, with, in particular, Chinese, Korean and Japanese observers conducting systematic observations of showers for more than a thousand years. Jenniskens (2006) provides a compilation of historic records of meteor observations from Asia and Europe: the earliest record is from China in 687 BC (March 26.7), possibly of the Lyrid meteor shower. However, in the West it was not until the early 1800s that meteors were considered extraterrestrial bodies, previously having been thought to be an atmospheric phenomena, or superstitious omens.

It is believed that Chladni (1798) first correctly attributed the origin of meteors to extraterrestrial bodies that are vaporised as they pass through the Earth's atmosphere. However, this explanation was not widely accepted, with little scientific interest in studying meteors or confirming their origin until the spectacular 1833 Leonid storm (Williams and Murad, 2002). In 1833 Denison Olmsted recognised that the Leonid meteors all appeared to have a common source direction in the sky, the radiant, and that this was the result of bodies moving parallel to each other entering the Earth's atmosphere from the direction of the star γ Leonis. It was Giovanni Virgínio Schiaparelli who determined that the near-parabolic orbit of the Perseid meteoroid stream was very similar to that of the comet Swift-Tuttle, thus discovering the first source of meteoroids. This was further confirmed in 1866 when a parent comet for the Leonid stream was observed (55P/Tempel-Tuttle) (Jenniskens, 2006).

Visual observations have continued to be important for understanding meteor behaviour. The invention of photography and television and the development of radar technology led to significant improvements in our ability to study meteors remotely as they enter the Earth's atmosphere. Additionally, the development of spacecraft allowed in-situ detection of meteoroids: that is, capture or study of meteors directly. This has become increasingly powerful with the development of dust detector technology, capable of determining speed, mass, and approximate trajectories of particles still in orbit around the Sun, Jupiter or Saturn. Such detectors are not limited by detection only of particles with orbits that intersect the Earth's. In general the masses of particles detected are much smaller than those detected by remote sensing methods within the Earth's atmosphere. Further detail on spacecraft and remote sensing methods is given in Section 3.1.

1.3 Sources of meteoroids

1.3.1 Cometary and Asteroidal streams

The most significant sources of meteoroids are comets and asteroids. After ejection from these objects, dust particles follow, to some extent, the orbit of the parent object, forming a cometary or asteroidal stream. In more detail, these ejection mechanisms are as follows. For comets, particles are expelled from the cometary nucleus as the comet approaches perihelion. Comet nuclei consist of conglomerates of dust and 'snow' (mainly of $\sim 80\%$ H_2O and $\sim 15\%$ CO_2), with a snow to dust ratio of ~ 2 (Hughes, 1993). Solid at large distances from the Sun, the increase in solar radiation as the comet nucleus approaches perihelion causes sublimation of the surface snow to occur within about 3-4 AU of the Sun. Momentum transfer from the expanding gas expels dust from the nucleus, thus creating a population of meteoroids with orbits similar, though not identical, to the parent comet. As dust is ejected in all directions (relative to the nucleus), it is eventually dispersed around the orbit of the comet: dust emitted in the opposite direction to the comet's direction of motion has a slightly lower velocity than the comet and thus falls behind, while particles ejected in the comet forward velocity direction start to move ahead of the comet in its motion. These particles form a cometary meteoroid stream, which can be observed at the Earth as a meteor shower if an orbital node (see Chapter 2) exists near the Earth. Further details of the cometary dust ejection mechanism can be found in Section 6.2.

Ejection of dust particles from asteroids can be accomplished by collisions between asteroids, spinup of asteroids as a result of the Yarkovsky-O'Keefe-Radzievskii-Paddack (YORP) effect (Rubincam, 2000), or electrostatic levitation of particles (Lee, 1995). Dust particles ejected from main belt asteroids or near-Earth asteroids both have the potential to form asteroidal streams in a similar manner to the cometary case, though the dispersal of particles will be larger, and thus the spatial density lower, than for cometary streams. Only streams from near-Earth Earth-crossing asteroids will be visible on Earth as meteor showers. In addition, asteroidal collisions create fragments with low geocentric velocities and with prograde orbits relative to cometary particles. Because the light and plasma produced by a meteor are highly speed dependent, these factors render asteroidal streams more difficult to observe on Earth. Such streams are thus among the minor meteor showers (Porubčan et al., 2004). An exception is the possible association of the Geminids with (3200) Phaethon, which was considered the first confirmed asteroidal stream (Stohl and Porubčan, 1993). However, there are indications that this body may be an extinct comet, and as such, there is still debate as to whether there is any direct evidence for an asteroidal meteoroid stream (Jenniskens, 2006). There is a high probability that one

of the increasingly-large number of near-Earth asteroids will coincidently appear to have a similar orbit to a current meteoroid stream. Verification of a true physical connection between an asteroid and an observed meteor shower requires numerical studies to trace the history of the meteor shower and the potential parent asteroid (Porubčan et al., 2004). Thus, while cometary meteor streams and their corresponding showers are relatively well understood, this is not the case for asteroidal streams.

1.3.2 Interstellar Particles

In addition to the various meteoroid sources within the Solar System, a small proportion of meteoroids have an interstellar origin. These particles enter the Solar System on hyperbolic orbits with respect to the Sun. Their orbits are either perturbed such that the particles assume bound parabolic or elliptical orbits, or remain sufficiently unaltered such that the meteoroids are carried back beyond the Solar System. Alternatively, the particles can be destroyed by collisions with other Solar System bodies. Observationally, these particles are initially identified by heliocentric velocities that are greater than the escape velocity from the Sun at that particular heliocentric distance ($\sim$ 42 kms^{-1} at 1 AU). If perturbed into elliptical orbits, generally no orbit information remains to determine an interstellar origin. Care must be taken in the identification of interstellar particles as other mechanisms exist in the Solar System with the ability to produce hyperbolic particles, including radiation forces (creating hyperbolic β particles), magnetic and electric fields accelerating small grains near Jupiter, and ejection of particles from near-parabolic comets. There are several dust populations in the galaxy that form potential sources for dust inflow to the Solar System, including interstellar dust originating in stars, dust clouds in the diffuse interstellar medium, dust in molecular clouds and circumstellar dust in young stellar objects (Dorschner, 1996). Objects that can act as individual sources of interstellar dust include expanding atmospheres of asymptotic giant branch, red giant branch carbon rich and Wolf-Rayet stars, protoplanetary dust disks and supernova (Baggaley, 2004).

1.3.3 Sporadic Meteoroids and Dynamical Effects

Lastly, there also exists an observed population of sporadic meteoroids which are members of no apparent cometary or asteroidal streams. Largely, these particles were originally ejected from comets or asteroids, but gravitational perturbations and radiation effects have dispersed their original orbits.

Such effects can be significant, being responsible for both the dynamics and survival of particles in the Solar System. In general, gravitational forces include gravitational perturbations that occur when a particle's orbit takes it close to a large gravitational mass such as Jupiter or Saturn; and resonance effects, which occur at specific locations

where the gravitational effect of giant planets is enhanced. Here we are concerned only with mean-motion resonances. These occur when the orbital period of the particle is a small-order ratio of a planet's orbital period (for example, 2:1 or 3:1): at such locations the same gravitational effect from that planet occurs repetitively, producing an enhanced effect. Non-gravitational effects include radiation pressure, the Poynting-Robertson effect and Lorentz forces. A summary of such effects follows in Chapter 2. A summary of resonance effects in the Solar System, as relevant to the meteoroid population, is given in Chapter 4. In particular, meteoroid resonances can have ramifications for the level of meteoroid dust that impacts the Earth: the 1998 Leonid shower showed significant enhancement due to the presence of a 'swarm' of particles trapped in a Jovian resonance (Jenniskens et al., 2008). Thus, understanding the effect of resonances on the meteoroid population is important for understanding the dust that is encountered at the orbit of the Earth, or indeed at any location in the Solar System at which knowledge of the dust environment is necessary. In particular, this includes determining the hazard meteoroids can pose to spacecraft.

1.4 The Taurid Meteoroid Stream

This thesis is largely concerned with resonant effects in the Taurid meteoroids stream - in particular, that of a resonant swarm at the 7:2 Jovian resonance. This choice is justified in Section 4.4. The Taurid meteoroid stream consists of Northern and Southern branches and a large dispersion in orbital elements is known to exist. The Taurid shower is active in October to December each year, with a radiant situated such that it is most visible from the northern hemisphere. Comet 2P/Encke is the expected parent object, though it is hypothesised that a fragmentation event occurred, perhaps leaving two or more bodies capable of populating the Taurid meteoroid stream. This may explain the presence of a number of asteroidal bodies with similar orbits to Taurid meteoroids. However, a competing theory is also capable of explaining this observation.

Early observations of the Taurids largely concerned the position of the radiant (such as Dennings (1928)). The first orbits were determined from photographic Taurid meteoroids by Whipple (1940), who used a rotating shutter technique to determine velocities for Taurid meteoroids from 1937 and 1948. Orbital element data were achieved for six meteoroids. These observations were used to associate the Taurids with Comet 2P/Encke, though this required an understanding of the perturbation history of this comet. Additionally, Whipple suggested that the dispersion in the orbital elements might be explained by the disintegration of one large comet into many fragments, possibly producing Taurid meteoroids. Using this model, a lower limit to the age of the Taurids of $\sim$ 14000 years

was provided.

Whipple and Hamid (1952) suggested that ejection of meteoroids occurred from two bodies: one being Comet Encke, and the other being a body that split from Comet Encke at some unknown time. They suggested that particle ejection occurred far from perihelion as a result of encounters with small bodies in the asteroid belt. They produced a reduced age for the Taurids of about 6000 years, with ejection of particles occurring approximately 4700 and 1500 years ago.

Identification of Northern and Southern branches requires a large dataset of precise photographic meteoroids. These branches were first isolated by Wright and Whipple (1950), who found structure comprising four branches in the stream. Kresák and Porubčan (1970) used a larger dataset to show that there were only two branches. The existence of two branches also implies an age of in excess of ~ 5500 years, as this is the minimum time required for the two branches to have been produced by the same parent comet (Jenniskens, 2006).

Steel and Asher (1996) found that an age of ~ 10000 years is consistent with the dispersion of orbital elements found for Taurid meteoroids. However, this scenario required higher ejection velocities than are consistent with the ejection of particles from Comet 2P/Encke. In addition, ejection near aphelion was found to be unable to produce this dispersion. Other age estimates include those of Levison and Duncan (1994) who found $\sim 2 \times 10^4$ years, and Jones (1986) who found a much greater age of $\sim 10^5$ years. The age of the Taurid stream is still highly uncertain.

Clube and Napier (1984) expanded the fragmentation theory first proposed by Whipple (1940), and hypothesised that a giant comet entered the inner Solar System and assumed an orbit similar to Comet 2P/Encke. It was thought to suffer a breakup event that produced Comet 2P/Encke and other asteroidal-type fragments that are observed to have orbits similar to the Taurid meteoroids. They make connections between Earth climate conditions and bombardment events on Earth and the presence of such a giant comet. This comet may have left a moderately large remnant (perhaps 30 km in diameter) that may no longer exhibit cometary activity. This object may have fragmented on more than one occasion over the past 20000 years, and may have produced dust through both cometary activity and during the fragmentation events. The breakup event producing comet Encke was thought to have occurred about 5000 years ago, or at a much earlier point.

Clube and Asher (1990) use observations of dust streams associated with the Taurids by the IRAS detector to hypothesis the presence of a swarm of particles at the 7:2 Jovian resonance. They suggest that this swarm is a result off, and perhaps direct observational evidence for, the giant comet hypothesis. Steel et al. (1991) studied the structure of the

Taurid meteoroid complex in photographic, TV and radar orbital element data archived by the IAU Meteor Data Center. They found evidence for clustering in semi-major axis at approximately 2.25 AU and at 1.91–2.1 AU. These correspond to the locations of the 7:2 resonance and 4:1 (or 9:2) resonances respectively. This may be evidence for a swarm at the 7:2 resonance.

Asher and Clube (1993) provide a detailed analysis of the characteristics and observational properties of a 7:2 resonance swarm. This includes a list of years in which it is expected that the geometry between the Earth and the swarm is favourable for observation of the swarm. While these years appear to agree with years of increased Taurid rates from 1938 to 1988, swarm at other nearby resonances would not be able to match these observations. In the following years several papers have found increased rates of visual meteoroids in years in which the swarm is expected to be near to the Earth (including Beech et al. (2004), Asher and Izumi (1998) and Dubietis and Arlt (2007)). A more complete review of this literature is found in Section 4.3.4.

Finally, we note that a breakup hypothesis is not the only model capable of populating the Taurid region with a number of observable asteroids. Valsecchi et al. (1995) find that dynamical processes involving secular resonances exist that allow asteroids to move from orbits within the Asteroid Belt to orbits within the Taurid region. However, such processes require several 10^5 years to work. This would imply a very old age for the Taurids that is much longer than that usually assumed for the stream or Comet 2P/Encke. Hence though a comet breakup model is not required to produce the observed population of asteroids with orbits similar to the Taurids, such a model is in better agreement with the expected age of the Taurid stream.

Furthermore, we would expect that the cumulative mass of the asteroidal objects in the Taurid region would be indicative of the total size of the cometary body that produced them (though of course this would not account for the loss of a fraction of the mass the original object, particularly in the form of small dust particles). Indeed, large objects of size $\sim$ 1 km exist in the Taurid region, including 2004 TG_{10}. Nevertheless, Jenniskens (2006) calculates that even if it is assumed that 20 large objects exist, most of which are unobserved, the original size of the 'giant comet' would not exceed 15 km in diameter. As this is the size of comet Halley, this does not represent a giant comet. Moreover, the theory implies that the asteroidal bodies we observe are actually extinct cometary fragments. This seems unlikely given that all except one of the objects associated with Comet Encke have asteroidal spectral types (Jenniskens, 2006).

Regardless of the validity of the giant comet fragmentation hypothesis, it is still possible that there exists a Taurid resonant swarm at the 7:2 resonance with Jupiter. This is supported by visual meteor data. In this thesis we are interested in the observability

of this swarm in meteor orbit radar data.

1.5 Purpose and Content of the Thesis

The purpose of this thesis is to evaluate the detectability of meteoroid resonances with meteor radar systems. Currently, resonance swarms have been identified in visual and photographic meteoroid datasets that, while precise, have low number statistics. Radar meteoroid individual orbits are less accurate, but are available in large numbers and additionally probe a different part of the dust mass range, sensing relatively small particles. Thus use of radar for resonance studies has the potential to provide new information on the properties of these resonant swarms.

To this end, this thesis studies the observability of a resonant swarm in the Taurid meteoroids stream associated with the 7:2 Jovian resonance, evidence for which has been found only in visual data (see Section 4.3.4). We approach this problem in two ways. First, we search for evidence of this swarm in Canadian Meteor Orbit Radar data (see Section 3.2.3), and analyse what improvements to present radar systems would permit the identification of such a swarm. This involves a variety of statistical techniques. This work is given in Chapter 4.

Second, numerical integrations are used to analyse the properties of the 7:2 Jovian resonance, and to determine the mass range of particles likely to be trapped in this resonance. Chapter 5 introduces these methods and determines the resonance width of the 7:2 resonance; while Chapter 6 develops a simple cometary ejection model in order to establish how resonant trapping of particles may occur. This latter search also demonstrates the effects of radiation pressure on such ejected particles.

Chapter 2

Relevant Dynamics

This chapter elaborates on relevant dynamical considerations, including the parameters used to describe meteoroid orbits, and the forces that act to change these orbits. Further detail on dynamics, with particular reference to resonance effects, is given in Chapter 5.

2.1 Orbits

Orbits of objects within the Solar System are usually described by one of two sets of coordinates. In general, at least six independent coordinates are required to describe an orbit in three dimensional space (three for its position; and three for its velocity). The most simple such system is that defined by heliocentric Cartesian coordinates: that is, a Sun-centred coordinate system where X and Y vectors are perpendicular and form a plane that lies within the ecliptic plane, and the Z vector is perpendicular to both X and Y vectors. The position and velocity of the particle can then form a set of coordinates X, Y, Z, V_X, V_Y, V_Z. The orientation of the vectors is usually such that the X axis points to the vernal equinox: that is, the point of the celestial sphere at which the Sun is located at the vernal equinox - also known as the first point of Aries.

In many situations, a system of coordinates that more easily describes the shape, orientation and position of the orbit is required. Thus, for describing orbital motion it is most common to use orbital elements based on the elliptical configuration in space.

2.1.1 Orbital Elements

The orbital motion of a body around a star, as a two dimensional ellipse, parabola or hyperbola in a three dimensional celestial sphere, may be uniquely described in terms of six orbital elements, as given in Table 2.1, and shown in Figure 2.1.

The six elements are defined as follows. The semi-major axis is a measure of the size of the orbit, given by a in Figure 2.1(b). In the elliptical case (the only case of concern in this thesis) the semi-major axis is half the length of the major axis of the ellipse. The eccentricity defines the shape of the ellipse, and is defined by $e = \frac{\sqrt{a^2-b^2}}{a}$, where a is the

Orbital Element	Symbol	Defines	Range
Semi-major Axis	a	orbit size	0.5AU – ∞
Eccentricity	e	orbit shape	0–1 ellipse > 1 hyperbola =1 parabola
Inclination	i	orientation of orbit in orbital plane	$0 - \pi$
Longitude of Ascending Node	Ω	orientation of orbit	$0 - 2\pi$
Argument of Perihelion	ω	orientation of orbit	$0 - 2\pi$
True Anomaly	ν	position in orbit	$0 - 2\pi$

Table 2.1: Elements of the Orbit.

semi-major axis and b the semi-minor axis (see again Figure 2.1(b)). Inclination I or i defines the tilt of the orbit, and is the angle between the ecliptic plane (the plane of the Earth's orbit) and the plane of the orbit. The longitude of the ascending node Ω defines the location of the ascending node of the object, and thus provides the orientation of the orbital plane with respect to the vernal equinox. An elliptical orbit has two nodes, or locations where the orbit crosses the ecliptic plane. The ascending node is that where an object on the orbit will cross from south of (below) the ecliptic plane to north of (above) it; the descending node is that where the opposite occurs. The longitude of the ascending node Ω is thus the angle between a reference point (the vernal equinox is standard) and the ascending node. The argument of perihelion ω defines the orientation of the ellipse in the orbital plane, and is the angle between the ascending node and the perihelion point. Alternatively, the longitude of perihelion ϖ is sometimes used, being the 'dogleg' angle that results from the addition of the longitude of the ascending node and the argument of perihelion: $\varpi = \Omega + \omega$.

Finally, a variable is required that provides information on the location of an object in this orbit: for this purpose we will use either the true anomaly ν or the mean longitude λ. The true anomaly describes a physical angle between the perihelion point and the location of the object (see Figure 2.1(b)). The mean longitude, however, describes the angle of the object on an 'eccentric circle' of radius a, thus is not a geometric angle on the orbit. The mean longitude is sometimes convenient as it can be calculated using $\lambda = M + \varpi$, where M is the mean anomaly, which can be calculated using any of:

$$M = (T - t)n = \frac{2\pi t}{T} = \sqrt{\frac{\mu}{a^3}}t$$

where T is the orbital period, t is the time of perihelion passage, and n is the mean motion

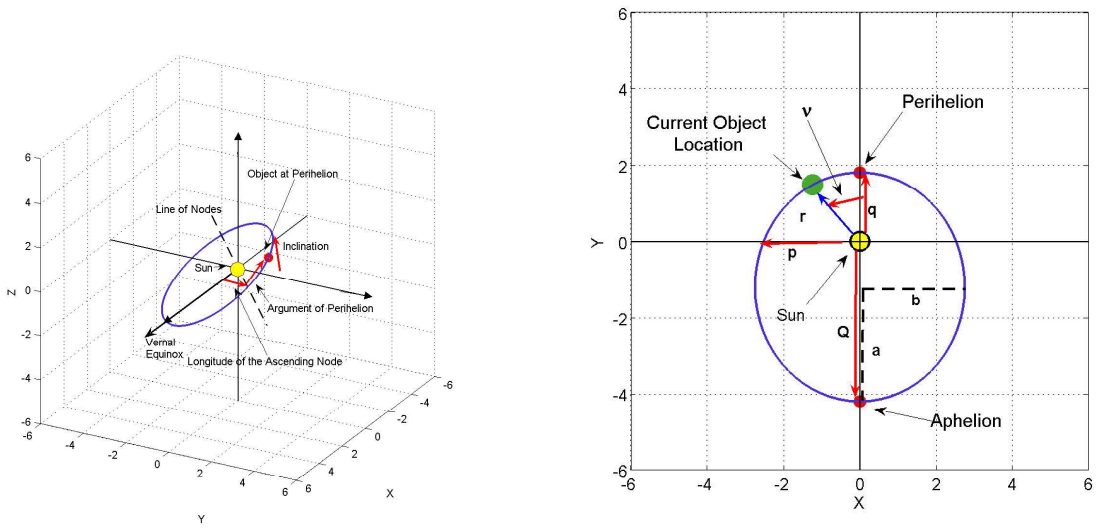

(a) (b)

Figure 2.1: *Orbital Elements, defined for a prograde orbit with* $a = 3$ *AU,* $e = 0.4$*,* $\Omega = 40°$*,* $\omega = 50°$*, and inclination is (a)* $40°$ *and (b)* 0*. In (a) we see the main angular parameters for an inclined orbit, and in (b) we have an orbit with no inclination in order to demonstrate the remaining orbital elements and other parameters of interest.*

given by:

$$n = \sqrt{\frac{\mu}{a^3}} = \frac{2\pi}{T}$$

where $\mu = G(M_\odot + m)$, where G is the gravitational constant, m is the mass of the orbiting object and $M_\odot$ is the mass of the sun. For cometary and meteoroid bodies, the approximation $\mu = GM_\odot$ is sufficient.

A conversion between the true anomaly and the mean longitude is given by:

$$\lambda = M + \varpi = E - e \cdot \sin E + \varpi$$

using mean anomaly $M = E - e \cdot \sin E$. E is the eccentric anomaly, given by:

$$E = 2 \cdot \arctan \sqrt{\frac{1+e}{1-e}} \tan \frac{\nu}{2}$$

A reverse conversion requires an iterative solution for the eccentric anomaly E.

Other orbital parameters in general use include:

- **The perihelion distance** q**:** This is the distance from the Sun (at the focus of the ellipse) to the perihelion position on the orbit (the closest point of the orbit to the Sun). It can be calculated by $q = a(1 - e)$.

- **The aphelion distance Q:** Similarly, the aphelion distance is the distance from the Sun to the aphelion point (the furthest point on the orbit from the sun). It is calculated by $Q = a(1 + e)$.

- **The semilatus rectum p:** This is the distance from the Sun 90° from perihelion, given by $p = a(1 - e^2)$.

- **The heliocentric distance r_h:** This is simply the distance of the object from the Sun, and is given by $r_h = \frac{a(1-e^2)}{1+e\cos\nu}$. In Cartesian coordinates it is equal to the modulus of the position vector $r_h = \sqrt{X^2 + Y^2 + Z^2}$.

- **The angular momentum per unit mass h:** This is the cross product of the position vector r_h and the velocity vector v. For an elliptical orbit: $h = \sqrt{a(1 - e^2)\mu}$.

These parameters allow us to transform from orbital elements to heliocentric Cartesian coordinates if required:

$$X = r_h(\cos\Omega\cos(\omega + \nu) - \sin\Omega\cos(\omega + \nu)\cos i)$$

$$Y = r_h(\sin\Omega\cos(\omega + \nu) + \cos\Omega\sin(\omega + \nu)\cos i)$$

$$Z = r_h(\sin(\omega + \nu)\sin i)$$

$$V_X = \frac{Xhe}{r_h p}\sin\nu - \frac{h}{r_h}(\cos\Omega\sin(\omega + \nu) + \sin\Omega\cos(\omega + \nu)\cos i)$$

$$V_Y = \frac{Yhe}{r_h p}\sin\nu - \frac{h}{r_h}(\sin\Omega\sin(\omega + \nu) - \cos\Omega\cos(\omega + \nu)\cos i)$$

$$V_Z = \frac{Zhe}{r_h p}\sin\nu + \frac{h}{r_h}(\cos(\omega + \nu)\sin i)$$

2.2 Gravitational and Non-Gravitational Effects

The above section describes an elliptical - thus recurrent - orbit around the Sun or any gravitating object (in the Newtonian case). Such an orbit of a meteoroid or other body in the Solar System is subject to gravitational and non-gravitational effects. In some cases these perturbations can cause the particle to move from an elliptical to a hyperbolic orbit, which may cause the particle to be lost from the Solar System. In many cases, the particles remain in bound orbits around the Sun, but may display dynamical features that indicate the effects of forces other than solar gravity. In this thesis we are primarily concerned with resonant perturbations. However, we first summarise the full extent of the

perturbations that can affect objects in the Solar System in order to understand which are likely to be important at the mass scales probed by meteor radar.

2.2.1 Gravitational Effects

Gravitational forces on a given meteoroid are largely those of the Sun or star and planetary bodies. The gravitational force of the Sun dictates the main elliptical, hyperbolic or parabolic form of the particle's orbit around the Sun. More interesting are the effects of planetary bodies, especially the larger gas giants. These bodies can produce planetary perturbations, which can be significant for particles passing sufficiently close to Jupiter or Saturn, or resonant effects - with particles in or near resonances with giant planets experiencing enhanced gravitational effects. The effect of gravitational perturbations depends on the closest approach distance of a particle to a given planet, and a sphere of gravitational influence can be defined around a planet inside which the gravitational effect of the planet on a small body is significant. Often a Hill's sphere is used for this purpose. Only the largest gas giants are expected to produce significant perturbations, though in some cases it is important to include the effects of all planets. Numerical methods are usually required to solve this three (or greater) body problem of the dynamics of the Sun, giant planet and meteoroid particle. Further details on solving the three body problem are given in Chapter 5.

Resonance effects occur when a commensurability of orbital periods exists. Here we are concerned primarily with mean motion resonances, which occur when the orbital period of the particle is a small-order ratio of the period of a given planet. For example, a particle in the $3:1$ Jovian resonance has an orbital period one third of that of Jupiter. Resonances are responsible for many dynamical structures in the Solar System, including Kirkwood gaps in the asteroid main belt, where the overlap of mean motion resonances, secular and secondary resonances creates chaotic motion that clears regions around low-order Jovian resonances (Murray and Dermott, 1999). Section 4.1 provides more detailed information on resonances in the Solar System.

Similarly, resonant perturbations may affect dynamics of meteoroid streams. Lindblad (1973) published the first attempt at searching for such effects in meteor data. He found considerable fine structure correlated with Jovian resonances in a histogram of $1/a$ for 1822 photographic meteoroids, and concluded that this structure was real. It is also possible for resonant swarms to develop within meteoroid streams, particularly when the parent body is in or near libration. A full review of the literature on resonances in meteoroid streams is given in Section 4.3.

Certain resonances, such as the 3:1 Jovian resonance, have the potential to act as a transport mechanism for meteoroids from the main asteroid belt. As mentioned above,

the main sources of meteoroids are comets and asteroids. However, meteorites - that is, objects that reach the Earth's surface - originate largely from the asteroid main belt. This is because it is difficult for comets to be able to eject meteoroids of sufficient size, of sufficient density, or of sufficiently low speed to survive passage through the Earth's atmosphere (despite these limitations, Campins and Swindle (1998) review material that indicates that cometary meteorites should exist, though they will be rare). Two main sources of asteroidal meteorites exist: Earth-crossing asteroids; and main belt asteroids. Collisions in the asteroid main belt can produce asteroid or meteoroid-sized fragments. One main mechanism for transporting such fragments to Earth crossing orbits is through interactions with Jovian (or Saturnian) resonances. Collisions can alter the orbital periods of asteroid and meteoroid-sized fragments such that they move into resonant regions. This mechanism can act to continually replenish resonances. Thus, there always exists a small population of objects, of asteroid and meteoroid sizes, even in well-defined Kirkwood gaps. Overlapping of resonances in low-order mean motion resonances creates chaotic regions, and objects that move into these regions can undergo rapid increases in eccentricity, followed by a decrease in the perihelion distance. This allows objects to move into Earth-crossing orbits, providing a continuing supply of Earth-crossing asteroids and meteoroids. For observed Near-Earth asteroids, approximately $(37 \pm 8)\%$ do so due to the ν_6 secular resonances with Saturn, and $(23 \pm 9)\%$ due to the 3:1 mean motion resonance with Jupiter. The remaining $(33 \pm 3)\%$ are from various other secular and mean motion resonances in the main belt (et al, 2003).

2.3 Radiation forces on Interplanetary Dust

Gravitational effects, including perturbations and resonance effects, affect all meteoroids in the Solar System. However, for some particles non-gravitational radiation effects may be significant or dominant. These include the Poynting-Robertson, the diurnal and seasonal Yarkovsky-Radzievskii effects, and solar radiation pressure effects. Such influences are most important for smaller particles, which have a high surface area to mass ratio. In consequence, radiation effects that act on the surface area are important compared to gravitational effects, which are dictated by the mass of the particle. Magnetic forces arising from any charge carried by the dust particles can also affect the motion of particles: this is particularly true if these particles interact with the solar or Jovian magnetic fields.

2.3.1 Solar Radiation Pressure and the Poynting-Robertson Effect

The force exerted by photons of solar radiation on a particle can be divided into radiation pressure, which applies an outward radial force and acts to remove the smallest particles

from the Solar System, and the Poynting-Robertson effect, which exerts a drag force that causes particles to spiral into the Sun on long timescales.

Radiation pressure is the result of the absorption of solar radiation. In consequence, the meteoroid receives a radially-directed outward force due to the momentum possessed by the photons. This pressure is proportional to the cross-sectional area of the absorbing particle, its albedo and the flux of the solar radiation field.

Poynting-Robertson drag occurs on re-radiation of encountered photons, and is the result of the transverse velocity of the particle. This re-radiation is, in the simplest cases, isotropic, and thus the particle feels no net force in its own frame. However, in the rest frame of the Sun, photons emitted in a forward direction relative to the orbital motion of the particle are relatively blueshifted (frequency increased) by the Doppler effect (and redshifted (frequency decreased) in the opposite direction): thus, more momentum is emitted in a forward direction. This creates a net braking force on the particle, which causes it to very slowly spiral inwards towards the Sun. Anisotropic emission and scattering are also important, particularly when the particle is irregularly shaped and has a fixed spin axis, in which case scattering is non-uniform and the particles are dispersed.

The Poynting-Robertson drag effect was first correctly described by Robertson(1937). The formalism used was complex, relying on the metric of special relativity for a mathematical description. However, Burns et al. (1979) show this is not necessary, and the Poynting-Robertson effect - and, indeed, the radial radiation pressure force - can be derived from purely classical considerations. They show by two separate approaches that the total force exerted by a solar photon on a dust particle, considering both absorption and scattering of photons, is given by the equation of motion:

$$m\dot{\mathbf{v}} \approx \frac{SA}{c} Q_{pr}[(1 - 2\dot{r}/c)\hat{\mathbf{r}} - (r\dot{\theta}/c)\hat{\theta}]$$

where m is the mass of the particle, $\dot{\mathbf{v}}$ is its acceleration, S is the integrated flux density of the solar radiation beam (Wm^{-2}), A is the geometrical cross-section of the heliocentric particle, c is the speed of light, $\dot{r} = \mathbf{v} \cdot \hat{S}$, and $\dot{\theta}$ is an angular velocity such that the particle velocity $\mathbf{v} = \dot{r}\hat{r} + r\dot{\theta}\hat{\theta}$ and $\hat{\theta}$ is normal to $\hat{\mathbf{r}}$. $Q_{pr} \equiv Q_{abs} + Q_{sca}(1 - < \cos\alpha >)$ is the radiation pressure coefficient, where Q_{abs} and Q_{sca} are the absorption and scattering coefficients, and represent the fractions of energy scattered and absorbed. In Q_{pr}, non-isotropic scattering is considered in the $< \cos\alpha >= \int_{4\pi} f(\alpha) \cos\alpha \mathrm{d}\chi$ term, with $\mathrm{d}\chi = 2\pi \sin\alpha d\alpha$, $f(\alpha)$ the phase function of the scattered particle and α is the angle between the scattered light and the incident beam. Since Q_{pr}, Q_{abs} and Q_{sca} depend on wavelength, often an average value integrated over the solar spectrum is used.

In this equation, the radiation pressure force is given by the constant radial term,

and the Poynting-Robertson drag by the velocity-dependent components.

2.3.2 Solar Wind Corpuscular Effects

The solar wind, comprised of continuous streams of charged electrons, protons and He^+ ejected from the upper atmosphere of the Sun, is also able to affect the dynamics of Solar System dust particles. This is similar to the force of solar radiation, but produces a much smaller effect due to the low, non-relativistic speeds of solar wind particles (of $\sim 350 \mathrm{kms}^{-1}$: 10^3 less than the speed of photons). The equivalent of radiation pressure by solar wind particles is not significant compared with the photon radiation pressure. The Poynting-Robertson solar wind drag can be important, however, because the aberration angle of the solar wind between the velocity of the particle and that of the solar wind $(\tan v/{v_{sw}}^{-1})$ is much larger than for solar radiation - given by $\tan v/c^{-1}$ (Meyer-Vernet, 2007). The ratio of the solar wind drag to the Poynting-Robertson radiation drag is about 30% of the total radiation effect (Grün et al., 2001). However, for particles with radii less than about one micron in size, this ratio increases significantly, being ~ 10 at a radius of $\sim 5 \times 10^{-2}$ μm (Burns et al., 1979).

2.3.3 Poynting-Robertson Timescales

The timescale on which a particle spirals from its current position to the Sun under the Poynting-Robertson effect is important for determining whether this effect creates a noticeable variation in a given particle's motion in a given time-frame. This timescale is related to the particle radius s (m) (or mass) and density ρ (kgm^{-3}), the energy output of the Sun L_0 (W), and the radiation pressure coefficient Q_{pr} (equal to 1 for pure absorption and 2 for direct reflection). It is usually defined approximately for an initial circular orbit as:

$$\tau_{pr,circ,0} = \frac{1}{4}\frac{16\pi c^2}{3L_0}\frac{\rho s}{Q_{pr}}a_{in}^2$$

for objects to spiral from $a = a_{in}$ to $a = 0$ (that is, the Sun). If necessary, this can be generalised to:

$$\tau_{pr,circ,a} = \frac{1}{4}\frac{16\pi c^2}{3L_0}\frac{\rho s}{Q_{pr}}[a_{in}^2 - a^2]$$

in order to calculate the time for the particle to reach a semi-major axis of a from its current position a_{in} under the Poynting-Robertson effect.

Inserting the constants for the $a = 0$ case produces:

$$\tau_{pr,circ,0} = 2.2 \times 10^{13}\frac{\rho s}{Q_{pr}}a_{in}^2$$

in seconds ((Grün et al., 2001)) or:

$$\tau_{pr,circ,0} = 7.0 \times 10^5 \frac{\rho s}{Q_{pr}} a_{in}^2$$

in years ((Dohnanyi, 1978) and (Klačka and Kocifaj, 2008)). In both cases the semi-major axes values are in AU. This formula can be derived for the circular case by integrating

$$\frac{\mathrm{d}a}{\mathrm{d}t} = \frac{-3E_0 Q_{pr}}{16\pi c^2 s\rho} \frac{(2+3e^2)}{a(1-e^2)^{3/2}}$$

with $e = 0$.

The finite e case is more difficult, requiring the integration of $\frac{\mathrm{d}a}{\mathrm{d}t}$ and

$$\frac{\mathrm{d}e}{\mathrm{d}t} = \frac{-5}{2} \frac{3E_0 Q_{pr}}{16\pi c^2 s\rho} \frac{e}{a^2(1-e^2)^{1/2}}$$

However, an analytic solution is possible, and produces the unexpected result that the Poynting-Robertson timescale is large for very small particles. However, the solar wind drag has an increased efficiency at these mass scales and acts to lower the inspiralling time.

A typical timescale for a perfectly absorbing particle ($Q_{pr} = 1$) with radius $s = 10^{-6}$m and density $\rho = 1000\mathrm{kgm}^{-3}$ starting at $a = 1$AU with $e = 0$ to spiral into the Sun (and thus be lost from the system by evaporation) is ~ 2450 years. A similar particle, but with a radius $s = 10^{-2}$ m, will take $\sim 24.5 \times 10^6$ years.

2.3.4 Yarkovsky-Radzievskii effect

A further effect of solar radiation is the Yarkovsky-Radzievskii effect, which is the result of non-isotropic emission from a rotating object. Two main types are usually distinguished: a diurnal version, in which the particle rotates between absorption of radiation on one hemisphere (the 'daytime' hemisphere) and emission; and a seasonal type, in which the warmer summer hemisphere absorbs radiation from a different direction to that in which it is emitted, because of a thermal-lag delay in re-emission. Due to the dependency of this effect on a number of variables - including the size and direction of rotation, and variations in emission due to irregular surface features - dust grains have largely arbitrary spin axes orientations, and the net effect of the Yarkovsky effects is dissipative. Yarkovsky effects are also small because of the low temperature differences between day and night-time sides of the particle: this is only 0.04 K for a 200μm diameter silicon particle, and ~ 0.0009 K for an iron grain (Jenniskens, 2006). This effect is most important for large particles: by considering figures in Burns et al. (1979) (p. 39) it is possible to estimate that particles

with radii greater than 0.1 m may have a Yarkovsky to Poynting-Robertson force ratio of greater than one, and particles less than 10^{-4}m will have a ratio $<< 1$. These values are dependent on the spin rates and composition of the affected particles. The Yarkovsky force F_Y to gravity force $F_{grav,max}$ ratio is approximately:

$$\frac{F_Y}{F_{grav,max}} \approx 5 \times 10^{-8} r_h^{-3/2}$$

where r_h is the heliocentric distance in AU. It is apparent that the Yarkovsky effect applies only a small perturbation to particle orbits, though this can affect the smooth inspiralling or long-term stability of objects (Burns et al., 1979).

2.3.5 Variations with particle size

It is clear that the above radiation effects will,except for the Yarkovsky-Radzievskii effect, only have a significant effect on low-mass particles. It is important to gain an idea of the mass regions for which radiation forces are negligible. For this purpose it is useful to define the parameter β as the ratio between the radiation force F_r and gravitational force F_g experienced by a particle. The gravitational force is expressed by:

$$F_g = \frac{GM_\odot m}{r_h^2}\hat{\mathbf{r}} = \frac{4}{3}\frac{\pi s^3 \rho G M_\odot}{r_h^2}\hat{\mathbf{r}}$$

where G is the gravitational constant, $M_\odot$ is the mass of the Sun, m is the particle mass, r_h is the distance of the particle from the Sun, s is the effective radius of the particle, and ρ is its density. $\hat{\mathbf{r}}$ indicates that the force is radial. The radiation pressure force is:

$$F_r = \frac{SAQ_{pr}}{c}\hat{\mathbf{r}} = \frac{L_0 s^2 Q_{pr}}{4\pi r_h^2 c}\hat{\mathbf{r}}$$

where S is the radiation flux of the Sun at distance r_h, A is the geometrical cross-section of the particle, L_0 is the solar luminosity, and Q_{pr} is the radiation pressure coefficient (as given above). This allows us to define β by:

$$\beta = \frac{F_r}{F_g} = \frac{3L_0 Q_{pr}}{16\pi G M_\odot c \rho s} = 5.7 \times 10^{-4}\frac{Q_{pr}}{\rho s}$$

which is now only dependent on particle properties (SI units).

Thus, for a purely absorbing particle (nearly true for particles larger than the effective wavelength of light, for which $< Q_{pr} > \approx 1$) with effective radius $s = 10^{-6}$ m, and density $\rho = 1000$ kgm^{-3}, we have $\beta = 0.57$ (Grün et al., 2001). From simplistic physical considerations, it can be seen that a particle with $\beta > 1$ has a stronger radiation

force than gravitational force, and will feel a net radiation pressure away from the Sun: it will be removed from the Solar System. However, when calculated fully particles only require $\beta > 0.5$ (even when $e = 0$) to be removed in this way. A particle with $\beta < 1$ (or $\beta < 0.5$) has a stronger gravitational effect than radiation effect, and will spiral into the Sun by the Poynting-Robertson effect on a timescale dependent on its physical properties. Broadly, it will take longer for the orbit of a more massive particle to undergo a significant change due to the Poynting-Robertson drag, and the importance of this drag effect will be dependent on whether the inspiralling time is significant relative to the time frame of interest.

Composition has a strong influence on the importance of radiation effects as a result of the density inverse proportionality of β. In general, β is sufficiently small for particles of radius greater than ~ 10 μm and less than 0.01 μm that these particles will not be pushed out of the Solar System. However, they may suffer small orbital perturbations. The peak in β for most materials is at ~ 0.1 μm. The reason for the decrease in the importance of radiation for particles smaller than this peak is that the characteristic wavelength of solar radiation is ~ 0.5 μm, which is too large relative to the particle size for significant absorption or scattering to occur. The ratio β is particularly large for graphite and various metals, and does not decrease as quickly for very small particle sizes (Burns et al., 1979). For the Poynting-Robertson effect, we consider the time taken for a particle to spiral in by 1% (to 99%) of its initial semi-major axis, when started at a semi-major axis of $a = 1$ AU. This is equivalent to:

$$\tau_{pr,circ,0} = 7.0 \times 10^5 \frac{\rho s}{Q_{pr}} [a_{in}^2 - (0.01 \times a_{in})^2]$$

Considering particles on circular orbits with a Q_{pr} of 1 and a density of $2 \times 10^3 \mathrm{kgm}^{-3}$ (roughly equivalent to graphite), a particle of radius 1 μm will spiral in to 0.99 AU in 1400 years; a particle of radius 20 μm will take 28000 years. Thus, a particle of 20 μm (the lower limit for the AMOR radar: see Section 3.1) will only suffer significant inspiralling under the Poynting-Robertson effect on very long timescales. At finite eccentricities the problem is more complex, generally increasing the timescales for very small particles. However, in this regime the solar wind drag becomes important (below ~ 1 μm): it is judicious to consider the Poynting-Robertson effect for all very small particles, in consideration of the time period of interest.

2.3.6 Electromagnetic Forces

Dust particles in the Solar System are also subject to electromagnetic effects, due to the interaction of their charge with the interplanetary magnetic field associated with the solar

wind. Particles acquire this charge largely by the photoelectric effect: photoemission of electrons after the absorption of ultraviolet solar radiation. This process is usually dominant as a charging mechanism over capture of solar wind electrons. Such particles usually have a small positive surface potential of $U \approx 5$V due to the photo-electric effect. The charge of a spherical particle can then be given by $q = 4\pi\epsilon_0 U s$, with ϵ_0 the permeability of vacuum, and s the particle radius. This can be generalised for non-spherical particles to $q = \epsilon_0 \eta U m^{1/3}$ where η is a constant containing information on the shape, structure and density of the particle (with $\eta = 7.8\rho^{1/3}$ for a sphere with density ρ). The electromagnetic Lorentz force exerted on the particle is then:

$$\mathbf{F}_L = q\mathbf{v}_{rel} \times \mathbf{B}$$

(Gustafson, 1994). Here $\mathbf{v}_{rel}$ is the velocity relative to the field, and the interplanetary magnetic field $\mathbf{B}$ (Parker spiral) is often expressed in spherical coordinates as:

$$B_r = B_{r0}(\frac{r_0}{r_h})^2$$

$$B_\phi = B_{\phi 0}(\frac{r_0}{r_h})\cos\theta$$

$$B_\theta = 0$$

where $\theta = 0$ is the latitude from the solar equatorial plane. The ratio of the Lorentz force to the solar gravitational force is:

$$\frac{F_L}{F_{grav}} \propto s^{-2} r_h$$

Thus, we see that Lorentz forces are important for small particles and at large heliocentric distances (Grün et al., 2001).

The size and direction of these Lorentz forces depend on the polarity of the solar magnetic field. Since this polarity varies faster (with the 11 year solar cycle) than the orbital period of typical micron-sized particles, the long-term average effects expected are small.

The solar magnetic field has a marked affect on small, interstellar particles entering the Solar System. In general, the motion of a 10 nm sized particle is dominated by Lorentz forces, while a 10 μm particle will feel little of this effect. Due to the variations in polarity, such particles are either deflected towards or away from the solar equatorial plane ($\sim 7^\circ$ variant from the ecliptic plane): they are alternately prevented from reaching the ecliptic plane and then concentrated to it. However, over the ~ 20 years it takes for interstellar

particles to travel the distance from the boundary of the heliosphere ($\sim$ 100 AU from the Sun) to the ecliptic plane, they will be affected by both polarities. This increased filtering of small interstellar dust particles in solar minima has been detected by the Ulysses dust detector (Krüger and Grün, 2009).

2.3.7 β Meteoroids

To understand the effect of radiation forces on the meteoroid distribution in general, potential particle sources resulting from such radiation effects must be identified. One possible detectable source of particles is β-meteoroids (see Section 2.3.5). These are interplanetary particles small enough to have a sufficiently large surface area to mass ratio to be significantly affected by solar radiation pressure, and thus have $\beta > 1$ (though a value of $\beta = 0.5$ is sufficient for the particle to escape from the Solar System) (Zook and Berg, 1975). Such particles can be detected on hyperbolic orbits moving out of the Solar System, with origins in collisions or partial evaporation of micrometeoroids close to the Sun.

β-meteoroids were first detected by cosmic dust sensors on the Pioneer 8 and 9 spacecraft (Berg and Grün, 1972). Subsequent measurements were made by the HEOS-2, Helios 1 and Ulysses missions. Zook and Berg (1975) were the first to name these particles β-meteoroids and to investigate potential sources. One potential formation mechanism is collisions of particles near the Sun. These collisions can produce fragments sufficiently small that the effect of solar radiation pressure creates particles on hyperbolic orbits. Another important mechanism may be partial vaporisation of particles that have spiralled towards the Sun by the Poynting-Robertson drag force. Radiation effects on such particles then exceed gravitational effects, thus creating hyperbolic particles. However, Zook and Berg (1975) conclude that collisional processes should be more efficient. This they justify by calculating collision probabilities for particles spiralling towards the Sun under Poynting-Robertson, showing that most of the mass of meteoroids will suffer a catastrophic collision before they are close enough to the Sun for vaporisation to occur. Later studies such as Mann et al. (2000) show collisional formation of β-meteoroids is still most consistent with observations.

Also detected is a population of more massive and more energetic β-meteoroids in the apex direction of spacecraft. These particles were later associated with a separate formation mechanism, and named α-meteoroids, by Grün and Zook (1980). In this scenario, so-called α-meteoroids, with origins in collision fragments, are too large to spiral outwards from the Sun like β-meteoroids and instead are observed spiralling inwards under the Poynting-Robertson effect. These particles are intermediate in mass between β-particles and the larger 'sporadic' particles, whose dynamics are dominated by solar gravity and

show no apparent directionality. Zook and Berg (1975) discuss also the possibility that there exist two distinct classes of particles: sporadic and β meteoroids. These would be visible in the mass distribution as two peaks - one for sporadics, and another (at smaller masses - $\sim 10^{-15}$ to 10^{-12} g) for β-meteoroids. Microcratering observations of the Moon may support this (Schneider et al., 1973). Grun and Zook (1980) expand this to three sources: α, β and sporadic meteoroids.

Results from the Ulysses dust experiment have provided important insights. In particular, this mission detected a significant flux of β-meteoroids at high inclinations (Wehry and Mann, 1999). Hamilton et al. (1996) suggest that solar magnetic field variations on an 11-year solar cycle may be responsible for the presence of such particles, naming them 'electromagnetic β-meteoroids'. Wehry et al. (2004) further investigate the non-negligible electromagnetic effects on β-particles created further than 0.5 AU from the Sun, and conclude that the Lorentz force can deflect these particles such that they are deflected out of the ecliptic during one polarity of the solar cycle (for example, 1991-2002), and focussed towards the ecliptic in the other (for example, 2002-2013).

2.4 Collisions

We also expect collisions between interplanetary particles to alter their orbits or destroy them. These collisions will remove particles from the meteoroid stream on a 'collision timescale' that is a function of both the mass of the particle and of its orbital elements. This timescale provides one estimation of the expected lifetime of a particular size of particles in a given stream. The lifetime of the particle will also be affected by various radiation effects, as given above. It is expected that the collision lifetime will have a minimum for particles of radius $\sim$ 1 mm (10^{-3} m). This is a result of an equilibrium condition between the increasing meteoroid cross-section and the decreasing population of meteoroids able to cause fragmentation.

Early estimates of the collision timescale were found by Dohnanyi (1978), who found a collisional lifetime of 1×10^4 years for 100 μm particles and 3×10^3 years for 1 mm particles. The model of Leinert et al. (1983) produced improved estimates by accounting for the semi-major axis and eccentricity of the orbit: at 1 AU this model gives 2×10^5 years for 100 μm particles and 4×10^4 years for 1 mm particles. The model of Grün et al. (1985) investigates the variation of collision lifetime with mass at 1 AU. They find that particles with mass greater than $\sim 10^{-8}$ kg (or radius $\sim$ 100 μm) are removed on a timescale of $\sim 10^4$ years. They conclude that collisions are the most important removal mechanism for such particles, while the Poynting-Robertson effect is the main loss mechanism for particles of mass 10^{-13} to 10^{-8} kg. Finally, Steel and Elford (1986)

determine the collisional lifetimes for 1 mm particles of individual meteoroids streams, accounting for the effect of their semi-major axes, eccentricities and inclinations. For Southern Taurids they find a collisional lifetime of $(85-90) \times 10^3$ years; for the Northern Taurids they find $(59-67) \times 10^3$ years.

Given that radar particles have radii less than about 1 mm, we can consider these values upper estimates for the Taurid stream. We expect the lifetimes of radar Taurid particles to be limited by collisions, and not by the Poynting-Robertson effect. Their lifetimes are likely to be between 6×10^4 and 9×10^4 years. This is in excess of the expected age of the Taurid stream of 10^4 to 2×10^4 years.

2.5 Summary

There is considerable dynamical structure in the Solar System dust cloud. It is valuable to know the dynamical structure in terms of the above effects in order to understand the formation of our Solar System, and hence be able to apply this knowledge to formation of planetary systems around other stars (Krivov, 2007). Geological studies of Solar System material, using both meteorites collected from Earth and returned material from various space missions (Lunar rocks from the Apollo and Luna missions, and cometary material from comet Wild 2 in the Stardust mission) have been valuable in understanding the origins of the Solar System (Russell, 2007). However, meteoroid studies can further explore the dynamical origins of the particles. Not all effects are important for all particles: gravitational effects dominate for larger particles; radiation effects for smaller particles. The relative importance of each type can be crudely understood using the ratio β: generally a β near to or greater than 0.5 indicates that radiation forces are able to expel particles from the Solar System. To study such radiation effects therefore requires a variety of detectors sensitive to particle mass on different levels.

Chapter 3

Determining Meteoroid Influx Trajectories: Observational Techniques

3.1 History and Development of Meteor Detection Methods

Meteoroids can be detected in two ways: either in-situ by use of dust-detectors on spacecraft; or by observation of the meteor phenomena produced by the meteoroid particles on impact with the Earth's atmosphere.

3.1.1 In-situ Detection of Meteoroids

Space detection of meteoroids began in 1950 when a ceramic microphone detector was attached to a V-2 rocket (Fechtig et al., 2001). The number of amplified signals received suggested a very high flux rate and led to suggestions of a dense 'dust belt' surrounding the Earth. It is now understood that a large number of the events recorded were most likely produced by other phenomena, and were not the result of particle detections (Grün, 2001).

Early satellites and space probes began to carry dust detectors, with the aims of studying dust particles as a component of the interplanetary system, and of determining the hazard such particles could pose to spacecraft. The latter aim focussed on relatively large particles (of size greater than 100 μm), as these pose the largest risk to satellites and spacecraft (Grün, 2001).

Later detectors investigated a variety of dust populations. These included the in-space dust at ~ 1 AU (Pioneer 8), in the inner Solar System (Pioneer 9 and Helios 1 and 2), and in the outer Solar System (Pioneer 10,11). Additionally of interest was the dust associated with various objects such as comets (Vega 1,2 and Giotto to Comet Halley; Stardust to Comet Wild 2) and to planets Jupiter (Galileo) and Saturn (Cassini). In addition, the Ulysses spacecraft travelled out to the orbit of Jupiter, then used a swing-by of this planet to reach an orbit inclined at 79° to the ecliptic plane. This allowed the spacecraft to obtain measurements of the dust distribution in three dimension (Krüger et al., 2007).

Highly sensitive impact ionisation detectors were developed by the dust group at the Max-Planck-Institut für Kernphysik in Heidelberg, Germany. First used on HEOS2, the detector size was increased by a factor of ten for inclusion on the Galileo and Ulysses spacecraft. Missions such as Stardust and Cassini also carried particle mass spectrometers/analysers in order to return information on particle compositions in addition to dynamics. Although particle collecting areas have been vastly improved since those on the earliest dust detectors, the incoming velocity direction of particles remains highly uncertain: producing uncertainties in individual velocities of a factor of 2 for (most recent) the Cassini mission (Altobelli et al., 2007).

Various advances made by space craft detectors include the discovery of the presence of β meteoroids leaving the Solar System on hyperbolic orbits by Pioneer 8 and 9 (and also Poynting-Robertson affected α meteoroids); discovery and understanding of interstellar meteoroids (various, including Pioneer 8 and 9 and Ulysses); discovery of Jovian dust streams from Io's volcanoes (Ulysses and Galileo); and achieving a greater understanding of the magnetic fields in the Solar System (in particular solar and Jovian) through their dynamical effects on interplanetary and interstellar particles (Grün, 2001). Enhancement of our understanding of dust dynamics, sources and behaviour can therefore lead to an improvement in our understanding of other Solar System processes.

3.1.2 Remote Sensing (ground-based) Detection of Meteoroids

Ground-based observations of meteoroids rely on the light and ionisation produced when a meteoroid is partially or fully vaporised in the Earth's atmosphere. A meteoroid which passes sufficiently close to the Earth may impact the atmosphere. It is the light and ionisation created by this impact that is termed a meteor. Here, collisions with air molecules heat the meteoroid surface. For meteoroids, where the free path of the air molecules (about 6 cm at meteor heights) is greater than the size of the meteoroid, no hydrodynamic cushion or 'air cap' is formed at the head of the meteoroid. Rather, the momentum and energy of each collision with air molecules is transferred to the meteoroid nucleus directly. The meteoroid is vaporised rapidly and little deceleration is observed before the body disintegrates. However, when the meteoroid is large compared with the free path of the air molecules, an 'air cap' is formed, which hinders the heat transfer and thus the vaporisation and also limits aerodynamic resistance. As a consequence, the meteoroid may penetrate significantly further into the atmosphere, and may hit the Earth as a meteorite before complete disintegration has occurred.

A special case exists for particles of mass less than $\sim 10^{-11}$ kg. As the ratio of the heat radiated to the heat absorbed via ablation is proportional to the ratio of surface area to volume, such particles may not reach sufficient temperatures for vaporisation.

They will be quickly decelerated in the atmosphere, and eventually settle to the ground as micrometeorites.

During their passage through the Earth's atmosphere more massive particles produce a meteor train consisting of excited and ionised atoms and molecules, and free electrons. This is formed from ablated (usually vaporised) atoms which are ionised in collisions with air molecules. Such a train may be 1m in width (at ~ 95 km), between 7 and 20 km long, and will persist while ablation occurs (usually at heights between 115 and 85 km).

Magnitudes

Before describing advanced visual methods of observing meteors, we discuss the role of apparent visual magnitudes. An apparent visual magnitude estimate provides the only means by which to estimate the size or mass of the observed meteoroid. Apparent magnitudes are a measure of the apparent brightness of an object from the distance at which they are observed. Absolute magnitudes are what their apparent magnitudes would be if the object was at a set observation distance - often 100 km for meteors - and in the zenith.

Originally devised as a mechanism by which to compare the brightness of stars, the magnitude is defined by:

$$M_1 - M_2 = 2.5(\log_{10} L_2 - \log_{10} L_1)$$

where M_1 and M_2 are the stellar or meteor magnitudes, and L_1 and L_2 are their respective luminosities. The result is a logarithmic inverse magnitude scale with an arbitrary zero point; such that a meteor of magnitude 7 has one hundredth of the luminosity of a magnitude 2 meteor. For reference, the Sun has an apparent magnitude -26; the brightest stars ~ -1. The visual limit for unaided naked-eye observations is $\sim 4-6$, depending on the conditions.

Meteor absolute magnitudes vary depending on the size, composition and the atmospheric velocity of the meteor, as well as the elevation of the meteor at observation. Empirical relationships are used to determine meteoroid masses from meteor magnitudes for visual, photographic and radar observations. For example, for radio meteoroids detected in the Harvard Radio Meteor Project in 1962 Verniani (1973) finds the following empirical relationship linking radio magnitude M, the pre-atmospheric velocity v_∞, the pre-atmospheric mass m_∞ and the zenith angle Z_R:

$$M = 62.3 - 9.8 \log_{10} v_\infty - 2.3 \log_{10} m_\infty - 2.5 \log_{10} \cos Z_R.$$

Observation Techniques

Visual observations dominated our understanding of meteor behaviour until the mid-1900s. Individual observers can record the apparent paths in the sky and their magnitudes. With multiple observers, information from two or more paths can be combined to determined the radiant, height, path length and velocity of the object. Accuracies of 10°-20° (inexperienced observers) to $\sim 1°$ (experienced observers) are achievable for radiant positions. However, velocity timing errors can be approximately 20-30%, and as such visual velocities are not reliable for dynamical information (Lovell, 1954).

Photographic techniques allow a significant improvement in radiant/position and velocity accuracy. High precision Super-Schmidt cameras can achieve $\sim 0.4\%$ accuracy in velocity and $\sim 0.1°$ in radiant position (Baggaley, 1995). However, the sensitivity of photographic methods does not exceed that of visual methods, with a magnitude limit of +2 for small cameras and +4 for Super-Schmidt cameras, compared to the limiting magnitude of the human eye of $\sim +4$ magnitudes in good conditions. More advanced photographic methods utilise two cameras, one with a rotating shutter which produces a fragmented trail on a photographic plate. From this trail, the path and velocity of the segmented trail of the meteor can be obtained, providing sufficient information to determine an accurate meteor orbit (Lovell (1954) provides further information).

Television camera methods have also proved valuable. A television camera is intensified either through the camera itself, or by attaching an image intensifier to the video detector. These systems have the advantage of improved sensitivity compared with photographic methods (to $\sim +10$ magnitude). However, technological limitations, including a low signal to noise ratio, restrict the accuracy to $\sim 3\%$ in velocity and $\sim 0.2°$ in radiant position (Hawkes, 1993).

Photographic methods provide small but highly accurate datasets, detecting relatively large bright meteors. In the following section we will see that radar methods produce large datasets, but with reduced velocity accuracy (~ 5 to 10%), and generally sample smaller particles (with magnitudes $\sim +8$ to $\sim +14$). Such radar techniques more heavily sample the smaller, sporadic meteor population. Photographic meteors are found to have a relatively higher proportion of more recently formed shower meteoroids. This is because they have not suffered the same level of collisions or perturbations that older sporadic particles have, and thus shower particles are generally larger in size than sporadic particles.

Radar detection of meteoroids is important because it allows detection of meteoroids to much smaller mass limits and at all times of day, regardless of the weather. Radar systems observe meteors by detecting the train of ionisation formed as atoms ablated (vaporised) from the surface collide with atmospheric molecules and become ionised. By

reflecting radio waves from this ionised train, information on the orbit and mass of the meteoroid can be obtained.

Development of radar (RAdio Detection And Ranging) type systems began in the early 20th century after the development of radio communication technology (Rinehart, 2004). Research into atmospheric phenomena using reflections of radio waves began in the 1920's, with the first publications of radar studies of ionized layers in the upper atmosphere in 1925 (Appleton and Barnett, 1925) and 1926 (Breit and Tuve, 1926). In 1929-30 unexplainable night-time radio echoes from the atmospheric E-region were recorded, and Nagaoka (1929) was the first to propose a meteoric origin, though the mechanism suggested was incorrect. In the early 1930's the definitive proof for the origin of these echoes was obtained by correlation of the occurrence of E-region radio echoes with visual observations of meteors (in particular, Leonid meteors in 1931 and 1932).

Robert Watson-Watt in Britain is credited with the invention of a practical radar system with his RDF (Radio Direction Finding) system in 1935. Though the original radar could only operate at low frequencies, the invention in 1940 by John Randall and Harry Boot of the cavity magnetron allowed radar operation with microwave frequencies up to 10GHz. This improved radar direction determination of the target (Rinehart, 2004) (Carey-Smith, 2003). These developments enabled radar to be used extensively during the Second World War as a means of detecting aircraft. Military development during this time also greatly improved radar technology (Rinehart, 2004). During the war, meteorological phenomena such as rain cloud and meteor trains had been detected but were considered clutter (that is, legitimate radar echoes which did not correspond to the object or phenomena required), to the extent that on many occasions meteor echoes were mistaken for aircraft.

With the conclusion of the Second World War, surplus military equipment (such as radar) was made available for research use (Rinehart, 2004). A number of these radars were used for atmospheric research. With radar technology now not exclusively military, various applications and new radar techniques were developed leading to radar for air traffic control, radar for monitoring traffic speed, and a number of meteorological applications.

As a result, the first radar meteor studies in the late 1940s involved ex-military World War II equipment (Hey and Stewart, 1947). From the mid 1950's, new methods were developed at Jodrell Bank (England), utilising Fresnel diffraction pattern methods and employing three station systems to deduce meteor trajectories. 2509 meteors to a limiting magnitude of +7 were detected (Davies and Gill, 1960). These techniques were later used in the Harvard meteor survey (Illinois, USA) during the 1960s. Eight stations were used to improve coverage, and a 2MW radar power allowed detection of

nearly 40000 meteors to a limiting magnitude of +12 from 1961-69 (Hawkins, 1963). A number of studies at Adelaide (Australia) in the 1960s also used three spaced receivers to detect meteors down to +6 (1960-61 survey) and +8 (1968-69) Gartrell and Elford (1975). Other studies in this period, such as those at Obninsk (Russia) in 1967-68 and Mogadisho (Somalia) in 1968-70, tended to focus on detecting specific meteor showers Galligan (2000).

More recently, the AMOR (New Zealand) and CMOR (Canada) respectively, have provided new datasets. AMOR (Advanced Meteor Orbit Radar), which has been in operation since the early 1990s, has produced $\sim 10^6$ orbits with a limiting magnitude of +13 (1990-1994: $\sim 3 \times 10^5$ orbits) and +14 (1995-1999: $\sim 6 \times 10^5$ orbits) (Galligan, 2000). CMOR (Canadian Meteor Orbit Radar) has been operating since late 2001 and archives approximately 1500 trajectories per day to a limiting magnitude of +8 (Jones et al., 2005). Meteor radar data from the Adelaide, Harvard and Obninsk surveys have been archived by the International Astronomical Union's Meteor Data Centre and are available on request.

3.1.3 Interstellar Meteoroids

Detection of interstellar particles has been achieved by both space-based (in-situ) and ground-based (remote) observation. It is described here as a case study to illustrate the benefits and issues associated with in-situ and remote-sensing methods of detection.

In-situ observations of interstellar particles have been possible with dust detectors on a number of spacecraft missions including Pioneer 8 and 9, Hiten, Galileo, Ulysses, Cassini, Helios and Stardust. These detectors are able to determine the flux and speed of particles, but velocity directions are only attainable to a low precision. Dust detected by a space-based detector with collecting area ~ 0.3 m^2 is small: of order ~ 0.05 μm to ~ 1 μm for the Ulysses detector. Ulysses, with its high inclination orbit that allows it to sample dust away from the interplanetary dust concentrated to the ecliptic plane, has provided particularly valuable data on interstellar dust entering the Solar System. This has been important in understanding the filtering effect at the heliospheric boundary due to the solar magnetic field of particles less than ~ 0.3 μm, and the focussing and defocussing of particles from the solar magnetic plane by changes in polarity of the solar magnetic field.

Ulysses also established an apparent inflow direction of interstellar particles in the Solar System which is in agreement with the flow direction of interstellar neutral hydrogen and helium. However, the latest 2005-06 data shows a 30° shift from the neutral hydrogen direction, the cause of which is not yet known. Furthermore, radiation pressure has a significant effect on interstellar particles of the size detected by Ulysses: this results in an increase in the masses of observed particles closer to the Sun (Krüger and Grün, 2009).

Radar has largely been the mechanism for ground-based observation of interstellar particles. The Advanced Meteor Orbit Radar (AMOR) in New Zealand first reported a significant detection of interstellar particles in 1996 (Taylor et al., 1996). These particles are larger than those detected by Ulysses or other spacecraft-based detectors: AMOR has a limiting particle size of ~ 20 μm. This demonstrates that interstellar particles of highly varying sizes are able to penetrate the heliosphere and reach the inner Solar System. The interstellar dust detected by AMOR includes a strong stream of particles that appear to have originated from near the dust-debris disk star β Pictoris ($\lambda \approx 260°$, $\beta \approx -58°$). The ability to trace the dynamics of interstellar particles back to a source is limited by the mean-free path of collisions between ambient interstellar dust and the particles from the source. This is radius dependent. For AMOR sized particles, the distance particles are expected to retain origin information of the source direction is ~ 1 kpc; for Ulysses sized particles it is considerably smaller (~ 0.1 kpc) (Grün and Landgraf, 2000).

3.2 Details of Radar Detection of Meteors

Radar detection of meteors relies on the ionisation produced by the meteoroid as it is heated on entry to the Earth's atmosphere. Both free electrons and positive ions exist in the resulting meteoric plasma: only the electrons are of interest here, as radio energy is not significantly scattered by the relatively massive ions.

Meteor radars, such as AMOR and CMOR, transmit evenly-spaced radar pulses (~ 400 s^{-1} for AMOR). The pulse of radio waves specularly (orthogonally) reflects from the ionised meteor train, allowing the pulse to be detected at one or more receivers. Significant (above noise) signals at all three receiving sites represent meteor detections for which velocity components and therefore orbital elements can be determined.

In the application of diffraction radio theory to meteor radar it is usually adequate to approximate the meteor train by a linear, stationary column of free electrons. This column extends from $-\infty$ to $+\infty$, with small diameter compared with the radar transmitted wavelength. It is assumed that this trail is underdense: that is, one in which electrons scatter independently; and the scattered radiation from each electron is not affected by the presence of scattered radiation from other electrons. Collisions with other particles are also neglected. The scattering cross-section of each electron in the train is given by $\sigma_e = 4\pi r_e^2 \sin\gamma^2$, with r_e the classical scattering radius, and γ the angle between the electric vector of the incident radar wave and the direction of scattering (also the direction to the receiving antenna) and $\sigma_e \simeq 10^{-28}$ m^2. For backscatter radar such as AMOR and CMOR, $\gamma = 90°$ (McKinley, 1961).

This backscatter or column echo is also known as the body echo. In addition, a head

echo is expected as a result of the spherical plasma generated near the meteoroid itself (Baggaley, 2002). The power that reaches the receiving antenna after reflection of radar waves from either the head or body is given by the radar equation. Knowing that the power flux at the train (at range R) is $P_T G_T / 4\pi R^2$ Wm^{-2} (where P_T is the transmitted power and G_T is the gain of the transmitting antenna), the receiving antenna receives flux of:

$$\frac{P_T G_T}{4\pi R^2} \frac{\sigma_e}{4\pi R^2}$$

If the receiving antenna has gain G_R and an effective collecting area $G_R \lambda^2 / 4\pi$, then the radar equation is:

$$\Delta P_R = \frac{P_T G_T}{4\pi R^2} \frac{\sigma_e}{4\pi R^2} \frac{G_R \lambda^2}{4\pi} = \frac{P_T G_T G_R \lambda^2 \sigma_e}{64\pi^3 R^4}$$

where ΔP_R is the power received by the receiver after scattering from a single underdense meteor train.

3.2.1 Calculating a meteor orbit from radar measurements

The raw information from a meteor radar system undergoes a number of transformations and corrections in order to provide the orbit of the detected particle, in orbital elements.

First, the velocity components of the observed meteor in the atmosphere are determined. This is achieved by combination of the returned meteor amplitude and phase signals at three stations. The end result is an in-atmosphere speed and trajectory for the particle.

In order to convert these to heliocentric coordinates, several corrections are required. First, the meteor will suffer deceleration in the Earth's atmosphere, which must be estimated and removed from the measured speed. Such estimation methods are a main source of error in the final orbit. For CMOR, decelerations are calculated by comparison of the raw radar speeds with the velocities determined from photographic major shower data (Brown et al., 2004). An improved CMOR II radar intends to measure this deceleration directly to reduce this uncertainty in the velocity determination (Brown et al., 2010).

Additionally, there will be a deviation in the particle orbit caused by the gravity of the Earth (zenith attraction); a velocity correction caused by the spin of the radar station on the Earth's surface; and a velocity correction due to the motion of the Earth around the Sun. Applying these corrections will produce heliocentric position and velocity coordinates. Finally, these heliocentric coordinates are converted to orbital elements using standard transformations (see Murray and Dermott (1999), pages 52-53). This completes the determination of a meteor orbit by radar methods.

3.2.2 Advanced Meteor Orbit Radar

We now provide specific information on two current meteor radar: The Advanced Meteor Orbit Radar (AMOR) and The Canadian Meteor Orbit Radar (CMOR).

AMOR is located at Birdling's Flat, near Christchurch, New Zealand (at longitude 172°39′E, latitude 43°34′S), and is operated by the Department of Physics and Astronomy, University of Canterbury, Christchurch. AMOR is a pulsed radar, which uses signals received at three stations to determine the radiant position and velocity of an observed meteoroid.

Prior to 2001, AMOR consisted of one transmitting array (radiating peak pulse power at 60 kW) and three receiving arrays at the central or 'Home' site, and two additional sites each containing receiving arrays. These outstations were roughly to the North-West (distance 10.54 km) and West (distance 8.18 km) of the Home site (Galligan and Baggaley, 2004). The transmitted radiation consisted of a 'fan' broad in elevation, but narrow ($\sim 2^\circ$) in azimuth, along the North-South meridian. Radiant coverage was limited to declinations $+20^\circ$ to -90°. The pulse repetition frequency was $\sim 400\text{s}^{-1}$, and the pulse length 66 μs. Upgrades to this configuration in 2001 added an antenna to transmit and receive perpendicular to the original antenna (towards the East and West).

The three receivers at the Home site act as a dual spacing interferometer, allowing unambiguous determination of the elevation of the meteor echo to an accuracy of $\sim 0.5^\circ$. The echo range is determined by the time difference between a pulse and its reflected echo, with several individual pulses contributing. The azimuth angle is constrained by the narrow extent of the radar beam, and thus has $\sim 1^\circ$ uncertainty. The zenith angle is calculated by determining the echo elevation found using the phase measurements on the dual-spacing interferometer. These parameters define the radiant direction and velocity vector. The speed is determined using the time difference between detection of the meteor at each of the three stations. This requires a comparison between points of maximum gradient on the rising leading edge of the three echo amplitude profiles. There is an uncertainty in the time lags between stations of approximately one radar pulse (2.64ms), which gives a heliocentric velocity uncertainty of $\sim 3\%$ for a 20kms^{-1} meteoroids. In general, uncertainties of up to 5% are expected.

A Fresnel velocity determination method, as was common prior to the AMOR radar, can be used for the small percentage of echoes that contain clear Fresnel oscillation patterns at one or more station. Fresnel oscillations are the result of Fresnel diffraction zones, which arise from constructive interference between the radar signal reflected at different points on the meteor train. Speed can be determined by measuring the size of the Fresnel zones. The result is an improved velocity accuracy for these meteoroids. (Galligan, 2000).

In excess of 10^6 meteor orbits have been collected by the AMOR system. In particular, the $\sim 5 \times 10^5$ collected from May 1995 to October 1999 represent almost continuous operation at the same radar configuration. This dataset contains orbits to a limiting magnitude of +14: corresponding to velocity-dependent mass and radius lower limits of $\sim 3 \times 10^{-10}$ kg and ~ 20 μm in radius respectively. With this high sensitivity to small particles, the AMOR dataset is ideal for investigating sporadic particles in the Solar System and interstellar dust; both of which tend to be smaller than the meteoroid stream dust observed as meteor showers and sampled by photographic and visual surveys.

3.2.3 The Canadian Meteor Orbit Radar

The Canadian Meteor Orbit Radar (CMOR) is also a three station pulsed meteor radar. Situated near Tavistock, Ontario, Canada (80.772°W, 43.364°N), it has two remote sites 8.1km and 6.2km away from the central site. The three stations form an angle of 96.8°. It is a SKYiMet radar system with a peak power of 6.0 kW capable of three frequencies (17.45, 29.85 and 38.15 MHz). It uses a 5-element interferometer that allows determination of echo directions to $\sim 1°$ (above 20° elevation). Vertically directed Yagi arrays are used, resulting in almost all-sky coverage down to $\sim 20°$ elevation. A pulse repetition frequency of 532 Hz is used, and a pulse length of 75 μs. Radiant directions have an uncertainty $\sim 6°$.

CMOR meteor velocities are determined with multi-station timing, in a similar way to AMOR. Time delay errors are given as ~ 0.7 of a pulse. The measured velocities have $\sim 10\%$ uncertainties. A pre-t_0 Fresnel oscillation method is used to provide speeds with uncertainties $\sim 5\%$ for a approximately 10% of meteors that have high signal-to-noise Fresnel patterns (Hocking, 2000). Deceleration corrections are computed using empirical expressions determined by comparing the raw radar-determined speeds with the speeds found in photographic studies of major meteor showers (Brown et al., 2004).

CMOR detects about 7000 meteors per day, of which about 1500 have usable amplitude profiles at all three stations, allowing orbit determination: as of 2008, the dataset contained more than 2.5×10^6 orbits. The 29.85 MHz system has an effective limiting magnitude of $\sim +8$, giving velocity-dependent mass and radius limits of $\sim 10^{-8}$-10^{-7} kg and 0.1 mm respectively. CMOR is more efficient at detecting meteoroid streams as it is sensitive to more massive particles than AMOR. Brown et al. (2008) outlines an initial search for meteoroid streams.

Chapter 4

A Search for Resonance Effects in Radar Meteor Orbit Data

4.1 Resonance effects in the Solar System

Resonance behaviour is observed in a variety of dynamical systems in the Solar System. As in any other physical application, resonances here arise when a simple numerical ratio exists between frequencies (usually orbital periods) of different objects in the system: a commensurability. At mass scales where gravitational forces are dominant, this allows small gravitational forcings to occur repeatedly over a number of orbital periods, the net effect of which is to produce a dynamical feature that may be observable. Several types of resonances are observed in the Solar System relating to ratios of different parameters. These are subdivided into spin-orbit coupling (ratios between spin and orbital rotation periods) and orbit-orbit coupling (ratios between two orbital parameters). The latter includes mean motion resonances involving orbital periods or mean motions, and secular resonances involving slower precession frequencies.

The Earth's Moon, with an orbital period approximately equal to its rotational period, represents a simple example of spin-orbit coupling. A more dramatic example is that of the Pluto-Charon system, where both objects are in a synchronous spin state: this is known as a totally tidally despun system (Murray and Dermott, 1999). This is considered the stable end state of the system (Farinella et al., 1979).

Mean motion resonances are the simplest manifestation of orbit-orbit coupling. In their simplest form, the ratio between mean motions can be converted to periods of revolution, which in turn can be related approximately to semi-major axis distances from the central body by Kepler's second law (see Section 2.1.1). Thus, resonances with respect to one major body often appear at particular semi-major axes distances. A planetary example of such resonance is the 3:2 commensurability between the mean motions of Pluto and Neptune which results in Pluto orbiting the Sun three times for every two of Neptune, and has dynamics that ensure that close approaches between the two planets are avoided. There are indeed a whole class of trans-Neptunian objects protected in this

manner by their location at the 2:3 Neptunian resonance: these are known as Plutinos. Other families of resonant Kuiper belt objects also exist.

Several examples of mean-motion resonances exist between the satellites of the giant planets in the Solar System. For example, three Galilean satellites of Jupiter - Io, Europa and Ganymede - exhibit a Laplace resonance. This is a configuration where there is a ratio between orbital motions of three bodies, and this is the only instance of such a resonance in the Solar System. In this case the relationship is given by $n_I - 3n_E + 2n_G = 0$ (n being the mean motion), with Io in a 2:1 resonance with Europa, which in turn is in a 2:1 resonance with Ganymede. This geometry ensures that whenever a conjunction occurs between any two of the satellites, the third is at least 60 degrees away, thus preventing a triple conjunction. The 2:1 resonance between Io and Europa is also responsible for the observed vulcanism on Io. Similar resonances exist between satellites of Saturn, such as 2:4 Tethys-Mimas and 3:4 Hyperion-Titan. Resonant perturbations also create gaps in Saturn's ring structure, such as the Cassini division between the A and B rings. Here the sharp inner edge, known as the Huygens Gap, is caused by the ring particles being at the 2:1 resonance with Mimas.

Secular resonances are also important in determining the dynamical structure of the Solar System. These are long-term resonances that occur when the precession frequency of a small body is nearly equal to an eigenfrequency of the planetary system. A linear secular resonance involves one of each frequency; other types can involve combinations of frequencies of both bodies. For example, the ν_6 (the name given to the resonance $g = g_6$) secular resonance occurs when the precession frequency of the longitude of perihelion g of an object is nearly equal to the average precession rate of the longitude of perihelion of Saturn (g_6). The ν_5 ($g = g_5$) resonance is similarly a resonance with Jupiter's longitude of perihelion g_5 (Froeschlé and Morbidelli, 1994).

Resonant structure in the asteroid belt has been recognised since Kirkwood (1867), who noticed gaps that corresponded to Jovian resonance locations: these gaps are now known as Kirkwood Gaps, and occur when the resonance at that mean-motion (and thus semi-major axis location) destabilizes the objects. In addition, certain resonances can stabilize and protect orbits, creating concentrations of particles. Thus, major gaps occur at 4:1, 3:1, 5:2 and 2:1, while concentrations exist at the 3:2 and 1:1 resonances, which correspond to the Hilda and Trojan families respectively. Furthermore, Kirkwood gaps are not entirely empty, with a small population of asteroids observed in each.

Acknowledging the effects of resonance dynamics at a variety of mass scales in the Solar System, it is probable that such effects may also affect the meteoroid-scale population. As we are dealing with a large population of objects dispersed throughout the Solar System, we expect such effects to be analogous to those seen in the asteroid belt

- specifically, gaps and concentrations at certain semi-major axis values in the distribution of orbits. Resonance effects in the meteoroid population are discussed in Section 4.3.

This chapter outlines a search for such effects in the *radar* meteor population. Though radar surveys suffer from large orbital uncertainties in comparison to photographic studies, these large radar datasets benefit from improved statistics. More details of resonance structure and formation in the asteroid belt are covered first, to serve as a basis for determining what we can expect for the meteoroid population. Combining this with radar limitations allows a narrowing of the search field in the Canadian Meteor Orbit Radar (CMOR) dataset. This is followed by analysis of the semi-major axis distribution of Taurid meteors selected from this data.

4.2 Resonances in the Main Asteroid Belt

The asteroid main belt exhibits three types of resonance structure: its relatively sharp confinement to the main belt; gaps created by Jovian and Saturnian mean-motion and secular resonances; and concentrations at other resonances.

The outer extent of the main belt is fairly well defined, with a significant decline in the number of asteroids beyond the 3:2 resonance at 3.97AU (except for a concentration of a small number of orbits at the 4:3 resonance (4.29AU)). The absence of orbits in the region is caused by chaotic motion due to a region of overlapping first order resonances extending ~ 0.9AU inside the orbit of Jupiter.

Explaining the formation of gaps at some resonances and enhancements at others can be difficult. Concerning the Kirkwood gaps in the asteroid belt, a number of theories for the origin of Kirkwood Gaps have been proposed - these can be classified (as by Greenberg and Scholl (1979)) into four types:

1. The Statistical Hypothesis: The gaps are purely an illusion, since an asteroid in resonance spends the majority of its time at the extremes of its orbit, and thus of its librational motion (defined as oscillation in the resonant argument: see Section 5.1). Thus, at any given time the asteroid is most likely to be at the edges of the resonance. Numerical studies indicate this is not the source of the gaps, however.

2. The Collisional Hypothesis: The gaps are depopulated by collisions of resonant gap objects with nearby asteroids, due to variations in orbital elements (such as eccentricity e). This may be due to corresponding increases in the velocity of the resonant particles, which increases the collisional probability. The effect could be either to alter the mean motions of resonant objects such that they move out of resonance and accrete in the regions in between, or to fragment or destroy the asteroids. This is the mechanism first proposed by Kirkwood.

3. The Cosmogonic Hypothesis: The gaps are formed in the early Solar System, either due to the failure of asteroids to form in those regions or due to early processes that no longer operate. An example of the latter is resonant sweeping during the expansion of Jupiter's orbit. While such theories may explain gap formation, they cannot explain the difference between resonance - such as between 2:1 and 3:2 resonance.

4. The Gravitational Hypothesis: This hypothesis is the favoured explanation for the asteroid belt resonant structure at present. This theory proposes that the gaps can be explained using three-body mechanics of the Sun-Jupiter-asteroid system. Here, motion is governed by processes described by resonance theory, and a removal mechanism should be apparent in a sufficiently long-term integration of the orbits of these objects..

Chaos is involved in many commensurabilities. In particular, it has been shown that the overlapping of secular resonances or mean motion resonances can create chaotic regions within resonances which actively remove objects. This was first demonstrated by Wisdom (1982) and Wisdom (1983) for the 3:1 resonance, who showed that significant variations in eccentricity would continually put objects orbiting in the 3:1 resonance on Mars-crossing orbits, and eventually such an object would impact, or be significantly perturbed by, Mars and removed from the resonance. In addition, the extent of the chaotic region agreed well with the size of the 3:1 gap.

Moons and Morbidelli (1995) studied the 4:1, 3:1, 5:2 and 7:3 gaps. They show that chaotic motion is present at each for the majority of the a-e phase space due to interactions between the ν_5 and ν_6 secular resonances. This chaotic motion leads to significant increases in eccentricity that cause asteroids in these resonances to assume orbits that cross the orbits of Mars, Earth and Venus.

More complicated combinations of resonant phenomena are needed for the 2:1 (Hecuba gap) and 3:2 (Hilda group) resonances. Again secular resonances ν_5 and ν_6 are responsible for chaotic motion, but for these resonances this is only present for high eccentricity objects. Between these chaotic regions a more stable zone exists. However, Henrard et al. (1995) found evidence for a dynamical 'bridge' between these two regions at high libration amplitudes, which allows lower eccentricity orbits to have their orbits sufficiently altered to leave the resonant region. Thus, the Hecuba gap is observed at the 2:1 resonance. Moons (1997) suggests that the observation of a concentration of Hilda asteroids at the 3:2 resonance is due to a difference in timescales: there has not been sufficient time since the formation of the Solar System for the bridge mechanism to remove these asteroids. In addition, the near 5:2 resonance between the orbits of Jupiter and Saturn ('the great

inequality') acts to enhance the depletion of the 2:1 resonance (Murray and Holman, 2001).

Trojan asteroids are a final example of concentration of particles by a resonance. These are located at the 1:1 resonance with Jupiter, situated 60° either side of its position in orbit at the L_4 and L_5 Lagrange points. It is thought asteroids exist at these locations as the stability of the resonance prevents close approach to Jupiter, thus ensuring their survival (Greenberg and Scholl, 1979).

The research summarised above on the origin of resonant structure in the asteroid belt demonstrates that determining the expected behaviour at a given resonance can be problematic. Though it is possible to determine the locations in semi-major axis at which resonance effects may be important in the meteoroid population, it may be difficult to ascertain the nature of such effects.

4.3 Resonances and the Solar System Meteoroid Population

The search for resonance effects in the meteoroid population has proved more elusive than within the asteroid belt. This is due to a number of factors, largely concerning the difficulties of observing these smaller objects and of determining their orbital properties with sufficient accuracy, leading to small number statistics in some (mainly photographic) datasets, and high uncertainties in others, including radar datasets. Much of the previous work on resonances in meteoroid populations has involved searching within meteoroid streams or meteor showers. These represent a manageable section of the population that is easier to understand dynamically than the effects of resonances on the overall distribution. This does not mean resonances do not affect non-stream sporadic particles, and, in particular, there may exist evidence of a transfer mechanism of meteoroids from the asteroid belt that utilises strong Jovian resonances: such a conveyor belt mechanism is observed for asteroids (40% of Near Earth Asteroids have moved from asteroid belt orbits to Near Earth orbits due to the ν_6 secular resonances with Saturn, and 25% due to the 3:1 mean motion resonance with Jupiter (Jenniskens, 2006)), and is expected to be present at lower mass scales.

Given the large number of possible resonances and meteor showers, we use previous research to provide a dataset of cases in which resonance effects are more likely to be present. Many have been studied previously and the presence of resonance effects established using a combination of observational results (in particular for outburst events), numerical studies of shower history, and analytic equations. An overview of this research is given below.

4.3.1 Types of Resonant Effects Detectable in Meteor Showers

There are two types of resonant phenomena that can occur in meteoroid streams. First, a structure of gaps, displaying similar significant decreases in the orbital density of objects to those observed in the asteroid belt, may be expected to occur. As particles are expelled from the (potentially) chaotic region within the resonance, they may temporarily settle down on the edges of these regions, forming apparent concentrations.

Secondly, particles injected into the stream by the parent comet each have slightly different orbits, with a small proportion having the correct dynamics to place them inside a resonance, particularly if the comet already librates within a given resonance. These particles can remain in this region for relatively long periods of time, their existence inside the resonance (or near a librating comet) protecting them from planetary perturbations and other such effects that act to more quickly disperse other stream particles. Inside the resonance, these particles librate through a narrow set of mean motions, thus forming an outburst on Earth when the displacement between the Earth's position and the resonance centre is small. Built up over a number of comet returns to the resonance centres, these regions are of relatively high density and are wider than outburst dust created by dust trails from a single comet pass. These dust trails produce outbursts simply because the particles are young and have not had sufficient time to disperse into the stream background. Thus, it is important to distinguish between relatively old, wider resonant swarms or filaments injected into the region over a number of years, and young dust trails of recently released material.

A third mechanism by which resonances are known to affect meteoroid streams also exists: dispersal of a meteoroid stream into arcs. This has been shown numerically, but has only been observed for the Quadrantids stream.

It was with regard to the Quadrantids that much early work on meteors in resonances developed. Initially, variations on ~ 59 year timescales in orbital elements were found in numerical studies (Hughes et al., 1979), which were incorrectly attributed at first to the 11:5 Jovian resonance. Murray (1982) showed analytically that such variations could in fact be produced by the 2:1 resonance. This is true for Quadrantids in near resonance, such as particles near the mean orbit with a semi-major axis of ~ 3.07 AU. For particles within the 2:1 Jovian resonance region (approximately $a = 3.24$ AU to $a = 3.26$ AU), Froeschlé and Scholl (1986) showed that gravitational splitting occurs, disrupting the stream into a number of arcs on timescales of $\sim 10^3$ years. This behaviour also requires high eccentricities $e \geq 0.4$ and high inclinations, as are observed for the Quadrantids stream.

4.3.2 Resonant Gaps and Concentrations in Meteoroid Streams

A search for structure in meteoroid orbits similar in nature to the Kirkwood Gaps was begun by Lindblad (1973). He found gaps at locations of mean motion resonances of Jupiter in the reciprocal semi-major axis (proportional to the orbital energy) distribution of photographic meteor orbits. Wu and Williams (1995) searched for gaps in the reciprocal semi-major axis distribution of photographic Perseids (as they have the largest population of all known showers in the IAU Meteor Data Centre database). Significant gaps were observed at many resonances, including the 1:1, 1:2, 2:1, 2:3 and 3:2 resonances of major planets. Numerical simulations were used to show that these gaps can develop after 150 years and remain present thereafter. Peaks are initially formed either side of gaps as particles are displaced from the gaps and settle temporarily on the edges, but these dissipate gradually. Svoreň et al. (2006) confirmed the presence of gaps in photographic Perseids at the position of mean motion resonances of Jupiter and Saturn to greater statistical significance. Additionally, they identified filamentary structure within the stream which occurs near to important resonances, and are expected to represent the peaks of expelled particles on resonance edges seen in the simulations of Wu and Williams (1995).

Murray (1996) commented on this paper (Wu and Williams (1995)) and noted that a distinction must be made between real gaps demonstrating actual removal of particles from the resonant region, and 'imaginary' gaps present as a result of resonant perturbations leading to the failure to identify some meteoroids of a given stream. For a gap detected at the 3:1 Jovian resonance location in Quadrantid meteors, an analytical method for determining the upper limits on the changes in orbital elements the resonance is capable of exerting is used to argue that this gap is probably 'imaginary'. In addition, the paper commented that it may not be resonant effects that create the gaps observed in the Perseids. Resonant effects need several orbital periods to occur. Thus, for cases such as the Perseids where the timescale for gaps to form ($\sim$ 150 years (Wu and Williams, 1995)) is roughly the same as the timescale on which new material is added to the stream by the passage of the parent comet P/Swift-Tuttle, it is difficult to see how the resonances can act to create gaps. It is suggested that perturbations from near approaches to major planets may provide an alternative mechanism, as it is noted that the numerical simulations of Wu and Williams (1995) do suggest that real physical structure exists in the Perseids.

4.3.3 Resonant Swarms Producing Meteor Shower Outbursts

The Perseids are also among showers that have displayed recent outbursts that have been attributed to resonant swarms, along with others such as the Leonids, Orionids, Taurids, and June Bootids. These outbursts consist of particles librating around a particular resonant centre, or which are sufficiently close to a librating parent body to be protected

by the libration of the comet. A common starting point for such studies is Emel'yanenko (2001a), which used simple analytic arguments to determine which showers (of a selection of eight) are capable of containing particles in libration near centres of nearby 1:j resonances. Aquarids, Orionids, Lyrids and Leonids were shown to be capable of showing such librations, and the role of the 2:1 resonance in shielding the June Bootid stream was demonstrated.

The following section will expand on some of the resonant behaviour seen in the streams mentioned above. The Leonids shower has produced a number of strong outbursts in recent history. These are largely meteoroid trails due to the crossing of the Earth through young debris clouds released by the parent comet 55P/Tempel-Tuttle on a previous orbit. Over time these clouds disperse, thus requiring the cloud to be the product of a recent comet pass in order to be visible as a storm or outburst. However, in 1998, a strong Leonid shower was observed 16 hours before the main shower was expected. This outburst was also visible, but to a lesser extent, in subsequent years. This outburst has now been attributed to relatively old dust released in 1333, which has been protected from Jovian perturbations and preserved for such an extended period of time by its injection into the 5:14 mean motion resonance with Jupiter. Such a concentration of dust represents a meteoroid swarm, which is in general wider than a meteoroid trail, and thus produces a wider feature. Numerical studies in Asher et al. (1999) have shown this to be possible.

This conclusion was supported by the observations and analysis of Jenniskens and Betlem (2000) and Jenniskens et al. (2008). However, the former notes that their results do not allow a distinction between a situation where the particles themselves are librating or where the particles are protected by their proximity to the parent comet in libration. This paper also points out a number of similarities of this filament with a similar structure in the Perseids, and from this speculates that these filaments are a common feature of streams resulting from Halley-type comets (comets with orbital periods of about 50 to 250 years which are the result of evolution of long period comets to smaller orbits), which may also prove a useful key to the dynamical evolution of cometary dust.

The Perseids demonstrate similar behaviour near the return of comet 109P/Swift-Tuttle. Two separate structures were identified in Jenniskens et al. (1998) from observations near the last return of this comet: a 'Perseid Filament' and 'Nodal Blanket'. They conclude that, in a similar way as for the Leonids, these are formed by the protection of particles of many comet returns by the libration of the comet in the 1:11 Jovian mean motion resonance. In particular, the Nodal Blanket may possess its smaller distribution of semi-major axes orbits because it contains dust that is itself librating around this same resonance centre.

The case of the Orionid meteor stream differs from the Perseids and Leonids in that

the parent comet (1P/Halley) is not in resonance with Jupiter or other major planets, and as such can theoretically inject meteoroids into all resonances over long timescales. There is a considerable body of research on the resonant origin of the 2006 Orionids outburst. However, there are large uncertainties in orbital parameters - particularly in the semi-major axis - even in photographic Orionid meteors. This is due to the high incoming speeds, and thus high semi-major axis values. This has lead to some variation in the Jovian resonance attributed to this outburst. Emel'yanenko (2001a) gave widths for three nearby resonances: 1:6, 1:5 and 1:4 with Jupiter, at semi-major axis values of 17.1AU, 15.22AU and 13.12AU respectively. Of these, the 1:6 resonance has the largest width ($\delta a = 1.0$AU) and thus is most easily populated. Two works use semi-major axis arguments to determine which resonance is populated by Orionids. Trigo-Rodríguez et al. (2007) found vastly different resonances for each of three CCD camera-observed meteors, attributing the discrepancies to large errors in entry velocities. In Spurný and Shrbený (2008) photographic data of ten fireballs recorded by the Czech section of the European Fireball Network gave a mean semi-major axis of $a = 14.8$ AU, corresponding most closely to the 1:5 resonance.

Sato and Watanabe (2007) and Rendtel (2008) employed a different strategy: use of the time difference expected between occurrences of an outburst caused by the same resonant swarm. This time difference depends on its orbit, and thus on the particular resonance it occupies. Both found a similar time difference: the former used numerical studies to determine that these outburst meteors have an orbital period of 70 to 72 years (and were ejected from the comet in -1265 (1266BC), -1197 (1198BC) and -910 (911BC)), and record two cases of records of high Orionid shower rates in 1936 (70 years prior to the date of the 2006 outburst); Rendtel (2008) described a detailed cumulation of datasets dating back to 1928 and concluded that the apparent increase in 1936 (through sketchy data collection) could also be evidence of a 70 year period. As six Jupiter revolutions take ~ 71.2 years for an orbital period of ~ 11.86 years, a strong signature of the 1:6 Jovian resonances appears to be present. The two year disagreement is suggested by Rendtel (2008) to be the result of observing the swarm at two different ends of the extent of the resonant-trapped meteoroids. Some further observations from the 2007 shower have also shown increased rates, giving weight to this proposal.

Asher and Emel'yanenko (2002) also propose that a large segment of the June Bootid meteors are in the 2:1 Jovian resonance, which protects them, and produced the unexpected 1998 outburst. The parent 7P/Pons-Winnecke, a Jupiter-family comet, librates irregularly in the 2:1 resonance. This argument is not universally agreed on, however (Jenniskens, 2006). Trapping of the Lyrids in the 1:10, 1:11 and 1:12 (or even 1:5) Jovian mean motion resonances has been a suggested explanation for its unusual 'far-

comet' outburst in 1982. Similarly, the 6:7 resonance has been suggested as an explanation for outbursts in 1945 and 1986 in the Ursid meteor shower (Emel'yanenko, 2001a).

4.3.4 The 7:2 Resonance and the Taurid Meteoroid Complex

The final stream to be covered here is the Taurid meteoroid complex. This consists of a vast number of objects from dust size to asteroid size, for which determination of a parent body has proved difficult: though comet P/Encke has been implicated widely, it is thought to be too small to generate the amount of material observed in the complex.

Resonance effects have been identified here, as for the Orionids, by a mixture of studies of semi-major axis characteristics and studies of the time-differences between observed increases in shower rates. The latter requires a more complex approach that involves using the displacement between the swarm and the Earth in the mean anomaly, rather than just time. The resonance implicated here is the 7:2 mean motion resonance with Jupiter.

Initial research came from a mixture of observations and historical data. Clube and Asher (1990) propose a meteoroid swarm due to a proto-Encke (a comet preceding, and producing, the rather weak comet 2P/Encke) with a period of about 3.35 years (close to the 7:2 resonance period of 3.38 years): this was done on the basis of combining observational data (including IRAS dust band detections (Sykes and Walker, 1992)), orbital integrations of near-Encke orbits, historic observations, and modulations of the Earth's climate. Clustering in the values of semi-major axis and values of longitude of the ascending node distribution of optical Southern Taurids at about 2.25 AU, close to the 7:2 resonance position of 2.256 AU, was detected in Steel, Asher, and Clube (1991). Clustering at 1.9 – 2.1 AU is also seen, close to the 9:2 and 4:1 Jovian resonances at $a = 1.9$ AU and $a = 2.06$ AU respectively.

Asher and Clube (1993) outline the expected properties of a Taurid resonant swarm at the 7:2 Jovian resonance. This paper is primarily concerned with understanding the possible fragmentation of an undiscovered parent body to Comet 2P/Encke and the Taurid Complex known as 'proto-Encke', which may inhabit the 7:2 resonance and produce a corresponding resonant meteoroid swarm and climate effects as indirect evidence. The supposition of the 7:2 resonance position is made based on a number of arguments. Tree-ring growth pattern data for Mount Campito bristlecone pine over 5500 years show high frequency variations at twice and $\frac{2}{7}$ of the Jovian period. This paper also examined records of elevated Taurid meteor observations from 1931 to 1988, and finds five have $|\Delta M|$ less than 40° (where, ΔM is the displacement in mean anomaly of the resonant centre from the point at which the Earth and swarm orbits cross in space and time), suggesting a potential link. The nearby 3:1, 4:1, 10:3 and 11:3 Jovian resonances were found incapable

of matching these observations. They construct a table of predicted years at which the swarm may be observed on Earth: these are years in which $|\Delta M| \leq 40°$. This covers both the usual pre-perihelion November observation of Taurids with a swarm peak date of November 3, and a post-perihelion June apparition expected to peak on June 23. The characteristics of the expected 7:2 Jovian resonance are also outlined. These include its development over many thousands of years, its distribution around the resonance centre, and its high libration amplitude and period (~ 400 years). This should produce maxima every 200 years, agreeing with the observed 200 years variations in climate. In concluding, they note that the arguments for a resonant swarm can stand alone from the theorising on an unconfirmed parent body, especially in consideration of the apparent observational support. This is important given that the presence of such a proto-Encke and associated climatic implications are not universally accepted (Jenniskens, 2006). Additionally, Asher and Clube (1998) expand on the proto-Encke theory, making use of numerical integrations to try and understand the dynamical history of such a body.

Further observational support of the resonant swarm was provided in Asher and Izumi (1998) with analysis of Taurid data obtained in Japan over several decades. A statistical test retrieved a result that the null hypothesis (that the agreement between the years of observed increase in Taurid numbers and the predicted swarm years is possible by chance) is rejected at the 98% level. Considering other factors that may affect results, such as returns of the parent comet 2P/Encke and the presence of moonlight interfering with observations, they conclude that the data support the presence of a 7:2 resonant swarm.

Fireball meteor numbers from six observing stations covering the period 1962 to 2002 are examined in Beech et al. (2004). It was tentatively confirmed that there exist enhancements in Taurid fireball numbers for all predicted swarm years, though two possible extra peaks were identified in 1974 and 1985: the suggestion is that they may represent 'missed' peaks in the predictions.

A more recent paper (Dubietis and Arlt, 2007) uses data collated in the Visual Meteor Data Base (VMDB) of the International Meteor Organisation for 1985 to 2005. Fireball rates are also examined separately. They find a correlation between observed enhancements and predicted swarm encounters, with enhancements in 1988, 1991, 1998 and 2005. The 1995 peak was absent, and this was attributed to the influence of the full Moon on observing conditions. Peaks in the fireball proportions also showed general agreement with swarm predictions. Overall the swarm theory is supported by their results.

4.3.5 Size and Mass Distributions of Resonant Swarms

One final point of interest is the mass distribution expected for particles exhibiting resonant behaviour. Particles small enough to be affected by radiation pressure or the Poynting-Robertson effect will be dispersed more rapidly than larger particles, such that even protected meteoroid swarms in libration will be stripped of their smaller particles over long periods of time. These effects may also broaden the resonant swarm. Furthermore, heavier particles may be more easily injected into resonance, if the comet itself is in or near libration.

Concerning the broadening of resonant peaks resulting from a mass distribution: particles affected by solar radiation pressure feel an outward force, the effect of which is to counteract the gravitational force from the Sun. Thus, the resonance appears to be closer to the Sun (in semi-major axis) from the perspective of the particle. This effect, of course, is different for particles of different masses and thus a continuum of particles of different (small) masses have a continuum of resonance positions. This leads to a broadened resonance location in semi-major axis, instead of the single semi-major axis resonance position that applied for larger bodies. Section 6.17 demonstrates that this effect is not significant for radar particles. This section also demonstrates the small alteration of orbital elements that will occur as a result of the instantaneous effect of radiation pressure on ejected radar-sized particles.

The mechanism by which particles are injected into libration can affect directly the mass distribution of such swarms. For the resonant particles detected in the Orionid, Leonid and Perseid streams, low mass indices of 1.5 – 1.7 have been reported (see below). The population index is defined as being the number of meteors in neighbouring magnitude intervals, given by $\chi = r = \frac{N_{M+1}}{N_M}$, where N_M is the number of meteors of absolute magnitude M and brighter (see Section 3.1.2 for the definition of absolute magnitude). The corresponding (differential) mass distribution index can be shown to be $s = 2.5 \log r + 1$, with a lower mass or population index thus indicating, in general, a higher proportion of larger, brighter meteors.

Rendtel (2008) find a population index $\chi = 1.6$ for the 2006 outburst Orionids, which corresponds to a mass index $s = 1.5$. Concerning Leonids, Jenniskens and Betlem (2000) find $\chi = 1.4$ to 2.3 for outburst meteors in successive years, giving $s \sim 1.6$. This compares with $\chi = 3.0 \pm 0.2$ for non-resonant outbursts, corresponding to $s = 2.19$. The resonant filament component was still visible during the 2006 outburst caused by the 1932 dust trail, and gave $\chi = 2.1$, compared with $\chi = 2.60 \pm 0.15$ for the 1932 dust trail outburst Leonids (which was indeed much brighter than expected, with a predicted population index of $\chi \sim 3.47$ or more). In Perseids, the observed mass distribution index for the 1998 observations of the resonant swarm was $s \sim 1.73 \pm 0.04$, whereas sporadic

meteors in the same range had $s = 2.3$ (Jenniskens et al., 1998).

For these streams it appears, in general, that the outbursts resulting from resonant swarms (as opposed to those caused by young dust trails) consist of brighter meteors, and thus larger meteoroids (low population and mass indices). This agrees with a model in which particles in resonant swarms consist of heavier particles ejected from the comet with small ejection velocities. These particles remain close to the orbit of the parent comet, and if the comet itself is in libration these particles can be either protected by the resonance, or can enter librational motion. Smaller particles have higher ejection velocities and are thus spread further from the comet: they are thus not protected by, or within, the resonance. This is clearly possible for cases such as the Perseids and Leonids where the comets are themselves librating, but is more problematic in the case of the Orionids that are not associated with a librational comet.

The Taurid case is also more complex. Dubietis and Arlt (2007) found no apparent trend in the population index of Taurid meteors. The population index was found to scatter around an average value of $\chi = r = 2.4$, and there was no correspondence between variations from this mean value and swarm prediction years. This was calculated from visual meteor observations: it is noted that there are insufficient data to produce a fireball mass distribution index. Contrastingly, they found some correspondence between production years and the 'fireball proportion'. This is measured as a number ratio of fireballs to total meteor numbers: $\frac{N_f}{N_{met}}$. The average fireball proportion was 1.09%. For the entire Taurid shower, peaks in the fireball proportion were seen in 1988, 1998 and 2005. When the proportions were calculated only for a reduced period of time corresponding to the maximum of the shower ($\lambda_\odot = 215^\circ$ to 235°), a peak was seen in these three years, and also in 1995. No peak is revealed for the remaining predicted year in the timespan of interest (1991). The weakness or absence of peaks in 1995 and 1991 is attributed to a larger ΔM than for other years. This elevated fireball rate in most prediction years is to be compared with previous research (such as Bone (1991)) that reported a roughly constant fireball proportion within the Taurid stream. Beech et al. (2004) also report a very good correspondence between fireball numbers and prediction years.

Thus, it appears unclear whether the Taurid swarm includes the bias towards heavier particles that is observed for other resonant swarms. In the original description of the structure and origin of such a swarm given in Asher and Clube (1993), the formation mechanism they proposed for the Taurid swarm was similar to that attributed to the Leonid and Perseid outburst swarms. That is; their method of population of the resonance involved the ejection at low velocities (≤ 50 ms^{-1}) of dust particles into the librating orbits occupied by their parent comets, while higher velocity particles were ejected into orbits beyond the 7:2 Jovian resonance. This would suggest a similar deficit in small particles,

but this remains to be shown observationally.

4.4 Choice of Meteor Shower for Resonant Study

From the above review of resonances in meteoroid streams, the strongest and best-studied meteoroid streams are the Quadrantids, Perseids, Leonids, Orionids (and potentially Eta Aquarids, which are associated with the same comet), June Bootids, Lyrids, Ursids, and Taurids. From analytic study of Emel'yanenko (2001a), Perseids, Eta Aquarids, Orionids, Lyrids, Leonids, and June Bootids have dynamics that may allow stable swarms to form at resonance locations. Some authors also note that the Geminid stream may contain a resonant concentration due to its close proximity to the narrow 7:1 and 8:1 resonance regions (Ryabova, 2005).

To evaluate the observability of resonance effects in these streams in radar data, the position of the radiant of the corresponding meteor shower, the velocity of incoming meteors, the zenith hourly rate, and the resonance width must all be considered. The radiant declination will determine whether a radar system at a given latitude can observe the shower. The velocity is used to determine semi-major axis values for the particle orbits, but most importantly gives an impression of relative uncertainties: observational radar uncertainties increase as the geocentric velocity of the particle increases, and are dependent on the relative impact geometry with the Earth, being greater for head-on collision. Therefore, high Earth-impact velocities can increase the difficulty of observing small-scale structure in the semi-major axis. The zenith hourly rate (ZHR) is the number of meteors expected to be observed per hour on a clear, moonless night with the shower radiant at the zenith (Murad and Williams, 2002). Here it is used as a relative measure of meteor shower strengths: showers of higher ZHR are more likely to produce statistics sufficient to overcome large measurement uncertainties. However, ZHR values are usually based on visual observations, and are not always indicative of the strength of the shower at radar level. Instead, therefore, we use the 'maxZ' parameter defined in the CMOR meteor shower search as 'the relative activity strength at maximum' (Brown et al., 2008). The resonance width will determine if a resonant feature is important with respect to uncertainties: a very small resonant width compared with measurement uncertainties will make observation difficult as the uncertainties will restrict the ability of the data to sense small-scale features.

Table 4.1 summarises approximate values for the above parameters for the showers of interest. All of the showers fall within the observing limits for CMOR (declinations$\gtrsim -20$). The effects of different impact velocities (V_g) is demonstrated by a representative semi-major axis uncertainty δa at the resonance semi-major axis, determined using CMOR

Shower	**Dec**	V_g	$\mathbf{a}_{(AU)}$	**res**	$\mathbf{aR}_{(AU)}$	**width**	δa	**maxZ**	**ratio**
Quadrantids	+48.5	42 ± 4	3.14	2 : 1	3.28	0.17	$1.5 - 3.5$	238	0.11
Perseids	+56.9	62.1 ± 7.2	~ 25	1 : 11	25.7	1.4	$128 - 230$	103	0.011
Leonids	+21.6	69 ± 6.8	9.8	5 : 14	10.3	0.13	$20 - 38$	82	0.0065
Orionids	+15.5	66.4 ± 6.3	18	1 : 6?	17.2	1.0	$55 - 105$	132	0.018
Eta Aquarids	−0.7	64.6 ± 6.2	16.16	1 : 5?	15.2	0.9	$45 - 80$	277	0.020
Lyrids	+32.6	47.3 ± 4.1	45.7	1 : 12?	27.3	1.8	$140 - 260$	36	0.013
N Taurids	+21.0	28.1 ± 2.9	2.12	7 : 2	2.25	0.05	$0.6 - 1.6$	31	0.083
S Taurids	+8.0	27.9 ± 3.7	2.07	7 : 2	2.25	0.05	$0.6 - 1.6$	56	0.083
Geminids	+32.1	35 ± 3.8	1.37	7 : 1	1.42	0.006	$0.17 - 0.57$	817	0.036
Ursids	+74.6	37.6 ± 5.1	4.62	6 : 7	5.76	0.09	$5.5 - 11.57$	29	0.016

Table 4.1: *Parameters of use in determining the suitability of meteor showers in resonant studies. Dec is the shower mean declination;* V_g *is the shower mean geocentric velocity; a is the shower mean semi-major axis; res is the known or theorised (marked with ?) resonance in which shower particles are involved;* a_R *is the approximate semi-major axis location of the resonance; width is the approximate resonant width, generally taken from (Emel'yanenko, 2001b);* δa *is the range of uncertainties in CMOR semi-major axis values at a; maxZ is the relative activity strength at maximum (a Zenith Hourly Rate); and ratio is the ratio between the resonant width and* δa*(a measure of the how appropriate the shower is for radar resonance studies)*

data. A useful measure for deciding the potential for resonance effects in a given meteor shower to be observed by radar is the ratio of the approximate width of the resonance to this representative δa. The greater the resonant width compared with the uncertainties (thus the higher the ratio), the higher the chance that the resonant feature will be visible above the uncertainty broadening of the radar data. These values are also given in Table 4.1. Indeed, a resonant feature that is too wide will blend easily into the background dust cloud. Thus we would prefer a relatively low resonant width, but a high ratio of resonant width to semi-major axis uncertainty. The best showers (in order), chosen for their relatively high ratio, are found to be the Quadrantids, Taurids, and Geminids.

The Taurids are chosen for continual study due to the lack of observational support for resonant effects in the Geminids, and the large radar meteor uncertainties that will result from the larger velocities and semi-major axis values of the Quadrantids. The observational evidence in visual meteor data for the Taurid swarm at the 7:2 Jovian resonance and the relatively low uncertainties in its velocities and semi-major axes make the Taurid 7:2 resonant swarm a good candidate for a radar search.

Below we present an evaluation of statistical and numerical information on CMOR Northern and Southern Taurids. A variety of tests are used in order to investigate whether the information the Taurid resonant swarm can be extracted from current meteor datasets.

4.5 The Taurid Meteor Complex

The Taurids are a Northern Hemisphere meteor shower observed in October-November each year. Commonly, the shower is defined by the Northern and Southern Taurid branches. These are both part of a wider Taurid Complex, to which a number of asteroids have been associated. It is from such associated bodies that a 'Giant Comet' hypothesis was formed (Asher et al., 1993): however, the apparent asteroidal nature of many Taurid complex bodies puts this hypothesis in doubt (Jenniskens, 2006).

The Taurid stream is very dispersed, and covers a number of named showers - Piscids, Arietids, Taurids, and χ Orionids - all with 'northern' and 'southern' components. June apparitions of the stream also exist (corresponding to the passage of the Earth through the stream's second node): these are the β Taurids and Southern May Arietids (both southern branches), ζ Perseids, and Northern May Arietids (northern branches) (Asher and Clube, 1993).

The Tunguska event, additional bombardment or meteorite-forming events, and various climatic influences on Earth have also been linked tentatively to the Taurid complex, leading to further interest in the study of the Taurid meteoroids.

As discussed above, it is the potential resonant concentration of particles at the 7:2

Jovian resonance that is of interest here. Though generally this is investigated using a time-based approach where the years in which the resonant swarm should be visible are calculated, here a semi-major axis method is used. A possible detection of the swarm in semi-major axis data was found by Steel et al. (1991). Furthermore, we do not expect there to be sufficient years of CMOR data to search for a evidence for increased Taurid rates in swarm years. Orbital element data only encompasses one swarm-encounter year (2005). Single-station data is available for more years, but this would not allow extraction of Taurid particles from the dataset, as a received signal from at least three stations is required for an orbit to be calculated. Additionally, despite the presence of stronger resonances in the Taurid vicinity (such as the 3:1 and 4:1 Jovian resonances) we only study the 7:2 resonance as Asher and Clube (1993) find that only this resonance can explain the observed yearly rates of Taurid meteoroids.

As for Kirkwood gaps, resonant effects should be evident as a peak around the location of the 7:2 resonance at a semi-major axis $a = 2.256$ AU (found using Kepler's third law $(\frac{a}{a'})^3 \approx (\frac{T}{T'})^2$, where $\frac{T}{T'} = \frac{2}{7}$ as defined by the resonance). Here a number of methods are employed to attempt to extract evidence of this resonant swarm in CMOR radar data, including statistical techniques and numerical studies.

4.6 Extracting Taurid Data

Parameter	**North Taurids**	**South Taurids**
Starting Solar Longitude	207°	172°
Ending Solar Longitude	235°	218°
Right Ascension α	53.3°	31.0°
Declination δ	21.0°	8.0°
Drift in RA $\Delta\alpha$	0.88°	0.82°
Drift in Dec $\Delta\delta$	0.19°	0.29°
Geocentric Velocity V_g	28.1 kms^{-1}	27.92 kms^{-1}
Standard Deviation in V_g	2.9 kms^{-1}	3.7 kms^{-1}

Table 4.2: *Properties of North and South Taurids.*

Initially, programs developed by Dr. P. Brown and the meteor group at the University of Western Ontario, London, Canada, were used to extract Taurids from the entire CMOR dataset as of July 2008 (thus encompassing Taurids from 2002 until 2007). Solar longitude limits, right ascension and declination, and velocity specifications were used in accordance with the findings of a wavelet coefficient search for shower structure given in Brown et al. (2008) (see Table 4.2). The $\Delta\alpha$ and $\Delta\delta$ values correspond to expected daily drifts in the radiant locations, which are applied in the extraction process. Meteoroids within an (α,δ) region 3° in size around the right ascension and declination values are

selected, provided velocity criterion agree within the given σV_g (which is required in percentage form). This resulted in separate datasets of Northern and Southern Taurids, of 1617 and 6032 meteoroids respectively. These are combined here, unless otherwise stated. The Taurid radiants are too far north and outside the detection area of AMOR.

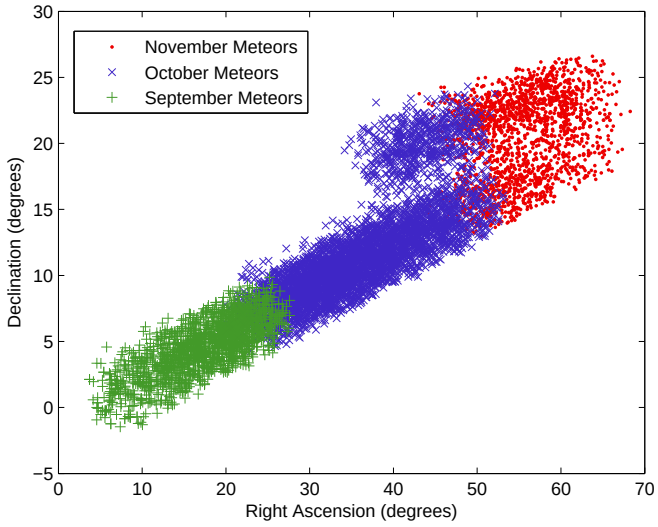

Figure 4.1: *Right Ascension and Declination for extracted Taurids. The movement of the radiant is clear when the meteors are grouped according to month.*

The selected Taurid dataset behaves as expected. The mean semi-major axis is 1.8AU. The mass distribution peaks around 2.4×10^{-7} kg. The inclinations and velocities are low, and peak at around 5° and 28 kms^{-1} respectively. Dates range from 9 September to 19 November. In Figure 4.1 the movement of the radiant is visible.

Given that the extended Taurid stream encompasses showers either side of the Northern and Southern Taurids, and also in June each year, additional resonance information may be acquired by extension of the dataset to include these showers. However, here we only extract Northern and Southern Taurids as determined by the previous CMOR shower survey of Brown et al. (2008).

Though we will examine only the CMOR dataset, the techniques that we develop in this chapter are applicable to the general problem. They can thus be used to investigate whether evidence exists for any dynamical feature in meteoroid streams in any radar dataset. Thus the purpose here is, in addition to searching for evidence of the 7:2 Taurid swarm, to establish a procedure for tackling searches for small-scale structure in radar meteoroid stream data.

4.7 Statistical Methods

In order to investigate the existence of a swarm at the 7:2 Jovian resonance, we search for evidence of a statistically significant feature at the location of the resonant centre (at $a = 2.25$ AU) in the semi-major axis distribution of the selected Taurid meteoroids. In Chapter 5 we determine the 'resonance width' (or width over which the resonance can produce an observable effect) for the 7:2 resonance at Taurid orbital elements. This resonant width provides the expected width of the feature in semi-major axis. However, no knowledge is available on the height of the peak the swarm can produce. In Sections 4.7.1 to 4.9 we search for evidence for the resonant swarm in the CMOR Taurid dataset. In Section 4.10 we investigate the effects of radar uncertainties on the ability the detect a resonant feature.

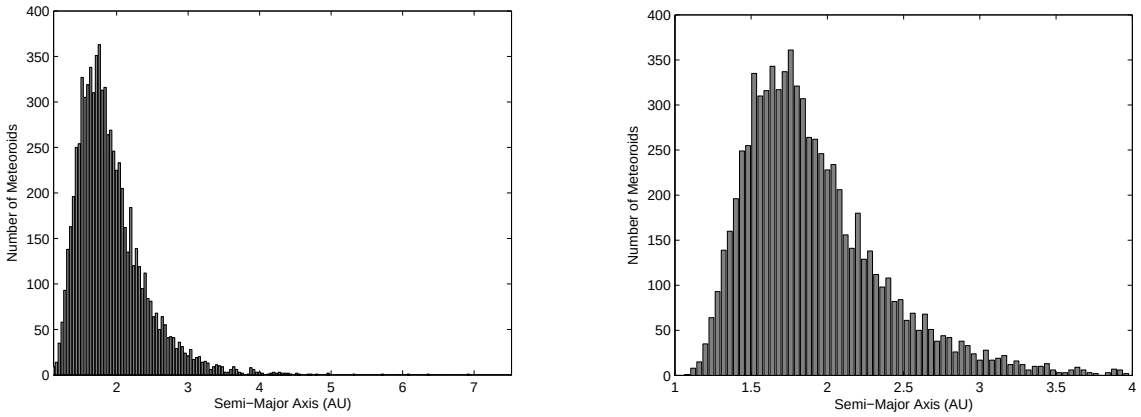

(a) (b)

Figure 4.2: *Histograms of CMOR Taurids, with bin width of* 0.04 *AU, for (a) all selected Taurids and (b) Taurids from* 1-4 *AU.*

We begin by constructing a histogram distribution of the Taurid semi-major axis values (see Figure 4.2). AS an initial test we investigate with the choice of the number of histogram bins employed: too many and visible structure may only be indicative of random variations; too few bins and important structure may be hidden within bins.

4.7.1 Optimum Bin Number Selection for Semi-major Axis Histograms

A method to determine the optimum number of bins in histogram creation was developed by Knuth (2006b). Determining an optimum number of bins, or an optimum bin size, can amount to a statistical test, as a good choice can eliminate the presence of random fluctuations that cause statistically insignificant structure in the resulting histogram. This 'OPTBINS' optimum binning method relies on a number of statistical tools. As further outlined in Knuth (2006b), the resulting method finds the optimum number of bins by

maximising the logarithm of the posterior probability:

$$\log p(M|\underline{d}, I) = N \log M + \log \Gamma(\frac{M}{2}) - M \log \Gamma(\frac{1}{2}) - \log \Gamma(N + \frac{M}{2}) + \sum_{k=1}^{M} \log \Gamma(n_k + \frac{1}{2}) + K$$

where M is the number of bins, N is the size of the dataset, I describes other known variables, k is the bin index, Γ is the Gamma function (an extension of the factorial function that can be used for real or complex numbers), and $\underline{d} = d_1, d_2, ..., d_N$ represents all data points.

This expression is derived by balancing the likelihood function and the prior probability of the model. Since the former increases with increasing number of bins while the latter decreases with increasing number of bins, there should exist a median point corresponding to an optimum number of bins. A full derivation is available in Knuth (2006b). Information and code for implementation are available at Knuth (2006a).

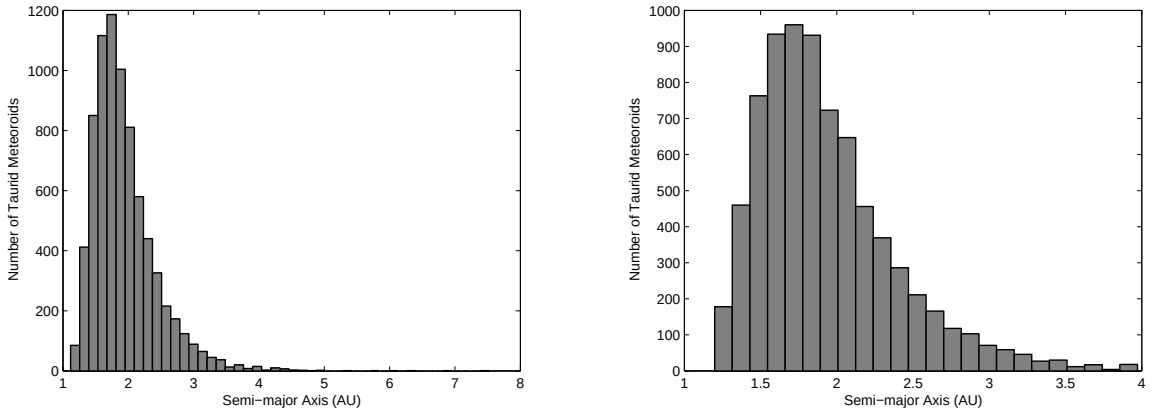

(a) (b)

Figure 4.3: *Resulting histograms from the OPTBINS procedures for (a) all Taurids in the CMOR dataset and (b) Taurids from (1-4 AU).*

For a dataset including all extracted Taurids, the optimum number of bins is derived to be 46. We also test a reduced dataset of Taurids in the most populated semi-major axis region (1-4 AU). These particles are most likely to be particles associated with the Taurid stream. In this reduced case, 24 bins are deduced (a slight increase on the full dataset). The resulting histograms are given in Figure 4.3. No structure at the location of the 7:2 resonance ($\sim$ 2.25 AU) is evident in either diagram. To check the result of the optimum binning program, plots of *logp* against M are made (see Figure 4.4). The diagrams have a shape consistent with successful examples given in Knuth (2006). The flat maxima suggests that the process is relatively insensitive to the number of bins. The program produces an error concerning the excessive rounding of the input data, but the

agreeable shape of the *logp* against M figures suggests that the results given are accurate.

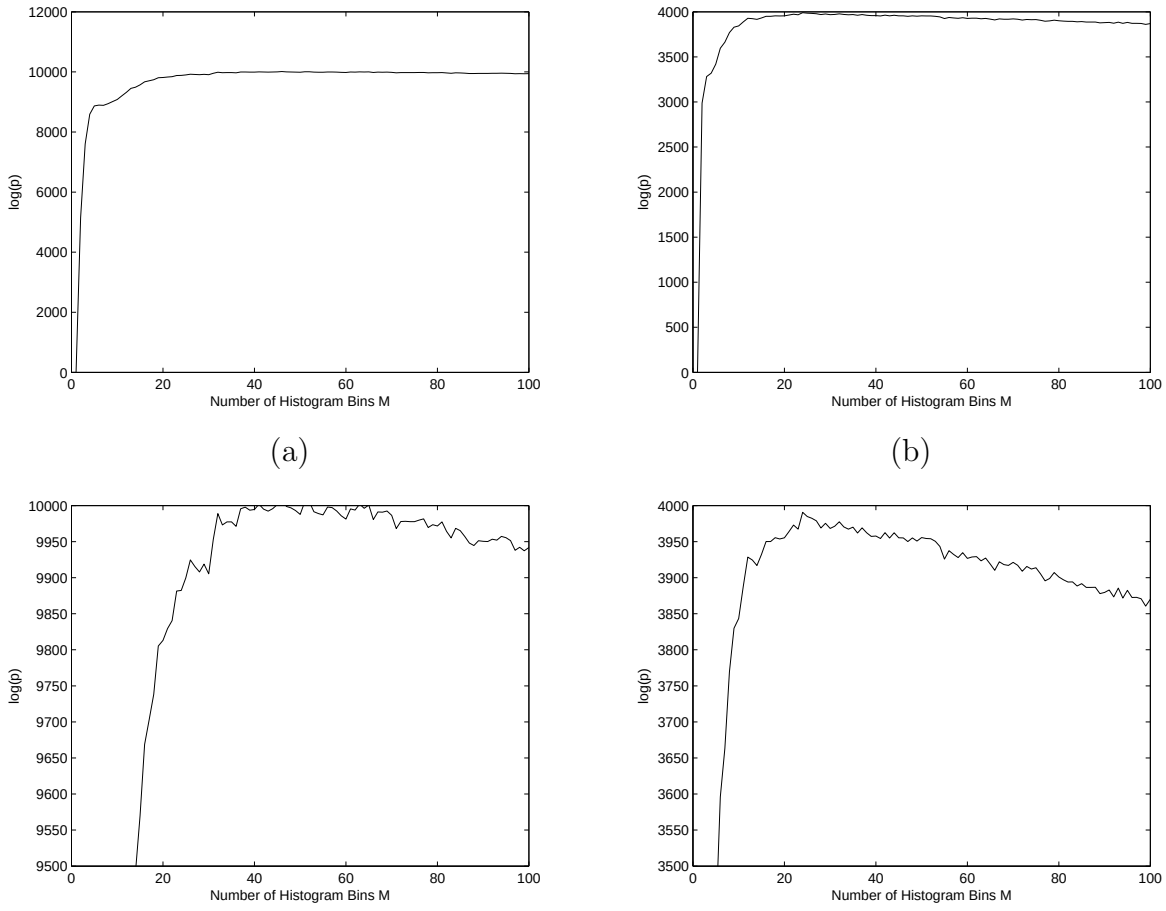

Figure 4.4: *The logarithm of the posterior against the number of bins in the histogram, as used for K H Knuth's optimal binning procedure. Data used are (a) all Taurids in the CMOR dataset and (b) Taurids from (1-4 AU). From the maxima of these graphs (shown more clearly in (c) and (d) respectively) the optimal number of bins are found to be* $M = 46$ *and* $M = 24$ *bins respectively.*

Examination of Figure 4.3 suggests there is no evidence for a resonant swarm in CMOR radar Taurids. However, this program provides no test as to whether the resulting distribution is smooth, as it appears to be. We now use simple statistical analysis and Monte Carlo simulations to provide knowledge on whether an anomaly exists at the 7:2 resonance position.

4.7.2 Statistics of Variations from a Mean Curve

A simple statistical test is used to determine whether the sizes of the small scale ($\lesssim$ 0.5 AU) variations in the CMOR Taurid semi-major axis distribution are consistent with the size of the random fluctuations expected for this size of dataset. This involves fitting

a model distribution to the data excluding the region in which we expect the resonance centre to be present. The resulting dataset should not contain any signature of the resonance region. Variations are obtained by subtraction of the model distribution and the data distribution. We can then compare the standard deviation of these variations with the size of the variations in the resonance region.

Ideally, we would use a model of the physical underlying distribution, including knowledge of observational biases. Since such a theoretical model is unknown, the actual model fit chosen is not a concern as long as it describes the data well: we choose an eighth order polynomial fit to model the underlying distribution of the data. Higher-order polynomials can produce non-monotonic behaviour or be overdetermined. Again, such issues are not of concern here provided the polynomial fits the data, particularly given we are not attempting to make predictions outside the data range. For the polynomials used here, we find that undesirable behaviour can occur beyond the range over which the polynomial fitting is applying, but that the eighth order polynomial works well within the range of the data.

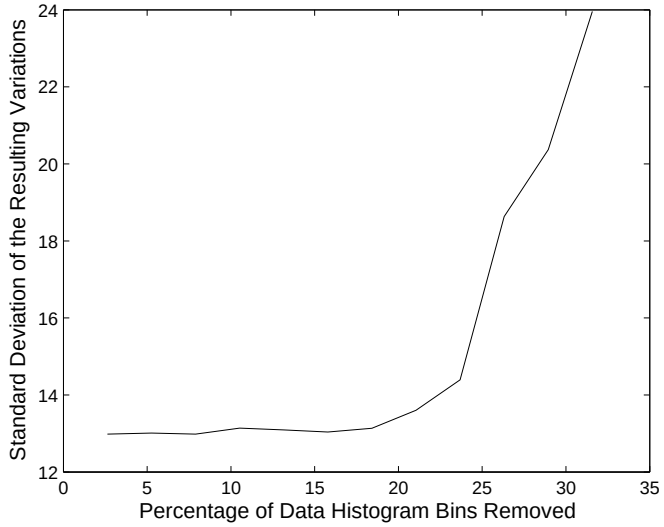

Figure 4.5: *The variation of the standard deviation of the resulting variations as an increasing percentage of the data around* 2.25 *AU is removed.*

A semi-major axis histogram is created with a bin width equal to 0.04 AU. This is chosen as it is approximately the size of the resonant width for the 7:2 resonance (see Chapter 5) and thus is approximately the expected size of the resonant feature. This produces 75 histogram bins, which is larger than suggested by the optimum bins algorithm. However, the insensitivity of the process to the number of bins suggests the choice in the number of bins is not critical. Also, the analysis used here will deal with

the statistical fluctuations that we expect to arise when the number of bins is increased. An area around the expected location of the resonance is removed in order to ensure any signature of the resonance does not bias the mean curve fit produced. In principle, the large measured uncertainties of the CMOR data will broaden such a resonant feature to cover a large area: this is further addressed in Section 4.10. The removed section is centred on the known resonance centre at 2.25AU.

We wish to remove the largest section possible around the resonance centre that still produces a satisfactory fit to the whole dataset. To test for the optimum number of data bins to remove the fitting of the data is monitored using the standard deviation. We progressively remove an increasing set of points either side of the position of the resonance centre, and find that the fitting is good and the standard deviation steady up until the removal of about 14 data bins. After this point the fitting diverges from the data distribution, and the standard deviation begins to rapidly increase (see Figure 4.5). This is the result of removing in excess of 20% of the data points before completing the fitting. We therefore remove the region 2.0 AU to 2.5 AU (a total of 12 histogram bins: a safe choice below 14 points) before fitting an eighth order polynomial to the histogram (see Figure 4.6).

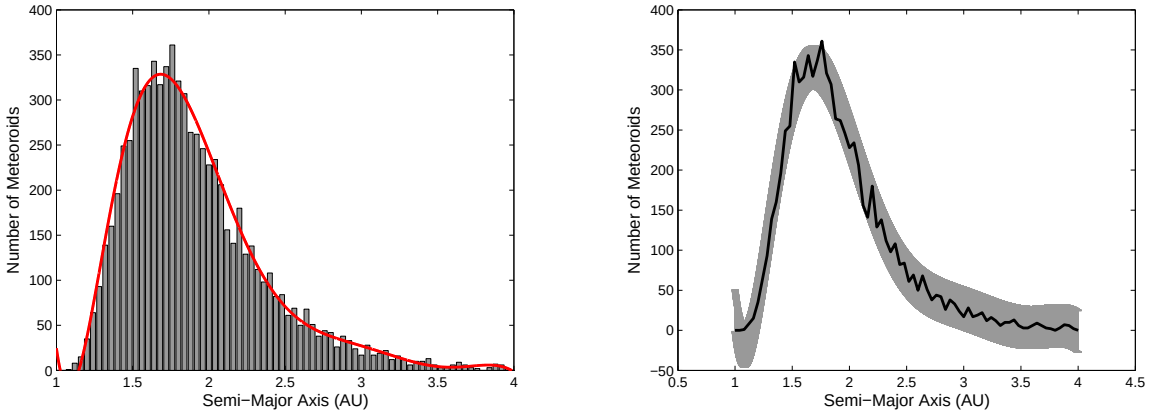

(a) (b)

Figure 4.6: *(a) The CMOR data semi-major axis histogram, with the fitted 8th order polynomial fit determined from the data (red line), but with the section* 2.0-2.5 *AU removed, as explained in the text. (b) The CMOR data semi-major axis histogram values (black line), with the error range created by the region two standard deviations either side of the fitted polynomial curve.*

We now analyse the variations between the polynomial fit and the CMOR data distribution. Figure 4.7(a) shows the variations in units of the standard deviation of the variations. The histogram shown in Figure 4.7(b) demonstrates the approximate Gaussian nature of the variations. We observe five peaks at or above 1.95 standard deviations: in a

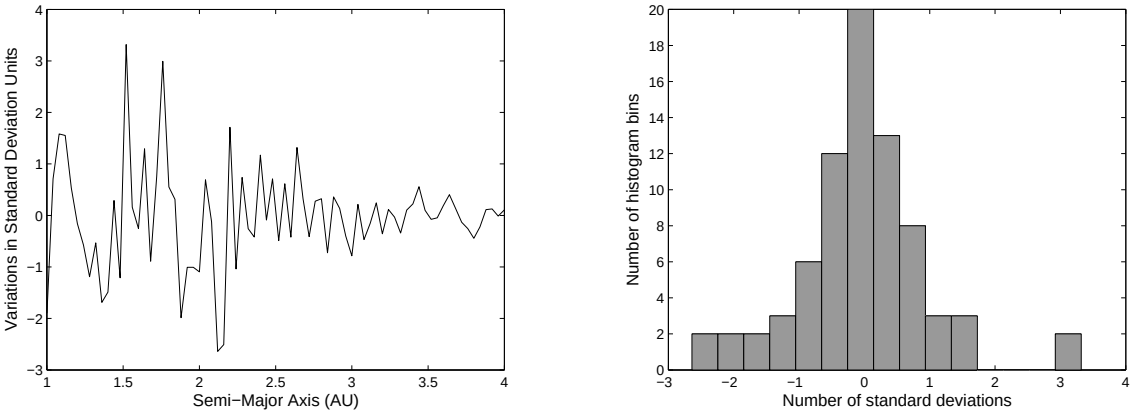

(a) (b)

Figure 4.7: *(a) The variations determined by subtraction of the CMOR data histogram bin numbers from the polynomial fitting to the reduced dataset. (b) A histogram of these variations, demonstrating an approximately Gaussian form.*

statistically random distribution we expect ~ 4, as we expect 5% of fluctuations to exceed 1.95 standard deviations. Similarly, there are 20 peaks above one standard deviation, and a statistically random distribution is expected to have $\sim$ 24 (32%). While these numbers do not match exactly, they are within acceptable fluctuation ranges given the small number examined. This suggests the fluctuations in the CMOR data distribution have random statistical origin. In particular, there is only one sample variation greater than two standard deviations in the region 2.0 AU to 2.5 AU (the region in which we expect resonance indications to be present). However, this feature is below the fitted curve (a variation of -2.64) and therefore is not evidence of a resonant peak. Moreover, there are fluctuations of this size in regions known not to contain a resonant swarm. These reasons allows us to disregard this feature as unrelated to our present problem. However, the resolution of the problem does benefit from an alternative approach: this is provided by the Monte Carlo method in the next section.

4.7.3 Monte Carlo Random Testing

We now describe an independent test for whether the fluctuations visible in the CMOR data distribution are consistent with the expected size of random variations. Here we determine whether a random selection of particles from the test distribution (an eighth order polynomial) can form, by chance, features of the same level of significance as observed in the Taurid meteor data. This would suggest no evidence for a resonant feature in the current data. To perform this analysis requires Monte Carlo simulation.

A simple Monte Carlo method is used to select a random sample of semi-major axis values from a cumulative distribution created from a model distribution, and this

distribution is then compared with the Taurid data. The method consists of the following steps:

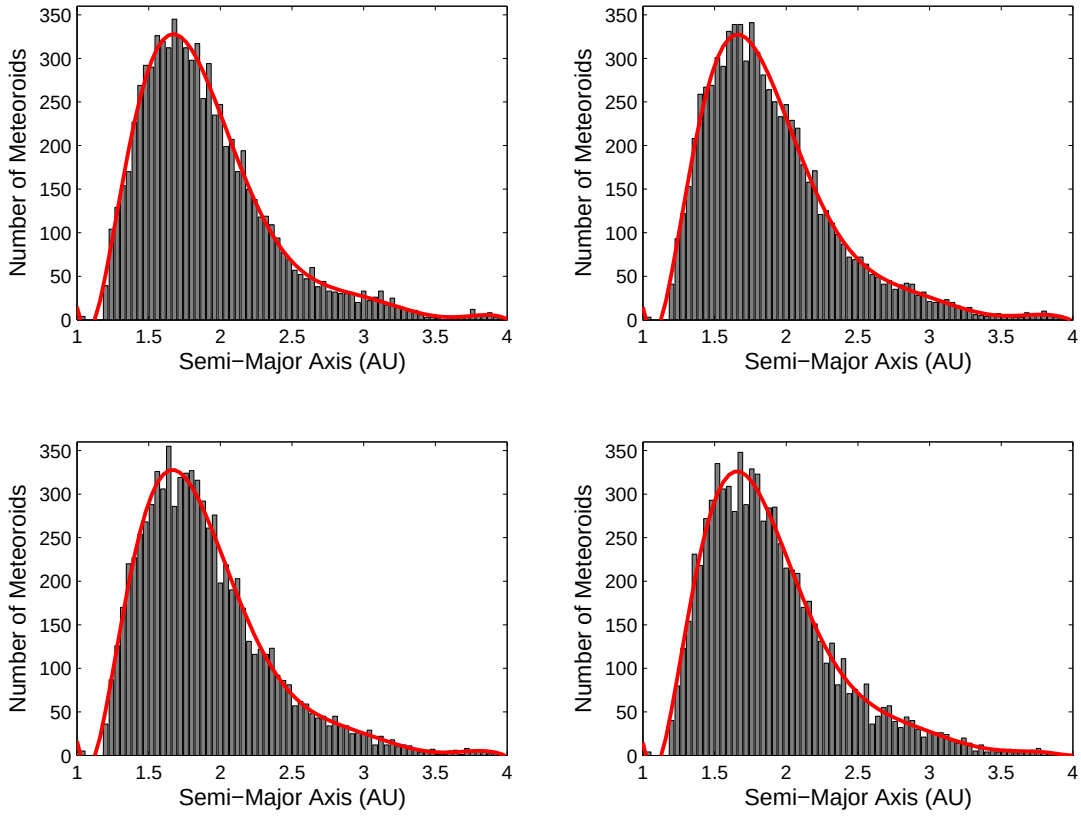

Figure 4.8: *Four examples of random selections of* 7649 *particles from an* 8^{th} *order polynomial distribution (shown as the overlying bold curve on each histogram). Note their similarly in appearance to Figure 4.2*

1. **Selection of a comparison function:** An eighth order polynomial fit was determined. The aim is to determine whether a random sample from this distribution gives the same level of fluctuations observed in the Taurids.

2. **Construction of a cumulative distribution from the comparison function:** Sufficiently small steps were taken along the comparison function, and the cumulative sum of all previous points was computed. Normalisation was not necessary. As this discrete function will act in the place of a difficult to compute continuous function, small steps of 1×10^{-4} AU are taken for 1-4 AU (after which very low rates of Taurids are observed) in order to produce a smooth cumulative probability distribution function.

3. **Random selection of values in the cumulative distribution:** A random number was chosen (up to the maximum of the cumulative distribution), and the value in the discrete cumulative distribution nearest to this was selected. The original semi-major axis distribution (from which the cumulative function was produced) was then used to provide a semi-major axis value, defining the property required for the test meteor. This process was repeated until a dataset of random meteors was created that was the same size as the original CMOR Taurid dataset (of 7649 meteoroids).

4. **Determining the histogram and statistics of the randomly selected dataset to compare with those of the real dataset:** We analyse the resulting set of random meteor semi-major axis values using the process given in Section 4.7.2. The variations (or residuals) between the random semi-major axis histogram distribution and a mean curve (an eighth order polynomial) were found. These variations would be close to zero in a very large dataset of semi-major axis values, as there would be little or no statistical fluctuations. Thus, in this case the size of the variations determines the size of fluctuations from the mean curve that can be expected from statistics alone. If the residual fluctuations in the real data are of the same size as or lower than these variations, then we can conclude that the fluctuations in the real data are statistically insignificant.

5. **Repetition of the process a large number of times:** This process was repeated a large number of times in order to obtain the average statistical fluctuations expected for a dataset of this size.

Figure 4.8 shows four example distributions created by this process. 600 such distributions of 7649 random meteor semi-major axis values are created. In order to compare the statistical fluctuations of the observed Taurid distribution and the random distributions from the Monte Carlo process, we count the number of variations in each dataset that exceed 2, 3 and 4 standard deviations. For the observational CMOR data, 12 features are 2 standard deviations above the mean of the eighth order polynomial fit, 3 exceed 3 standard deviations, and 2 exceed 4 standard deviations. For the artificial data, the average numbers of features (over the 600 datasets) exceeding 2, 3 and 4 standard deviations respectively are 12.12, 3.92 and 1.13. These can be seen to have converged appropriately after 600 datasets (Figure 4.9).

A second simple test using these random datasets involves the simple maximum and minimum of the random datasets at each point. We produce 500 random distributions and determine the maximum and minimum bin height at each semi-major axis. These we plot in Figure 4.10, along with a line plot of the number of CMOR meteors in each

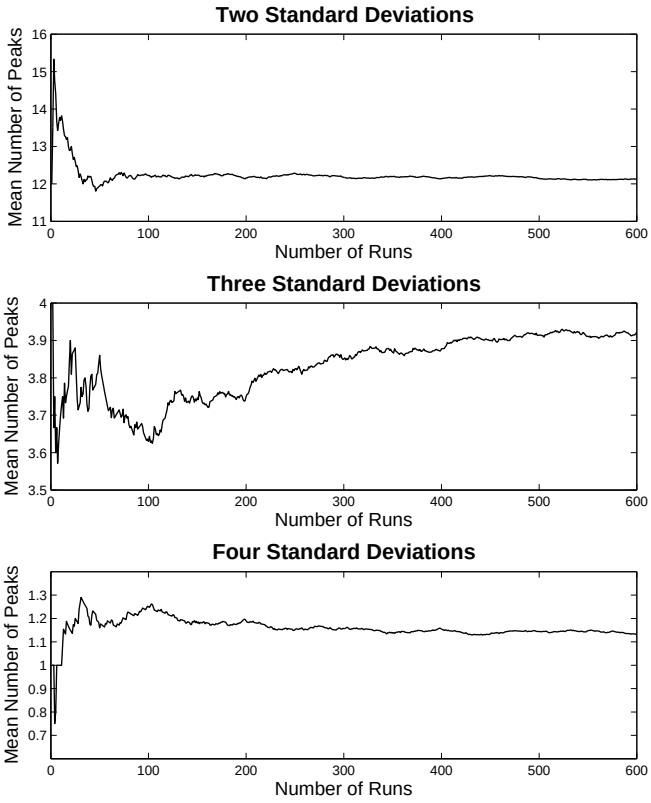

Figure 4.9: *Convergence of the average number of features exceeding* 2, 3, *and* 4 *standard deviations respectively. As the number of runs increases, the average number of features within all preceding runs converges to* ~ 12.12, ~ 3.92 *and* ~ 1.13.

semi-major axis bin. It can be seen that the CMOR data distribution falls within the maximum and minimum bounds produced by the random distributions except for the sharp section with positive gradient ($a < 1.5$ AU). In this region the errors are a result of the poor fitting of the polynomial distribution. These errors are tolerated as this is not the region in which resonant signatures are expected. We therefore conclude that the CMOR data fluctuations can be produced by random distribution for at least the region $a > 1.5$ AU.

4.8 Yearly Variations

Traditionally, the Taurid resonant swarm is investigated by comparison of data over several years. It is possible to compute a measure of the distance of the swarm from the Earth. This is given by ΔM, which is defined as the displacement in mean anomaly of the resonant centre from the point at which the Earth and swarm orbits cross in space

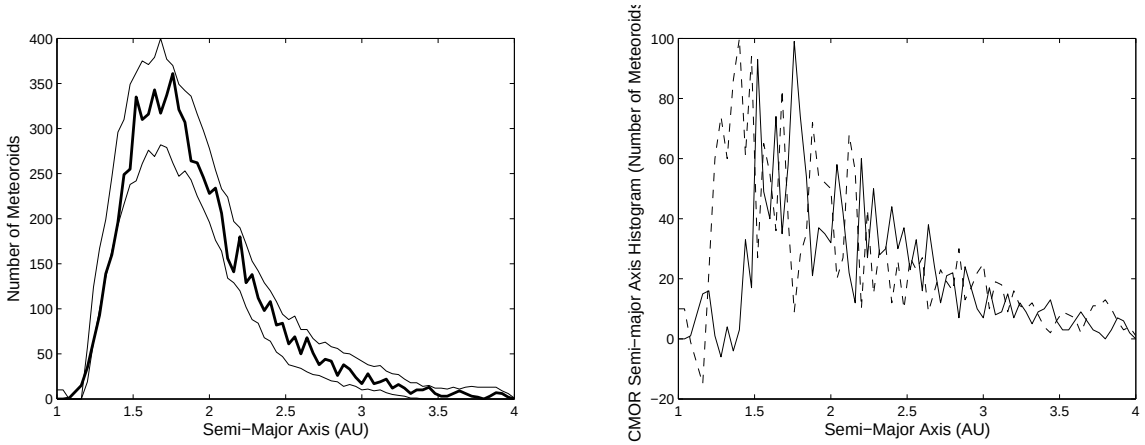

(a) (b)

Figure 4.10: *(a) The maximum and minimum bin values (thin black lines) at each point here form a band inside which the majority of the CMOR data semi-major axis histogram distribution falls. (b) The dotted line shows the differences between the maximum curve and the CMOR data; the solid line represents the differences between the CMOR data and the minimum curve. These differences are calculated such that positive values indicate that the data distribution is within the maximum and minimum limits. We can see that only on the sharp upward section (semi-major axis less than* 1.5 *AU) does the CMOR data exceed the maximum or minimum boundaries. In particular, there are no deviations outside these limits in the resonance region (*2.0 *to* 2.5 *AU).*

and time. In years in which ΔM is small, significant increases in Taurid meteors numbers are expected due to the resonant swarm. Asher and Clube (1993) produce a list of such 'swarm encounter' years, defined as year for which $|\Delta M| < 40^\circ$ on November 23 (the expected swarm encounter date). In the period of the CMOR observations available, only 2005 year is a 'swarm encounter' year. In this year $|\Delta M| < 11^\circ$, which confirms that this is expected to be a good year for observations of this swarm: it is the closest November swarm encounter for 17 years.

4.8.1 Yearly Data

In the above sections a search for a resonant feature in the semi-major axis distribution in the complete CMOR Taurid dataset is presented. We here repeat this analysis to determine whether a resonant feature is visible in the 2005 swarm encounter year.

The statistical analysis of Section 4.7.2 is repeated for the years 2002 to 2007, to determine whether there is any significant difference in the semi-major axis distribution of 2005 relative to non-swarm years. However, in contrast to the method given in this section, only five points either side of the resonant centre location are removed before a mean fit curve is produced. This is because the 2005 data produces unstable fits for six or more points removed each side (see Section 4.7.2 for the test used to determine this).

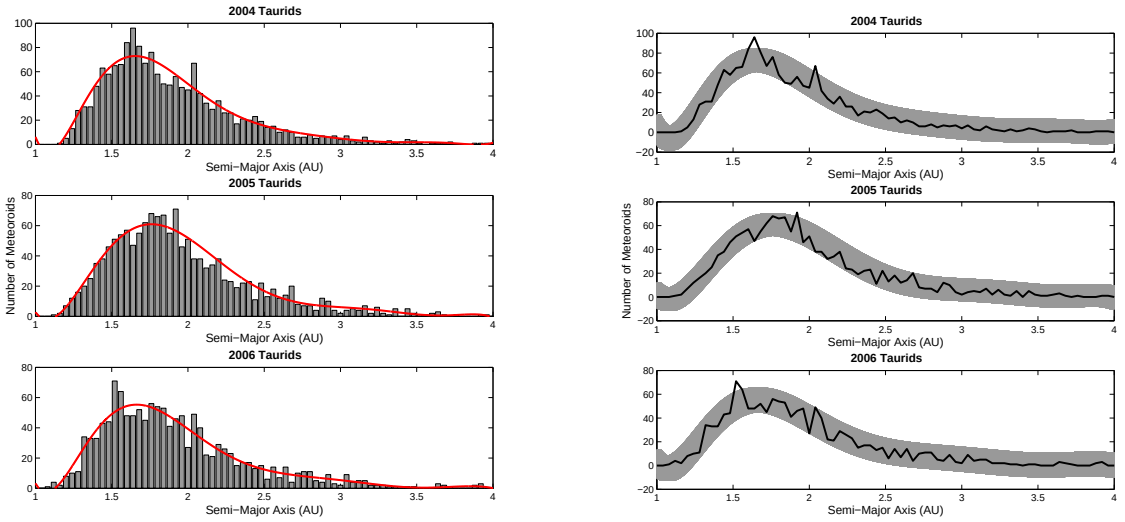

(a) (b)

Figure 4.11: *(a) Histograms and mean curve fittings for 2004, 2005 and 2006 CMOR Taurid data. (b) The Histogram bin values (solid line) on a shaded area that described the region 2 standard deviations away from the mean curve fittings (an eighth order polynomial). For all three years the data fits mostly within this region, and thus is largely consistent with random.*

This is a consequence of the reduced size of the dataset.

The histograms and the resulting mean curves for 2004, 2005 and 2006 are displayed in Figure 4.11(a). Figure 4.11(b) demonstrates that the data variations fit within a region 2 standard deviations either side of the mean curve for all except a few randomly located histogram bins. Figure 4.12 shows the variations of the data from the mean curve more explicitly. Table 4.3 gives the number of features that are more than 1, 2 and 3 standard deviations above the mean curves for the years 2002 to 2007. We now make two observations:

1. The size of the data variations are nearly, but not exactly, consistent with the size expected for random statistical fluctuations. The histograms in Figure 4.12(b) have a roughly Gaussian form. For this number of histogram bins, the numbers of features expected to be more than 1, 2 and 3 standard deviations are ~ 24, ~ 4 and ~ 1 respectively. These numbers of features do not agree exactly with those given for 2005 is Table 4.3. However, the differences are not sufficient to conclude that there are significant differences between the variations observed and Gaussian random variations.

2. The data variations, as quantified in Table 4.3, are consistent between each year. There is no significant difference between the variations for 2005 and those for other

Year	# 1 **std**	# 2 **std)**	# 3 **std**
2002	18	6	1
2003	18	6	1
2004	15	6	2
2005	17	7	1
2006	17	6	1
2007	19	6	2
Approx. Expected Number	24	4	0 or 1

Table 4.3: *The number of features in excess of* 1, 2 *and* 3 *standard deviations for CMOR Taurid data for 2002-2006. Here '# 1 std' denotes the number of features that are more than* 1 *standard deviation away from the mean curve for that year. The final row gives the expected (comparison) numbers for the number of histogram bins used here.*

(non-swarm encounter) years. Thus, there is no evidence of additional features due to the presence of the resonant swarm in 2005.

Analysis therefore suggests that there is no evidence for a resonant swarm in CMOR-detected Taurids either in the combined datasets, or in the 2005 dataset. This may indicate that the measurement uncertainties are too large for such small scale structure to be visible; or that the mass distribution of the swarm is such that there are few radar-sized particles in the swarm. The former is tested in the following sections, while the latter is investigated in Chapter 6.

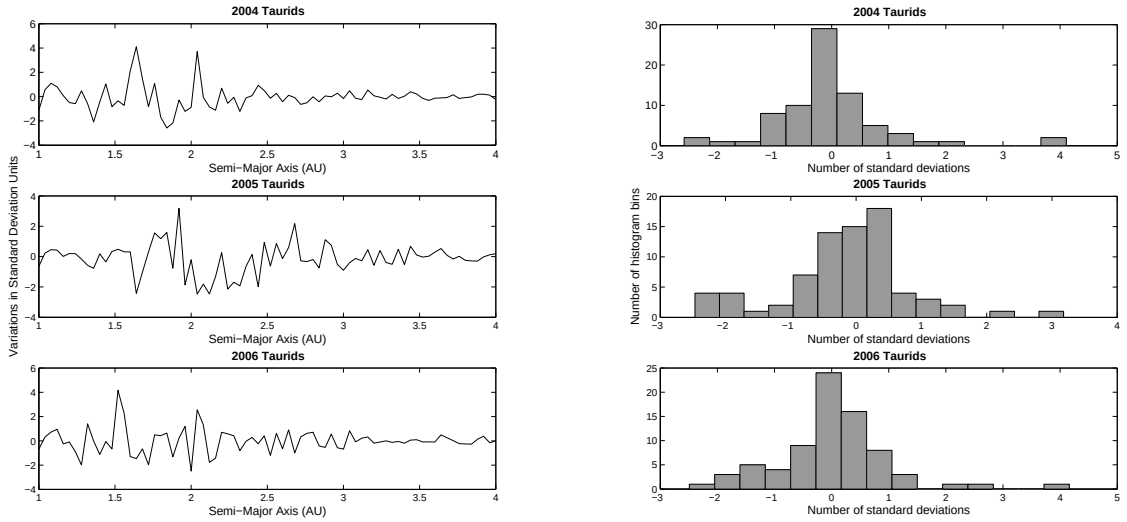

(a) (b)

Figure 4.12: *Variations of 2004, 2005 and 2006 CMOR Taurids from a mean curve, in units of standard deviations.(a) Variations for each year (b) Histograms of the variations (which we expect to be Gaussian).*

4.9 Higher Quality Taurid Orbit

Year	**# 1 std**	**# 2 std)**	**# 3 std**
All Years	19	4	1
Approx. Expected Number All Data	24	4	0 or 1
2005	8	1	0
Approx. Expected Number 2005 Data	10	1 or 2	0

Table 4.4: *The number of features in excess of* 1, 2 *and* 3 *standard deviations for CMOR Taurid data for a restricted dataset containing higher-quality orbits, defined by echoes for which the time-lag and Fresnel/pre-*t_0 *velocities agree to* 3%*. Results are shown for the whole dataset, and for echoes from the year 2005 only. Here '#* 1 *std' denotes the number of features that are more than* 1 *standard deviation away from the mean curve for that year. Alternate rows gives the expected (comparison) numbers for the number of histogram bins used for each dataset.*

Additionally, it is possible to extract higher quality orbits from the total CMOR Taurid dataset. These are the result of higher-precision velocity measurements made possible by the presence of Fresnel oscillations in the amplitude and phase of the meteor echo (see Section 3.2.2). Such echoes will then have about $\leq 5\%$ speed errors instead of about $\leq 10\%$ (Jones et al., 2005), and should therefore provide more reliable semi-major axis values. If the Fresnel oscillation pattern is sufficiently distinct (generally for meteors with a high signal-to-noise ratio), then both a time-lag speed and a hybrid Fresnel/pre-t_0 speed are achievable (see Hocking (2000) for further detail). Following Wiegert and Brown (2005), we form a new dataset containing only echoes for which a Fresnel/pre-t_0 speed is given, and for which the two speeds agree within 3%. The resulting dataset has 1025 meteors, 200 of which are from the year 2005. However, neither the new dataset nor the meteors from 2005 in this dataset display evidence of the 7:2 resonant swarm: using the method given in Section 4.7.2 we find that the variations of both datasets do not significantly exceed those expected as a result of random fluctuations (see Table 4.4).

As mentioned above, these meteors have in-atmosphere speed uncertainties of approximately $\leq 5\%$, as opposed to about $\leq 10\%$ for the time-lag speed method. Heliocentric velocity (V_H) uncertainties are related to semi-major axis (a) uncertainties by:

$$\left(\frac{\Delta a}{a}\right) = \frac{V_H^2}{1 - \frac{V_H^2}{2}} \left(\frac{\Delta V_H}{V_H}\right). \tag{4-1}$$

The derivation of this equation, given by Galligan (2000), uses units such that $V_E = 1$, $GM_\odot = 1$, $R_E = 1$ and assuming $r_h = 1$ AU. Here V_E and R_E are the velocity in space and the radius of the Earth, respectively; G is the gravitational constant and $M_\odot$ is the Solar mass.

The uncertainty in heliocentric velocity ΔV_H will include errors from several sources, most notably from errors in atmospheric deceleration calculations. Thus, we can deduce that reducing the error in the in-atmosphere speed by a factor of two will reduce the semi-major axis uncertainties by not more than a factor of two. We will see in Section 4.10 that such a reduction is not expected to allow us to resolve a resonant feature of the size expected.

4.10 Numerical Study of Observational Uncertainties

It is important to gain an understanding of what issues observational uncertainties may cause in the identification of any resonant peak. In particular, such uncertainties will broaden the Taurid semi-major axis distribution and individual resonant features. It is useful, therefore, to determine whether such features are detectable after they are broadened by the meteor radar orbital uncertainties, or what level of reduction in these uncertainties is required for such features to become significant. The uncertainties used are semi-major axis uncertainties. The results are applicable to velocity uncertainties also, as reducing the velocity uncertainties by a factor x will reduce the semi-major axis uncertainties by the same factor x. This can be determined using equation 4-1 in Section 4.9.

This involves a 'convolution' (or, here, an addition) of:

1. **The overall distribution of non-resonant Taurids:** This is modelled here by the observed Taurid distribution from the CMOR dataset. This may contain a small component of resonant swarm meteors, but this would make little difference to the results obtained, as we have shown that the level of fluctuations from a random curve are consistent with the expected level of statistical fluctuations.

2. **A modelled resonant peak:** This is modelled by randomly selecting a number of meteors N_R from a Gaussian curve with the standard deviation equal to one quarter of the resonance width (determined to be ~ 0.0470 in Section 5.5.2). This is because the full resonant width is equated with the 2σ 95% confidence section of the Gaussian distribution: we define the resonant width as spaning 4σ across the Gaussian distribution. The number of meteors N_R injected into the swarm determines the height of the peak. This is varied as no information is available on the height of the resonant features in semi-major axis distributions. We will usually express this as a percentage of the total number of particles in the combined dataset.

3. **The (assumed) Gaussian profiles for the uncertainty on each individual observed particle:** Each data value from (1) and (2) above is converted from a

point into a Gaussian profile in order to simulate the effect of uncertainties. The given semi-major axis uncertainties in the CMOR datasets are taken as the standard deviations σ for each Gaussian profile. Each Gaussian is scaled to have an area of 1 under the curve.

We conduct two separate tests using this model. The first assumes zero uncertainties and thus only combines distributions (1) and (2) above. This 'perfect' data case can demonstrate the absolute lower size limit of a resonant feature that can be detected in a meteor radar dataset (of the size of the CMOR Taurid dataset used here). This is given in Section 4.10.2. The second test includes uncertainty broadening and thus all three distributions above are used. This test is given in Section 4.10.3.

The addition of uncertainty broadening can also be thought of as two distributions - the Taurid distribution and a model resonant feature - each composed of many individual Gaussians instead of many individual points (delta functions). This convolution is dealt with numerically by creating a histogram Gaussian to represent each point. Each Gaussian histogram meteor is defined from -4σ to $+4\sigma$, with steps of 0.04 AU (approximately the expected width of the resonance feature): thus, each meteor will cover a different number of bins depending on its corresponding uncertainty. The standard Gaussian formula is used:

$$G = \frac{1}{\sigma\sqrt{2\pi}} exp{-}(\frac{z^2}{2\sigma^2})$$

where z defines the size of the region covered by the Gaussian meteor in semi-major axis (-4σ to $+4\sigma$). By adding these Gaussian-broadened meteors we achieve a histogram of the semi-major axis distribution similar to that seen in Figure 4.6, but in which each meteor is fractionally split over several bins. The resulting distribution is scaled in situations where the peak of the convolved distribution exceeds the peak of the original CMOR distribution. This is to ensure that the statistics remain comparable (to allow the standard deviation for the original dataset variations to be used: see Section 4.10.1).

Figure 4.13 shows a representative model resonant feature peak of 200 meteoroids (2.5%) randomly selected from the model Gaussian, and the complete distribution achieved by the addition of the fictitious resonant feature meteors to the Taurid dataset.

We are now able to apply uncertainties to this combined dataset (Figure 4.13(b)) and determine whether the peak is statistically significant on application of uncertainty broadening. The percentage or number of meteors in the swarm, which is unknown, can then be varied. The applied uncertainties are reduced by applying a fractional multiplication factor to the orbital uncertainties in the CMOR dataset.

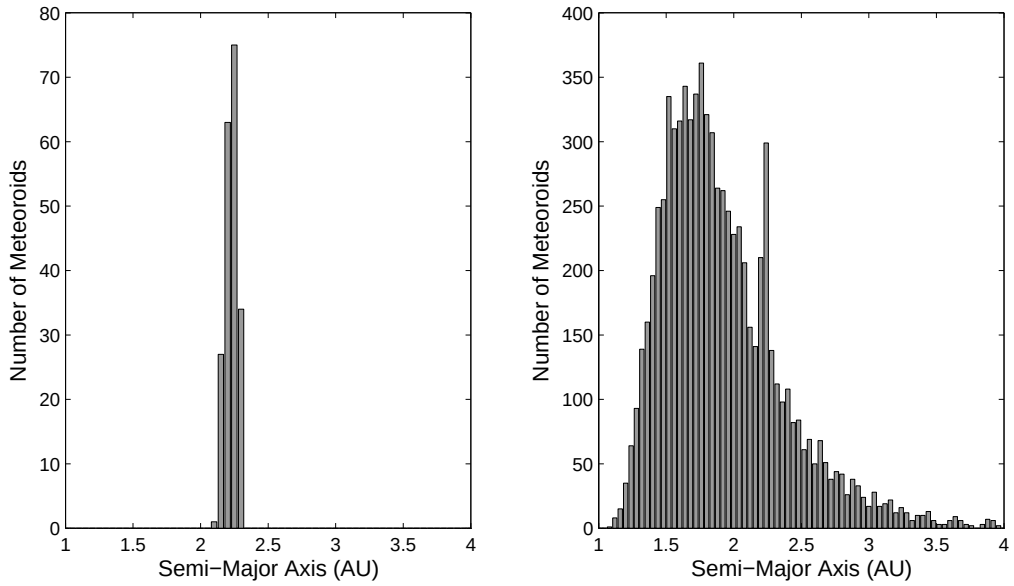

Figure 4.13: *Model resonant features with $N_R = 200$ meteoroids in the resonance (that is, 2.4% of the total dataset are in the model resonant feature). We first show the selected peak alone, and then its addition into the Taurid distribution.*

4.10.1 A Statistical Test

A statistical test is required to evaluate whether the resonant feature is statistically significant, both in the 'perfect' data case and in the uncertainty-broadened case. This is, for consistency, the first statistical test carried out on the CMOR data distribution (see Section 4.7.2). In summary, this involves:

1. Removal of the resonant area of the distribution (approximately 2.0 AU to 2.5 AU)
2. Fitting of a test distribution to the remaining sections of the distribution
3. Analysis of the variations between the distribution of interest and the fitted distribution

Previously this was completed by comparing the variations (of (3) in the statistical test summary) to the standard deviation of the variations themselves. Here the comparison value is the standard deviation of the variations of the original data distribution. This is because the uncertainty broadening will remove the small statistical fluctuations. Thus the statistical fluctuation information is contained only in the standard deviation of the variations of the original CMOR data.

By comparison with the statistical fluctuations in the CMOR data distribution, we conclude that a peak will be considered significant if two conditions are fulfilled:

1. The peak is above three standard deviations

2. Two adjacent points are above two standard deviations

The second condition is required because it is expected that these peaks will cover more than one histogram bin, and will not resemble the sharp statistical fluctuation features seen in Figure 4.7. We expect the feature to be a peak, not a trough, such that the variations should be positive (if we are subtracting the distribution of interest from the fitted distribution).

In addition, the model resonant peak involves a random element in the selection of particles from a Gaussian. This means that the decision as to whether a particular resonant feature peak size is significant may vary each time the process is run. Thus, we require a positive detection of the peak in 20 successive tests in order to conclude that the peak is statistically significant for that uncertainty level and peak size.

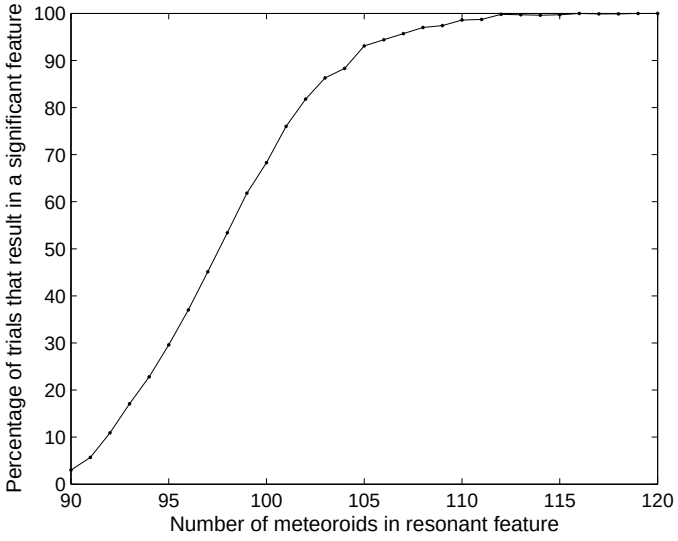

Figure 4.14: *The variation in the number of trials for which a significant peak is found, for a variety of fictitious resonant peak sizes. Above* 112 *meteoroids in the peak we can see that* 99% *of trials result in a significant peak.*

4.10.2 Perfect Data

Here we apply a statistical test to 'perfect' datasets with a range of sizes for the test resonant peak. Here 'perfect data' is defined as data with no uncertainties or negligible uncertainties in the measured semi-major axis values: it is a consideration of the case in which statistical variations are larger than observational uncertainties. Therefore, no uncertainty broadening is included at this stage: we only add a resonant peak of a specific

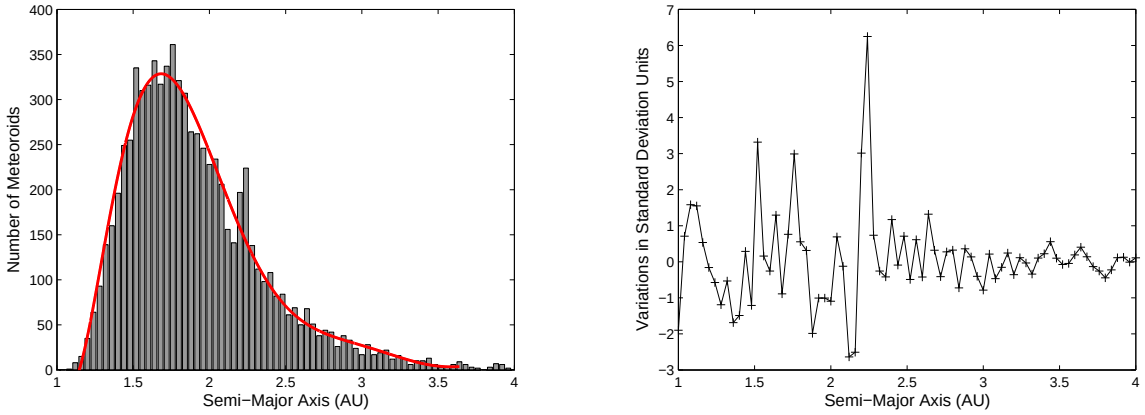

(a) (b)

Figure 4.15: *The lowest resonant peak which is statistically significant for 'perfect' data (that is, data with no uncertainties) for* 99% *of trials is one with* 112 *meteoroids (*1.4% *of a dataset of this size). The combined semi-major axis distribution containing the CMOR Taurid data and the ficticious resonant peak is shown in (a), along with the* 8*th order polynomial fit to the dataset (without the resonant region* 2.0 *to* 2.5 *AU).(b) shows the variations between the data histogram (with resonant peak) and polynomial fit distributions, scaled to the standard deviation of the variations of the original CMOR dataset.*

size, determined by the number of particles in the peak, and determine whether the resulting peak is statistically significant, and thus observable. The size of this resonant peak is also called the 'resonant feature strength'.

This test is first run 20 times and the first peak size that is significant in all 20 tests is determined. This is a peak of 108 meteoroids: 1.39% of the total number of particles in the distribution (for a dataset of this size). This provides a result that can be compared with the uncertainty broadening case (Section 4.10.3). A higher accuracy test is then run, where this process is run 1000 times and the point at which 99% of trials result in a significant peak is determined (see Figure 4.14). It is found that an added resonant feature greater than or equal to 1.44% (112 meteoroids) fulfills this criterion. Additionally, any peak with size greater than 1.53% (119 meteoroids) produces significant features 100% of the time. An uncertainty of 4 meteoroids is determined from the difference between the limiting values determined in 20 and 1000 consecutive tests. Thus, $\sim 1.44 \pm 0.05\%$ is the lower limit on the proportion of the stream that must be resonant in order for detection to be made by radar for this size of dataset. A distribution with a peak of this limiting size, and the variations from the polynomial fit are shown in Figure 4.15.

4.10.3 Data with Varying Uncertainty Levels

Here we determine the approximate uncertainties (relative to those of CMOR) required of a meteor radar system for it to be capable of detecting a Taurid resonant swarm. This requires the addition of uncertainty broadening, as outlined in Section 4.10. To accomplish this we apply a range of fractional multiplicative factors to the uncertainty Gaussians based on CMOR uncertainties, and determine which result in statistically significant detections of the modelled resonant peak, for a range of sizes for this peak.

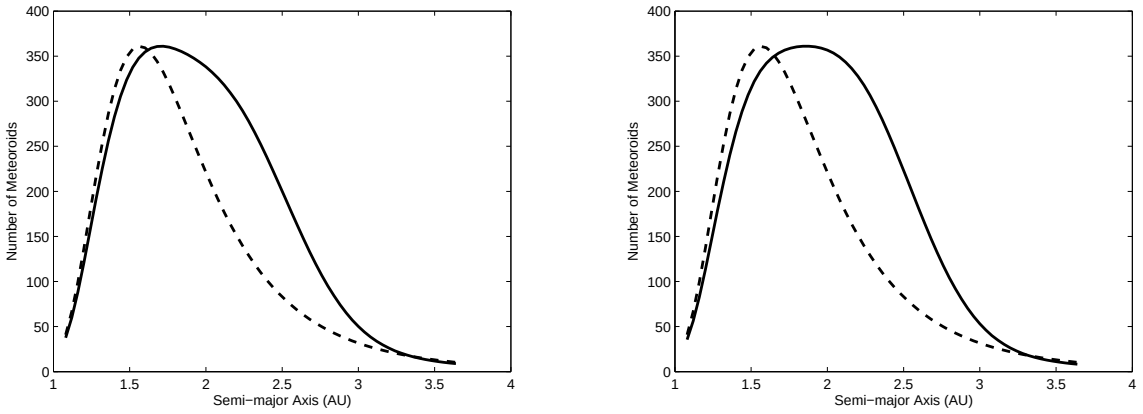

(a) (b)

Figure 4.16: *The effect of high resonant feature particle numbers on the convolved dataset. Here we see two examples of the behaviour of the numerical convolution at an uncertainty reduction factor of* 2*: (a) at a resonant feature strength of* 4500 *and (b) at a resonant feature strength of* 6000*. Therefore in (a) the resonant feature comprises* 37% *of the total dataset, and in (b) it comprises* 44%*. We can see that for the first example , elements of the underlying (dotted) original distribution remain, but that in (a) the distribution is dominated by the resonant feature. However, in neither case would a statistical test be able to determine that there was evidence for a resonant feature unless the underlying Taurid distirbution is known.*

We explore the range of integer-value 'uncertainty reduction factors' from three to fourteen. These factors represent values by which the uncertainties are divided: that is, an 'uncertainty reduction factor' of three represents a reduction in the uncertainties to $\frac{1}{3}$ of their original values. An uncertainty reduction factor of 2 requires an unrealistically large number of particles to be in the resonant swarm in order for a statistically significant peak to be observed. We therefore do not include uncertainty reduction factors less than 3. Furthermore, the method is less robust after the modelled resonant swarm comprises $\sim 40\%$ to 50% of the total dataset, as after this point the convolution starts to move the peak of the distribution away from the Sun (see Figure 4.16). However, the percentage of the total number of Taurid particles that are in the 7:2 Taurid resonant swarm is unlikely to be higher than 40% (see below). If this method were to be applied in a situation

where a swarm may comprise more that 50% of the total dataset, use of this numerical convolution would require a different model for the overall distribution of non-resonant Taurids.

Also, this restriction implies that an uncertainty reduction factor of 1 (that is, no change to the current uncertainties) will not result in a significant detection of the resonant swarm, unless more than 50% of observed Taurids are resonant, which is unlikely. Thus, the broadening as a result of the uncertainties of the CMOR dataset used here will not allow observation of the Taurid resonant swarm.

For uncertainty reduction factor values greater than fourteen the method reaches its limitation as the uncertainties begin to become smaller than the histogram bin size used. This only affects the smallest semi-major axis values at first, but will affect the whole distribution for very high uncertainty reduction factor values. An improved algorithm would be able to deal with this situation. However, given that by a reduction factor of 14 the resonant feature values required for significance are almost equivalent to those required in the 'perfect' case, this is not pursued here.

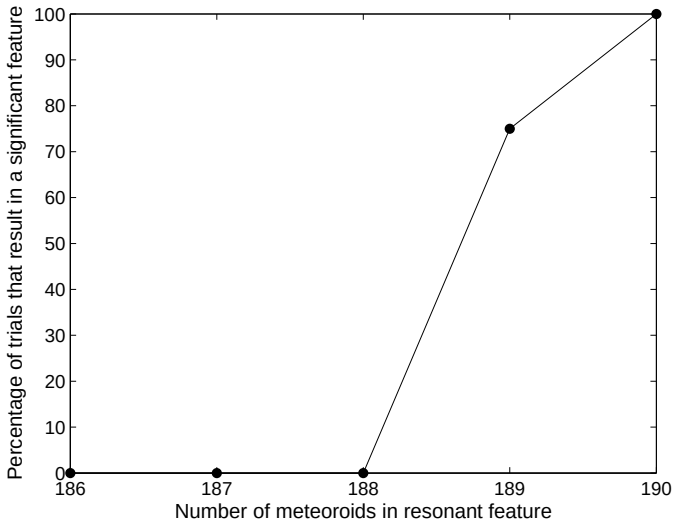

Figure 4.17: *The variation in the number of trials for which a significant peak is found, for a variety of fictitious resonant peak sizes, and at an uncertainty reduction factor of* 9. *Above* 190 *meteoroids in the peak we can see that* 100% *of the* 20 *consecutive trials resulted in a significant peak.*

For each uncertainty reduction factor we determine the minimum modelled resonant peak size required. The method for this is given in Section 4.10.1. Uncertainties are given by the difference in resonant peak size between a size for which $\frac{1}{20}$ tests provide a statistically significant result, and one that allows $\frac{20}{20}$ to pass. This is usually a maximum of ~ 3 meteoroids, though in some cases it is 1 meteoroid or less. As an example, we use

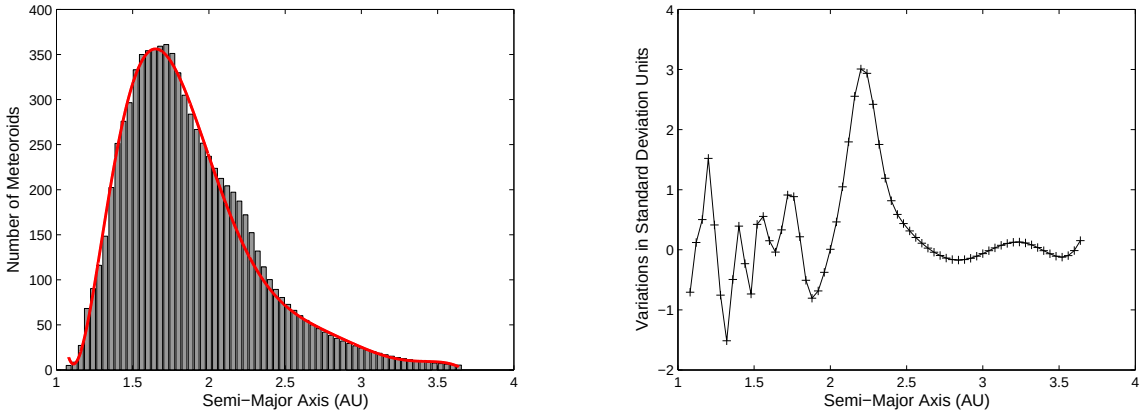

(a) (b)

Figure 4.18: *The lowest resonant peak which is statistically significant in* 100% *of* 20 *trials for uncertainty broadened data with an 'uncertainty reduction factor' of* 9*. This is a feature with* 190 *meteoroids (*2.4% *of a dataset of this size), with an uncertainty* ±3 *meteoroids. The combined semi-major axis distribution containing the CMOR Taurid data and the ficticious resonant peak, both uncertainty broadened, is shown in (a), along with the* 8*th order polynomial fit to the dataset (without the resonant region* 2.0 *to* 2.5 *AU).(b) shows the variations between the data histogram (with resonant peak) and polynomial fit distributions, scaled to the standard deviation of the variations of the original CMOR dataset.*

the size of the resonant feature required at an uncertainty reduction factor of 9. Figure 4.17 shows the percentage of tests that produced a significant result for resonant feature sizes of 2.37% to 2.42% (equivalent to 186 to 190 particles for an initial dataset of 7649 meteoroids). The minimum significant resonant feature size for which all 20 tests produce a significant result is 2.42% (190 meteoroids). The uncertainty is 1 meteoroid (or 0.013% of this total dataset), as only one 'resonant feature size' below 190 meteoroids can produce a significant result (see Figure 4.17). The resulting broadened distribution and variations from the mean curve are given in Figure 4.18

Figure 4.19 shows the resonant feature strengths that are observable for a given reduction in the radar uncertainties. This figure can be used to either:

- Determine the required minimum uncertainty reduction factor for a CMOR type radar for a given resonant feature size.
- Determine the required minimum resonant feature size for a given level of uncertainty reduction.

The values given in Figure 4.19 are only valid for the size of CMOR dataset used here. We note that an uncertainty reduction factor of 14 will allow a swarm of a similar size to be detected as for the perfect data (120 meteoroids for a reduction in uncertainties of 14; and

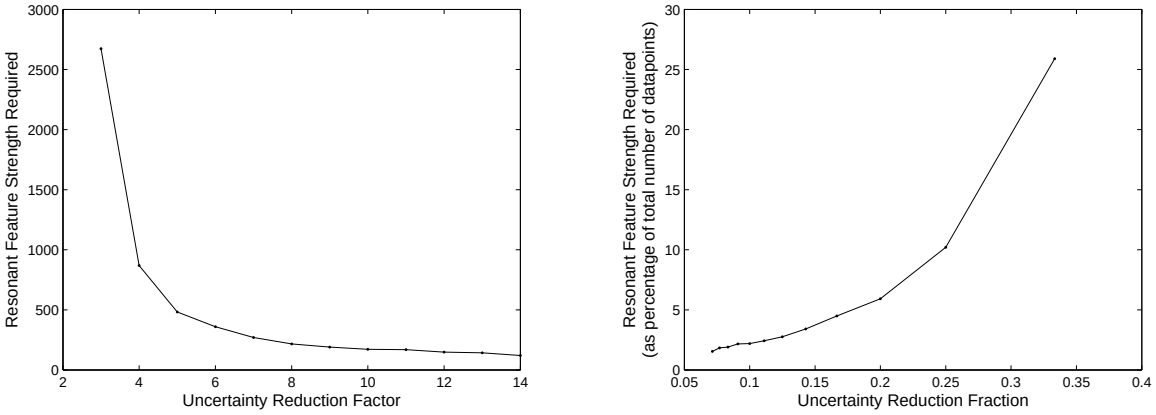

(a) (b)

Figure 4.19: *The resonant feature strength detectable for each uncertainty reduction fraction. We can see that, for example, a reduction in uncertainty by a factor of about* 9 *is required to observe a resonant feature with* 200 *particles (*2.6% *of the dataset). Here the 'uncertainty reduction fraction' is the reciprocal of the 'uncertainty reduction factor'. The former is the fraction by which CMOR uncertainties must be multiplied in order to detect a resonant feature of that size.*

108 for a 'perfect' data). This implies that a limit is reached by the radar uncertainties: after a reduction in uncertainties of 12 to 14 statistical variations will largely govern the visibility of resonant swarms, and further improvement in the radar will not assist greatly in detection. This study, and the 'perfect' data study, thus imply that for radar datasets of this size, swarms which comprise less than $\sim 1.5\%$ of the meteoroid stream are unlikely to be detectable using this methodology, regardless of the uncertainties of the radar system.

Therefore, for a radar dataset of this size, and with the requirement that resonant meteoroids comprise more than 2% of the radar Taurid dataset, a radar with improvement in uncertainties given by a reduction factor of 12 or higher (equivalent to 8% of the current uncertainties) should be able to detect a resonant swarm in Taurid meteoroids (assuming that the radar system has approximately the same mass sensitivity as CMOR). A resonant peak that is 2.2% of the number of Taurids in the dataset should be detectable by reducing CMOR uncertainties to 10% of their current values (reduction factor of 10). Such an enhancement is considered feasible with the current techniques of radar systems and signal processing.

The uncertainty reduction levels considered above require knowledge of the approximate proportion of Taurids that are resonant. This is difficult to determine, and is dependent on the location of the swarm with respect to the Earth, the number of particles in the swarm and the size distribution of these particles. Visual observations are used to obtain estimates of the size of the resonant swarm: since no radar observations of the

Taurid swarm exist, we must use such visual observations. Results from visual meteoroid studies will only be applicable to radar data if the number of radar-sized particles in the swarm is similar to the number of visual particles. We use the activity profile (of ZHR as a function of solar longitude) for visual Taurids of 2005 given in Dubietis and Arlt (2007) to estimate the maximum proportion of 2005 Taurids that are resonant. ZHR is an indicator of particle numbers: an actual mass flux is dependent on the population index. However, Dubietis and Arlt (2007) find that the population index of visual Taurids is roughly constant, fluctuating around a population index of 2.4. Simple area calculations are used to determine the approximate number of meteoroids in the 2005 profile, compared with the number of meteoroids in a typical annual profile averaged over 1985-2004. We find that the enhanced 'swarm' region of the profile (the region that differs markedly from the typical annual profile) contains $\sim 30\%$ of the meteoroids contained in the total 2005 profile. For 1988 and 1998 we obtain 23% and 41% respectively. These values are only accurate to an estimated $\sim 20\%$. We note that the three years tested here represent optimal years for swarm detection, with the mean longitude of the resonant centre of the swarm being within 15° of the mean longitude of the Earth; but also that the proportion of swarm meteoroids and maximal ZHR values (calculated by Dubietis and Arlt (2007)) are not well correlated with the proximity of the swarm to the Earth. This is still an issue after consideration of the presence of a full moon in some years - particularly in 1995 and 1998. This could reflect other variations in observational geometry of the swarm. Additionally, the proportion of swarm particles detected by visual methods may be larger than that detected by radar methods, because it is expected that larger particles are more easily trapped in the resonance if ejected from a resonant or near-resonant comet (see Chapter 6). For these reasons we are not able to be precise on the expected proportion of swarm particles in radar datasets. In general, however, we expect that the proportion of particles will not exceed 20-30% of the total dataset for a swarm year. This is equivalent to ~ 5–8% of the CMOR dataset spanning 2002-2007.

4.10.4 Variation with the Dataset Size

Here we determine how the results of Section 4.10.3 vary for datasets of different sizes. A larger dataset will contain relatively smaller random statistical variations, and thus a large radar dataset with a given measurement uncertainty level will detect, to a given significance, a smaller resonant feature than a smaller dataset. This serves two purposes here:

- To determine the effect if an improved radar is operated for a shorter or longer time than the 2002-2007 period producing the CMOR dataset used here.

- To determine the required number of particles in any one year required to produce a statistically significant result for a given reduction in uncertainties.

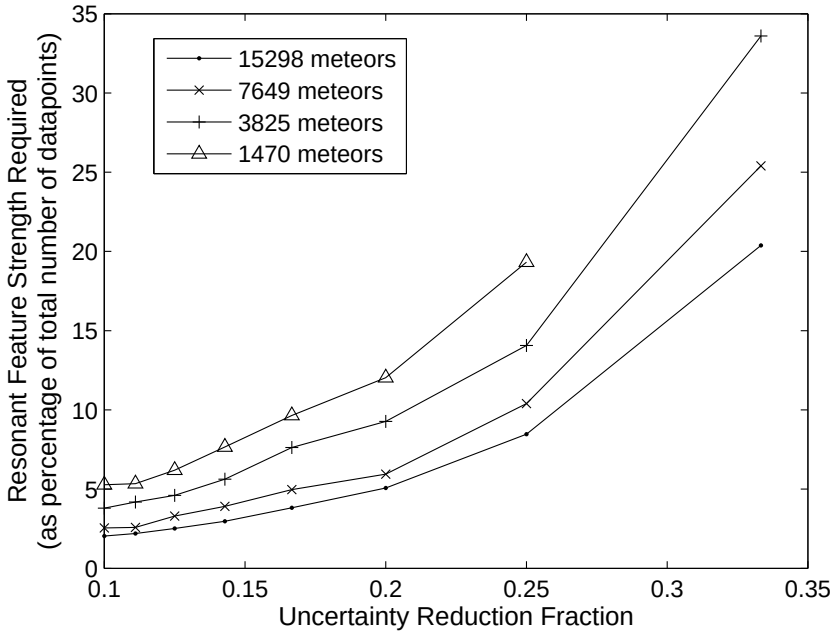

Figure 4.20: *The variation in the size of the resonant peak (as a percentage of the size of the total dataset) required for a statistically significant detection at each level of uncertainty reduction, relative to the CMOR uncertainties of the current dataset. Each line shows a different number of particles in the source dataset. The lower three lines (*15298*,* 7649 *and* 3825 *meteors) represent datasets of double, equal and half the size of the CMOR dataset used in this chapter. The upper line (*1470 *meteors) represents the number of particles detected in the 2005 swarm year by CMOR: that is, this provides the approximate percentages of meteoroids that must be in the observable radar Taurid stream in order for detection to be made based only on one year of data. This is important given that the swarm's location relative to the Earth is only optimal for observation every* 3 *to* 5 *years. The uncertainty reduction fractions are the inverse of the uncertainty reduction factors.*

These aims require modifications to be made to the numerical method given in Section 4.10. To obtain a representative dataset that has the same distribution shape as the CMOR Taurid semi-major axis distribution, but is composed of a different number of particles, the Monte-Carlo method given in Section 4.7.3 is employed. This allows the random selection of a given number of particles from an eighth order polynomial fit to the CMOR Taurid semi-major axis distribution. A standard deviation of the variations of the random dataset from this fitted curve is determined in order to perform the statistical test given in Section 4.10.1. The uncertainty values for each semi-major axis are determined

using a quadratic fitting to the CMOR data uncertainties, which provides the uncertainty as a function of semi-major axis. A random component is added to each uncertainty to model the scatter in uncertainty values, again using a fitting to the CMOR data. The remainder of the methodology is identical to that used in Section 4.10. Due to the fact that the distribution is now randomly produced, the uncertainty levels will be much higher than previously (where only the model resonant feature was produced randomly). However, this method is more robust as it accounts for the variations in the statistical fluctuations that can occur (whereas the results of Section 4.10.3 depend on the statistical fluctuations of an improved dataset being the same as those in the current CMOR Taurid dataset).

We choose four sizes of test datasets:

- the size of the CMOR dataset used here (7469 meteors)
- half size of the CMOR dataset (3825 meteors)
- double size of the CMOR dataset (15298 meteors)
- the size of the CMOR dataset for 2005 (1470)

The final dataset size is important as it illustrates the approximate uncertainty reduction factor or proportion of resonant meteors required to detect the swarm in one year of data, which is necessary because the swarm is only in a good location for observation relative to the Earth once every 3 to 5 years (see Section 4.8).

For each dataset, and for each integer-value uncertainty reduction factor of 3 to 10, the first resonant feature strength that produces 20 consecutive significant tests is found (see Figure 4.20). Figure 4.20 identifies the approximate resonant feature size that can be observed for a given uncertainty in meteor radar semi-major axis data. It can also provide the approximate uncertainty reduction required in order to detect a feature of a given size. As expected, a smaller dataset requires a larger resonant feature for significant detection to be made. However, the differences in the required resonant feature strengths are not as large as the size of the dataset. For example, doubling the size of the dataset from 7649 to 15298 meteors only decreases the size of the resonant feature required by 15-25%. Similarly, a dataset of half the size (3825 meteors) can produce significant detection of a resonant feature 25-40% smaller.

As mentioned above, there will be significant fluctuations in the results due to the random element of the method. We evaluate this error by testing a region around a number of the points on Figure 4.20. For each dataset size, for uncertainty reduction factors of 4 and 8, we test between 50 and 100 resonant feature strength values (in steps of 5 or 10) either side of those resonant strength values given in Figure 4.20. Again, 20

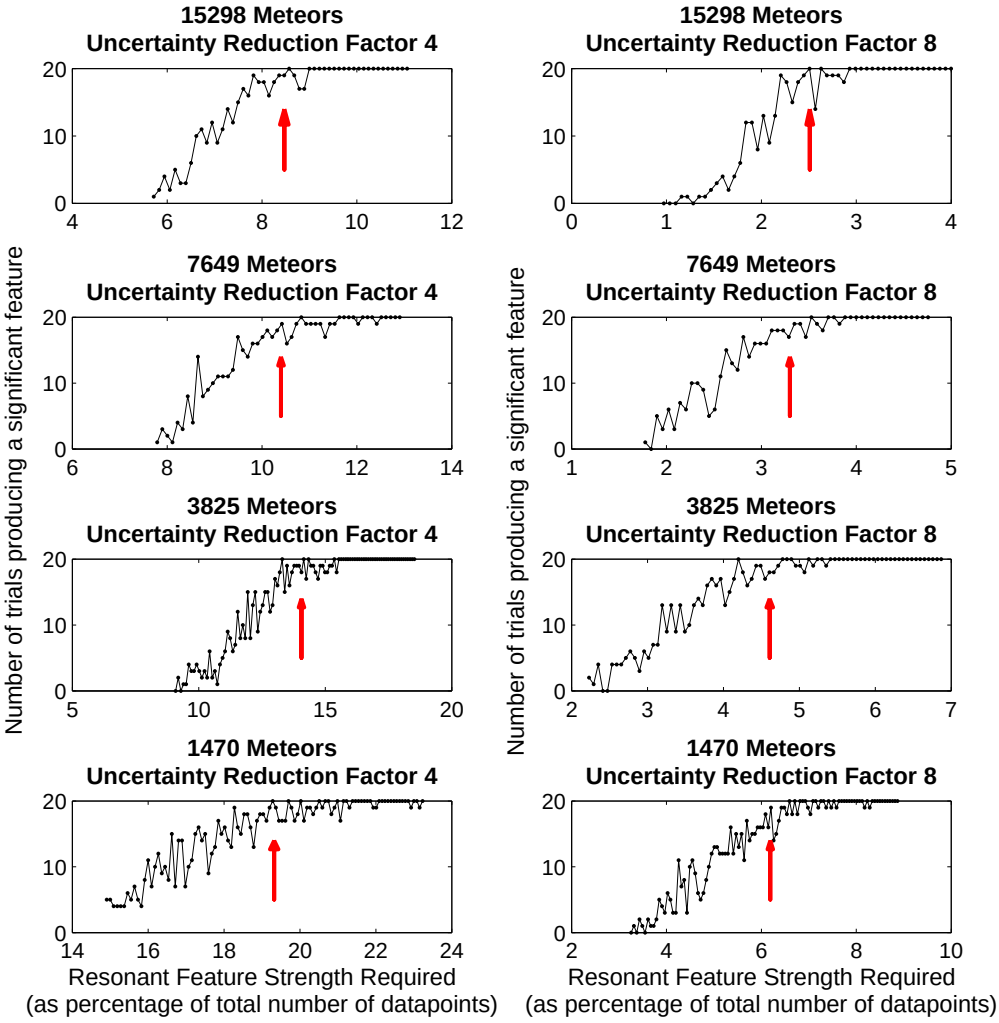

Figure 4.21: *The number of tests resulting in a significant resonant feature for each resonant feature strength at datasets of sizes* 1470, 3825, 7649 *and* 15298, *for uncertainty reduction factors* 4 *and* 8. *Arrows on each graph indicate the values of resonant feature strength plotted on Figure 4.20.*

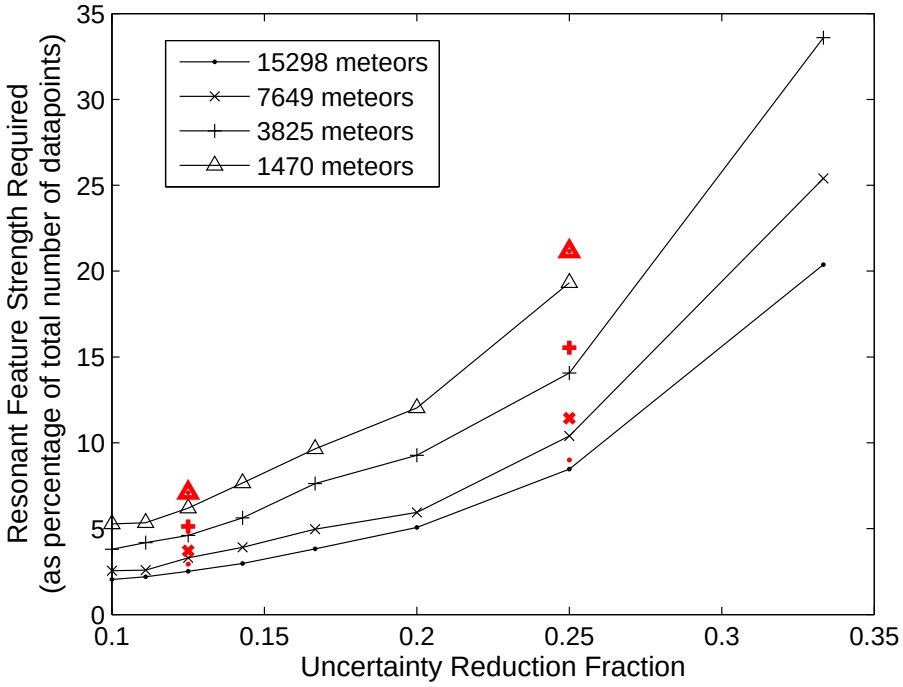

Figure 4.22: *Figure 4.20 with the addition of points (in red) demonstrating the resonant feature strengths required for a 95% probability of a significant detection of the resonant swarm for a given uncertainty reduction factor and dataset size. Again, each line shows a different number of particles in the source dataset:* 15298, 7649 *and* 3825 *and* 1470 *meteors.*

tests are run for each set of values. In Figure 4.21 the number of tests out of 20 that produce a significant result for each resonant feature strength is plotted. The resonant feature strength values used to produce Figure 4.20 are indicated by red arrows on each graph. It is evident that the values given in Figure 4.20 refer to the resonant features strengths that will in all but two cases provide a greater than 80% chance of detecting a significant feature. The two exceptions are for datasets of size 15298 and 1470 meteors, with uncertainty reduction factor 8: in these cases there is a greater than 70% of detecting a significant feature. In both cases an increase in the resonant feature size of less than 5% would produce a greater than 80% chance of sucess.

We are interested also in what resonant feature strength (for each uncertainty reduction factor) would allow a significant detection of the resonant feature in 95% (19 out of 20) of cases. It is at this level of confidence that we would expect a radar with such an orbital measurement uncertainty (or uncertainty reduction) to be able to detect a swarm of that resonant feature size. For an uncertainty reduction factor of 4, values $\sim$ 10% greater than those in Figure 4.20 are required to achieve a significant resonant

peak in 95% of cases. For an uncertainty reduction factor of 8, values 11 - 17% greater are required. A revised version of Figure 4.20 is given in Figure 4.22. This demonstrates with red points the 10-17% improvement in the results required to provide a 95% probability of detecting the resonant swarm in the given values.

If one year of data from a swarm close-approach year is available, then the expected proportion of resonant swarm particles will be higher than in a general dataset: it may be as high as 20-30% for a strong swarm encounter year (see Section 4.10.3). If this is the case, it is possible that a radar with an improvement of measurement uncertainties of only a factor of 4-5 could detect this resonant swarm (this can be seen from Figure 4.22). The required improvement in uncertainties will depend on whether there are approximately the same number of radar-sized swarm particles as visual-sized particles (see Chapter 6). However, as long as the resonant swarm results in a 5–6% increase in particles, a radar with uncertainties one tenth of those of the CMOR dataset used here should be capable of detecting the swarm.

4.11 Summary

In summary, the detection of a resonance swarm with a meteor orbit radar requires improvement of the orbital uncertainties. In this work we find no evidence for the 7:2 resonance swarm, which should theoretically be amongst the most easily observed resonance effects in radar data (see Section 4.4). In addition, the uncertainties of the CMOR dataset used here are too large to allow observation of the resonant swarm. The level of improvement required is highly dependent on the size of the resonant swarm, and the resulting increase in the number of Taurid particles observed in a swarm year. If the resonant swarm comprises 20-30% of resonant particles in a swarm year, then potentially one year of observations with a meteor orbit radar with orbital uncertainties a factor of 5 lower than CMOR could detect the swarm; however, if the swarm comprises only 5–6% of the total Taurids, a factor of 10 improvement in the radar uncertainties would be required. We recall here that these factors of reduction in semi-major axis uncertainties are equivalent to the required reduction factors for the velocity uncertainties. The size of swarm that can be observed to plateau after an improvement in orbital uncertainties of a factor of ~ 10 (see Figure 4.19). At this point a swarm $\sim 5\%$ of the Taurid dataset would be observable in about one year of radar data. Therefore, improvements above a factor of 10 are not likely to greatly improve the chance of observing a resonant swarm.

Such improvements in meteor radar measurement uncertainties, though they present technical difficulties, may be feasible with current techniques of radar systems and signal processing. In particular, the addition of more stations with the ability to recover phase

information would produce independent speed measurements. These would allow calculation of the deceleration of meteors in the Earth's atmosphere, and would significantly improve the velocity uncertainties for detected particles. This approach is the motivation behind an improved CMOR II radar which will have five remote stations in addition to the home site (Brown et al., 2010). Higher sampling rates (by an improvement in the pulse repetition frequency) would also improve orbital uncertainties. The Fresnel velocity method can provide a factor of ~ 2 improvement in the velocity uncertainties in comparison to the time-lag method (see Section 4.9). An additional important method of determining meteoroid velocities is the Fresnel transform method, developed by Elford (2001). This method is capable of producing speeds with precision of $\sim$ 0.1 km^{-1}, compared with uncertainties of $\sim$ 3 kms^{-1} for a 30 kms^{-1} meteor with the time-lag method: equivalent to a 10% velocity uncertainty (Baggaley and Grant, 2004). However, it is limited to use for meteors with high signal-to-noise ratios. It is therefore expected that improvement of deceleration calculations provides the greatest chance of reaching the required accuracy.

Chapter 5

Modelling Resonance Dynamics

We now examine more fully the dynamics of the 7:2 Jovian resonance. Such a background is required for a number of purposes: to gain knowledge on the resonant width (as it is utilised in several occasions in Chapter 4); and to determine the likelihood of resonant trapping of CMOR-sized particles.

This chapter is largely concerned with introducing the dynamical problem and determining the resonant width, or size of the region of influence of the resonance. This is important here as such knowledge aids in the search for such a resonance in the dataset; in the confirmation that a particular feature meets resonant feature criterion; and in determining the upper limits on radar sensitivities and orbital resolution that would enable detection of the resonance.

5.1 Available Analytic and Semi-Analytic Methods

We discuss here two existing methods for determining the width or strength of a given resonance. First, the derivation for an approximate libration width expression is outlined as given in Murray and Dermott (1999): this comprises the purely theoretical standard libration width approximation, valid at low eccentricities. This approximation can be used to give an approximate resonant width. The theory also allows the introduction of various concepts important for understanding resonant dynamics, including the disturbing function and the resonant argument. Second, there exists a semi-analytic or numerical method available for determining resonance strength, developed by Tabare Gallardo (Gallardo, 2006b). Both methods have limitations that lead to the decision to turn to a numerical method for the purposes of this investigation (see Section 5.2).

5.1.1 Defining the Resonant Width

Before attempting to determine its value, it is useful to understand the concept of the resonant width. Broadly, it describes the influence of the resonance: the variations in orbital elements (here particularly semi-major axis) that the resonance can produce; or

the extent (again usually in semi-major axis) over which the resonance exerts a significant effect. We expect values from these two definitions to match and also expect these values to agree with the observed widths of physical resonance features, such as the Kirkwood Gaps in the Asteroid Belt. This also demonstrates the interest in the resonance width in semi-major axis over the width in other parameters, as it is most closely related to observable quantities of resonances in the Solar System. In this chapter it will be assumed that the resonance width refers to a semi-major axis width, unless otherwise stated.

Mathematically, the width can be defined (from the first definition above) as a maximum libration amplitude or libration width by considering the librational motion within resonance. Considering a particle at the exact resonance position, the width is then equal to the maximum change in energy or semi-major axis that can occur and still leave the particle in resonance (defined by the presence of libration - which is discussed further in Section 5.3). Note that this defines a half width, and care must be taken to determine whether a full width (from resonance edge to resonance edge) or half width (from resonance centre to resonance edge) is given by a particular method.

5.1.2 Resonance Theory and Derivation of an Analytic Approximation to the Resonant Width

Before expanding on the resonance width, it is valuable to mention herein aspects of resonance theory that are necessary for this chapter. This will be explained as far as is required to understand the origin of an analytic approximation to the resonant width in semi-major axis. This theory is limited to a low order approximation, assuming zero inclinations and eccentricity, and a negligible mass for the inner body. This renders this method not directly useful for this meteoroid problem as Taurid meteoroid stream particles have high eccentricity, with an average of $e = 0.83$. It is, however, useful as a comparison method, and can be used to verify the results from the numerical method used later. The theory outlined here is as given in Murray and Dermott (1999) Chapters six and eight. Additional analytical details (also from Murray and Dermott (1999)) that assist in the understanding of the following material are given in Appendix A .

Resonance derives from the argument of the disturbing function. The disturbing function results from considering a general three-body problem, where the motion of a third body is determined by the gravitational effects of the other two bodies. The disturbing function is given by:

$$\mathcal{R} = \frac{\mu'}{|\mathbf{r}' - \mathbf{r}|} - \mu' \frac{\mathbf{r} \cdot \mathbf{r}'}{r'^3}$$

where $\mu' = \mathcal{G}m'$, and $\mathbf{r}'$ and $\mathbf{r}$ are the position vectors of the two secondary bodies relative

to the central (primary) body (here the Sun). This is derived in Appendix A. The use of the three body problem here implies that the only bodies of interest are the Sun, Jupiter and one particle. This is a good approximation given the large mass of Jupiter: in Section 5.7 it is confirmed that exclusion of other planetary bodies does not produce significant errors.

It is now shown how this disturbing function leads to resonant terms, and how this theory can be simplified to give an approximation for the resonant width.

5.1.3 Series Expansion of the Disturbing Function

The disturbing function is required for many problems in Solar System dynamics. A non-integratable expression is encountered, however, which can only be solved by numerical methods. For many cases, some knowledge of variations in orbital elements is required, and it is more convenient to express the disturbing function as a series expansion in orbital elements. This is achieved using Legendre polynomials, and it can be shown that such an expansion has the form:

$$\mathcal{R} = \mu' \sum S(a, a', e, e', I, I') \cos\varphi$$

in which $\mu = \mathcal{G}m$, and φ has the general form:

$$\varphi = j_1\lambda' + j_2\lambda + j_3\varpi' + j_4\varpi + j_5\Omega' + j_6\Omega \tag{5-1}$$

where j_i are integers, λ is the mean longitude, ϖ is the longitude of perihelion and Ω is the longitude of the ascending node. Here λ' denotes the mean longitude of the perturbing body, and λ the mean longitude of the perturbed body. Also required is the d'Alembert relation:

$$\sum_{i=1}^{6} j_i = 0$$

That is, that the coefficients j_i sum to zero. This symmetry also requires an appropriate choice of angles referred to a fixed direction: the longitudes here fill this criterion.

It can be shown that the 'strength' term S that describes the variation with orbital elements can be approximated, for lowest order terms in eccentricities and inclinations, as:

$$S \approx \frac{f(\alpha)}{a'} e^{|j_4|} e'^{|j_3|} s^{|j_6|} s'^{|j_5|} \tag{5-2}$$

where $f(\alpha)$ is a function of Laplace coefficients, with $\alpha = a/a'$. Murray and Dermott (1999) provide an explanation of the origin of this approximation. This equation can provide an indication of the importance of each of the terms in equation 5-1, dependent

on the orbital elements of the bodies involved. For example, in a situation where the eccentricity of the perturbed body is high, while the eccentricity of the perturbing body and the inclinations of both bodies are all low, then it can be seen that only the $e^{|j_4|}$ term is important in the strength equation 5-2, and thus the $j_4\omega$ term will produce the most significant term in the argument φ (from equation 5-1).

The disturbing function is a sum of terms containing many arguments φ, only some of which are of interest here, specifically those that cause long term variations. Those of particular interest are secular and resonant terms. Secular terms arise when mean longitudes are not present in the argument. As mean longitudes are the only rapidly varying longitude used, their absence means the argument varies slowly with time. Resonant terms are different long period terms that arise when a commensurability exists between mean motions. Considering that the mean longitude λ can be related to the mean motion n of the orbit by: $\lambda \approx nt + \epsilon$, then $j_1\lambda' + j_2\lambda \approx (j_1n' + j_2n)t + constant$ (where the angle ϵ is the mean longitude at epoch defined by $\lambda = nt + \epsilon$). If $j_1n' + j_2n \approx 0$ (a commensurability) the argument will only change very slowly with time. Converting n to semi-major axis a using $n = \frac{2\pi}{T}$ and $T^2 = \frac{4\pi^2}{\mu}a^3$, this is equivalent to a resonant situation such that $a \approx (|j_2|/|j_1|)^{\frac{2}{3}}a'$. The resonant argument is the argument φ such that this semi-major axis condition holds.

5.1.4 Defining Resonant Motion

Exact resonance is defined as the behaviour seen when a resonant argument has a time variation equal to zero: $\dot{\varphi} = 0$. Using the general form of the argument given by equation 5-1, the time variation is given by:

$$\dot{\varphi} = j_1(n' + \dot{\epsilon'}) + j_2(n + \dot{\epsilon}) + j_3\dot{\varpi'} + j_4\dot{\varpi} + j_5\dot{\Omega'} + j_6\dot{\Omega}$$

If only mean motion contributions are considered (neglecting all angle contributions) this reduces to:

$$j_1n' + j_2n \approx 0.$$

It is now possible to define $j_1 = p + q$ and $j_2 = -p$, with p and q both positive integers, and q is the order of the resonance. Using relations between T, n and semi-major axis a it can be seen that:

$$a_n = (\frac{p}{p+q})^{2/3}a'$$

defines the resonant position of the inner body. For example, for the 3:1 resonance with Jupiter ($a' \approx 5.2$AU) in order to be at the resonance location, the inner body must have

a semi-major axis of: $a_n = (\frac{1}{3})^{2/3} \times 5.2 = 2.50$ AU.

This is only an approximate definition of the resonance position because of the exclusion of angle terms in the time derivative of the resonant argument. Inclusion of these precession terms leads to a range of different time derivatives of the resonant argument, and thus resonance positions in semi-major axis. Considering the 3:1 resonance, and ignoring mean longitude of epoch variations, there are six possible time derivatives of the resonant argument:

$$\dot{\varphi}_1 = 3n' - n - 2\dot{\varpi}$$

$$\dot{\varphi}_2 = 3n' - n - \dot{\varpi} - \dot{\varpi}'$$

$$\dot{\varphi}_3 = 3n' - n - 2\dot{\varpi}'$$

$$\dot{\varphi}_4 = 3n' - n - 2\dot{\Omega}$$

$$\dot{\varphi}_5 = 3n' - n - \dot{\Omega} - \dot{\Omega}'$$

$$\dot{\varphi}_6 = 3n' - n - 2\dot{\Omega}'$$

The presence of these terms produces resonant splitting of the resonance position over a range of semi-major axes. This will depend on the strengths of different terms, and also whether they are positive or negative.

5.1.5 An Analytic Resonant Width Expression

Determination of the resonant width of a given resonance requires both the disturbing function and Lagrange's planetary equations (see Appendix A or Roy (1988)). Lagrange's planetary equations describe the variations in orbital elements experienced by a body as a result of external perturbations, which in turn are described by the disturbing function. A simplification of the disturbing function is then required in order to allow an analytic derivation of an expression for the resonant width: this requires reduction to a circular ($e = 0$), planar (all inclinations zero) case. Negligible mass for the inner perturbed body is also assumed: this is known as the restricted case. These restrictions provide simplified equations of motion in orbital elements (see Appendix A Section A.2). Use of a pendulum model to provide an expression for the total energy of the system then provides an expression for the resonant width in semi-major axis, which is given by:

$$\delta a_{max} = \pm \left(\frac{16}{3} \frac{|\mathcal{C}_r|}{n} e^{|j_4|} \right)^{\frac{1}{2}} a. \tag{5-3}$$

This can be used to directly obtain a resonant width from knowledge of the resonance and the three bodies involved. Here $\mathcal{C}_r/n = (m'/m_c)\alpha f_d(\alpha)$, where m' is the mass of

the outer perturbing body (Jupiter), m_c is the mass of the central body (Sun), $f_d(\alpha)$ is a function of Laplace coefficients describing the direct terms of the expansion of the disturbing function, $\alpha = a/a'$, n is the mean motion and $\mathcal{C}_r$ describes a strength term (see equation 5-2), and is given by:

$$\mathcal{C}_r = \frac{\mathcal{G}m'}{na^2a'} f_d(\alpha) = (\frac{m'}{m_c}) n\alpha f_d(\alpha). \tag{5-4}$$

Here $\mathcal{G} = n^2a^3/m_c$ is used, from Kepler's third law.

For first order resonances it is more appropriate to use:

$$\frac{\delta a_{max}}{a} = \pm \left(\frac{16}{3}\frac{|\mathcal{C}_r}{n}e\right)^{\frac{1}{2}} \left(1 + \frac{1}{27j_2^2e^3}\frac{|\mathcal{C}_r|}{n}\right)^{\frac{1}{2}} - \frac{2}{9j_2e}\frac{|\mathcal{C}_r|}{n}. \tag{5-5}$$

These expressions are valid for orbits with low eccentricities ($e \lesssim 0.3$) and low inclinations, and are only easily computable for resonances for which the product $\alpha f_d(\alpha)$ is easily obtainable. These values are given for certain first and second order interior resonances in Chapter 8 of Murray and Dermott (1999). These include the 2:1, 3:2, 4:3, 3:1, 5:3 resonances, but do not include the 4:1 or 7:2 resonances, which are both used later.

5.1.6 The Resonance Strength program of Gallardo (2006)

An additional comparison method is given by the semi-analytic method of Gallardo (2006b). This evaluates the disturbing function $R(\sigma)$ numerically, and then calculates a resonance strength $SR(a, e, i, \omega) = \langle R \rangle - R_{min}$, where $\langle R \rangle$ is the mean value of $R(\sigma)$ with respect to σ (equivalent to the resonant argument φ), and R_{min} is the minimum value of $R(\sigma)$. These resonance strengths are notably different from the other methods in that they are in energy units with $k^2m = 1$, k being the Gaussian constant of gravity: the square root of the Newtonian gravitational constant in a particular set of astronomical units. In order to compare these values to semi-major axis resonant widths of other methods, it is necessary to convert SR in energy units to a semi major axis width. We derive this conversion using the expression for the expansion of the disturbing function for the circular, planar restricted problem as given by Murray and Dermott (1999):

$$\langle \mathcal{R} \rangle = \frac{\mathcal{G}m'}{a'}[f_{s,1}(\alpha)e^2 + f_d(\alpha)e^{|j_4|}\cos\varphi]$$

where

$$\varphi = j_1\lambda' + j_2\lambda + j_4\varpi.$$

We can simplify this using $\mathcal{C}_r$ as given in equation 5-4 and:

$$\mathcal{C}_s = \frac{\mathcal{G}m'}{na^2a'} f_{s,1}(\alpha) = (\frac{m'}{m_c}) n\alpha f_{s,1}(\alpha)$$

This simplification produces:

$$\langle \mathcal{R} \rangle = \mathcal{C}_s n a^2 e^2 + \mathcal{C}_r n a^2 e^{|j_4|} \cos\varphi$$

Gallardo's resonant strength is the amplitude of the disturbing function $R(\sigma)$. Murray and Dermott's expression is a simple cosine function with amplitude $\mathcal{C}_r n a^2 e^{|j_4|}$. Thus we find:

$$SR_{approx} = \mathcal{C}_r n a^2 e^{|j_4|}. \tag{5-6}$$

We can substitute this into the expression for δa_{max} (given in Section 5.1.5) to obtain an expression for the resonant width as a function of Gallardo's resonant strength:

$$\delta a_{max} = \pm \left(\frac{16}{3} \frac{SR_{approx} a^3}{GM_\odot} \right)^{\frac{1}{2}} \tag{5-7}$$

Here we have also used $n = \sqrt{\frac{\mu}{a^3}}$ where $\mu = GM_\odot$.

For first order resonances, we obtain instead

$$\frac{\delta a_{max}}{a} = \pm \left(\frac{16}{3} \frac{SR_{approx}}{n^2 a^3} \right)^{\frac{1}{2}} \left(1 + \frac{SR_{approx}}{27 e^4 n^2 a^2} \right)^{\frac{1}{2}} + \frac{2SR_{approx}}{e^2 n^2 a^2} \tag{5-8}$$

Because this method relies on low eccentricity approximations, it is expected that these conversion formulae will only be valid for eccentricities less than ~ 0.3.

A program (ATLAS) to implement this method is available on Gallardo's website (Gallardo, 2006a). The strengths determined using the Gallardo (2006) programs for the region 2-2.5 AU are shown in Figure 5.1.

5.2 A Numerical Width Determination Method

The resonance width can also be determined by simple examination of the dynamics of a body within the resonance over time. This can be accomplished using an integrator such as the Hierarchical N-Body (HNBody) integrator designed by K. Rauch and D. Hamilton (Rauch and Hamilton, 2002). Here HNBody is used to inject particles into Taurid-like orbits in the vicinity of the 7:2 resonance and study their continuing motions over 10^4 years. The maximum size of oscillations of a particle in resonance provides the width. An additional measure of the width is the size of the region inside which librational motion occurs.

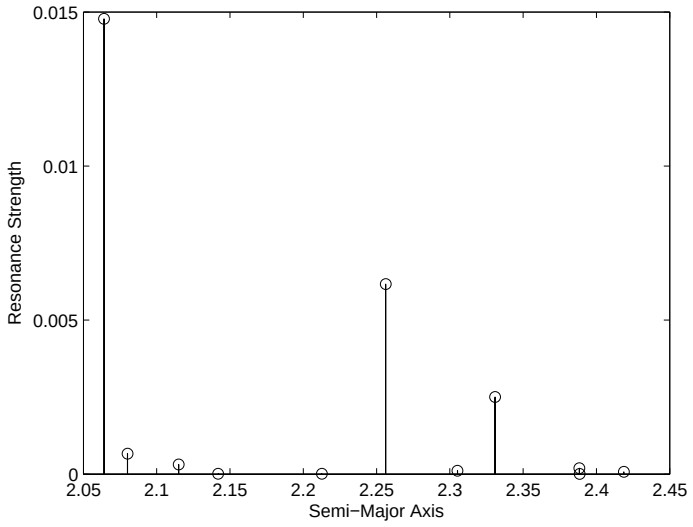

Figure 5.1: *Resonant strengths as calculated for Taurid orbital elements e, i and ω from the amplitude of the disturbing function using $SR(e, i, \omega) = \langle R(\sigma)\rangle - R_{min}$ using numerical techniques and programs developed by Gallardo (2006b)*

HNBody is appropriate for use in self-gravitating systems with one object dominating the mass of the system, such as is the case for the Solar System. It is primarily a symplectic integrator, but provides Runge-Kutta and Bulirsch-Stoer integrators that are useful in cases where the symplectic integrator cannot provide sufficient accuracy. It is capable of dealing with the cases of objects orbiting the Sun or planetary bodies, and of dynamical systems outside the Solar System, provided they represent a self-gravitating system. It also allows distinction of particles as heavy weight particles (HWPs), light weight particles (LWPs) and zero weight particles (ZWPs), and treats each class differently according to their interactions via gravity. All gravitational interactions with all bodies are included for HWPs, only interactions with HWPS are included for LWPs, and all gravitational interactions are ignored for ZWPs (thus assuming they are massless). The central body of the system (for the Solar System, the Sun) is always a HWP. Input and output orbit coordinates can be given as orbital elements or Cartesian coordinates. Together with the particle mass (usually in solar mass units), seven values are required to specify each particle. Coordinates are either 'bodycentric' (heliocentric in the case where the Sun is the central object) or Jacobi coordinates. In this chapter we use bodycentric coordinates; Jacobi coordinates are used in Chapter 6 as this requires a conversion from orbital elements to Cartesian coordinates. Other radiation forces can be included by use of the extension HNDrag: these are not considered at present. In Section 6.17 we will show that the effect of radiation pressure on the resonant width for CMOR-sized particles

is small.

Parameters in HNBody are set by changing individual values in the input file. If large numbers of input particles are required, it is possible to include an input text file containing the orbits of all particles. This can be generated automatically if necessary using a Perl script. HNBody is then run as an executable. Runtimes for the program are several seconds for the case with only one particle and Jupiter orbiting the Sun; less than an hour for the case of 200-300 particles in a similar model; and several hours for the case where all Solar System planets are included (which is only dealt with in section 5.7). Output files are text files containing the orbital elements of Cartesian coordinates of particles at the specified time intervals (set at 10 years here).

In our implementation of the meteoroid resonant problem, we consider the Sun, Jupiter, and a number of test meteoroid particles. The exclusion of other planets and asteroids will cause a small error: this is dealt with in Section 5.7. The Runge-Kutta integrator is most suitable for this problem due to the highly eccentric Taurid orbits. This requires a maximum timestep, which is set here at 1 year. However, the Runge-Kutta integrator uses a variable step size. This is defined by the stepsize that limits the error in the state vectors (x, y, z, V_x, V_y, V_z) to a specified accuracy. In this case we use an accuracy of 10^{-10} years. Over a 10^4 year integration this produces an error in the semi-major axis in the fifth decimal place compared to use of an accuracy of 10^{-11} years: this accuracy is sufficient for this problem. Jupiter is defined as a heavy weight particle, and meteoroids are set as light-weight particles, whose interactions with each other are ignored. This is acceptable for cases where the masses of the heavy weight bodies are significantly greater than those of the light weight particles: this is certainly true for the giant planet-meteoroid case here. The mass and orbital elements used here for Jupiter are taken from the Astronomical Almanac 2009 (US Naval Observatory and The Royal Greenwich Observatory, 2007): $M_J = 9.54 \times 10^{-4} M_\odot$; $a_J = 5.204$ AU; $e_J = 0.04890$; $i_J = 1.3038°$; $\Omega_J = 100.509°$; $\varpi_J = 14.5926°$. The meteoroids are given initial orbital elements of Taurid meteoroids, with the exception of the semi-major axis, which is varied slowly between each of the test meteoroids. A Perl script is used to generate a file containing the input orbital elements. The Taurid orbital elements used are $e = 0.83$, $i = 5.4°$, $\Omega = 152.7°$, $\Omega + \omega = 37.3°$ (Jenniskens, 2006). Particle masses are set small ($M_P < 10^{-34} M_\odot$) to approximate meteoroids. The mean longitudes of both Jupiter and the particles are currently given a value of zero: the implications of this choice are discussed in Section 5.5. The result is a set of meteoroids that scan through the resonance, having starting semi-major axis values first outside the resonance; then inside the resonance region; and outside the resonance again.

We begin by analysing a region constrained near the 7:2 resonance centre, intended

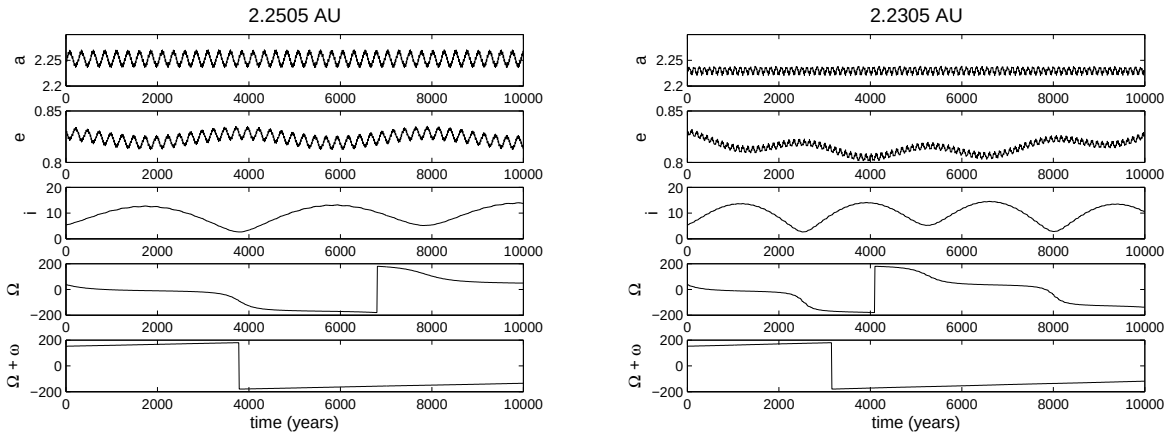

(a) (b)

Figure 5.2: *Behaviour of orbital elements over* 10^4 *year of numerical integration, for particles at Taurid elements* $e = 0.83$, $i = 5.4°$, $\Omega = 152.7°$, $\Omega + \omega = 37.3°$, *and at (a)* $a = 2.2505$ *AU and (b)* $a = 2.22305$ *AU. The axes for the semi-major axis results is the same for both figures in order to aid comparison. Medium-period resonant oscillations (of period* ~ 260 *years) and long-term variations are clearly visible in the former, and only longer-term variations are seen in the latter (which is outside of the resonance).*

to show only the behaviour close to the resonance. The results obtained for one meteoroid particle in interaction with the Sun and Jupiter are presented first. It is given a semi-major axis which starts it within the resonance (2.2505AU) and its motion is integrated for 10^4 years in 1 year time steps. HNBody produces output files of time and orbital elements (a (AU), e, i (°), Ω, $\Omega + \omega$ and mean longitude λ) at specific set time intervals (10 years). Figure 5.2(a) shows the orbital element variations of such a particle over 10^4 years. This particle can be identified as resonant by the relatively long period and large amplitude oscillations in semi-major axis (of period ~ 260 years). These oscillations are also present in the eccentricity, superimposed on much longer scale oscillations caused by planetary (Jovian) perturbations (with period ~ 3000 years). In addition, smaller scale variations exist, also the result of Jovian perturbations, which will be discussed in Section 5.4.

A small movement in the starting semi-major axis of the meteoroids (to 2.2305 AU) moves the particle outside the resonance. Figure 5.2(b) shows the orbital element variations for this particle: the absence of the large resonant oscillations in the semi-major axis and eccentricity confirms that this particle is not resonant. While the characteristics of semi-major axis oscillations are a good indicator of resonant behaviour, a more rigorous test using the resonant argument is often required (see Section 5.3).

To examine the effects of all the oscillations at once, we test a range of particles that scan through the resonance. These provide an indication of the size of the oscillations in

semi-major axis over the whole resonance region. This is achieved by stepping through the 7:2 resonance region in steps of 0.0005 AU, with starting semi-major axes from 2.22 to 2.28 AU. For each particle, an approximate maximum size for the oscillations in semi-major axis is computed by taking the difference of the maximum and minimum values over the 10^4 year integration. The result is equal to twice the amplitude of the oscillations. This method is limited in accuracy for several reasons, including the presence of long-term variations, but it is sufficiently accurate for our purposes. These approximate 'resonant widths' (as defined in Section 5.1.1) can be plotted as a function of semi-major axis position to create a picture of the resonance effects in that region (Figure 5.3). Figure 5.4 shows the changing size of the semi-major axis oscillations at a number of points indicated on Figure 5.3 that scan through the resonance.

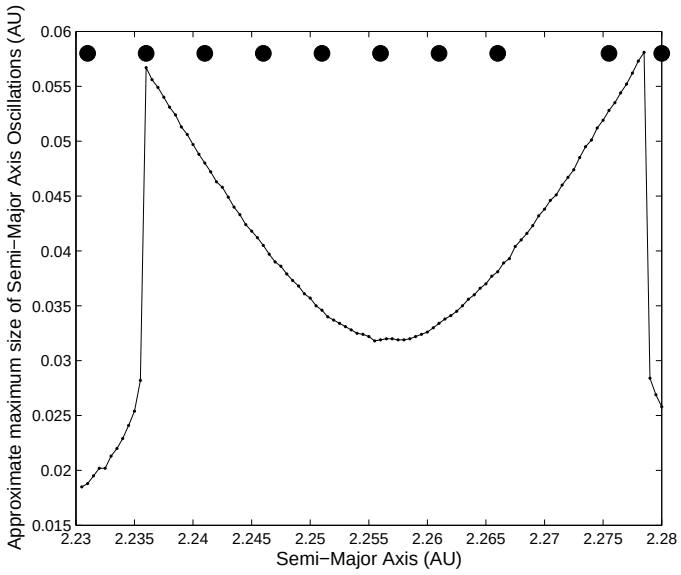

Figure 5.3: *The variation in approximate size of resonant oscillations for particles at starting locations of* 2.22 *to* 2.92 *AU. The black points marked above this resonant feature indicate the starting locations for the particles shown in Figure 5.4.*

5.2.1 Analysing the Resonance Feature

The structure seen in Figure 5.3 defines the 'resonant feature' form that is the subject of the remainder of this chapter. Such resonant features can contain valuable information on the dynamics of the resonance. The general structure can be described by three main parameters (indicated in Figure 5.5): the width, height and dip height. We will refer to the width as the 'resonance feature width' to avoid confusion with the 'resonance width', although as we will see they should be equivalent.

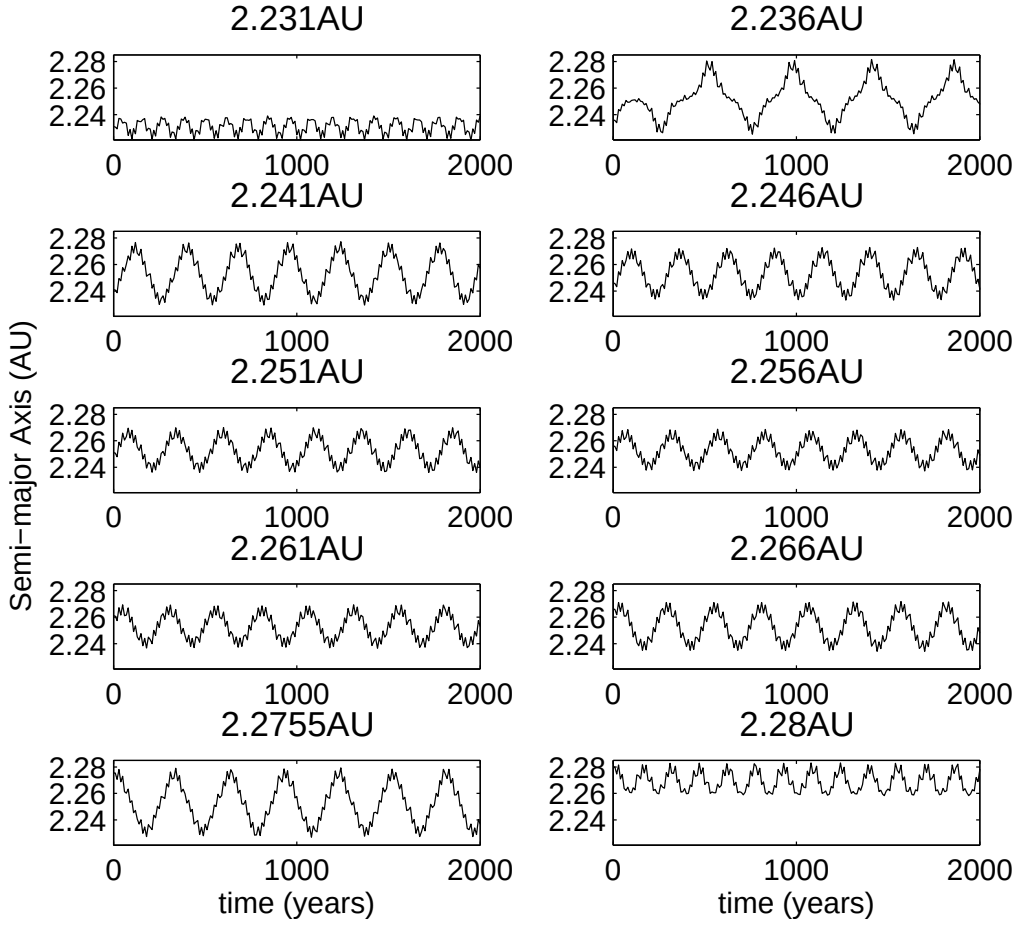

Figure 5.4: *The variation in semi-major axis with time, for particles inside and outside of the resonance (over a reduced period of* 2×10^3 *years). The numbers above each plot indicate the starting semi-major axis locations of each particle.*

The height of the feature, equal to the height of the peaks at approximately 2.236 AU and 2.2785 AU, gives the maximum size of the oscillations a particle is able to undergo within the resonance. This is similar to the classical definition for resonant width or libration width: the maximum librational motion possible without the particle being lost from the resonance. In Figure 5.3 these heights are 0.0569 and 0.0578 AU respectively. The width of the feature (between 2.237 AU and 2.2795 AU, giving a width of ~ 0.0425 AU) provides a more physical definition of resonant width: it is the width of the resonant region in which amplified oscillations are present. The minimum inside the dip occurs approximately (and, theoretically, exactly) at the position of the resonance centre in semi-major axis. The dip height (equal to 0.0321 AU, and located at a semi-major axis of 2.2575 AU), therefore, physically represents the size of the oscillations at this resonant

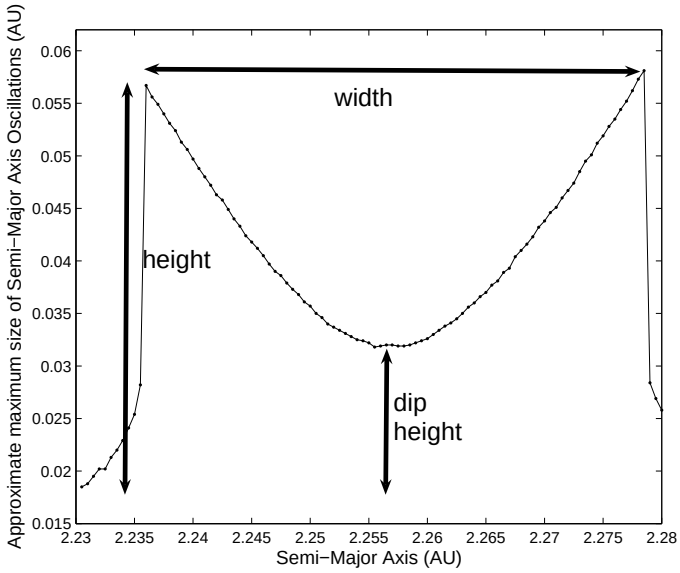

Figure 5.5: *The variation in approximate size of resonant oscillations for particles at starting locations of* 2.22-2.92 *AU, showing the resonance feature parameters width, height and dip height that will be used extensively for the remainder of the chapter.*

centre. This is theoretically zero at the mean longitude of the resonant centre, and in the case where no other underlying perturbations exist. Its large finite value in Figure 5.3 provides us with extra information, in particular that we are not at the resonant centre, and must adjust the mean longitude to find this.

There are, therefore, other factors that must be considered in order to obtain the resonant width from this resonant feature. We will now consider the variations in the resonant feature width and depth with mean longitude; the effect of small scale Jovian perturbations; and the use of the resonant argument to determine what particles on the resonant feature undergo resonant librations.

5.3 Librations within the Resonant Feature

Given that the location of the 7:2 resonant feature of Figure 5.3 matches well with the expected location of $\sim$ 2.256 AU, and given that inside these features high amplitude oscillations are observed that are not present immediately outside these features, it is reasonable to conclude that they do indeed represent the dynamical presence of the resonance, and therefore its width. However, to prove this is the case it must be shown that particles inside these features undergo librational motion. This can be determined using the resonant argument. From Section 5.1.1, libration exists when the resonant argument oscillates through only a limited range of angles. Circulation is expected to be

found just outside the sharply defined edges of the resonance features, and is observable as slow 'circulation' of the resonant angle, continuously passing through the full 360°. In consequence, in this section we test that librational motion is occurring in the 2:1, 3:1, 4:1 and 7:2 resonances, after which we are satisfied that the dynamics within all such strong resonant features fulfil the libration requirement.

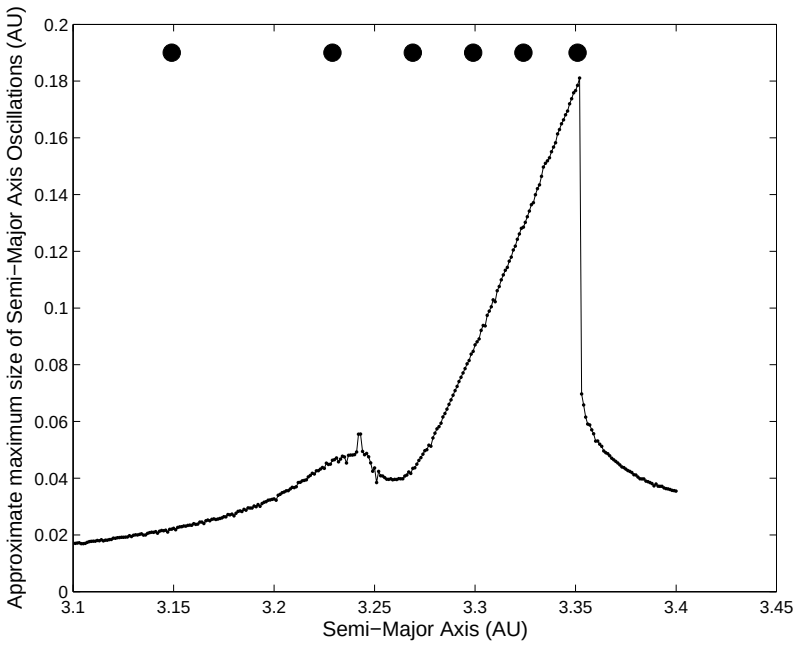

Figure 5.6: *The 2:1 resonant feature (approximate widths distribution). Points mark the location of particles studied in Figure 5.7 below.*

5.3.1 The 2:1 Jovian Resonance

We begin with the 2:1 Jovian resonance at an eccentricity of 0.1. As the strongest resonance under examination here, it demonstrates the clearest transition from non-resonant motion, to circulation, and finally to libration, before returning to circulation on the opposite side of the resonance. The main resonant argument here is:

$$\varphi = 2\lambda_J - \lambda_P - \varpi_P$$

where λ_J is the mean longitude of Jupiter, λ_P is the mean longitude of the particle and ϖ_P is the longitude of perihelion of the particle.

Six particles are selected to study the resonant argument and probe different behaviour in and near the 2:1 resonance: a first particle well outside the resonance (which should show non-resonant behaviour, including fast, non-oscillatory variations in resonant

argument), a second particle just outside the resonance to demonstrate circulation, and four particles inside the resonance showing increasing libration amplitudes. The 2:1 resonant feature and the location of these particles is shown in Figure 5.6.

The semi-major axis variations and resonant argument variations for these particles are shown in Figure 5.7. The first particle chosen shows no resonant signatures in the semi-major axis or resonant argument, with no coherent oscillations visible in either. The second particle has semi-major axis oscillations. However, it can be seen that the resonant argument undergoes long period circulation, not libration. This highlights the necessity of checking the dynamics in the resonance, as semi-major axis variations alone may not indicate of whether circulation or libration is present. The third particle is in libration: it demonstrates the restriction of resonant argument to a small range of values. Semi-major axis oscillations are not large, which is expected as they should tend to zero as the resonant centre is approached. Indeed, they are not significantly different to the semi-major axis oscillations for the previous circulating particle. Particles four to six are all also in libration. The size of their librations increases steadily, such that the librations in particle six cover nearly a full 360°. This is still defined as libration as the particle never quite completes a full circle in the resonant argument.

This is more clearly demonstrated by applying a mixed canonical transformation (as used by Murray and Dermott (1999) Sections 8.8 and 8.9)(see Figure 5.8). This consists of a radial distance determined from the eccentricity, and a polar transformation of the resonant argument. The transformation is given by $x = \sqrt{2\Phi}\cos\phi$ and $y = \sqrt{2\Phi}\sin\phi$, where the radial distance is given by:

$$R = \sqrt{2\Phi} = \left[\frac{-3}{f_d}(j-1)^{\frac{4}{3}} j^{\frac{2}{3}} \frac{m_c}{m'}\right]^{\frac{1}{3}} e$$

with parameters defined in Section 5.1.5.

Figure 5.8(a) shows each of the particles in turn. The increasing size of the libration in particles three to six is clearly shown, with near 360° libration for particle six. The out-of-resonance and circulating particles cover all resonant argument values and so form full circles. The influence of the resonance on particles that are not exactly in resonance causes the circle for circulation to not be centred on the origin. This is a result of the resonance imposing a forced eccentricity. In the Figure 5.8 (b) the innermost curve is the circulation case (particle two), while the second curve is the out-of-resonance particle (particle one). The four librational particles form concentric curves.

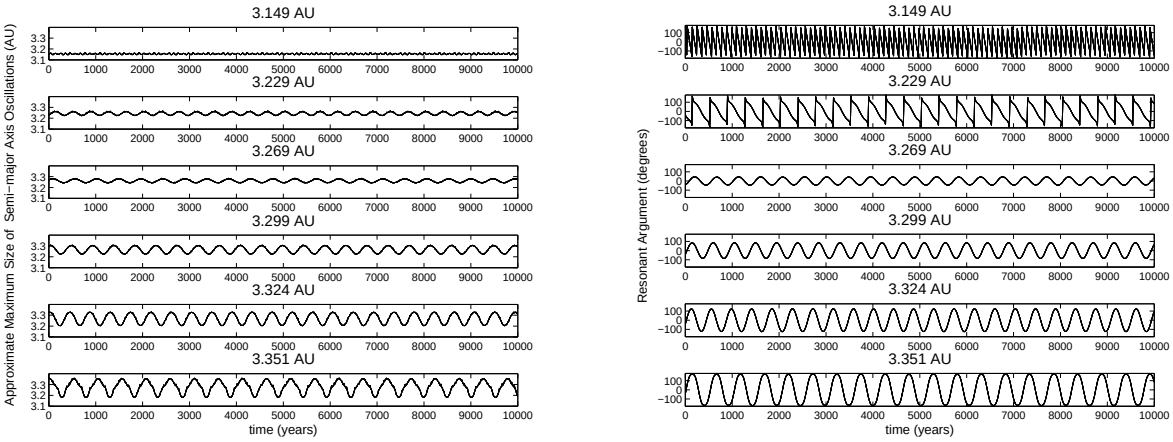

(a) (b)

Figure 5.7: *Using the six points cutting through the 2:1 resonance defined in Figure 5.6, we have (a) the semi-major axis variation over the* 10^4 *year integration period, and (b) the corresponding variations in resonant argument.*

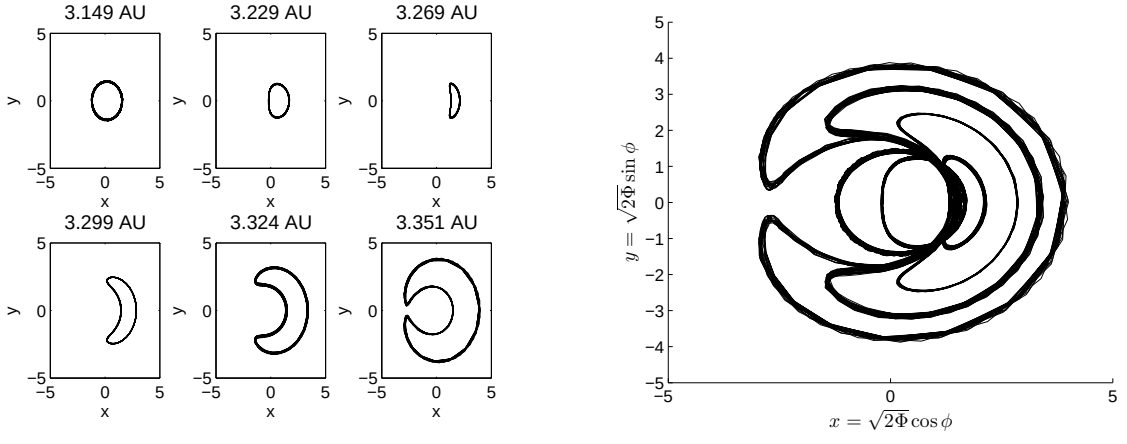

(a) (b)

Figure 5.8: *Demonstration of libration within the 2:1 Jovian resonance feature, and lack of libration outside of this. The semi-major axes values above each graph refer to the starting values for each particle. The locations of each particle relative to the resonant feature are seen in (a).*

5.3.2 The 3:1, 4:1 and 7:2 Jovian Mean Motion Resonances

We now present evidence for librational motion within the observed resonant features of the 3:1, 4:1 and 7:2 resonance. Low eccentricities are used for the 3:1 and 4:1 resonances ($e = 0.1$). The Taurid average eccentricity of 0.83 is used for the 7:2 resonance as this is more relevant to the current application. The strongest resonance arguments are:

$$\varphi = 3\lambda_J - \lambda_P - 2\varpi_P$$

for the 3:1 resonance;

$$\varphi = 4\lambda_J - \lambda_P - 3\varpi_P$$

for the 4:1 resonance; and

$$\varphi = 7\lambda_J - 2\lambda_P - 5\varpi_P$$

for the 7:2 resonance.

For the 3:1 resonance, we take one particle in circulation either side of the resonant feature, and three within the libration. Figure 5.9 (a) shows the particles studied: Figure 5.9 (b) and (c) show the particle librations (or circulation for particles 1 and 6) in standard and polar form.

We show similar graphical representation of libration within the 4:1 and 7:2 Jovian resonances in Figures 5.10 and 5.11. We are satisfied that resonant librations for the strongest resonant argument exist within the clear resonant structures observed.

5.3.3 Libration Detail in the 3:1 Resonance

The examples above illustrate librations in the main resonant argument. Here we evaluate the role of other resonant arguments (to second order), using the 3:1 resonance as an example. The mean longitude for each particle is optimised (as is described in Section 5.5 below) for the $\varphi = 3\lambda_J - \lambda_P - 2\varpi_P$ argument, so as to produce the widest resonant feature possible. The eccentricity and inclination of Jupiter are set to zero.

There are six possible resonant arguments for the 3:1 resonance (to second order). These are discussed in Section 5.1.4; we rewrite them here in terms of λ_P and λ_J as:

$$\varphi_1 = 3\lambda_J - \lambda_P - 2\varpi_P$$

$$\varphi_2 = 3\lambda_J - \lambda_P - \varpi_P - \varpi_J$$

$$\varphi_3 = 3\lambda_J - \lambda_P - 2\varpi_J$$

$$\varphi_4 = 3\lambda_J - \lambda_P - 2\Omega_P$$

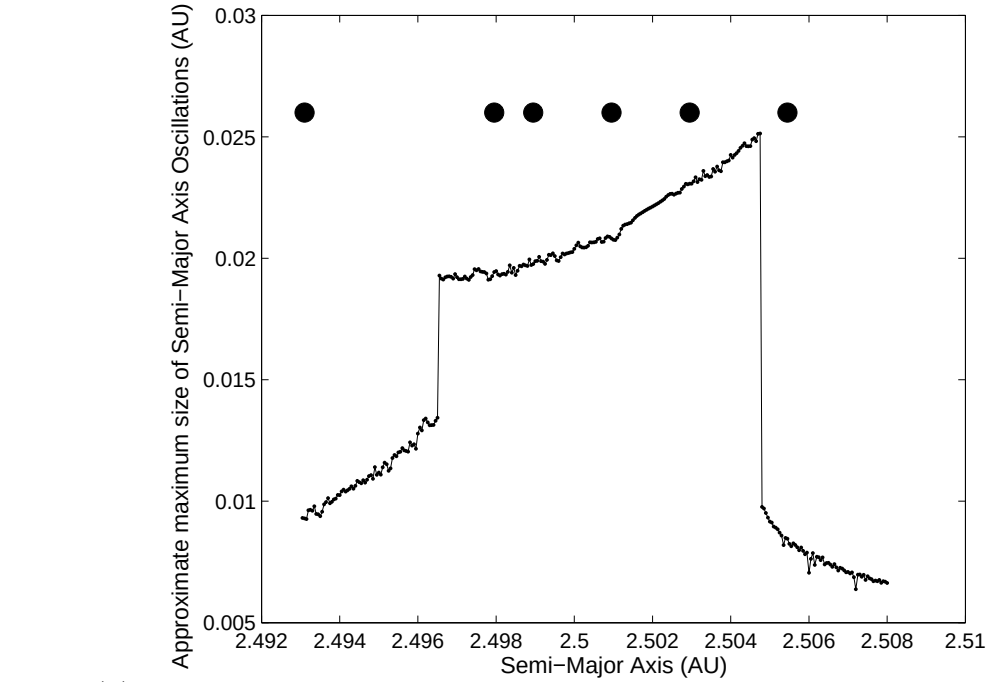

(a)

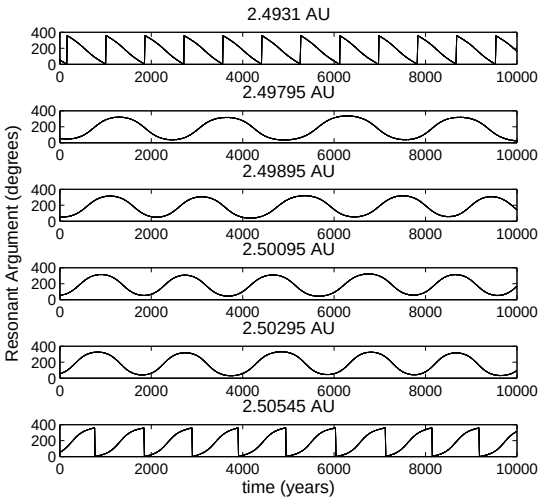

(b)

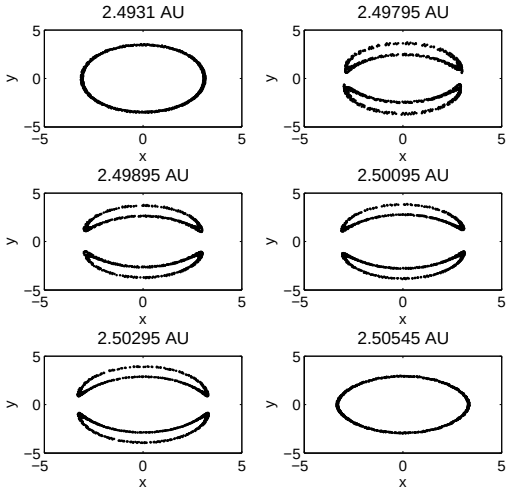

(c)

Figure 5.9: *(a):The 3:1 resonant feature (approximate widths distribution). The points mark the location of particles studied in (b) and (c). (b) and (c): Demonstration of libration within the 3:1 Jovian resonance feature. The semi-major axes values above each graph refer to the starting values for each particle. The locations of each particle relative to the resonant feature are seen in (a).*

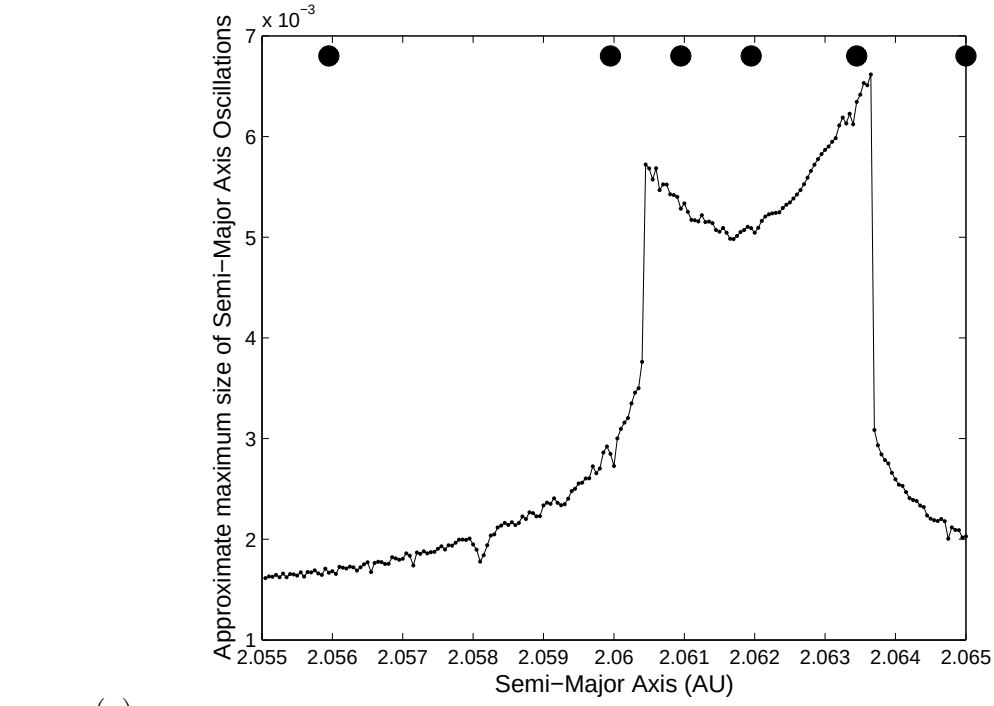

(a)

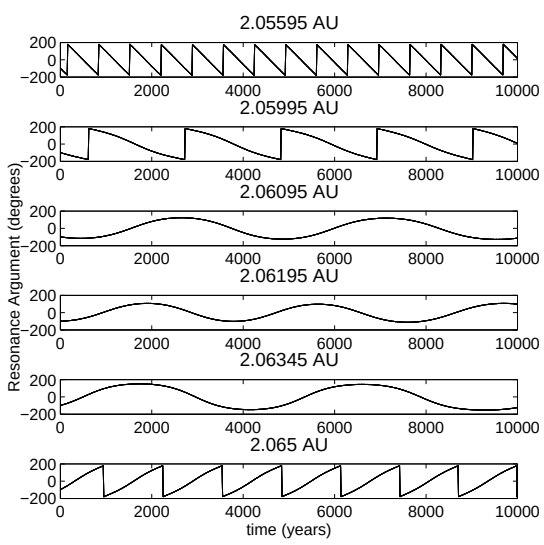

(b)

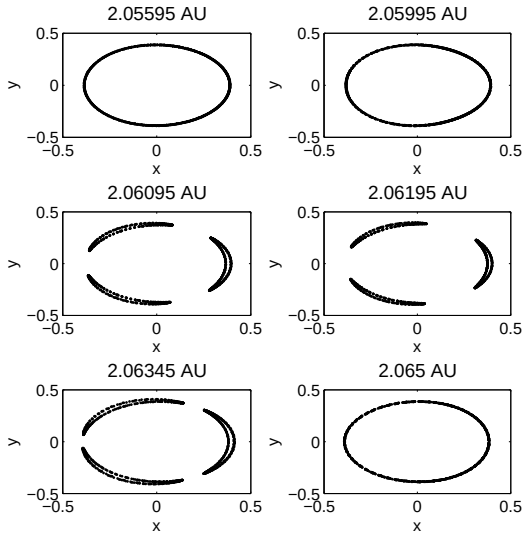

(c)

Figure 5.10: *(a): The 4:1 resonant feature (approximate widths distribution). The points mark the location of particles studied in (b) and (c). (b) and (c): Demonstration of libration within the 4:1 Jovian resonance feature. The semi-major axes values above each graph refer to the starting values for each particle. The locations of each particle relative to the resonant feature are seen in (a).*

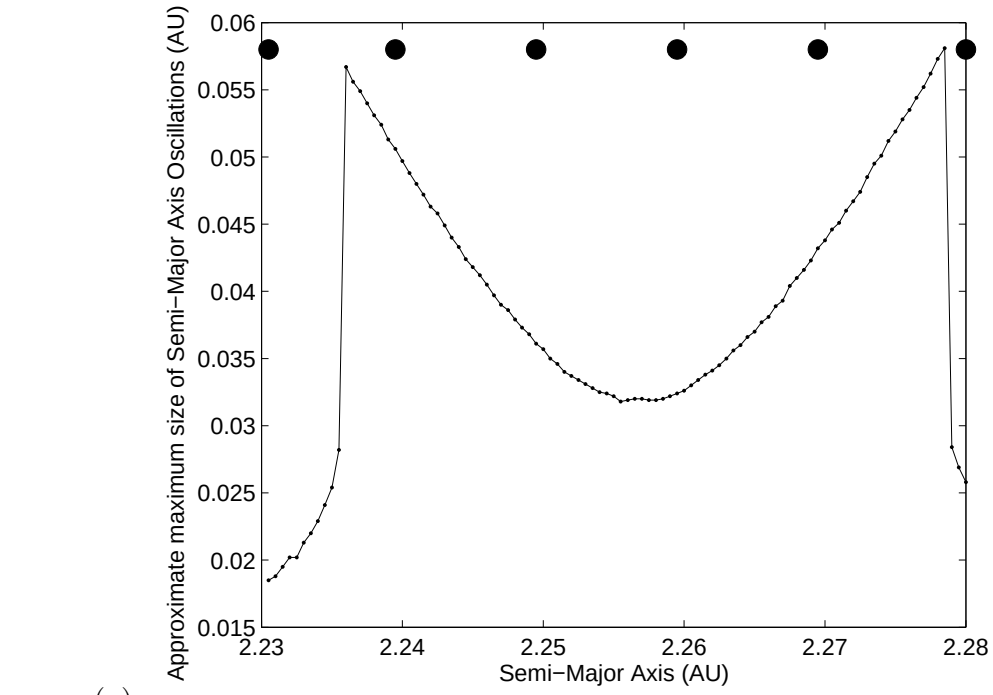

(a)

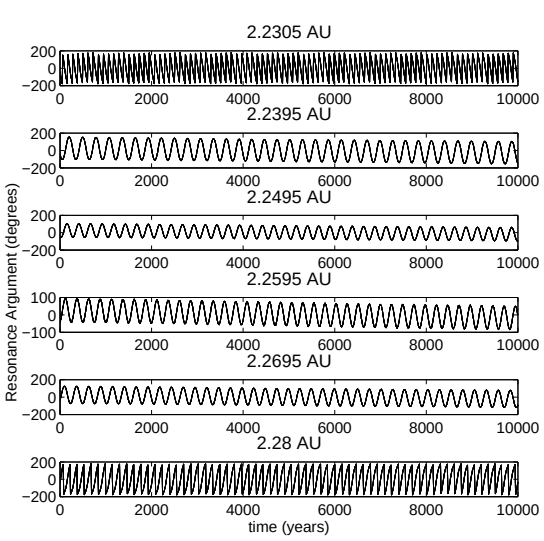

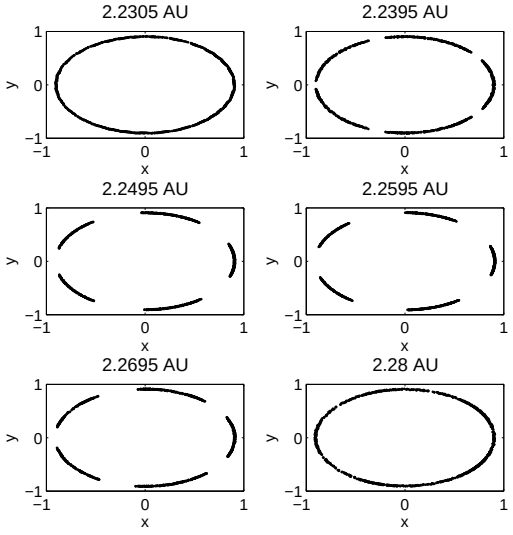

(b) (c)

Figure 5.11: *(a): The 7:2 resonant feature (approximate widths distribution). The points mark the location of particles studied in (b) and (c). (b) and (c): Demonstration of libration within the 7:2 Jovian resonance feature. The semi-major axes values above each graph refer to the starting values for each particle. The locations of each particle relative to the resonant feature are seen in (a).*

$$\varphi_5 = 3\lambda_J - \lambda_P - \Omega_P - \Omega_J$$

$$\varphi_6 = 3\lambda_J - \lambda_P - 2\Omega_J$$

Each argument has two similar terms ($3\lambda_J$ and $-\lambda_P$). The third term is composed of an allowed combination of longitudes of perihelion or of the ascending node of Jupiter and the test particle. This must meet symmetry requirements such that the sum of all coefficients of longitudes is zero and the sum of all ascending node terms is even.

A simple method is used to determine where on the resonant feature librations exist, by finding where the resonant argument has a range of less than 360°: that is, a finite libration amplitude exists. Figure 5.12 demonstrates this for the resonant argument φ_1, for two eccentricity values. The range, or double the libration amplitude, of this argument is equal to $\sim 360°$ everywhere except inside the resonance. For high eccentricities (here $e = 0.83$ is shown), the resonant feature in semi-major axis is symmetrical around the resonant centre, as are the variations in the resonant argument. The agreement between the region in which the resonant argument undergoes libration and the region encompassing the resonant feature is good. However, the resonant feature becomes increasingly asymmetric at lower eccentricities (here $e = 0.1$ is shown). This is speculated to be a result of the equilibrium points in mean longitude not being where expected due to the strength of the indirect term in the disturbing function (indirect terms are strong relative to direct terms for n:1 resonances). At $e = 0.1$ there is still a good general agreement between the region inside which librations occur and the resonant feature. There is some disagreement at the sunward edge of the resonance. The reason for this disagreement is not clear, but may be the result of resonant interactions other than the simple mean-motion resonances considered here. This behaviour is also seen for the ϖ_4 resonant argument, libration regions for which are demonstrated in Figure 5.13.

By this process we establish that libration is possible, at low and high eccentricities, in resonant arguments φ_1, φ_4, φ_5 and φ_6, but not in φ_2 or φ_3. We do not expect these latter two arguments to be important as the eccentricity of Jupiter is zero (see equation 5-2). At high eccentricities, the region of libration for φ_1 matches the extent of the resonant feature, supporting our decision to assume that this is the main resonant argument (which was also supported by examination of equation 5-2). It is also important to check that this is the main resonant argument as the derivation of an analytic description (in a circular, planar restricted case) for the maximum resonant width in semi-major axis also assumes that the main resonance is given by φ_1.

The libration test used here additionally addresses a further issue concerning the resonant feature. It is possible that the particles that appear at the edge of the resonance do not start in libration, but instead in circulation, and that a minor perturbation allows

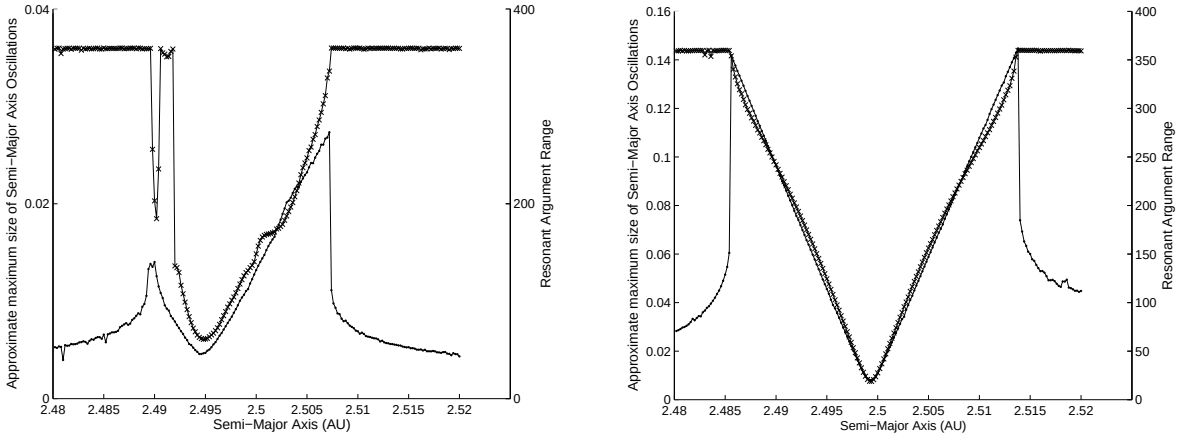

(a) (b)

Figure 5.12: *Demonstration of libration in resonant argument φ_1 within the 3:1 Jovian resonance feature, at eccentricities $e = 0.1$ and $e = 0.83$. Here dots represent the approximate double amplitude of semi-major axis variations (left-hand axis), and crosses represent the range in resonant argument values (right-hand axis). Inside the resonance, the 'resonant argument range' used here is equal to double the libration amplitude.*

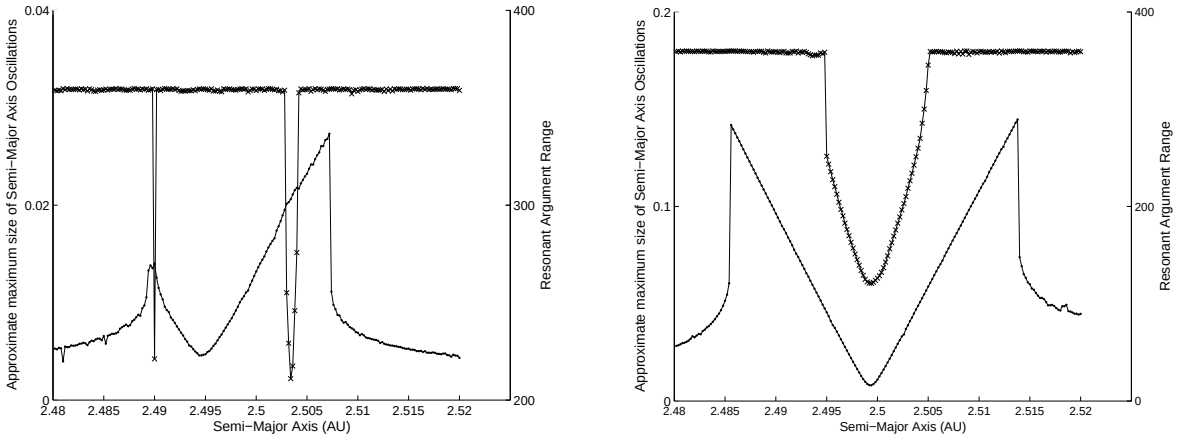

(a) (b)

Figure 5.13: *Demonstration of libration in resonant argument φ_4 within the 3:1 Jovian resonance feature, at eccentricities $e = 0.1$ and $e = 0.83$. Here dots represent the approximate double amplitude of semi-major axis variations (left-hand axis), and crosses represent the range in resonant argument values (right-hand axis). Inside the resonance, the 'resonant argument range' used here is equal to double the libration amplitude.*

them to enter the resonance after a period of time. Thus, over the 10^4 year period their orbits have maximum and minimum values (and thus maximum oscillation size) equivalent to a resonant particle, even if their starting semi-major axis was not within the libration region.

This behaviour is displayed in Figure 5.14, where the librations for six particles near and at the second peak of the resonant feature at a mean longitude of zero are shown. The first four particles exhibit librations immediately. The fifth particle, which is at the peak of the resonant feature, shows circulation initially, with librations starting at around 2300 years. We consider that this demonstrates that a particle started at this semi-major axis (2.2795 AU) is not in libration, and as such is outside the resonance. The resonance edge therefore ends at 2.279 AU (the second point within the resonant feature). Even though particles three and four appear to exhibit resonant arguments which do not strictly vary between $\pm 180°$, we still consider these particles to be in libration, as the resonant argument is noticeably bounded compared with particles five and six. This may be due to the long-scale oscillations that the resonant argument undergoes underneath the resonant variations.

The libration test above will detect particles that are in libration and not in circulation, providing a potentially more accurate test than the use of just the semi-major axis resonance feature alone. However, we note that this method will only detect strict librational motion, and as such would indicate that particles three and four are non-librational. Such a strict definition may not be necessary for our purposes, though this method does crucially allow an automatic determination of the width. The error in this case is a maximum of 0.015 AU between the width from semi-major axis variations; the width from libration strictly less than $\pm 180°$ (for the 7:2 resonance); and the width from libration defined as clearly bounded resonant argument variations. This uncertainty is doubled as this error occurs on both resonance feature edges. This magnitude of error is typical for resonance features: we will, however, individually deal with these errors for 50 different starting mean longitude values in Section 5.5. Similar errors occur for the peak heights: the height of the left hand peak decreases from 0.0569 AU to 0.0560 AU if the outer edge of the resonance is more strictly defined.

5.4 Non-Resonant Variations

Resonant oscillations are only one of the variations present in the semi-major axis distribution, such as seen in Figure 5.2 (a). Jovian perturbations cause small-scale (small amplitude and period) repetitive variations that are seen superimposed on top of the resonant oscillations for a particle in resonance. These are more clearly visible when a small

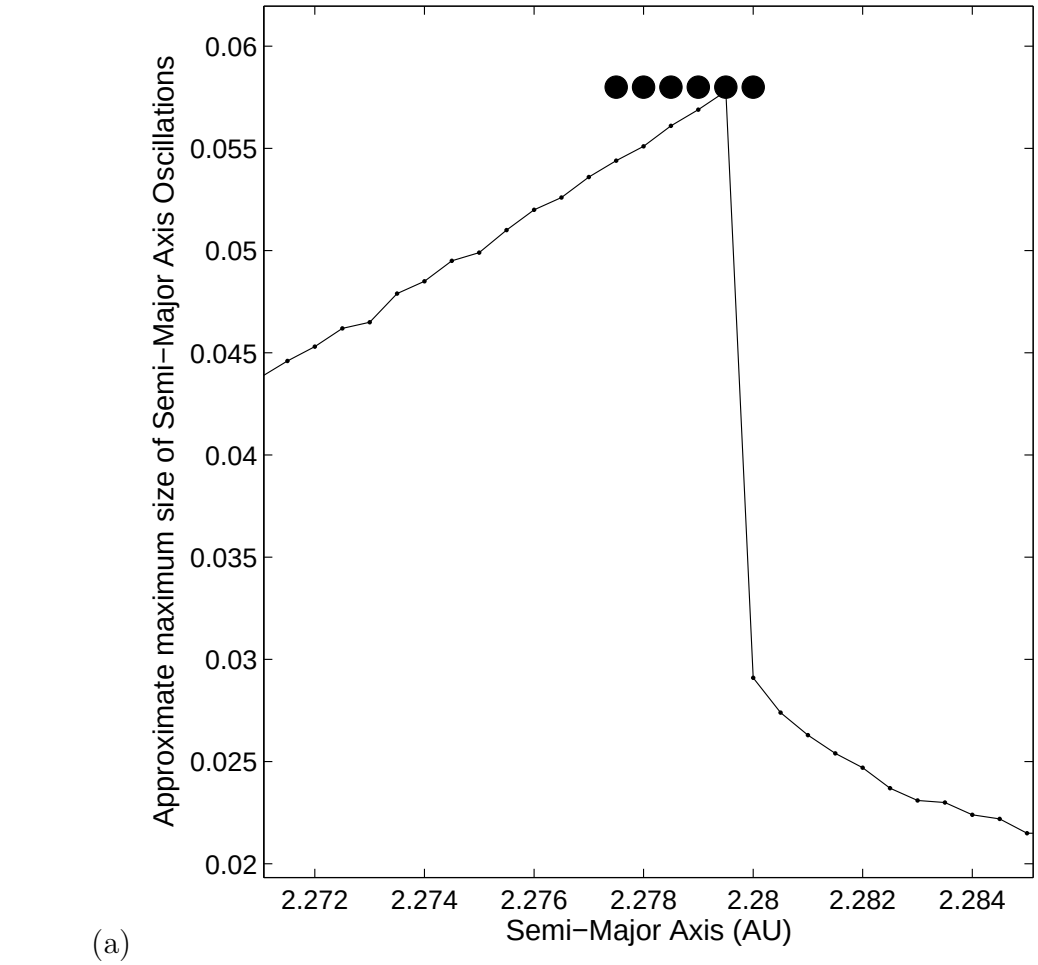

(a)

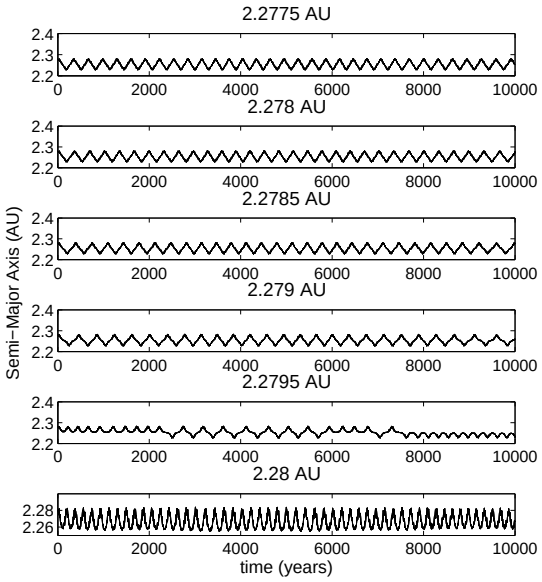

(b)

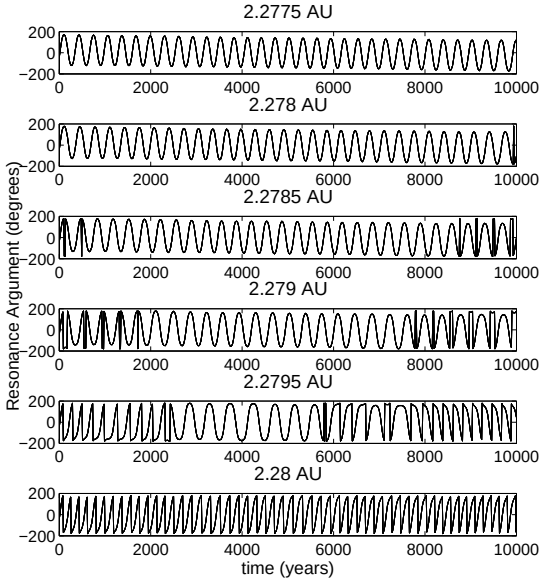

(c)

Figure 5.14: *Demonstration of the absence of librations at the peak of the resonance feature (at 2.2795 AU). (a) shows the section of the resonant feature of interest, with points marking the locations of particles with the semi-major axis and resonant argument variations shown in (b) and (c) respectively. The far left point in (a) has semi-major axis variations and librations given by the first particles in (b) and (c).*

section of the semi-major axis variations is examined, as seen in Figure 5.15. This shows the small-scale variations of particles inside and outside the resonance. The particle inside the resonance demonstrates large resonant oscillations with a period of approximately 250 years and small scale irregularly shaped Jovian perturbation oscillations with a period of 24 ± 1 years. Outside of the resonance, the small scale oscillations with this period are still visible. The same dynamical configuration between Jupiter and the particle occurs every 23.7 years, as this is the time between conjunctions that are as close to Jupiter as possible. This number is derived using the resonance ratio 7:2, from which it can be seen that the closest approaches between the two objects occur on a frequency equal to twice Jupiter's period, or seven times the particle's period. This time (23.7 years) is in agreement with the 24 ± 1 year period of the small scale variations in both the resonant and the non-resonant particles. It can be inferred from this that the small scale oscillations are the result of gravitational forcing. Their size will therefore increase as the distance between Jupiter and the particle decreases. Their frequency will also change as the ratio of periods between Jupiter and particle varies: only at or near the 7:2 resonance centre will a period of ~ 24 years be observed.

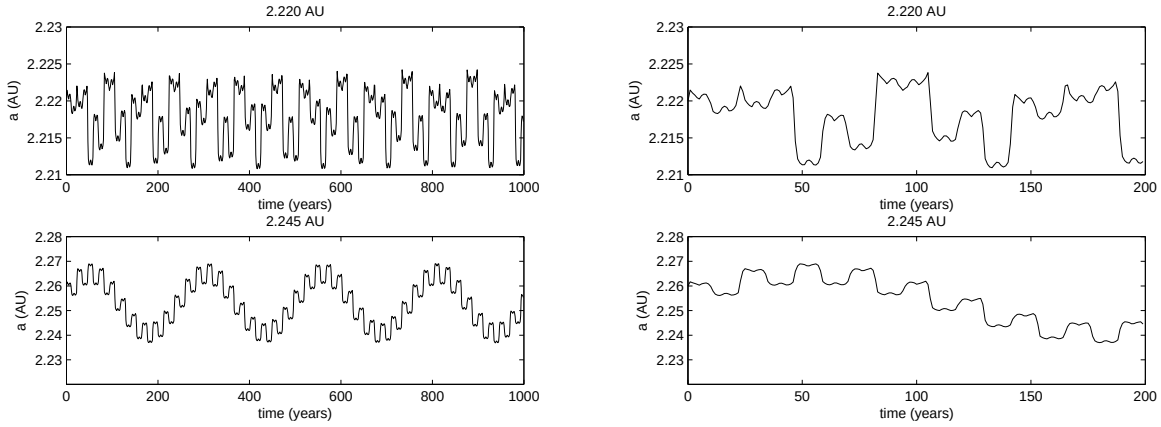

(a) (b)

Figure 5.15: *Small-scale variations in motion for a particle outside the resonance zone at* 2.220 *AU (so is not displaying significant resonant oscillations) and a particle inside the resonance at* 2.245 *AU (close to the resonant centre. Here (a) displays the variations over a* 1000 *years cycle; (b) shows the detail of the small scale variations, with only* 200 *years integration shown.*

In consequence, the removal of these small scale variations is required in order to obtain an accurate estimation of the size of the resonant oscillations. We accomplish this by estimating manually the size of the small-scale variations and subtracting this from the total size of the oscillations, which includes resonant and small-scale amplitudes. The variations in the size of the small-scale variations found at different points on the resonant

feature are less than 0.001 AU: mostly these errors are in the range 0.0002-0.0006 AU. We are left with a more accurate representation of the size of resonant oscillations alone.

For the example of the resonant feature in Figure 5.3, generated with the particle mean longitude set to zero, the small scale variations are 0.007 ± 0.0005 AU at the left hand peak, and 0.0078 ± 0.0002 AU at the right hand peak. This gives us final left and right peak heights (originally 0.0569 and 0.0578, decreased to 0.056 AU and 0.0569 AU after libration checks) of 0.0490 AU and 0.0491 AU respectively.

5.5 Mean Longitude Variations

Here we seek to understand the effect of the initial mean longitude of the particle on the resonant feature. The aim is to determine the optimum mean longitude of the resonant centre, which is expected to be the most appropriate mean longitude at which to determine the resonant width.

In the above numerical integrations of the orbits of particles and Jupiter, it was assumed that the initial mean longitude of all bodies was equal to zero: that is, the starting positions of both Jupiter and particle were in the direction of the vernal equinox as viewed from the Sun. As the particle and Jupiter orbit the Sun, the difference between their mean longitudes will increase from zero and eventually reach a 360° difference. This is a fairly random process for particles not in the vicinity of the resonance. However, within the resonance a particular combination of mean longitudes, given by the resonant argument, remains roughly constant, or oscillates through a small range of values around the resonant centre (often $\lambda = 0$ or 180°). This defines resonant libration. Circulation of the orbit is defined by a slow change of the resonant argument that does complete 360° 'circulation'. Thus, the relative mean longitudes of the particle and Jupiter are important for determining whether a particle's motion is resonant.

First we consider what variations in particle behaviour with mean longitude are expected, and how such variations may affect our determination of the resonant width. This is not easy to appreciate using orbital elements or heliocentric coordinates: instead, a mixed canonical transformation is used, as given in Section 5.3.1. We consider the 2:1 resonance for simplicity: in this case we have $\sqrt{2\Phi} = 15.874e$ and $\phi = 2\lambda_J - \lambda - \varpi$.

Figure 5.16 shows several curves demonstrating the librational motion of five particles at different locations inside the resonance. The outermost curve shows nearly maximal libration. Since the angle $\phi = 2\lambda_J - \lambda - \varpi$ is a scaled difference of mean longitudes (plus an additive constant), changing the starting mean longitude of the particle, while holding Jupiter's starting mean longitude constant at 0, is equivalent to taking slices at different angles through this librational motion. Each slice will produce a resonant feature. The

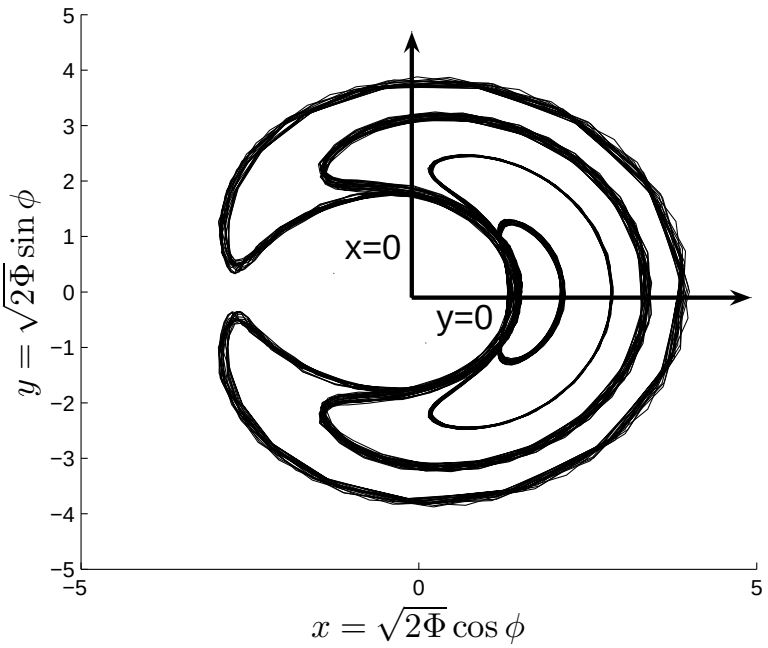

Figure 5.16: *Libration curves for four locations inside the resonant feature. The outer curve is close to the maximal possible libration.*

radial axis in Figure 5.16 is measured in eccentricity units. As we have seen (see Figure 5.2) the behaviour of semi-major axis mimics that of eccentricity in terms of oscillation time period and amplitude changes:both sharp at the defined resonant edges and smooth through the resonance itself.

We now consider two slices through the polar libration curves: one along $y = 0$; another along $x = 0$. Both slices pass through the near-maximal curve. However, while the $y = 0$ slice cuts through the widest part of the libration curve, the $x = 0$ line slices through a much narrower section. The near-maximal libration curve corresponds to the (near) greatest amplitude variations in eccentricity or semi-major axis which form the resonant feature edges; the inner curves correspond to particles inside these edges and progressively closer to the resonant centre, at which point there is theoretically no variation in resonant argument. The maximal curve is therefore equal to the height of the resonant feature. This defines the maximum variation in semi-major axis possible within the resonance, which is also the standard definition of 'resonant width'. The maximal or near-maximal libration curve passed through does not vary for the $y = 0$ or $x = 0$ slices, and by extension is independent of the slice taken, and thus independent of the difference in mean longitudes.

However, as mentioned above, the width of the region enclosed by the libration curve does vary. This is the distance between two maxima of librational amplitude in eccentricity

or semi-major axis, and is therefore equal to the width of the resonant feature: it is the distance between the two peaks of the resonant feature. The $y = 0$ curve produces a large difference between maximal libration peaks, while $x = 0$ sees a narrower region between peaks, and thus a reduced width. A cut taken through one of the far ends of the libration curve produces a lower width again. As the widths of the features are dependent on the slice taken, they are also dependent on the difference in mean longitudes between Jupiter and the test particle.

Additionally, the 'dip height' (defined in Section 5.2.1) will vary depending on the slice taken through the libration curve. The dip height is the minimum oscillation size possible for a resonant particle. At different mean longitudes, different minimum (or inside) curves are intersected: in Figure 5.16, a $y = 0$ slice intersects four curves, including the smallest libration curve, while a $x = 0$ slice only intersects larger libration curves. The libration halfway through the resonant feature is therefore low for the $x = 0$ slice, giving a low dip height. At the $x = 0$ slice only large libration curves are intersected and therefore a high dip height occurs. Note also that this is opposite to the resonant feature width, which is large for the $y = 0$ slice and low for the $x = 0$ slice. Hence, at a maximum in resonant feature width, we have a minimum in dip height, and vice versa.

In summary, the height of the resonant features used here should be insensitive to mean longitude. However, there will be strong variations in the width and dip height of these features, with maximum width and minimum dip height occurring at the mean longitude of the resonant centre.

Determination of the maximum resonant feature width for 7:2 resonant Taurids requires the mean longitude of the resonant centre. This can be accomplished analytically using the resonant argument, or numerically, by finding the resonant feature width for a number of different mean longitude values and determining the one that gives the maximum width.

5.5.1 Analytic Determination of the Mean Longitude of Maximum Width

We expect the maximum width to occur at resonance centres; and we expect resonance centres to occur at a resonant argument of zero. There are a large number of resonant arguments associated with the 7:2 resonance, and six that involve longitudes of perihelion. From equation 5-2 (and accompanying discussion) it can be seen that the importance of perihelion arguments depends on the relative magnitude of the eccentricities of the perturbing body (Jupiter) and the perturbed body (the particle). As the eccentricity of the Taurid particle ($e_P = 0.83$) is much greater than the eccentricity of Jupiter ($e_J =$

0.0489), it is expected that the main resonant argument important for the Taurid case is:

$$\varphi = 7\lambda_J - 2\lambda_P - 5\varpi_P.$$

This is consistent with use of the 7:2 resonance elsewhere for similar problems (see Asher and Clube (1993)).

Setting $\lambda_J = 0$ and knowing $\varpi = 152.7°$ for Taurid meteoroids, we determine two values of mean longitude of the particle λ_P that will achieve $\varphi = 0$:

$$\lambda_P = -21.75° = 338.25°$$

and

$$\lambda_P = 158.25°$$

As expected the 7:2 resonance has two resonant centres in mean longitude. This can also be inferred from the multiplier 2 for the mean longitude of the dust particle λ_P in the expression for the resonant argument.

5.5.2 Numerical Study of the Variations with Mean Longitude for the 7:2 Resonance

We now numerically analyse at the variations in the width and height of the resonant feature with mean longitude for the 7:2 resonance. We begin by generating a resonant feature, such as in Figure 5.3, for each of a range of 50 mean longitude values between 0 and 360°. For each mean longitude, the width and the height of the feature are determined. The size of the small-scale variations in height are subtracted from the left and right hand side peaks (see Section 5.4). The heights of the two peaks are averaged to provide one height value for each resonant feature. A libration correction, as discussed in Section 5.3.3, is also necessary. As discussed in this section, two possible correction methods are possible: the first considering a particle in libration when it demonstrates clear bounded oscillatory motion in the resonant argument (distinct from circulation); the second considering particles in resonance only when they demonstrate libration strictly within ±180°.

Figure 5.17 shows the corrected widths for the first method superimposed on the original data, and heights from the left and right hand sides. Figure 5.18 shows the widths from both libration correction methods. As expected, widths by the stricter definition are lower. The locations of peaks and troughs are the same for both sets of widths. We choose to use the more lenient libration test here: the results from this for the widths and heights are shown in Figure 5.19. The heights given in this figure are the averages of the

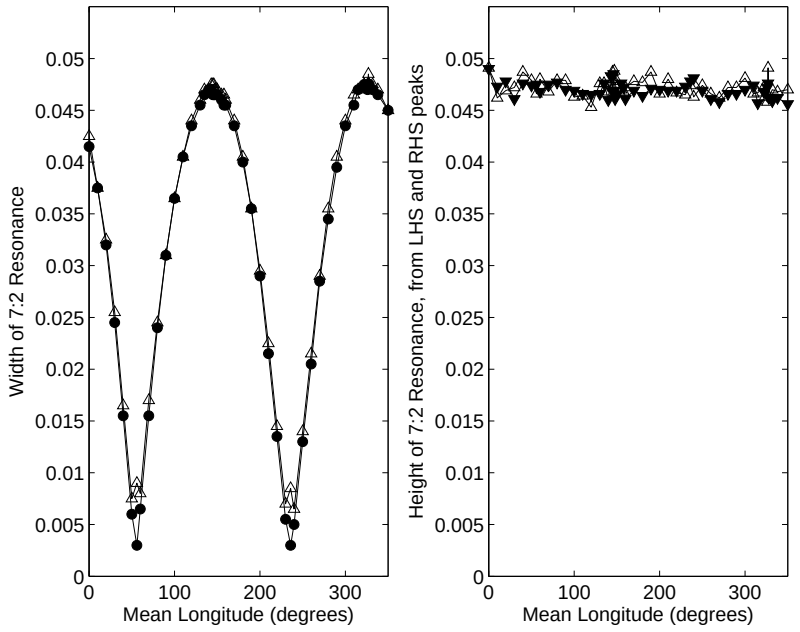

Figure 5.17: *The variations of resonant feature width and height with mean longitude. The widths plot shows the widths not corrected for librations with triangles, and the corrected widths as dots. The largest variations are observed to occur at minima. The heights plot shows the heights of the left hand side peak as downwards pointing triangles, and right hand side heights as upward pointing triangles. All heights are corrected for small-scale variations and the actual starting point of librations.*

left and right hand side values.

We now examine the structure of the final resonant width data with mean longitude. The width values have clear maxima of (0.047 ± 0.001) AU at mean longitudes of $(43 \pm 5)^\circ$ and $(327 \pm 5)^\circ$, and minima of (0.003 ± 0.001) AU at $(56 \pm 1)^\circ$ and $(236 \pm 1)^\circ$. Uncertainties in the widths are a result of the 0.001 AU resolution between semi-major axis steps, which gives a total uncertainty of 0.0005 AU over the two peaks. Uncertainties in the mean longitude positions of maxima and minima result from the difficulty of determining the exact locations of maximum or minimum: the uncertainty is found using the greatest movement away from the optimum value that can still be considered at the maximum/minimum of the width plot.

The height of the resonant feature is relatively robust against variations in mean longitude, varying between 0.0459 AU and 0.0490 AU, with a mean of 0.0471 AU. Since the variations appear random over the 360° of mean longitude, and variations of height with mean longitude are not expected theoretically, we assume that the resonant feature height and uncertainty are defined by the mean, maximum and minimum. This gives

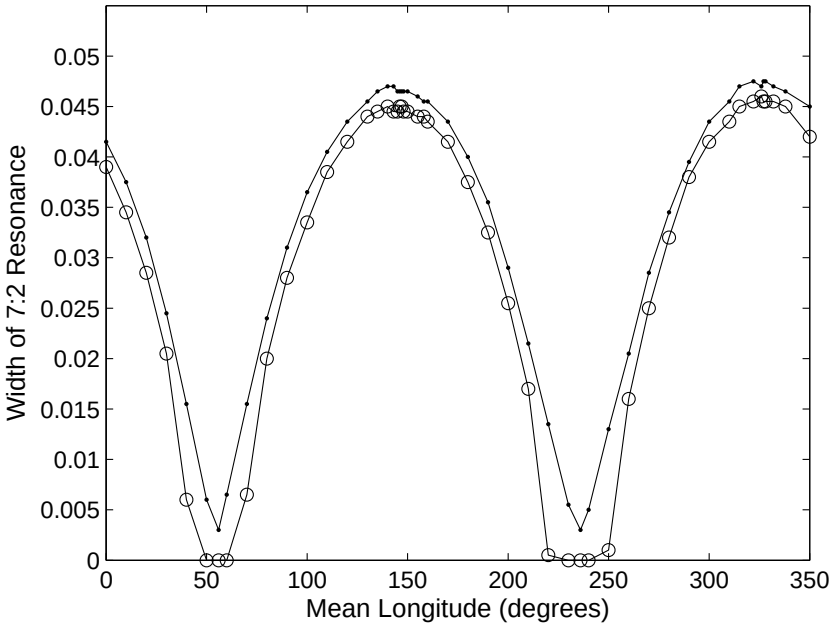

Figure 5.18: *The variations of resonant feature width and height with mean longitude for both libration tests. Widths for librations defined as when clear bounded oscillatory motion in the resonant argument (distinct from circulation) is demonstrated are shown by dots and widths where libration is defined only when they demonstrate libration strictly within* $\pm 180^\circ$ *are given by circles.*

a height of $0.0471^{+0.0019}_{-0.0012}$ AU or (0.0471 ± 0.0019) AU for simplicity. The addition of the ± 0.001 uncertainty in the estimation of the size of the small scale variations gives: (0.0471 ± 0.0029) AU.

As an illustration, Figure 5.20 shows the change in the resonant feature with mean longitude: narrow features with high dip heights are visible at the mean longitudes of the width minima in Figure 5.19; and wide features with low dip heights are seen for the mean longitudes near the width maxima. The vertical dotted lines at the expected resonant centre location of 2.256 AU highlight the small variations in the position of the feature relative to the expected position. This is most likely due to resonant splitting: small variations in the exact resonance centre location occur because of the presence of multiple resonant argument terms (see Section 5.5.1) and thus produce slightly different resonant centre locations.

The final concern is the level of the agreement between the resonant centres, or location in mean longitude of maximum width, determined by the numerical method and by the analytical approach. The resonant argument method gives values for the particle mean longitude required for a resonant centre as 158.25° and 338.25°. The numerical

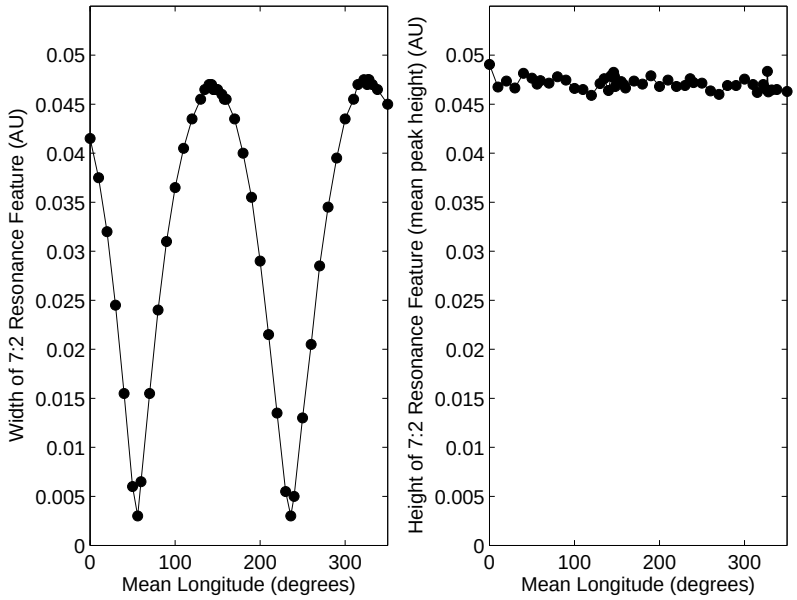

Figure 5.19: *The variations of resonant feature width and height with mean longitude. The widths plot shows the widths corrected for when librations begin. The heights plot shows the mean of corrected heights at the left and right hand sides.*

method gives $(143\pm5)^\circ$ and $(327\pm5)^\circ$. We speculate that the disagreement between these values could indicate the presence of more than one resonant argument term (besides the $\varphi = 7\lambda_J - 2\lambda_P - 5\varpi_P$ term assumed here). A significantly larger uncertainty in the numerical results, sufficient to encompass the mathematical resonance centre values, is not expected given the smooth form of the variation of the resonant feature width with mean longitude in Figure 5.19. We additionally convert the mean longitude scale in Figure 5.19 to the resonant argument (see Figure 5.21). This demonstrates that the maximum width is not coincident with the theoretical resonance centre location of $\varphi = 0$.

Consideration of mean longitude variations represents the final correction required in the analysis of the 7:2 resonant feature. This allows us to draw conclusions on the width of the 7:2 Jovian resonance at Taurid orbital elements. The resonance width has been shown to be given both by the width and height of the resonant feature: these have values (0.047 ± 0.001) AU and (0.047 ± 0.003) AU respectively. We consider the width of the resonant feature is the more accurate measure of the resonant width as it has a lower uncertainty and is less susceptible to other factors, such as asymmetry of the resonant feature. We therefore use this to give our final resonant width:

$$(0.047 \pm 0.001)\text{AU}$$

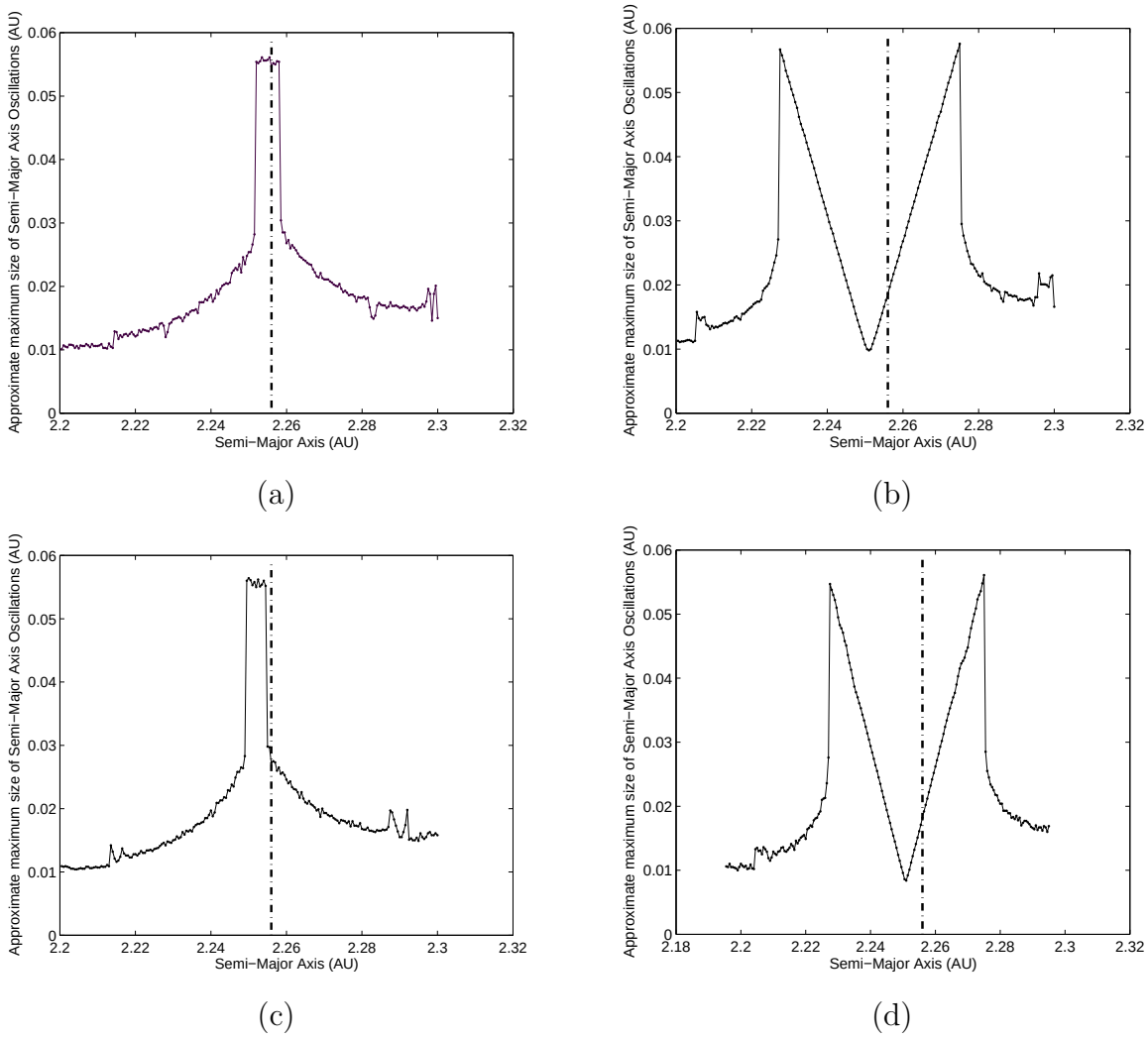

Figure 5.20: *The variation in the shape of the resonant feature with mean longitude. The mean longitudes used to generate each figure are (a)* 56°*, (b)* 146° *(c)* 236° *and (d)* 327°*. They represent roughly the maxima and minima in dip height and width. Note the width and dip height of the feature varies greatly, as does the position of the peaks used to define the width and height. However, the height of the feature and the position of the minimum of the resonant feature dip are roughly constant. The vertical line on each represents the location of the expected resonance centre in semi-major axis at* 2.256 *AU (as predicted using the* $(\frac{a}{a'})^3 \approx (\frac{T}{T'})^2$ *approximation from Kepler's third law). Due to resonant splitting we do not expect an exact agreement between the minima of the resonant features and this location.*

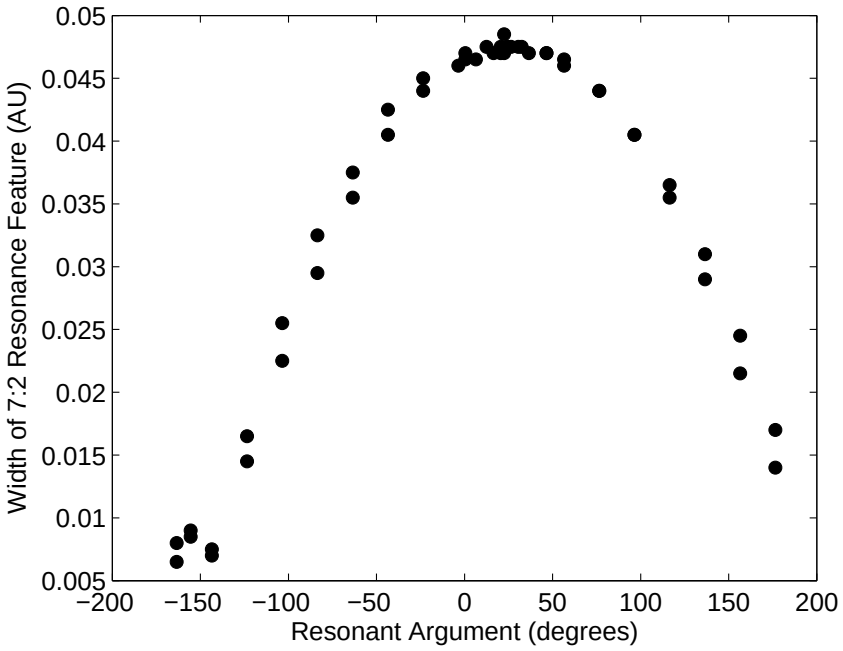

Figure 5.21: *The variations of resonant feature width with resonant argument.*

The only previous result for the resonant width of the 7:2 resonance at Taurid orbital elements is that given by Asher and Clube (1998), who find that librations are possible between 2.23 and 2.28 AU, implying a libration width of ~ 0.05 AU. Our final resonant width is in good agreement with their result, and represents a significant improvement in accuracy.

5.6 Resonance Behaviour in the Inner Asteroid Belt and the Variation with Eccentricity

The region of interest is now extended beyond the 7:2 resonance. Figure 5.22 shows the resonance activity for Taurid-like particles (with high eccentricity $e = 0.83$) between 1.0 AU and 4.0 AU in steps of 0.002 AU. The corresponding Jovian resonance is marked above each prominent resonance feature. The inclusion of only Jupiter in the integration means only Jovian resonances will be seen: inclusion of other planets is discussed in Section 5.7. For particles with semi-major axes larger than about 2.6 AU the highly eccentric particles have a high chance of close Jupiter encounters, which can drastically alter their orbits. Such significant changes in the semi-major axis are responsible for the large number of semi-major axis spikes after this point. Figure 5.23 demonstrates the large variations of four particles started at 2.9 AU 2.902 AU, 2.924 AU and 2.938 AU respectively.

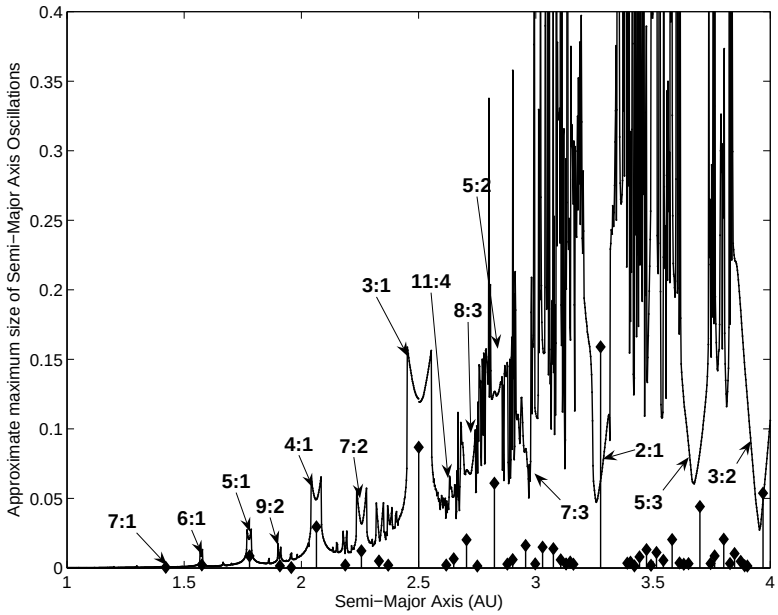

Figure 5.22: *The resonance activity at Taurid orbital elements ($e = 0.83$, $i = 5.4$, $\omega = 115.4$) at semi-major axes values* 1.0 *to* 4.0 *AU. Gallardo resonant strengths (doubled for visibility) are given by the stem plot below.*

In Figure 5.22 the resonant features between 2.5 and 4.0 AU are generated only using the 200 years of iterations. This limits the spikes and provides a clearer view of the resonant activity in this region. Notably, the action of the resonances to protect particles from close encounters and preserve their initial conditions for much longer than non-resonant particles is evident, particularly in the 2:1, 5:3 and 3:2 resonances. The Gallardo strengths (see Section 5.1.6) are doubled (for visibility) and graphed as a stem plot underneath the resonant features. This reconfirms the good agreement of the positions of resonant features with the locations of strong resonances. For clarity, Figure 5.24 shows the resonant activity from (a) 1.0 AU to 2.0 AU , and (b) 2.0 to 2.5 AU. The latter represents the immediate vicinity of the 7:2 resonance. We note that the 7:2 resonances is relatively strong at $e = 0.83$, but this region is still dominated by the strong 3:1 resonance at 2.5 AU.

We now use this 2.0 to 2.5 AU 'resonant map' to illustrate the variations of resonance strengths/widths with eccentricity. Figure 5.25 shows this region for particles with eccentricities of 0.1, 0.3, 0.5 and 0.7 respectively. As the eccentricity increases, the width or strength of higher order resonances increase relative to that of lower order resonances. Thus, high order resonances are increasingly important with increasing eccentricity.

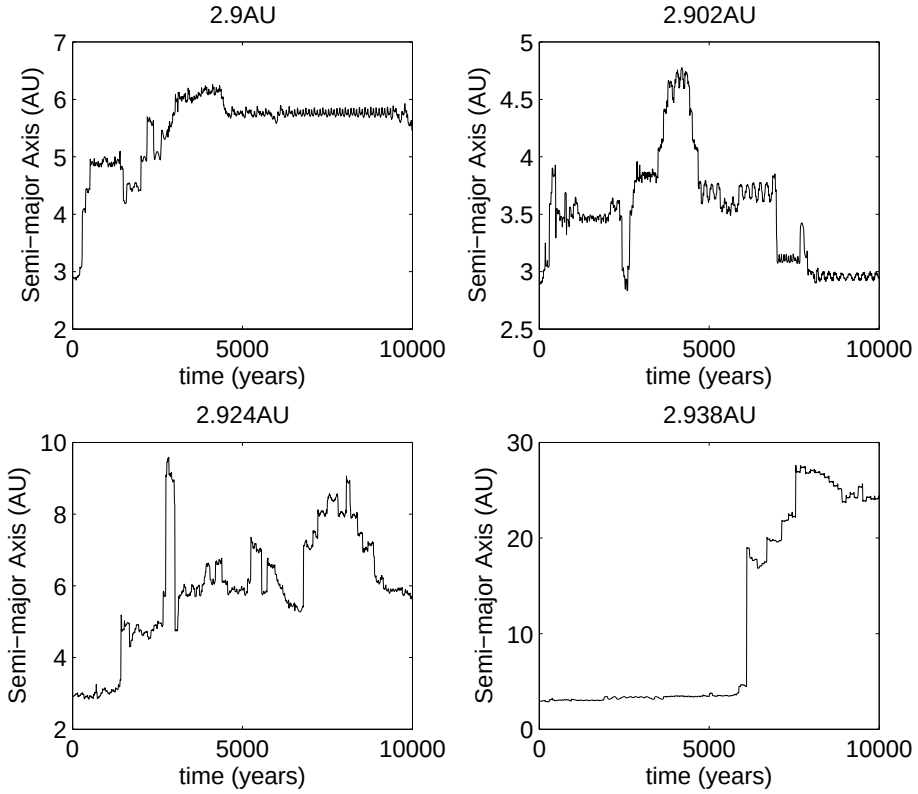

Figure 5.23: *Demonstration of the effect of close approaches to Jupiter for particles at four different starting semi-major axis values (given above each figure).*

5.7 Addition of All Solar System Planets

The above use of the HNBody numerical integrator includes only the Sun and Jupiter as heavy weight particles: all other planetary bodies in the Solar System are excluded. We now examine the impact of the inclusion of all planetary bodies Mercury-Neptune, and include Pluto for completeness.

This procedure requires knowledge of the mass and orbital elements of each of Mercury, Venus, Earth, Mars, Jupiter, Saturn, Uranus, Neptune and Pluto. These are obtained from the Astronomical Almanac 2009 (US Naval Observatory and The Royal Greenwich Observatory, 2007). An approximate set of mean longitudes from which to start the integration are also taken from the Astronomical Almanac (for the date 1 January 2009 (Julian date 2454840.5)). The behaviour of the particles will vary with the choice of the starting particle mean longitudes. In particular, this may vary the distance of the particle from a resonant centre, thus varying the effect of each resonance. Input particles are again given initial conditions equal to the mean Taurid orbital elements, except for semi-major axes, which scans through starting values of 2.0 AU to 2.5 AU, in steps of

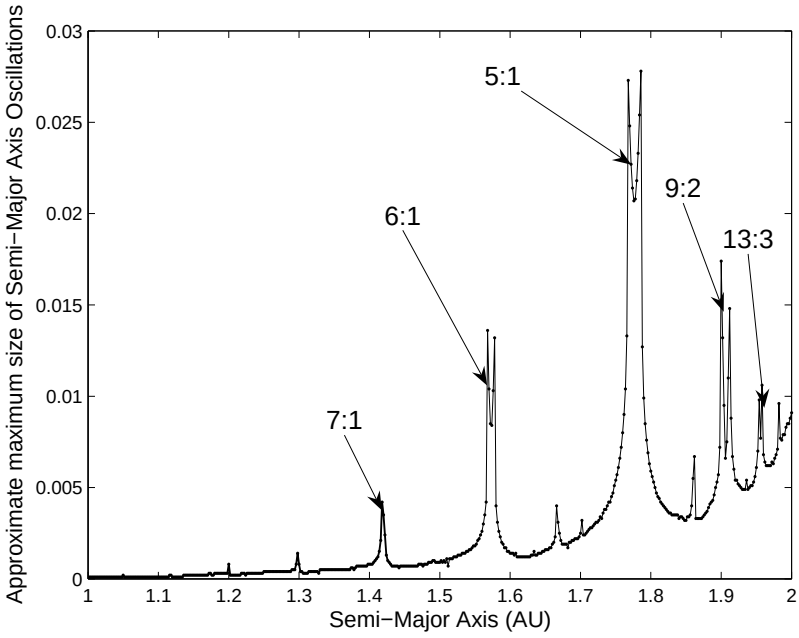

(a)

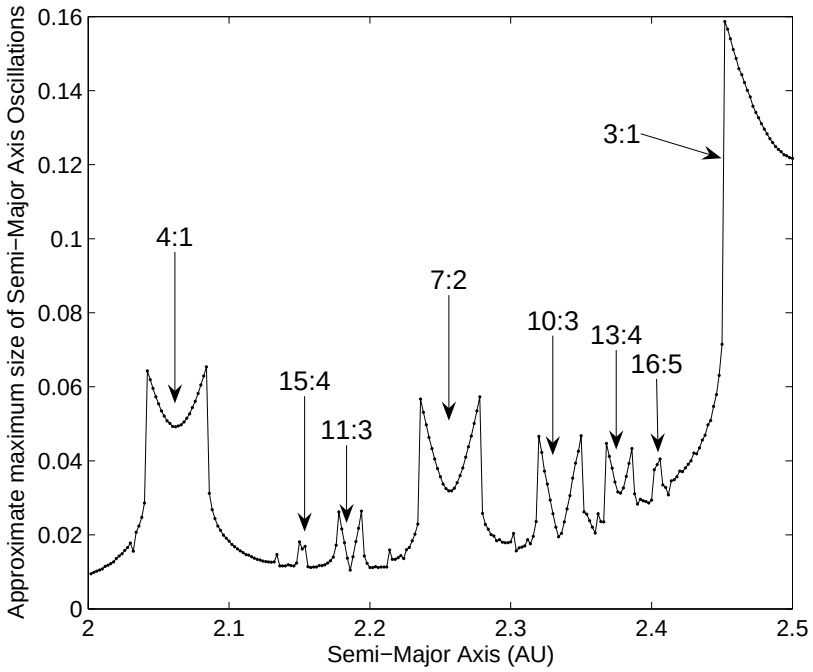

(b)

Figure 5.24: *A closer view at the inner Asteroid Belt: (a) shows Jovian resonant activity between* 1.0 *and* 1.5 *AU (note that this is a region that may be have be significantly affected by resonances involving inner planets); (b) shows the 7:2 resonance region (*2.0 *to* 2.5 *AU)*

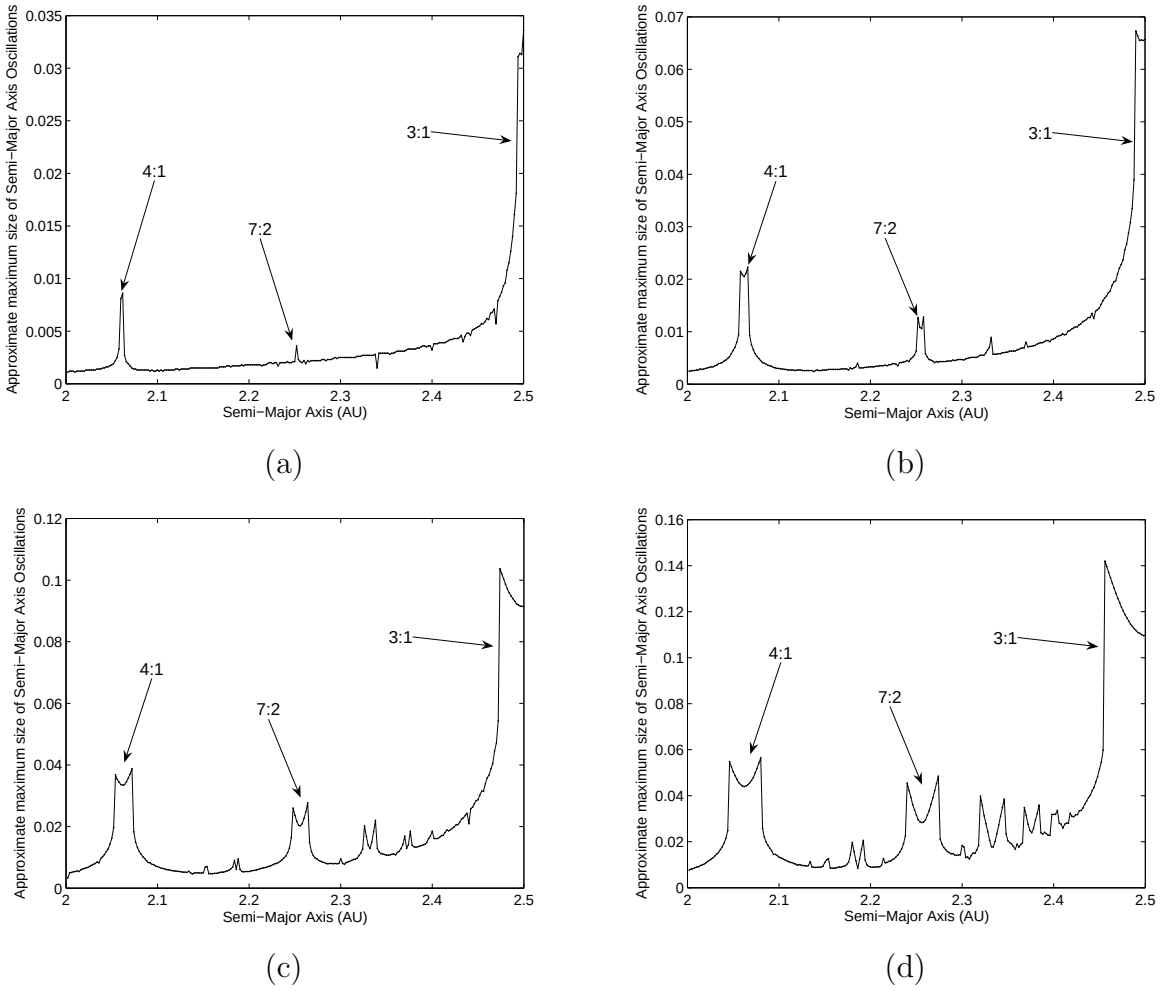

Figure 5.25: *The variation in the resonant feature with eccentricity, between* 2.0 *and* 2.5 *AU. Eccentricities used are (a) 0.1, (b) 0.3, (c) 0.5 and (d) 0.7. Compare with Figure 5.24(b), which shows an identical plot to those shown here, but for 0.83. The positions of the three strongest Jovian resonances in this region are marked (others are present). Note the increase in strength/width of the resonances as the eccentricity increases, and the relative increase in the strength of higher order resonances (such as the 7:2 resonance) with eccentricity.*

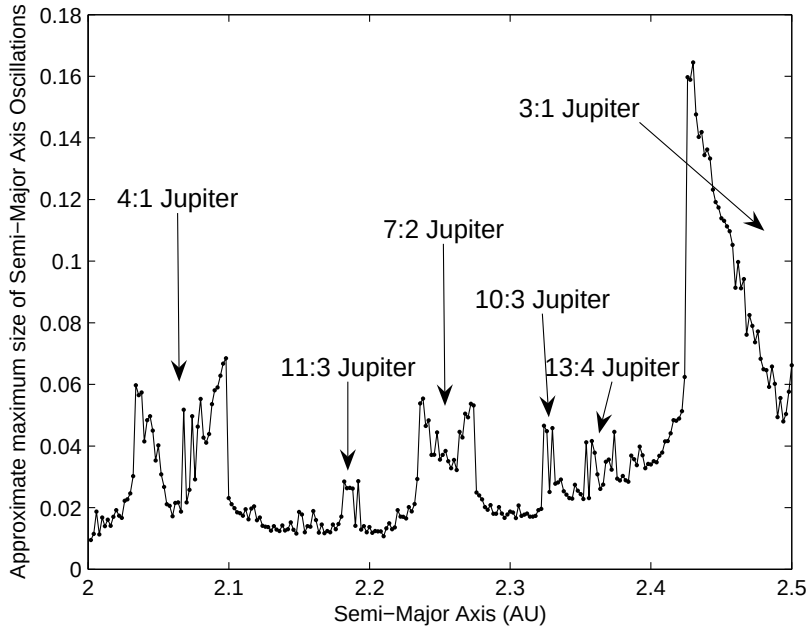

Figure 5.26: *Resonant activity of Taurid orbits with starting semi-major axes* 2.0 *AU to* 2.5 *AU, in steps of* 0.002 *AU. All planets Mercury-Neptune and Pluto are included in the integrations.*

0.002 AU.

Figure 5.26 shows the results of this integration, with maximum oscillations calculated only from the first 100 time steps ($\frac{1}{10}^{th}$ of the total). This reduction lowers the number of spikes caused by planetary gravitational perturbations that can drastically shift the orbit of the particle and cause large variations in semi-major axis. Features resulting from strong Jovian resonances (such as seen in Figure 5.24(b)) are clearly visible. The additional structure has two sources: planetary perturbations causing drastic alterations to particle orbits; and resonances of planets other than Jupiter.

We present two examples of particle behaviour that lead to an unrealistic impression of the size of the oscillations at a particular semi-major axis. Figure 5.27 compares the motion of two particles with starting semi-major axis values of 2.066 AU (dotted line) and 2.068 AU (solid line). The larger oscillations of the second particle are responsible for the first major spike within the 4:1 Jovian resonance (see Figure 5.26). The first particle demonstrates the expected level of semi-major axis oscillations at that location in this resonance. The second particle experiences larger oscillations after a perturbation occurs approximately half an oscillation into the integration due to an inner planet. At about 8000 years the particle suffers a second perturbation which causes it to leave the resonance altogether, and the size and period of the oscillations decrease. Since the approximate

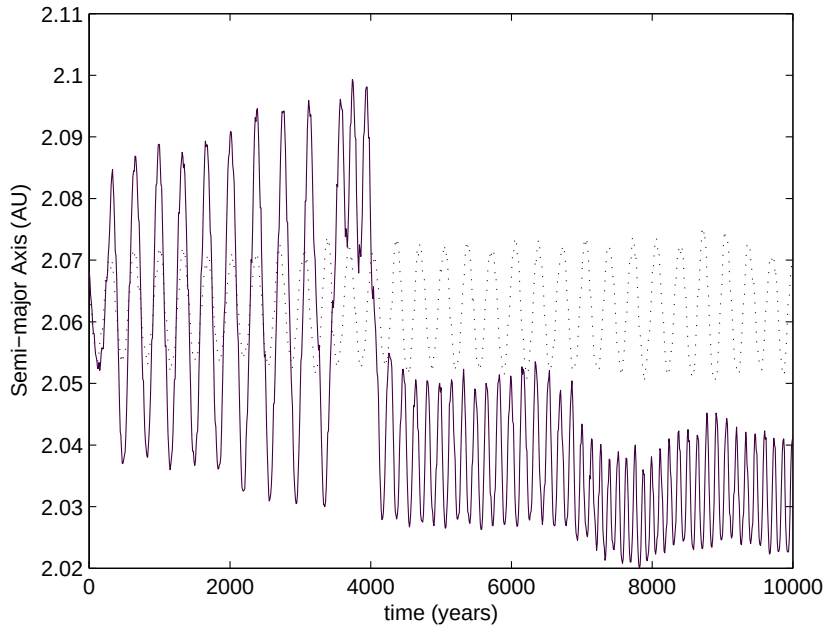

Figure 5.27: *Comparison between a particle that remains in the resonance (dotted line), and particle that might suffer a gravitational perturbation from a planet and therefore does not remain in the resonance (solid line).*

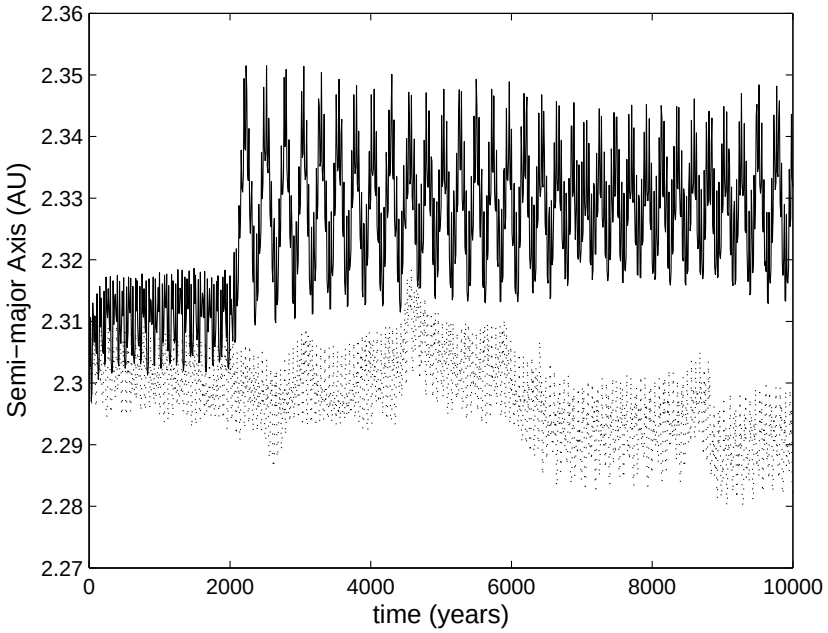

Figure 5.28: *Comparison between a particle that is perturbed into resonance (solid line), and one that does not (dotted line).*

method calculates the oscillation width by taking the difference between the maximum and minimum values from the first 1000 years, the large variation in semi-major axis caused by the early perturbation is included for the width determination. This is effectively giving the oscillation size for a particle with a larger starting semi-major axis: hence the peak.

Figure 5.28 shows the semi-major axis behaviour of two particles with starting semi-major axes of 2.304 AU (dotted line) and 2.306 AU. The former undergoes non-resonant motion suffering occasional perturbations that affect its motion. The second particle also begins outside of the main resonances, but is subject to a perturbation at $\sim$ 2000 years which is significant enough for it to reach the 10:3 Jovian resonance, the resonance centre of which is at $\sim$ 2.33 AU. However, the perturbation for this particle occurs after the first 1000 years, and therefore it is not seen in Figure 5.26.

Possible signatures of other resonances can be investigated by superimposing the resonant strengths of Gallardo (2006b) on to the maximum oscillation distribution (see Figure 5.29). Here eighty strengths between 2.0 AU and 5.1 AU are computed (5.1 AU is chosen instead of 5.0 AU to allow inclusion of the 3:1 Jovian resonance at 2.50045 AU). Inputs to Gallardo's 'atlas' program used are maximum q and p of 20, and maximum $|p + q|$ of 30. Orbital element inputs eccentricity, inclination and argument of perihelion are the approximate Taurid values of 0.83, 5.4° and 115.4° respectively. The resulting list of resonances includes those of planets from Mercury to Saturn. The square root of the Gallardo strengths is taken for clarity: values should be considered indicative of relative strength only.

Figure 5.29 shows that strong features seen in the numerical distribution correspond to the locations of the 4:1, 11:3, 7:2, 10:3, 13:4 and 3:1 Jovian resonances. In addition, weaker features may be evidence of the 15:4 and 16:5 resonances with Jupiter. Gallardo's strength program predicts that the 1:3 resonance with Earth and the 1:5 resonance with Venus should be the most important resonances with planets other than Jupiter. We are not able to verify this, possibly due to interference with other resonances.

We are most interested in verifying that the resonant width resulting from our one-planet approximation (with Jupiter only) agrees well with that from the integrations including all planets. To this end we superimpose the approximate oscillation width distributions from integrations with all planets and with Jupiter only (see Figure 5.30). The widths of the 7:2 resonance and 4:1 resonances do not vary at this resolution, and we are thus satisfied that perturbations from other planets will not significantly interfere with the edges of these strong Jovian resonances. Integrations with all planets can take seven times longer to run ($\sim$ 3 hours for 200 particles using HNBody) than integrations with Jupiter and the Sun only: in consequence, below only the one-planet approximation is used.

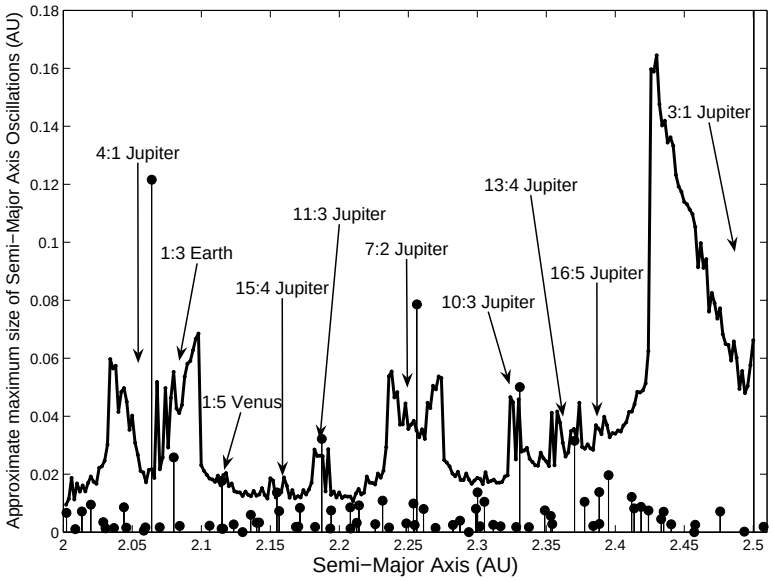

Figure 5.29: *Comparison of visible resonant features to positions of strong resonances of all planets from Gallardo's strength 'atlas' program.*

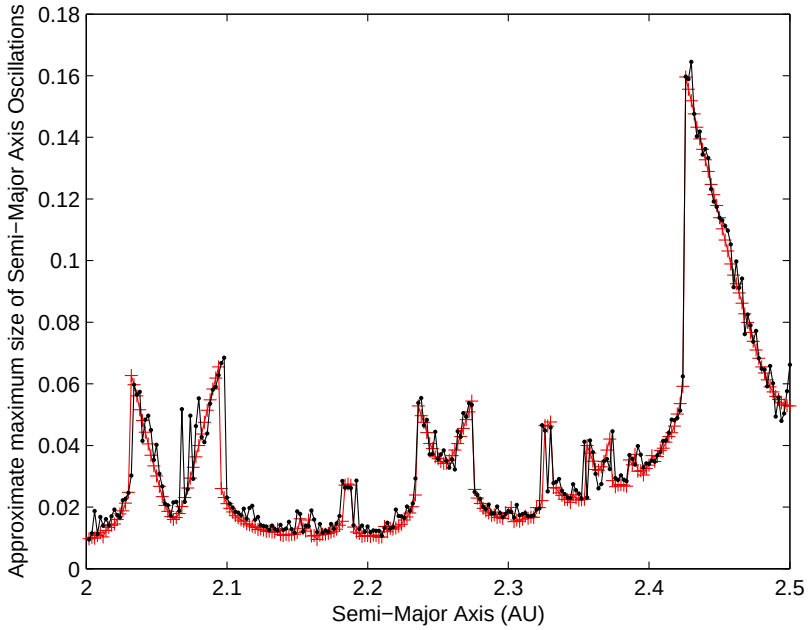

Figure 5.30: *Resonant features for the region 2.0–2.5 AU, with a comparison between the case with Jupiter only (crosses), and the case with all planets (dots). Errors in resonant widths are within 0.002 AU.*

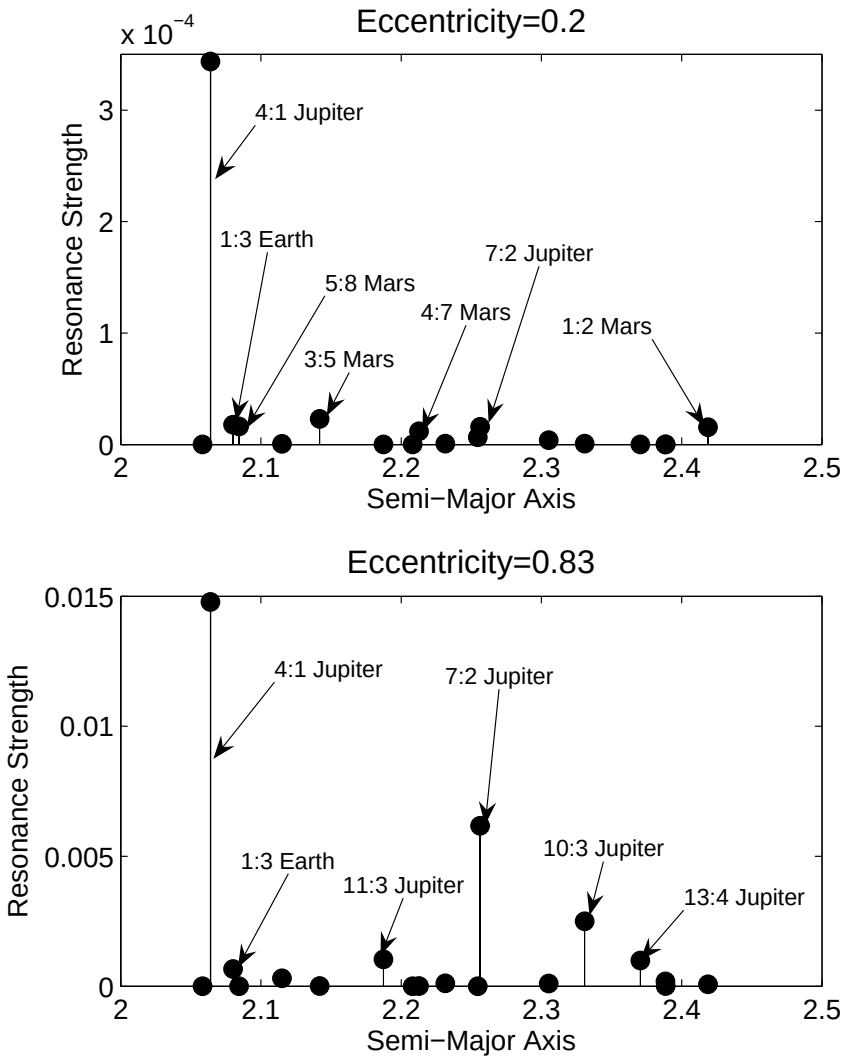

Figure 5.31: *Comparison of the resonant strengths determined by Gallardo for eccentricities of* 0.2 *and* 0.83. *Notice that the relative importance of resonances of inner planets is higher for smaller eccentricity. Also note the increase in the relative importance of the 7:2 resonance with higher eccentricity. The locations of the 1:3 Earth and 1:5 Venus resonances are marked, but no librational evidence was found to support their detection.*

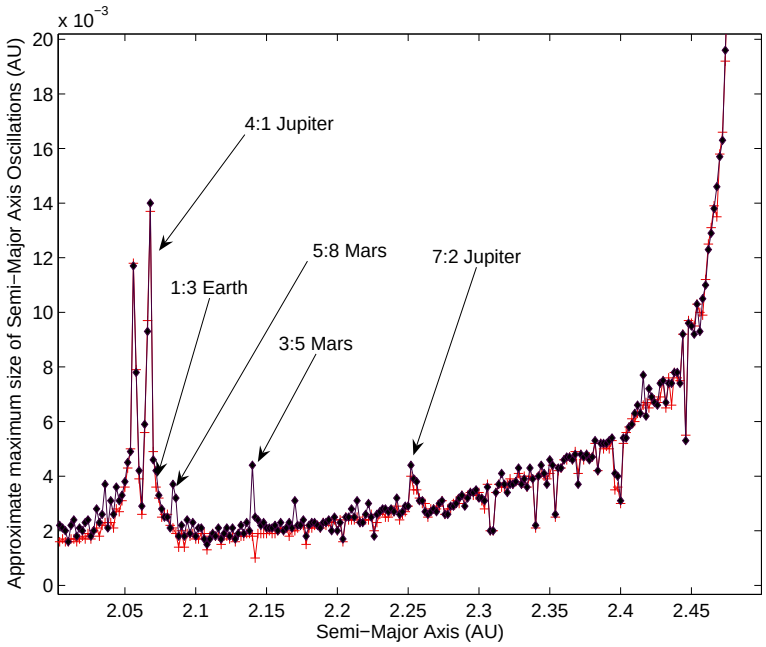

Figure 5.32: *Comparison between the resonant feature map with Jupiter only, and including all planets, for an eccentricity of 0.2. Crosses are Jupiter only, dots are all planets. Errors in resonant widths are within* 0.002 *AU. Resonance features (and thus widths) of the strong 4:1 and 7:2 Jovian resonances are in agreement within uncertainties.*

Gallardo's resonant strengths program demonstrates that resonances with rocky inner planets are relatively more important than higher order Jovian resonances (such as 7:2 and 8:3) at low eccentricities (Figure 5.31). This is because these inner planet resonances are low order, and so their strength increases at a lower rate with eccentricity than the higher order resonances. However, Jovian resonances are always the strongest resonances present due to the large mass of Jupiter. We therefore repeat this test at a low eccentricity of 0.2 (see Figure 5.32). It can be seen that the low-order resonances of Earth and Mars are now comparable in strength to the 7:2 Jovian resonance. The strong 4:2, 7:2 and 3:1 Jovian resonances are present. However, we are able to confirm the presence of librations within the 1:3 Earth, 5:8 Mars and 3:5 Mars resonances. Again the resonances from the inner planets do not affect the width of Jovian resonances. Inner planet resonances can be seen as small variations from the Jupiter-only width distribution.

Finally, we note the existence of several large asteroids in the Taurid region. We now repeat the above integration for $e = 0.83$, with the addition of four asteroids. This should indicate whether such asteroids are able to significantly alter the orbits of particles in this region. The asteroids included are Ceres, Pallas, Juno and Vesta, which have semi-major axes of approximately 2.7664, 2.7729, 2.6716 and 2.3616 AU respectively. The results

find no significant differences from Figure 5.26. This confirms that the exclusion of major asteroids and planets apart from Jupiter has no significant effect on the resonant width of the 7:2 Jovian resonance.

5.8 Comparison of Analytic, Semi-Analytic and Numerical Methods

Here we will directly compare the resonant width values (in semi-major axis) that are given by the three methods outlined in this chapter. The analytic method is as given in Murray and Dermott (1999): it is derived using a simple pendulum model, and applies in the circular, planar restricted case (see Section 5.1.5). The semi-analytic method is that developed in Gallardo (2006b) (see Section 5.1.6), which can output a 'strength' for a given resonance, at a given set of orbital elements. The numerical method (see Section 5.2) is the subject of the majority of this chapter, and involves a numerical determination of the resonant width directly from integrated particle orbits. The purpose of this comparison is to determine the accuracy of the numerical method, and to verify that it agrees with the resonant widths expected by other methods.

The HNBody numerical method will have limitations in accuracy. The procedure presently has only Sun, Jupiter and meteoroid particles as input masses: neglecting other planets (in particular, minor planets) may have some effect on dynamics, though this does not have a significant effect on resonant widths (see Section 5.7). Radiation effects are also ignored: this again is only likely to cause a small error, in consideration of the relatively large mass of CMOR particles used in the integrations.

However, the numerical method is not restricted by the assumptions of other methods. The analytic approximation requires low eccentricities and zero inclinations, and the Gallardo semi-analytic method assumes that the perturbing planet has zero eccentricity and inclination. HNBody integrations make no orbital element assumptions, and are valid for all orbital elements. Both the analytic and semi-analytic methods deal with an individual resonance, which does not allow for interference effects between different resonances. HNBody considers all gravitational effects, so interference effects of included planets are accounted for. The comparison methods will also not include separate resonant splitting components of the same resonance: these are dealt with by HNBody.

In consequence, there will be intrinsic discrepancies between the brute-force numerical HNBody method and the verification methods, but there should still be a good level of agreement, particularly if HNBody is limited in order to restrict the differences (by not adding gravitational effects of other planets; and by restricting eccentricity and inclination of the perturbing body to zero). Thus, the eccentricity and inclination of Jupiter are set

to zero for agreement between the three methods.

The numerical widths used here are the 'width' of each resonant feature. To obtain an accurate width we first determine the mean longitudes that describe the resonant centres (see Section 5.5). We can estimate these using the equations for the most important resonant argument for each resonance (see Section 5.3.2), using the method given in Section 5.5.1. There will be a small error in this due to the presence of resonant splitting terms, but as seen in Section 5.5.2 this will not create a large error in the resulting resonant width.

Resonance	**Numerical**	**Analytic**	**Semi-Analytic**	**% Variation Analytic**	**% Variation Semi-Analytic**
2:1	0.0635	0.0701AU	0.0648AU	−9.4%	−2.0%

Table 5.1: *Numerical resonant widths, analytic width, and semi-analytic widths approximations for 2:1 resonances. Percentage variations are with respect to the numerical widths.*

Eccentricity	**Numerical** ($\times 10^{-3}$AU)	**Analytic** ($\times 10^{-3}$AU)	**Semi-Analytic** ($\times 10^{-3}$AU)	**Variation Analytic**	**Variation Semi-Analytic**
0.10	0.00870	0.0960	0.0091	−9.4%	−4.1%
0.15	0.01375	0.0144	0.0138	−4.5%	−0.36%
0.20	0.01825	0.0191	0.0183	−4.5%	−0.27%
0.25	0.0225	0.0239	0.0226	−5.9%	−0.044%
0.30	0.0275	0.0287	0.0267	−4.2%	+3.0%
0.40	0.0365	0.0383	0.0344	−4.7%	+6.1%
0.50	0.0460	0.0479	0.0413	−4.0%	+11%
0.60	0.0545	0.0574	0.0474	−5.1%	+15%
0.70	0.0625	0.0670	0.0528	−6.7%	+18%
0.83	0.0700	0.0795	0.0588	−12%	+19%

Table 5.2: *Numerical resonant widths, analytic width, and semi-analytic widths approximations for 3:1 resonances. Percentage variations are with respect to the numerical widths: that is, a variation of −7.27% indicates the analytic width is 92.73% of the numerical width.*

For the analytic case, we can use equation 5-3 to provide direct comparison values. However, its use is expected to be limited to low eccentricities (below values of 0.3) due to the circular orbits assumption inherent in its derivation. In order to evaluate this equation, we must also know the values for the relevant direct term in the expansion of the disturbing function $f_d(\alpha)$. These are difficult to compute, but are given as products $\alpha f_d(\alpha)$ with $\alpha = a/a'$ for simple first and second order internal resonance in Murray and Dermott (1999). We therefore restrict this comparison to the 2:1 and 3:1 resonances: at an eccentricity of 0.1 for the 2:1 resonance (as high eccentricity orbits in the vicinity of the

2:1 resonance are subject to close encounters with Jupiter); and at eccentricities between 0.1 and 0.83 for the 3:1 resonance.

To compare the resonant strengths calculated by Gallardo's semi-analytic method with our numerical approach, we must convert Gallardo's strengths into semi-major axis units. This is given in Section 5.1.6 in equations 5-7 and 5-8, which we developed from the circular planar restricted form of the disturbing function given by Murray and Dermott (1999). The resulting resonant widths are thus are only valid for low eccentricity, zero inclination cases.

Table 5.1 sumarises the analytic, semi-analytic and numerical widths for the 2:1 resonance; while Table 5.2 contains the same information for the 3:1 resonance. The numerical widths are divided by two in order to give a half width or amplitude that can be directly compared to the analytic and semi-analytic amplitudes. Variations between the methods are also given. It can be seen that these do not exceed 10% for low eccentricity values $e \leq 0.4$. As expected, higher differences between the methods occur at high eccentricities, as a result of the circular assumption used to generate the analytic and semi-analytic equations. This is also illustrated in Figure 5.33, which shows that the analytic strength model we use (given by equation 5-6) diverges from Gallardo's resonant strengths after $e \sim 0.4$.

Because the $\alpha f_d(\alpha)$ terms cancel out for the Gallardo width equation for comparison of the Gallardo method and the numerical method only we are not restricted to certain simple resonances such as the 3:1 and 2:1 resonances. We do not study the 7:2 resonance here as this is very weak at low eccentricities. Table 5.3 compares the numerical and Gallardo widths for the 4:1 resonance at various eccentricities. The percentage differences in the methods are less than $\sim 5\%$ for all eccentricities except $e = 0.83$.

Eccentricity	**Numerical** ($\times 10^{-3}$AU)	**Semi-Analytic** ($\times 10^{-3}$AU)	**Variation Semi-Analytic**
0.10	1.29	1.32	-1.5%
0.15	2.40	2.52	-4.8%
0.20	3.76	3.92	-4.3%
0.25	5.35	5.49	-2.6%
0.30	6.98	7.39	-5.3%
0.40	10.70	10.80	-0.93%
0.50	14.55	14.60	-0.34%
0.60	18.50	18.35	-1.1%
0.70	22.75	21.87	-3.9%
0.83	27.25	25.73	-6.0%

Table 5.3: *Numerical resonant widths, analytic width, and semi-analytic widths approximations for 4:1 resonances. Percentage variation are relative to the numerical width.*

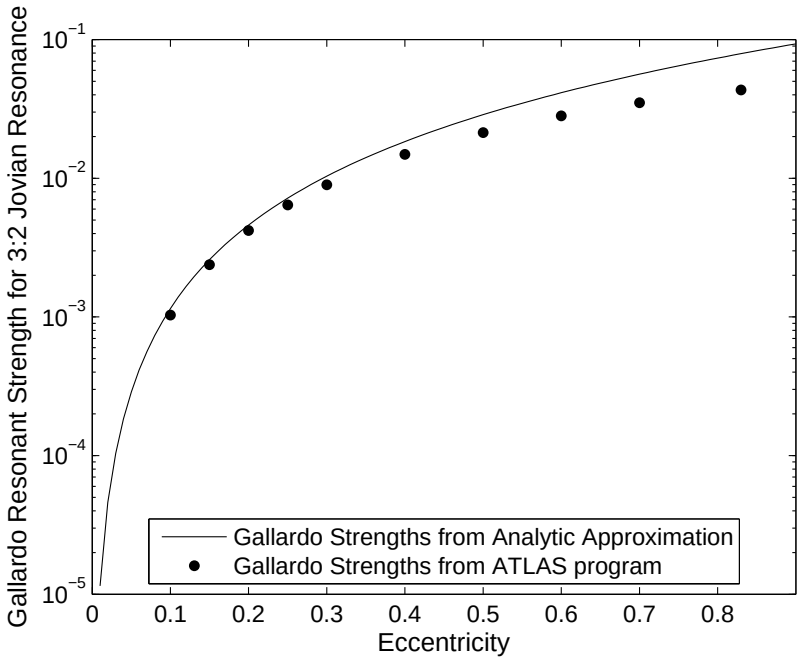

Figure 5.33: *Comparison of 'Gallardo' strengths determined analytically (given by equation 5-6), and the Gallardo strengths given by the ATLAS program, for the 3:1 Jovian resonance. It can be seen that divergence between the Gallardo strengths given by the ATLAS program, and those we determine from the analytic approximation diverge after an eccentricity of* ~ 0.4*. The divergence here indicates the error from our conversion of the Gallardo strengths (in energy units) to semi-major axis widths, using equation 5-7*

We also test whether the analytic and semi-analytic widths are within the resolution uncertainties of the numerical widths. This resolution uncertainty arises as a result of the step-size between the starting semi-major axes values of each particle used to create the resonant feature. For the 2:1 resonance this is 0.002; for the 3:1 resonance this is between 0.0002 and 0.001 AU; and for the 4:1 resonance this is between 0.00003 and 0.0005 AU. For the 2:1 resonance, neither the semi-analytic or analytic values are within the uncertainty. For the 3:1 resonance, the analytic and semi-analytic values at $e = 0.1$ are not within the uncertainty of the numerical value. However, those values between $e = 0.15$ and $e = 0.4$ are. For higher eccentricities we do not expect an agreement between the method, and indeed the semi-analytic and analytic values are again not within the uncertainties of the numerical widths. For the 4:1 resonance however, six of the eccentricity values do result in agreement, and four do not, with no particular preference of agreement at low eccentricities. We conclude that we cannot expect our numerical method values to agree with the analytic or semi-analytic values within the uncertainties. This is not unexpected, due to the limitations of the various methods, as described at the beginning of this section.

We now discuss the adequacy of $\sim 10\%$ differences between the numerical widths and the comparison methods for eccentricities $e < 0.4$. It is difficult to know what fraction of the variation is from HNBody, and what is fraction is a result of inadequacies of the analytic and semi-analytic approximations. The variation is limited by setting the eccentricity and inclination of Jupiter to zero. Nevertheless, the worst-case scenario is that the differences in the numerical resonant widths are in fact $\sim 10\%$: this can be considered an upper limit for the total inaccuracy of this numerical width method. While the accuracy of the numerical width method is interesting from a theoretical perspective, in this case we are interested in the accuracy required for application to meteor orbit radar data. Such 10% uncertainties are supportable for this problem: CMOR uncertainties in semi-major axis can be $\sim 34 - 40\%$ in individual Taurid orbits.

5.9 Summary

In this chapter we have determined a numerical value for the width of the 7:2 resonance for Taurid-like orbits, and evaluated the agreement of this method with respect to two existing methods for determining the resonant width. The former produced a resonant width of (0.047 ± 0.001) AU. The latter has provided what may be considered an upper limit of this error in the numerical width method of $\sim 10\%$. We can therefore conclude that the resonant width for the 7:2 resonance for Taurid orbital elements is:

$$(0.047 \pm 0.005)\text{AU}.$$

This is in agreement with the resonant width given in Asher and Clube (1998). Our resonant width method is able to give accurate results for orbits with high eccentricities, and is notably capable of providing a physical semi-major axis width, as opposed to the resonant 'strengths' given by the the work of Gallardo (2006b). The simple conversion formula used to convert the Gallardo resonant strengths to resonant widths is found to provide results that agree with our numerical width values to within $\sim 10\%$ for eccentricities below 0.4. The analytic width method is also found to agree with the numerical widths to this level. Thus, to this level of accuracy, both the Gallardo and analytic methods are able to give reliable width estimates provided $e < 0.4$. However, our simple numerical width method is capable of determining the importance of resonances at any orbital elements (as given by Gallardo (2006b)), and additionally provides a physical value whch defines the region of influence of the resonance.

One benefit of the Gallardo strength progam is the computation time: the strengths of a large number of resonances can be calculated to high precision in seconds; while the numerical width method may require 20 - 30 minutes to calculate the resonant width (or

several hours if several planets are included), and requires use of both HNBody and a MATLAB script to process the output orbital elements. This numerical width method is thus most useful in the case where information is required on a specific resonance, or in which there is a requirement for a semi-major axis width, as is the situation here. In other situations, the method of Gallardo (2006b) may provide a faster approach to analysing the effects of several resonances for objects with high eccentricity or inclination.

Chapter 6

Mass Selection Effects in Resonant Swarms

As discussed in Section 4.3, evidence for resonant swarms of meteoroids exists largely in visual meteor data. In this work we are concerned with radar detection of meteoroids, which involves particles of a much smaller mass regime. It is therefore important to know the mass distribution of swarm particles, and in particular whether we expect there to be more particles of visual or radar-detectable mass in the Taurid resonant swarm. In other words, we need to determine whether the mass distribution of the swarm helps or hinders efforts to observe radar resonant Taurids.

If we assume that the formation mechanism for these swarms is by ejection of particles by a librational or near librational comet directly into the nearby resonance, then the value of the ejection velocity of such particles is critical for determining whether individual particles are likely to enter the swarm. Particles with high ejection velocities are expected to assume an orbit far from the resonance, while particles with low ejection velocities are likely to assume orbits close to the parent comet, and thus also be librational or near librational. As, in general, ejection velocity (as given by models) is related to particle mass, this will produce a filtering of ejected particles by mass (see Section 4.3.5). This is discussed further from Section 6.1 to Section 6.16.

Radiation pressure can alter the orbit and apparent location of the resonance for small particles and thus alter the trapping of very small particles in the resonance. Radiation effects are discussed in Section 6.17. Poynting-Robertson inspiralling may similarly strip particles, but is not expected to be important for resonant particles except as a result of gravitational perturbations (see Section 6.18.1).

6.1 Comet Ejection Velocities and Mass Selection Effects in Resonance Particles

The heliocentric velocity of a particle ejected from a comet is the sum of the comet's velocity and the ejection velocity the particle receives. For gas drag cometary ejection, this is mass dependent as given by simple cometary ejection models, with a heavy particle

having a lower ejection velocity. Ths situation is different for the case of fragmentation ejection of particles (see section 6.2). Here we will examine the first situation. If the ejection velocity is small (larger particles), the particle's velocity will be very close to the original comet velocity, and the orbit it assumes will be very similar to that of the comet. Similarly, a smaller particle will have a larger ejection velocity, which will result in a particle orbit that is much further from the comet orbit. If this comet is in or near libration, there is then a possibility that the ejected particles will librate, and thus form a resonant swarm. Whether this occurs is dependent on the orbit and thus the velocity, and therefore the mass of the particle: large particles have orbits more similar to the librational orbit of the comet than small ones and, in consequence have a higher chance of librating.

It is necessary to model the ejection behaviour of cometary particles in order to understand what fraction (or amount) is likely to land in a resonant swarm. This is achieved by integrating the orbits of particles ejected from a comet and using the resonant argument to establish whether each particle is librating. The particles span a variety of ejection angles using spherical coordinates θ and ϕ , and a range of points of ejection along the comet orbit, determined by the true anomaly ν or mean longitude λ. The particle mass, specified by effective radius s, is also varied. This model is used to determine whether particles of AMOR or CMOR mass ranges are likely to be present in the 7:2 Taurid resonant swarm.

Radiation pressure will dictate a minimum particle size for an ejected particle that can survive in the 7:2 resonance, such that particles below this size limit will assume hyperbolic orbits that may cause them to be lost from the Solar System. This mass limit is dependent on the eccentricity of the particle, and the β ratio dictated by the radius and density of the particle (see Section 2.3.5). The β required for a particle ejected at perihelion to be lost from the Solar System is given by Burns et al. (1979) as:

$$\beta \geq \frac{(1-e)}{2}$$

and the β required for ejection at aphelion is given by:

$$\beta \geq \frac{(1+e)}{2}.$$

For Taurid-type particles, with eccentricity 0.83, this implies that $\beta \geq 0.085$ is required for loss of the particle at perihelion, and $\beta \geq 0.915$ is required at aphelion. We can thus calculate that particles of a minimum size of 2.68 μm will survive (with orbits that are not hyperbolic) when ejected at perihelion, but particles down to a minimum size of 0.25 μm

will survive if ejected at aphelion. Given that both limits are lower than the limiting mass for AMOR and CMOR particles (~ 20 μm and ~ 100 μm respectively) we expect radar particles to be capable of surviving after ejection from the comet. We now investigate their capture in the 7:2 resonance.

6.2 Ejection of Cometary Particles

The motion of ejected particles is governed by the comet's position and velocity, and by the ejection velocity they receive. The former can be determined from the comet's orbital elements; the latter requires application of an ejection velocity model for the comet.

The current view of the ejection of dust particles from comets, which then form meteoroid streams, stems from the 1950 model of Fred L Whipple (Whipple, 1950) (Whipple, 1951). In this he introduced his 'icy-conglomerate' model of the nucleus, more commonly referred to as the 'dirty snowball' model. This envisages a spherical ball of ice embedded with dust grains with radii less than a few centimeters. These ices consist of H_2O, CO_2, NH_3 and CH_4, among others. Currently we understand this model to be inadequate, with nuclei composition known to consist of much higher levels of solid meteoritic material, giving rise to the term 'icy dirtball' (Jenniskens, 2006).

Regardless, the ejection mechanism for cometary particles as proposed by Whipple (1950) still holds. As the comet in its orbit approaches the Sun, it reaches a point at which sublimation of the surface ice is possible: within $\sim 3-4$ AU of the Sun for H_2O; larger distances for other ices. This process releases dust particles from the comet, which are then propelled away from the nucleus by momentum transfer from gas molecules.

Alternately, ejection may be as the result of a fragmentation event, which may produce small particles as well as large resulting fragments. Such a mechanism would populate the resonance in the same way as the cometary ejection modelled here, except that the ejection velocity would be different. The ejection velocity of particles produced by a fragmentation event is difficult to define. It would also be dependent on the mechanism by which the fragmentation event occurred, such as by collision with an asteroidal body, by comet spin-up, or by disruptions caused by tidal forces. In literature, models of the ejection of particles by comet fragmentation use a wide variety of ejection velocities. For Comet 79P/Schwassmann-Wachmann 3, Weigert et al. (2005) use ejection velocities between 1 ms^{-1} and 100 ms^{-1}. For a fragmented parent comet for the Quadrantids, Tanigawa et al. (2010) uses 1 ms^{-1} while Wiegert and Brown (2004) use velocities between 1 ms^{-1} and 1000 ms^{-1}. For fragmentation of comet 3D/Biela, Jenniskens and Vaubaillon (2007) use ejection velocities of 'a few ms^{-1}'. Jenniskens and Lyytinen (2005) expect that ejection velocities of meteoroids as a result of comet fragmentation will be comparable to

or lower than ejection velocities due to cometary activity (under a Whipple-type model: see Section 6.2). In general, these ejection velocities for fragmentation models do not differ significantly from those used for cometary activity ejections. The most significant difference to the model that we develop is that these simple estimates for the ejection velocity do not vary with particle mass. In addition, ejection by fragmentation can occur further from perihelion, whereas cometary activity is limited to within ~ 2 or 3 AU from the Sun. Given the uncertainty in the ejection velocities required, we do not develop a model of particles from a fragmented comet. It is likely that both ejection mechanisms produce a significant amount of Taurid meteoroids.

6.2.1 Ejection Velocity Models

The velocity obtained by particles ejected from the comet is important for modelling and understanding the formation and evolution of meteoroids streams.

An early model for this was provided by Whipple (1951). This model adds the force from the momentum transferred to the particle to the gravitational force of the comet restraining the particle. This produces the following formula for the relative velocity of the particles at infinity, assuming $\rho_{particle} = 4$ gcm^{-3} and $\rho_{comet} = 1$ gcm^{-3}:

$$V_\infty = 3.28 \times (\frac{1}{nsr^{\frac{9}{4}}} - 0.052R_c)^{\frac{1}{2}} R_c^{\frac{1}{2}}$$

in ms^{-1}. Here n is the efficiency of the solar radiation in sublimating cometary gases; s is the radius of the ejected particles (m); r is the heliocentric distance (AU); and R_c is the radius of the comet (km).

If we generalise this for $\rho = \rho_{particle}$ and $\rho_c = \rho_{comet}$, and combine everything under the square root we obtain, in ms^{-1}:

$$V_\infty = \sqrt{\frac{43.0R_c}{\rho nsr^{\frac{9}{4}}} - 0.00559\rho_c R_c^2}$$

A number of assumptions are inherent in his derivation. These include that water vapour dominates the momentum transfer from gas to dust; that this water vapour evaporates radially from the comet surface; that the particle velocity is always small compared to the gas velocity; that the gas velocity obeys a Maxwellian speed distribution; that evaporation only on the sunward side of the comet need be considered; that the whole sunlit face is active and that the radiation balance is defined by input solar radiation and output blackbody radiation.

While all these assumptions produce inaccuracies in the model, the most important to address is the radiation balance. Whipple's model neglects the role of heat loss to

sublimation: indeed, sublimation of ices is the primary heat loss mechanism of comets close to the Sun. We expect radiation to only be important once the comet is beyond about 2.5 AU from the Sun.

Jones (1995) accounts for this heat loss in his model of cometary dust ejection, and adds the effect of the adiabatic expansion of the gas to the gas velocity. The result is an equation similar in form to Whipple's, with varying coefficients, but which neglects the gravitational attraction of the comet nucleus:

$$V_\infty = 20.3 R_c^{\frac{1}{2}} m^{-\frac{1}{6}} \rho^{-\frac{1}{3}} r^{-1.038}$$

with m the ejected particle mass in kg, and other parameters are as given for the Whipple model. This expression still assumes the resulting meteoroid speed is low compared to that of the gas molecules. Additionally, Jones (1995) includes a model for ejection in jets from a discrete region, and finds that the resulting speed is almost independent of the polar angle of ejection, but varies strongly with the size of the active region or spherical 'cap' of the water ices. This is modelled with an empirical fit to data, giving:

$$V_\infty = V_{\infty,isotropic} [\sin \frac{\alpha}{2}]^{0.37}$$

where α is the 'cap angle', denoting the size of the active region, and:

$$V_{\infty,isotropic} = 41.7 R_c^{\frac{1}{2}} m^{-\frac{1}{6}} \rho^{-\frac{1}{3}} r^{-1.038}$$

is the velocity for a spherical comet with uniform solar flux over its surface equal to the actual solar flux at the sub-solar point: this is a simple approximation which neglects the effect on velocity of variations in the solar zenith angle of the cap. However, it will be sufficiently accurate in the limit of a small cap, and can be replaced with a spherical model (as given above) in the case of a large cap. In particular, Brown and Jones (1998) choose an ejection cone angle (the angle of the particle trajectory away from the comet) of 90° which, from empirical models in Jones (1995), implies a cap angle of 60°. This gives:

$$V_\infty = 32.3 R_c^{\frac{1}{2}} m^{-\frac{1}{6}} \rho^{-\frac{1}{3}} r^{-1.038}$$

Brown and Jones (1998) also propose a modified heliocentric distance dependence, encompassing the observational result that the heliocentric distance dependence of the velocity is closer to $V_\infty \propto r^{-0.5}$:

$$V_\infty = 32.3 R_c^{\frac{1}{2}} m^{-\frac{1}{6}} \rho^{-\frac{1}{3}} r^{-0.5}$$

in units ms^{-1}.

Various other models for comet ejection velocities have been proposed. In particular, the hydrodynamic models of J F Crifo and collaborators have a very different form compared to that of Whipple. In Crifo (1995) a 'distributed production' model is developed, in which sublimation causing release of dust particles occurs not only on the spherical nucleus surface, but also throughout the coma. This is possible as fragments of intermixed ice and particles are ejected from the comet, which then undergo sublimation. His ejection velocity is expressed as:

$$V_\infty(X) = \frac{W}{0.9 + 0.45X^{0.615/2} + 0.275X^{0.615}}$$

where W is roughly the terminal gas velocity (of sublimated gas):

$$W = \sqrt{(\frac{\gamma+1}{\gamma-1})\frac{\gamma k_B T_g^0}{m_g}}$$

where γ is the ratio of specific heats (equal to $\frac{4}{3}$); $k_B = 1.38 \times 10^{-23}$ $\mathrm{m^2 kgs^{-2} K^{-1}}$ is the Boltzmann constant; T_g is the gas temperature of the comet's coma; and m_g is the mass of a gas molecule, taken to be that of H_2O.

$$X = \frac{2\pi a_d \rho_d W r_h}{m_g \mathcal{Q}_g}$$

where a_d is the ejected dust particle radius, and ρ_d its density; r_h is the heliocentric distance (AU); m_g is the mass of one gas molecule; and $\mathcal{Q}_g$ is the total gas production rate. As with the Whipple-type models, subtraction of the gravitational attraction of the nucleus (or escape velocity $V_{esc} = \frac{2Gm}{r} = \frac{8\pi}{3} G\rho_c R_c^2$) may be necessary, using $V_{eject}^2 = V_\infty^2 - V_{esc}^2$. This model is most valid at high gas densities (small r_h).

In Crifo and Rodionov (1997) an altered version of this model is given, with:

$$V_\infty = W\Phi = \frac{W}{1.2 + 0.72\sqrt{a_d/a_*}}$$

where

$$W = \sqrt{(\frac{\gamma+1}{\gamma-1})\frac{\gamma k_B T}{m_g}}$$

as before, and

$$a_* = \frac{m_g(1-A)c_\odot}{\rho_d \alpha_s L_s V_g^0} R_c \frac{f(r_h)cosz}{r_h^2}$$

is a characteristic particle size. Here A is the comet albedo; $c_\odot = 1353$ $\mathrm{Wm^{-2}}$ is the

solar flux at Earth; α_S is the coefficient of sublimation for H_2O (assumed to be 1); L_s is the latent heat of sublimation; $V_g^0 \sim \sqrt{\gamma k_B T/m_g}$ is the initial gas velocity; R_c is the comet nucleus radius; $f(r_h)$ is the active surface icy area fraction; z is the zenith angle; and r_h is the heliocentric distance. This expression cannot be used in situations where the fluid approximation is invalid (true at large enough values of r_h and z) or where the gravitational force from the comet nucleus becomes important. The latter occurs when $a_d \sim a_m$, where a_m is the maximum ejectable grain radius. The value a_m is found by considering the point where the free-molecular drag force on a spherical particle at the surface is equal to the gravitational attraction of the nucleus, at which point the particle would have an ejection velocity of zero.

Various authors have compared the different ejection velocity models, with the aim of establishing the most appropriate for their situation. Five models of interest are:

1. Whipple (1950): $V_\infty = 3.28 \times (\frac{1}{nsr^{\frac{9}{4}}} - 0.052R_c)^{\frac{1}{2}} R_c^{\frac{1}{2}}$ ms^{-1}

2. Jones (1995): $V_\infty = 32.3 R_c^{\frac{1}{2}} m^{-\frac{1}{6}} \rho^{-\frac{1}{3}} r^{-1.038}$ ms^{-1}

3. Crifo (1995): $V_\infty(X) = \frac{W}{0.9+0.45X^{0.615/2}+0.275X^{0.615}}$ where W is roughly the terminal gas velocity: $W = \sqrt{\frac{\gamma+1}{\gamma-1}\frac{\gamma k_B T_g^0}{m_g}}$ ms^{-1} and $X = \frac{2\pi a_d \rho_d W r_h}{m_g \mathcal{Q}_g}$

4. Crifo and Rodionov (1997): $V_\infty = W\Phi = \frac{W}{1.2+0.72sqrta_d/a_*}$ where $W = \sqrt{\frac{\gamma+1}{\gamma-1}\frac{\gamma k_B T}{m_g}}$ as before, and $a_* = \frac{m_g(1-A)c_{odot}}{\rho_d \alpha_s L_s V_g^0} R_c \frac{f(r_h)cosz}{r_h^2}$ ms^{-1}

5. Jones (1995) modified: $V_\infty = 32.3 R_c^{\frac{1}{2}} m^{-\frac{1}{6}} \rho^{-\frac{1}{3}} r^{-0.5}$ ms^{-1}

Brown and Jones (1998) compare models (2), (2) with a parabolic velocity distribution (to account for variations in the particle shape), (3) and (5) (with the Crifo velocity distribution). They conclude that (5) (the Jones (1995) model with a modified heliocentric dependency) provides the best fit between their simulated Perseid stream and observed features. Gockel and Jehn (2000) test the same set of models against 1999 Leonid observations and find the Crifo (1995) model with a high particle density ($\rho = 4000$kgm^{-3}) provides the best fit (though it is noted that the particle density chosen has a greater effect on how close the fit is than the ejection model chosen). Welch (2003) tests models (2),(3),(4) and (5), and finds the Crifo and Rodionov (1997) model produces streamlets that are too narrow, and selects the standard Jones (1995) model (number (2)) for use in his work on the Leonid stream as it requires less fine tuning of parameters.

Stream modellers continue to use different models: Vaubaillon, Colas, and Jorda (2005) uses Crifo and Rodionov (1997); Meng (2005) uses Jones (1995) with $V_\infty \propto r^\alpha$.

It is apparent that though the hydrodynamic models of Crifo et. al. may provide more accurate models in some cases, they are more difficult to implement.

For our present problem, which involves no long term integration of orbits over time, a simple 'Whipple' form model should be sufficient. We select the Jones (1995) model, with a heliocentric radius distribution $V_\infty \propto r^{-0.5}$:

$$V_\infty = 32.3 R_c^{\frac{1}{2}} m^{-\frac{1}{6}} \rho^{-\frac{1}{3}} r^{-0.5}$$

where R_c is is km, m is in kg, ρ is in kgm^{-3} and r is in AU, and the velocity V_∞ is in ms^{-1}. However, for completeness we add the gravitational term, given by $V_{esc}^2 = \frac{2Gm}{r} = \frac{8\pi}{3} G \rho_c R_c^2$, using $V_{eject}^2 = V_\infty^2 - V_{esc}^2$ (however, we rename V_{eject} as V_∞). This gives a final velocity model of:

$$V_\infty = \sqrt{(32.3 R_c^{\frac{1}{2}} m^{-\frac{1}{6}} \rho^{-\frac{1}{3}} r^{-0.5})^2 - 0.00559 \rho_c R_c^2}. \quad (6\text{-}1)$$

6.3 Modelling the Ejection of Cometary Particles

We employ the HNBody numerical integrator to assist in developing an understanding of 7:2 resonant particles in the Taurid stream. We simulate ejection of cometary particles by releasing particles from various positions along the comet's orbit, with velocities given by the sum of the comet velocity and the ejection velocity. A variety of ejection angles are used: these are produced by changing the relative sizes of the x, y and z ejection velocity components. The only other objects included in the integrations are Sun, Jupiter and a model comet.

This procedure requires the determination of the types of the comet required to inject particles into the 7:2 resonance. Two clear candidates are the current Comet 2P/Encke, and the proto-Encke body proposed by Asher and Clube (1993). Comet 2P/Encke itself is not directly in the 7:2 resonance: proto-Encke, however, may have exhibited strong or weak resonant activity for at least part of its lifetime, allowing it to more easily populate the resonance with cometary dust. We test three model cometary bodies: Comet 2P/Encke in its current orbit (Comet 1); a model Comet Encke in a proto-Encke orbit (Comet 2); and a proto-Encke fragment (of size proposed in Asher and Clube (1993) in their proposed proto-Encke orbit (Comet 3)). The orbital parameters and masses used for all comets are given in Table 6.1. Orbital parameters for Comet 2P/Encke are from Jenniskens (2006); the mass is as determined in Sosa and Fernández (2009). The orbital elements and mass of a potential (unobserved) proto-Encke fragment are as estimated by Asher and Clube (1993).

A modification of the ejection velocity formula of Jones (1995), given in equation 6-1, is used here. We understand that the simplicity of the model, and our choice of model,

Comet	**mass (kg)**	**mass ($M_\odot$)**	a **(AU)**	e	i	Ω	ϖ
2P/Encke	9.2×10^{13}	4.623×10^{-17}	2.21	0.85	11.93	334.72	160.99
Disp. Encke	9.2×10^{13}	4.623×10^{-17}	2.256	0.847	11.9	334.2	160.2
Proto-Encke	2.5×10^{18}	1.256×10^{-12}	2.256	0.847	11.9	334.2	160.2

Table 6.1: *The mass and orbital elements for three model comets. We may refer to Comet 2P/Encke, Displaced Comet Encke (Disp. Encke) and proto-Encke in later text as 'Comet 1' , 'Comet 2' and 'Comet 3' respectively.*

Body	**mass (kg)**	**mass ($M_\odot$)**	a **(AU)**	e	i	Ω	ϖ
Jupiter	1.898×10^{27}	9.538×10^{-4}	5.202504	0.0489	1.3	100.5	14.6

Table 6.2: *Mass and orbital elements for Jupiter, as used for the comet ejection model. Values are from the Astronomical Almanac (2009)*

may affect the accuracy of our results: this is addressed below (Section 6.12). The density of Taurid meteoroids, required to provide the density of ejected particles ρ_m, is not well known. In general, we do not expect the density of cometary particles to exceed 2700 kgm^{-3} as such densities usually apply to meteoroids of asteroidal origin. However, there may be reasons to believe that Comet Encke does not possess a typical comet composition. Borovička (2006) notes that Taurid meteoroids are 'stronger' than those of Halley-type comets which have a density 800 kgm^{-3}. Konovalova (2003) finds the density of bright Taurids to be 2300-2800 kgm^{-3}, with an average of 2500 kgm^{-3}. In addition, Sosa and Fernández (2009) find the density of Comet 2P/Encke itself is 800 ± 800 kgm^{-3}, using the mass they determined and an estimated comet radius of 3 km. These studies suggest that the average Taurid particle density lies in the range 800-2800 kgm^{-3}. We thus use test values of 1000 kgm^{-3} and 2500 kgm^{-3}.

The meteoroid mass m and comet distance from the Sun r_h are altered by varying the meteoroid radius s and comet true anomaly ν (or mean longitude λ) respectively. For this we use $r_h = \frac{a(1-e^2)}{1+e\cos\nu}$ and assume spherical particles such that $m = \frac{4}{3}\pi s^3 \rho$.

The effective comet radii used are given in Table 6.3. The radii of Comet 2P/Encke is as determined in Fernández et al. (2000). Their given uncertainty is ± 0.3 km; but in consideration of the range of radius values found for Comet 2P/Encke (discussed in Sosa and Fernández (2009)) we will later adopt an uncertainty of ± 1km in this value. The radius for the proto-Encke fragment is calculated from the mass given by Asher and Clube (1993) (and shown in Table 6.1), and a density for the current Comet 2P/Encke from Sosa and Fernández (2009) of 800 kgm^{-3}.

A number of ejection angles and comet mean longitudes at particle ejection are possible. We start by considering a simplified case: that of a particle ejected at perihelion in the direction of the comet's motion. The resulting ejection velocity is expected to

Comet	R_c
Comet 1: 2P/Encke	2.4km
Comet 2: displaced Encke	2.4km
Comet 3: proto-Encke	14.4km

Table 6.3: *The effective comet radius R_c (km) used for each of the three model comets.*

be greatest at this point, as the resulting difference in the meteor orbit from the comet orbit will be maximised. This situation is shown in Figure 6.1. The ejection of particles in different directions and ejection from different points along the comet orbit is then included.

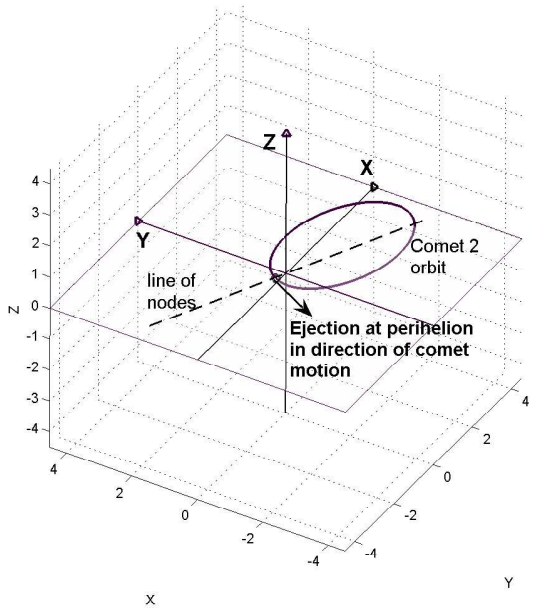

Figure 6.1: *Dust particle ejection at perihelion in the direction of the comet's motion. This gives the ejection velocity that results in maximal variation between the orbit of the comet and the orbit of the ejected meteoroid.*

HNBody can accept input orbit coordinates as either orbital elements, or as Cartesian position and velocity components (in an arbitrary reference frame). We assume the frame here is a heliocentric coordinate system with the ecliptic plane as the reference plane in which the orthogonal X and Y vectors lie. The Z vector is perpendicular to both

and to the ecliptic plane. Thus the X, Y and Z vectors are Sun-centred. This is also seen in Figure 6.1. Velocity vectors V_X, V_Y and V_Z are the velocity components along these directions. Orbital element inputs are a, e, i, ϖ, Ω and λ.

Since the velocity of the ejected meteoroids is the sum of the comet and ejection velocities, it is more appropriate to deal with input parameters as Cartesian position and velocity. Output coordinates are osculating orbital elements.

A conversion from the initial orbital elements of Jupiter and the comet into heliocentric Cartesian position and velocity coordinates is required. This is accomplished using HNBody. By integrating Jupiter and comet with orbital element inputs but with Cartesian coordinate output specified, the first line of the resulting output file will provide the Cartesian coordinate conversion of the input orbital elements. Jacobi coordinates are used. We initially start both the comet and Jupiter at the mean longitude of perihelion of the comet.

This conversion process also provides part of the meteoroid parameters. The position of the comet (X, Y and Z) gives the position of the meteoroid; and the velocity components of the comet (V_X, V_Y, V_Z) are added to the ejection velocity components to obtain the final meteoroid velocity components. The following section involves the determination of these ejection velocity components.

6.4 Ejection Velocity Components

The approximate 'ejection velocity' of particles leaving the surface of a comet is discussed above, and is given by equation 6-1. This, however, should more properly be referred to as a speed, as we have yet to involve a directionality component. We will refer to this scalar velocity below as V_∞.

In the simple case, a vector in the plane of the comet's orbit is required. Thus we define Sun-centred Cartesian vectors x, y and z in the orbit plane, which are separate and distinct from the ecliptic plane vectors X, Y and Z that are described above (see Figure 6.2 for a demonstration of this for Comet proto-Encke (or the displaced Encke)). It is clear that at perihelion a velocity vector along the y direction defines an ejection in the direction of the comet's motion: thus the velocity in the orbit plane is:

$$V = 0.\underline{\widehat{x}} + V_\infty.\underline{\widehat{y}} + 0.\underline{\widehat{z}}$$

or:

$$\begin{pmatrix} V_{x,ej} \\ V_{y,ej} \\ V_{z,ej} \end{pmatrix} = \begin{pmatrix} 0 \\ V_\infty \\ 0 \end{pmatrix}$$

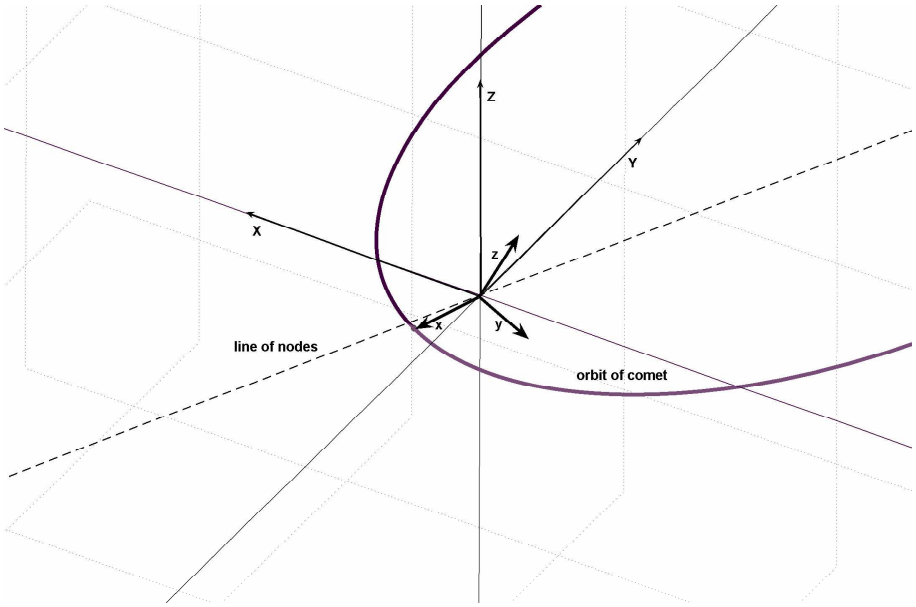

Figure 6.2: *Demonstration of vectors with the reference plane as the ecliptic plane (X, Y and Z) and with the reference plane as the orbital plane of the comet (x, y and z). We begin with vectors with respect to the orbital plane, and later transform them so the x-y plane is coincident with the X-Y plane.*

In the general case, the ejection velocity vector will have x, y and z components. This situation is seen in Figure 6.3. This figure shows two angles that completely define the direction of the ejection velocity vector in three dimensions. These angles can be used to express the components $V_{x,ej}$, $V_{y,ej}$ and $V_{z,ej}$ in terms of the scalar velocity V_∞:

$$V_{x,ej} = V_\infty \cos\theta \sin\phi$$

$$V_{y,ej} = V_\infty \sin\theta \sin\phi$$

$$V_{z,ej} = V_\infty \cos\phi$$

or:

$$\begin{pmatrix} V_{x,ej} \\ V_{y,ej} \\ V_{z,ej} \end{pmatrix} = V_\infty \cdot \begin{pmatrix} \cos\theta \sin\phi \\ \sin\theta \sin\phi \\ \cos\phi \end{pmatrix} \tag{6-2}$$

These vectors are, as discussed above, referred to the plane of the comet orbit. It is more usual to deal with a coordinate system with the ecliptic plane as the reference plane. A transformation from the comet orbit frame to the ecliptic frame is therefore required. This can be given as a combination of three rotations, which are: (i) a z axis rotation through angle ω; (ii) a x axis rotation through angle $I = i$; (iii) a z axis rotation through

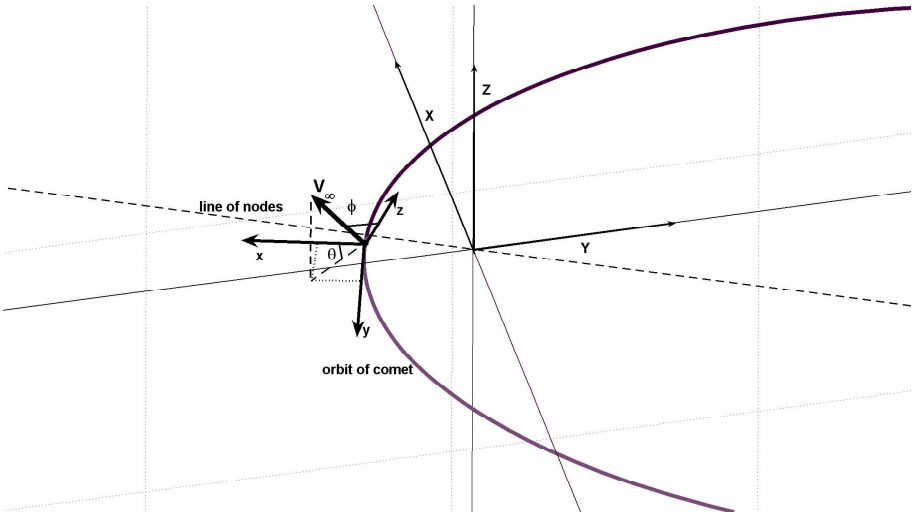

Figure 6.3: *Demonstration of the ejection angles θ and ϕ, with respect to vectors with the reference plane as the ecliptic plane (X, Y and Z) and vectors with the reference plane as the orbital plane of the comet (x, y and z).*

angle Ω. These can be expressed by three rotation matrices:

$$\mathbf{P_1} = \begin{pmatrix} \cos\omega & -\sin\omega & 0 \\ \sin\omega & \cos\omega & 0 \\ 0 & 0 & 1 \end{pmatrix}$$

$$\mathbf{P_2} = \begin{pmatrix} 1 & 0 & 0 \\ 0 & \cos I & -\sin I \\ 0 & \sin I & \cos I \end{pmatrix}$$

$$\mathbf{P_3} = \begin{pmatrix} \cos\Omega & -\sin\Omega & 0 \\ \sin\Omega & \cos\Omega & 0 \\ 0 & 0 & 1 \end{pmatrix}$$

The ecliptic plane referenced coordinates (X, Y, Z) can then be derived from the orbit plane referenced coordinates by:

$$\begin{pmatrix} X \\ Y \\ Z \end{pmatrix} = \mathbf{P_3 P_2 P_1} \begin{pmatrix} x \\ y \\ z \end{pmatrix} \tag{6-3}$$

For completeness, the opposite transformation is given by:

$$\begin{pmatrix} x \\ y \\ z \end{pmatrix} = \mathbf{P_1}^{-1}\mathbf{P_2}^{-1}\mathbf{P_3}^{-1} \begin{pmatrix} X \\ Y \\ Z \end{pmatrix} \tag{6-4}$$

Where $\mathbf{P_1}^{-1}$ is the inverse of $\mathbf{P_1}$, etc.

Thus, knowing the argument of perihelion $\omega = \varpi - \Omega$, the inclination $I = i$ and the longitude of the ascending node Ω for the orbit, a transformation $\mathbf{P} = \mathbf{P_3}\mathbf{P_2}\mathbf{P_1}$ can be constructed. By applying this to the (V_x, V_y, V_z) components of the ejection velocity we can to obtain (V_X, V_Y, V_Z) : the ejection velocity components in a Cartesian coordinate system with the ecliptic plane as the plane of reference.

$$\begin{pmatrix} V_{X,ej} \\ V_{Y,ej} \\ V_{Z,ej} \end{pmatrix} = \mathbf{P_3}\mathbf{P_2}\mathbf{P_1} \begin{pmatrix} V_{x,ej} \\ V_{y,ej} \\ V_{z,ej} \end{pmatrix} \tag{6-5}$$

For a general model with specification of the ejection direction through the angles θ and ϕ (see Figure 6.3), the heliocentric velocity components are thus given by a combination of equations 6-2 and 6-5:

$$\begin{pmatrix} V_{X,ej} \\ V_{Y,ej} \\ V_{Z,ej} \end{pmatrix} = \mathbf{P_3}\mathbf{P_2}\mathbf{P_1} \cdot V_\infty \cdot \begin{pmatrix} \cos\theta \sin\phi \\ \sin\theta \sin\phi \\ \cos\phi \end{pmatrix} \tag{6-6}$$

We choose here to study the angles 0 to 360° in θ and 0 to 180° in ϕ, in 20 degree steps. The expected ejections areas of the comet surface are further addressed in Section 6.11.1. These angles will not provide a uniform distribution of particles, and as a result a correction factor of $\cos(90 - \phi)$ must be applied.

Finally, generalising this model to account for ejection at any given point on the comet's orbit requires specification of the true anomaly ν, or mean longitude λ. This will affect the initial comet position and velocity coordinates. New values for these are found by altering the mean longitude in the orbital elements set before it is converted to Cartesian coordinates. This will also affect the scalar ejection velocity V_∞, which is dependent on $r_h(\nu) = \frac{a(1-e^2)}{1+e\cos\nu}$.

A conversion from true anomaly ν to mean longitude λ is necessary, as the true anomaly is required to determine r_h, and the mean longitude is required to give an input position to HNBody (given in Section 2.1.1). True anomaly values 0° to 340° in steps of 20° are used.

6.5 Additional Considerations

Before proceeding with ejection of particles and study of their resultant dynamics we consider two final issues required for running the model.

In particular, careful placement of Jupiter is necessary when ejecting particles at different positions on the comet orbit. As discussed in Chapter 5, the resonance condition arises when a certain combination of mean longitudes and angles sums to zero: that is, for the 7:2 Jovian resonance, when $\varphi = 7\lambda_J - 2\lambda_P - 5\varpi = 0$. It is shown in Section 5.5.1 that when Jupiter is placed at $\lambda_J = 0$, the width or strength of the resonance varies with the mean longitude of the particle, and that two maxima exist at approximately 158.25° and 338.25°. If a similar strategy is adopted here, holding the position of Jupiter fixed and moving the position of the comet and ejected particles, the effect of the resonance on the particles would vary strongly as a function of mean longitude as a result of simple resonant dynamics. In order to find the maximum effect of the resonance on particles at each point in the orbit, Jupiter is positioned each time so that the location of the comet is a resonant centre. Using the equation $\varphi = 7\lambda_J - 2\lambda_P - 5\varpi = 0$ we find that for each comet mean longitude, there are seven Jupiter mean longitudes that will satisfy this condition. For example, if the comet is at a true anomaly of 160°, then in order to have a resonant centre at this location we can use $\lambda_J = 26.9938°$, 78.4224°, 129.8509°, 181.2795°, 232.70807°, 284.1366° or 335.5652°. The solution closest to the comet mean longitude is used for the mean longitude of Jupiter.

Secondly, only at perihelion will an ejection velocity vector along the y direction represent ejection in the direction of the comet's motion. At all other points the forward motion direction of the comet can be deduced knowing the components of the velocity vector in the x and y directions. These can be calculated from the orbital elements. A conversion from orbital elements to X, Y, Z, V_X, V_Y and V_Z Cartesian coordinates is required, with the ecliptic plane as the reference plane. This can be calculated using standard transformations:

$$X = r_h(\cos\Omega\cos(\omega+\nu) - \sin\Omega\cos(\omega+\nu)\cos i)$$

$$Y = r_h(\sin\Omega\cos(\omega+\nu) + \cos\Omega\sin(\omega+\nu)\cos i)$$

$$Z = r_h(\sin(\omega+\nu)\sin i)$$

$$V_X = \frac{Xhe}{r_h p}\sin\nu - \frac{h}{r_h}(\cos\Omega\sin(\omega+\nu) + \sin\Omega\cos(\omega+\nu)\cos i)$$

$$V_Y = \frac{Yhe}{r_h p}\sin\nu - \frac{h}{r_h}(\sin\Omega\sin(\omega+\nu) - \cos\Omega\cos(\omega+\nu)\cos i)$$

$$V_Z = \frac{Zhe}{r_h p}\sin\nu + \frac{h}{r_h}(\cos(\omega+\nu)\sin i)$$

where $r_h = \frac{a(1-e^2)}{1+e\cos\nu}$, $p = a(1-e^2)$ and $h = (\mu a(1-e^2))^{1/2}$. Here we expect $V = \sqrt{V_X^2 + V_Y^2 + V_Z^2}$ should equal $V = \sqrt{\mu(\frac{2}{r} - \frac{1}{a})}$. The conversion from ecliptic plane referenced coordinates to orbit plane referenced coordinates (equation 6-4) is then applied to the heliocentric velocity components, producing velocity coordinates V_x, V_y and V_z in the orbital plane.

The angle between the comet's velocity and the positive x direction is now determined. The angle α between the V_x and V_y components is calculated using simple right-angle trigonometry. Using knowledge of whether V_x and V_y are positive or negative the required angle is then found. These angles, as a function of the true anomaly, are shown in Figure 6.4. These comet velocity directions are important as they correspond to the directions of maximum velocity for the ejected particles, and therefore indicate where the maximum variation of the particle orbits from the comet orbit occurs (along with the corresponding opposite ejection direction in angle θ).

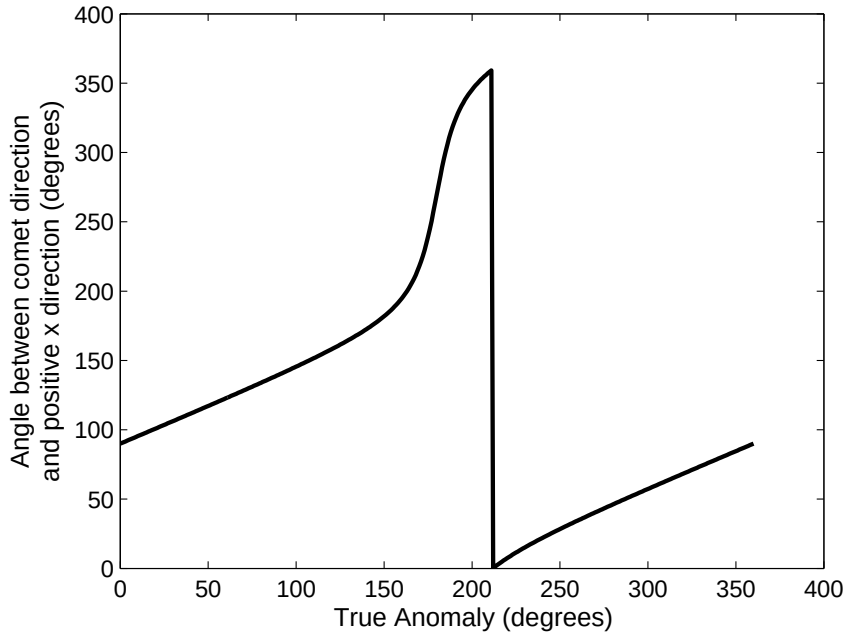

Figure 6.4: *Variation of the angles between the comet velocity vector and x direction as a function of true anomaly.*

6.6 Combined Model for the Ejection of Cometary Particles

Here we assemble of the components required to integrate the motion of a particles ejected from a model comet. We required two elements: the initial comet and Jupiter position and velocity components in Cartesian coordinates; and the ejection velocity components, also in Cartesian coordinates. The former is obtained by conversion from orbital elements given in Tables 6.1 and 6.2, using HNBody in the manner described in Section 6.3. The ejection velocity components are given by equation 6-6, using equation 6-1 to determine the scalar velocity V_∞.

We use particle radius values s in the range 100 μm to 700 μm (the size range of CMOR particles). The radius to mass conversion is achieved assuming a spherical particle of density $\rho = 2500$ kgm^{-3} or 1000 kgm^{-3}. The resulting mass is divided by the solar mass $M_\odot$ to give mass in units of solar masses, as required by HNBody. HNBody is used to integrate each ejected meteoroid for 500 years, with (Cartesian) input parameters mass (in units $M_\odot$), X_{com}, Y_{com},Z_{com}, $V_{X,com}$+$V_{X,ej}$, $V_{Y,com}$+$V_{Y,ej}$, $V_{Z,com}$+$V_{Z,ej}$. We find it is most convenient to choose orbital element outputs for HNBody. We thus input each particle as an object at the location of comet, but with a slightly variant velocity; and from the orbital element output can deduce the particle's subsequent orbit, and follow its dynamical behaviour. The 500 year time period is short to reduce computation time, but is sufficient to determine whether the particle is exhibiting resonance behaviour.

Our primary objective is to know if each ejected particle achieves a resonant orbit. This is determined using the resonant argument, as discussed in Section 5.3. We calculate the resonant argument $\varphi = 7\lambda_J - 2\lambda_P - 5\varpi_P = 0$ for each particle for each timestep. Particles for which the variations in resonant argument (with time) are less than 360° are considered resonant. In practice, 354° is used in order to limit false positives generated by cases that are clearly circulating rather than librating: this can be a consequence of the finite timesteps. The choice of 354° as a cut off point is subjective, and is based on surveying a representative fraction of the data. It is out of concern for the possibility of false negatives that this cut-off is not set lower.

For each HNBody run, we automatically eject 614 particles that cover θ from 0 to 360° and ϕ from 0 to 180°, both in 20° intervals. This would provide 703 directions, but this is reduced to 614 when redundant (repeated) angles are removed. Once we have determined which particles are in resonance using the variation in the resonant argument (the libration amplitude), it is possible to produce a map of ejection directions that result in capture of the particle in the resonance. The number of particles that enter resonant motion can also be summed to calculate the percentage of the 614 particles that successfully reach resonance.

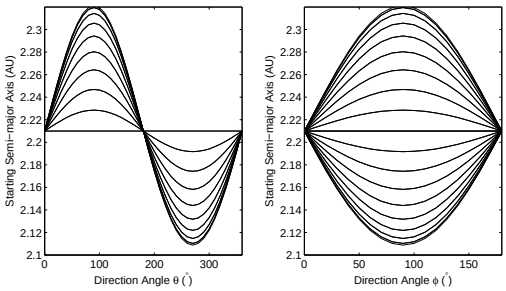

(a)

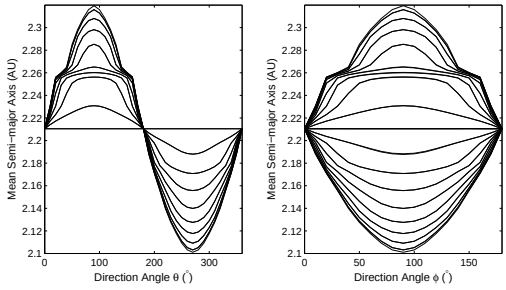

(b)

Figure 6.5: *Variation in the (a) starting semi-major axis and (b) mean semi-major axis with θ and ϕ, for ejection of a 100 μm particle at perihelion by Comet 1. Each curve represents a different ϕ value (for graph one) or θ value (for graph two).*

This approach will concentrate particles to the poles when compared with uniformly spaced ejection directions from the comet surface. As a consequence of this non-uniform distribution of ejection angles, the number of particles at each angle ϕ is multiplied by $\cos(90 - \phi)$. The resulting percentages can be compared when this process is repeated at a number of mean longitudes, particles radii and particle densities. The chance of false positives (or negatives) in the automatic determination of the resonant status of the particles is expected to contribute a maximum uncertainty in the number of particles in resonant of ± 8 of the 614 particles ($\sim 1.3\%$). Other uncertainties in input parameters will produce much larger overall uncertainties (see Section 6.12).

6.7 Ejection of Particles at Perihelion

6.7.1 Comet 1: 2P/Encke

As an illustration, we analyse the results for ejection of 100 μm particles in 614 directions at perihelion, for all three model comets. We first examine various semi-major axis distributions to demonstrate the effect of the resonance. The starting semi-major axis should be a smooth function of θ and ϕ, as it is directly related to the velocity of the particle: this is demonstrated in Figure 6.5 (a). We see a broad sine function shape, with

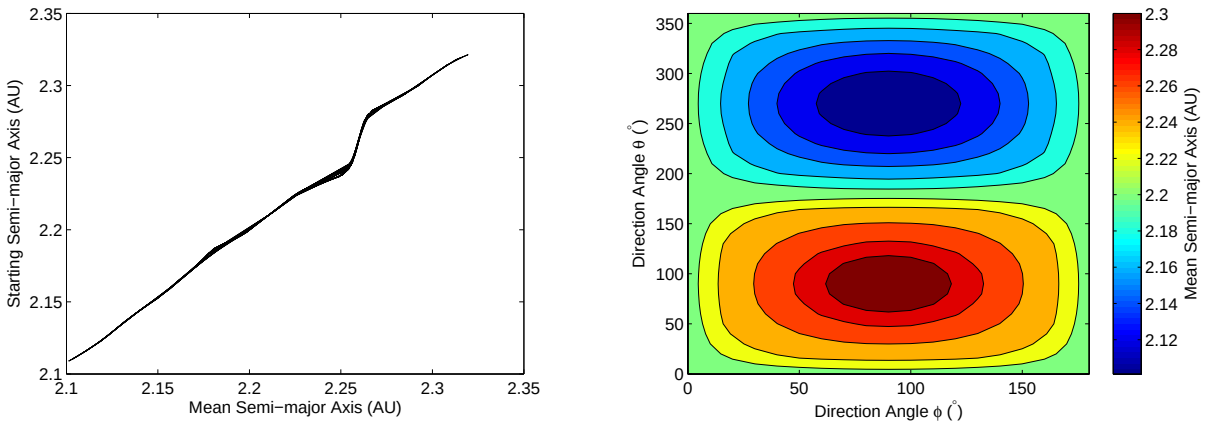

(a) (b)

Figure 6.6: *(a):The mean semi-major axis against the starting semi-major axis: deviations from a straight line of gradient equal to one indicate the presence of resonances. (b):Contour plot of the mean semi-major axis of the final orbit for each ejection velocity direction, given by the angles θ and ϕ .*

the maximum in the comet forward velocity direction ($\theta = 90°$ at perihelion: see Figure 6.4) and minimum in the opposite θ direction. This shape is expected as a result of the vector addition of the comet forward velocity and the ejection velocity.

The mean semi-major axis demonstrates the location of the resonance. The mean semi-major axis is different to the starting semi-major axis for particles that are trapped in a resonance. For non-resonant particles the mean is approximately equal to the starting semi-major axis. However, resonant particles will undergo resonant oscillations around the resonant centre and thus their mean value will be equal to the location of the resonant centre. The variations in the mean semi-major axis over 500 years as functions of the angles θ and ϕ are seen in Figure 6.5 (b). The presence of resonances is demonstrated by deviations from a smooth sine curve and, in particular, by the indents at approximately 2.26 AU as a result of the 7:2 resonance: this is where the mean value for these (resonant) particles changes from the starting values to the resonant centre value. It is possible that the features seen at approximately 2.18 AU are indicative of the presence of the 11:3 Jovian resonance.

Figure 6.6(a) shows directly the variation between the starting semi-major axis and the mean semi-major axis for each particle. The deviation in the straight line at 2.25 AU demonstrates that these particles have a depressed mean semi-major axis due to the resonant-centre oscillations induced by the resonance. Figure 6.6 (b) shows more clearly the variations in mean semi-major axis for each θ and ϕ.

We now select particles that are exhibiting resonant behaviour. This is achieved using the method given in Section 6.6: by determining whether the variation in the

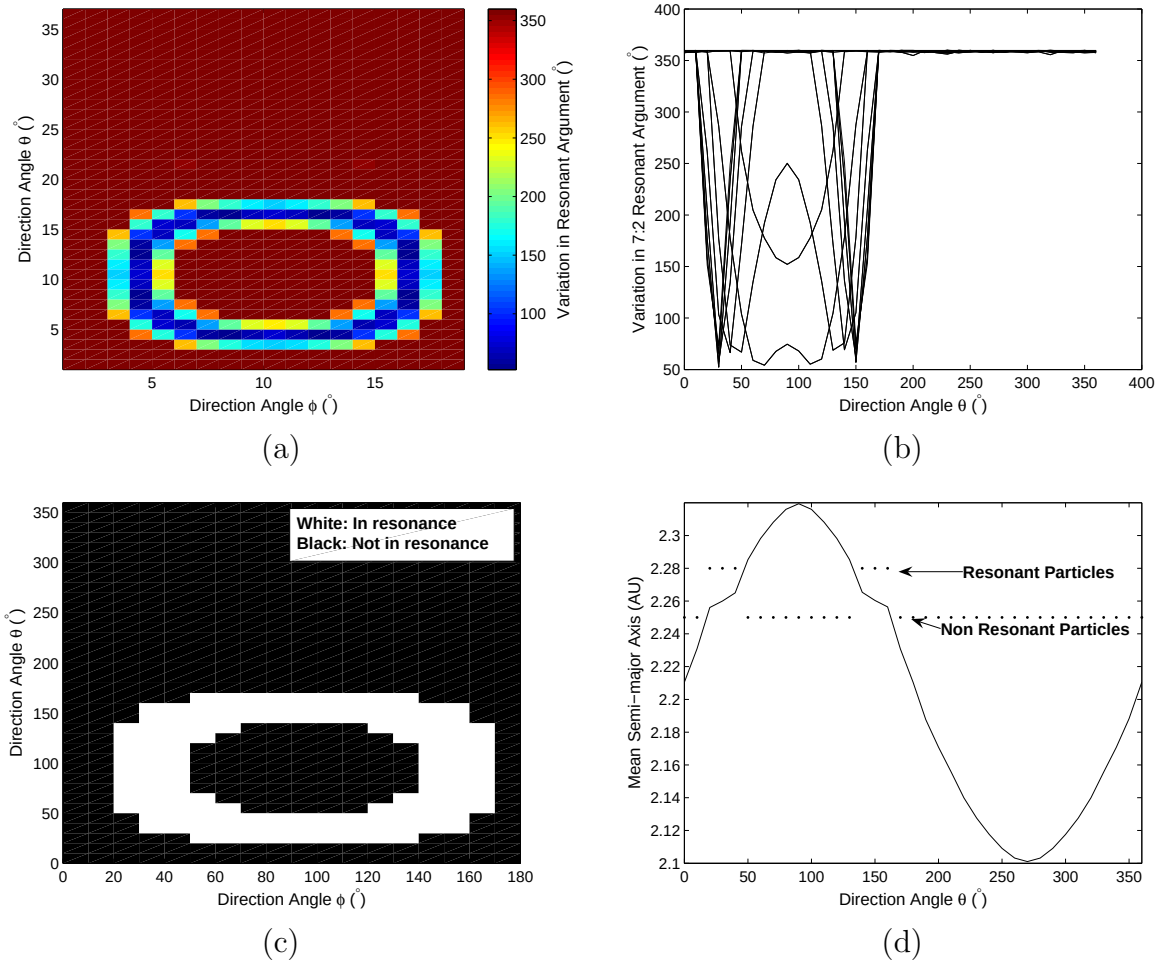

Figure 6.7: *(a):Contour plot of the maximum variation in the resonant argument over* 500 *years for each ejection velocity direction given by the angles* θ *and* ϕ *(b):The maximum variations in resonant argument of each orbit, against* θ*. (c):Contour plot demonstrating the ejection directions of resonant particles ejected at perihelion (d):The mean semi-major axis distribution with direction angle* θ *with* $\phi = 90°$*. The superimposed dots represent whether the particles at each* θ *are inside or outside of resonance (with the higher dots representing resonance particles as indicated on the figure). We observe that the deviations in the mean semi-major axis distribution do indeed represent regions where the particles are in resonance.*

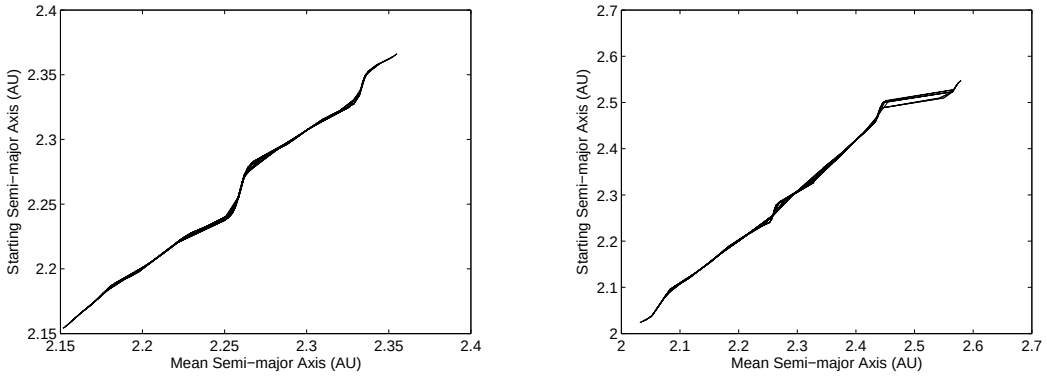

(a) (b)

Figure 6.8: *Mean semi-major axis as a function of the starting semi-major axis, for (a) Comet 2 (2P/Encke displaced to a proto-Encke orbit) and (b) Comet 3 (proto-Encke)*

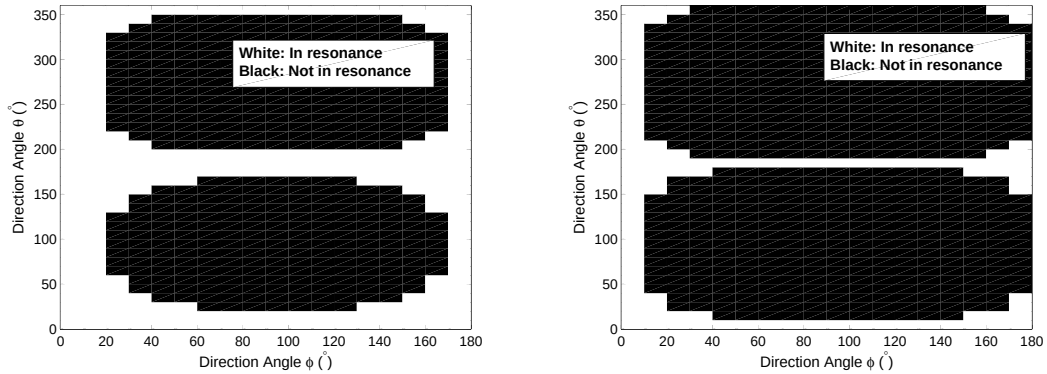

(a) (b)

Figure 6.9: *Resonant particles, for each θ and ϕ, for (a) Comet 2 (2P/Encke displaced to a proto-Encke orbit) and (b) Comet 3 (proto-Encke)*

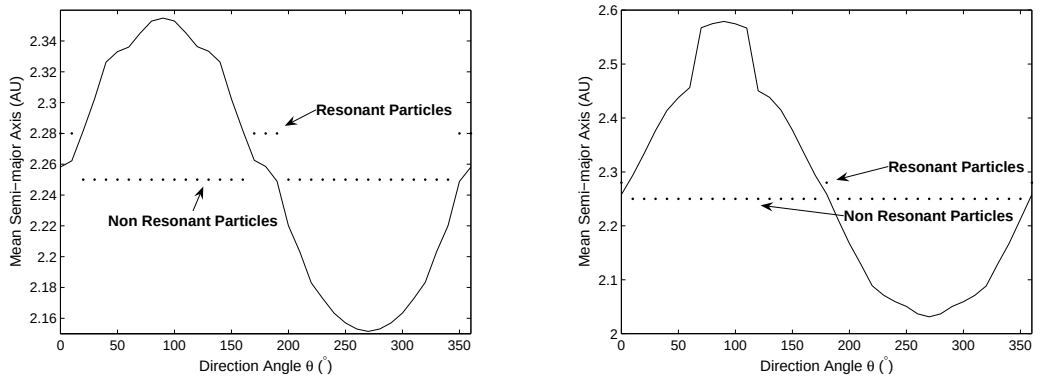

(a) (b)

Figure 6.10: *Mean semi-major axis as a function of θ, with information on which particles are resonant given by dots, for (a) Comet 2 (2P/Encke displaced to a proto-Encke orbit) and (b) Comet 3 (proto-Encke). Note that deviations caused by other Jovian resonances are visible.*

resonant argument is limited to less than 360°. However, 354° is used to limit false positives). The variations in the resonant argument for each particle ejection direction are shown in Figure 6.7(a); and the variations as a function of θ in Figure 6.7(b). In Figure 6.7(c) the contour plot of Figure 6.7(a) is repeated, but in this resonant particles are marked in white; non-resonant particles are shown in black. Finally, we check whether this selection of resonant particles matches with the deviations observed in Figure 6.6(b) (with ϕ equal to 90°): Figure 6.7(d) shows that this is indeed the case. In total, 23% of 100 μm particles ejected from Comet 2P/Encke at perihelion are trapped in resonance. Since Comet 2P/Encke (Comet 1) orbits interior to the resonance, the particles that are trapped in resonance are only those emitted in the comet forward direction, and that therefore assume more distant orbits to that of the comet.

6.7.2 Comets 2 and 3: Displaced Encke and Proto-Encke

We now present the results for the remaining two comets, also at perihelion, and for 100 μm particles. These are seen in Figures 6.8, 6.9 and 6.10. Both comets orbit in the proposed position of proto-Encke, but with different masses. These orbits start within the resonance so particles ejected in both forward and backward directions (relative to the comet velocity direction) are able to populate the resonance. The resulting distribution of resonant particles is symmetric in θ and ϕ. The heavier comet (Comet 3) produces particles with higher ejection velocities, the majority of which are too energetic to be trapped in a resonance close to the comet. Thus while 24% of particles ejected by Comet 2 are trapped in resonance, only 8% of Comet 3 particles are trapped.

6.8 The Effect of Meteoroid Mass on the Percentage of Particles Trapped in Resonance

The process of Section 6.7 is now repeated with different particle radii (or masses). We choose radii of 50 μm to 1000 μm, in steps of 50 μm, as we expect radar-detected meteoroids to fall within this range. This choice is justified using distribution of masses of CMOR Taurid particles (given in Figure 6.11 (a)). These masses are determined from observable quantities using a relationship between mass, velocity, magnitude and electron line density for radio meteors determined by Verniani (1973) (see Brown et al. (2008)). The masses can be converted to radii by making an assumption on the density of the observed particles. The corresponding radius distributions for densities of 2500 kgm^{-3} and 1000 kgm^{-3} are shown in Figure 6.11 (b). The range of radii is approximately 100 μm to 600 μm for $\rho = 2500$ kgm^{-3}, and 200 μm to 800 μm for $\rho = 1000$ kgm^{-3}.

The percentage of ejected meteoroids trapped in resonance as a function of particle

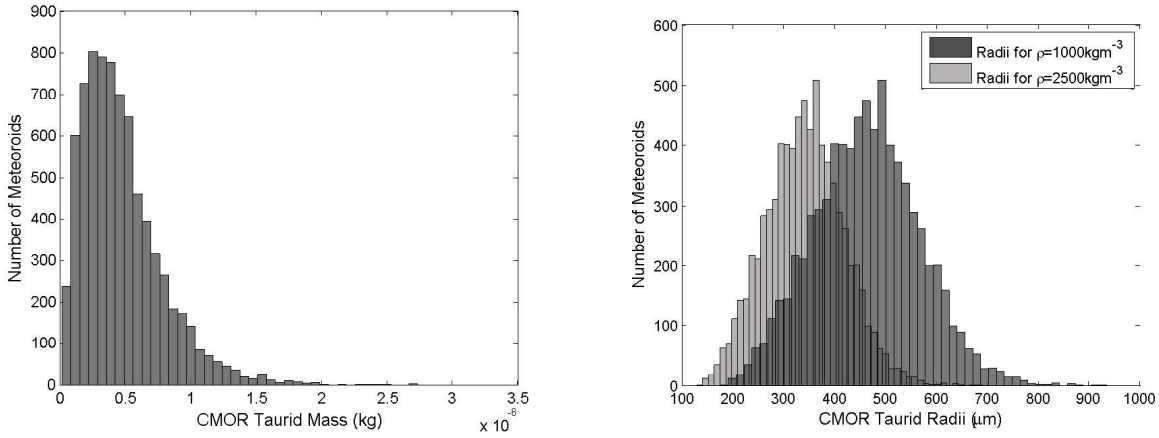

(a) (b)

Figure 6.11: *(a) Distribution of the masses of CMOR Taurids. (b) Distribution of the radii of CMOR Taurids, for densities* 2500 kgm^{-3} *and* 1000 kgm^{-3}.

radius is seen in Figure 6.12. This is given for all three model comets, at particle densities of 2500 kgm^{-3} and 1000 kgm^{-3}. Increasing particle size is accompanied by a decrease in ejection velocity. For Comets 2 and 3, this means that an increasing number of particles stay sufficiently close to resonance to be captured: hence the percentage of trapped meteoroids is a strictly increasing function of radius. However, as Comet 1 is not directly in the resonance, many particles of low radii reach orbits beyond the resonance as their total velocity after ejection is too high, and only a small fraction are trapped. As the particle radius increases, more particles have the correct velocity for resonant orbits to occur. With even larger values of radius, most particles are not able to reach the position of the resonance, as their orbits are increasingly close to that of their comet. Thus, for Comet 1 an initial increase in the percentage of trapped particles is seen for smaller particles, while at large particle masses the capture percentage decreases with mass.

We now convert the scale on Figure 6.12 from radius (in μm) to mass (in kg), and limit the scale to values less than 2×10^{-6} kg (see Figure 6.11 (a)): the result is shown in Figure 6.13. We will extend this to visual meteoroid masses in Section 6.15

6.9 The Effect of Density on Percentage of Particles Trapped in Resonance

It can be seen from the results of Section 6.8 that the density of the ejected particles can significantly affect their final orbits. This is due to the $\rho^{-\frac{1}{3}}$ dependence of the ejection velocity model used. Here we show the variations possible in the captured percentage of 100 μm particles ejected at perihelion for densities between 800 kgm^{-3} and 2700 kgm^{-3}.

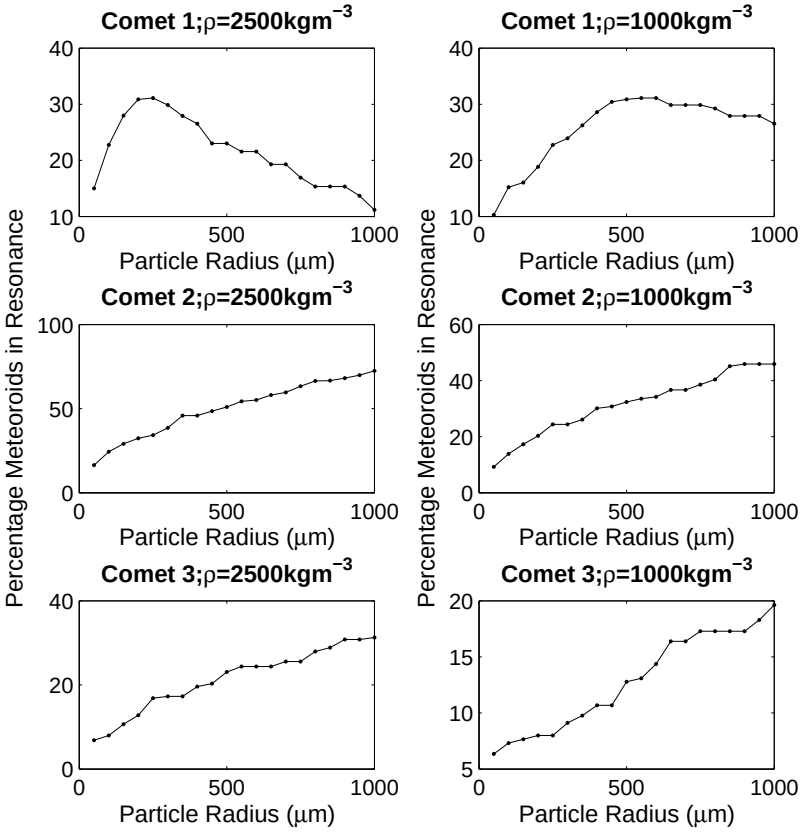

Figure 6.12: *The variation in the percentage of ejected meteoroids trapped in resonance as a function of particle radius, shown for all three comets, for two different particle densities.*

Over this choice of realistic densities for Taurid meteoroids, the percentage of particles in resonance increases with density. The percentage variations over the whole region (normalised to the result at 2700 kgm^{-3}) are 45% for Comet 1, 55% for Comet 2 and 31% percent for Comet 3. We conclude that the density can affect the percentage of particles that are captured by the resonance by up to $\sim 60\%$.

6.10 Variation of Resonant Trapping with True Anomaly

We expect the percentage of particles that enter the 7:2 resonance to vary with the position of ejection on the comet's orbit, and thus with true anomaly ν. This is due to the variations with heliocentric distance of solar radiation and thus of comet temperatures. Such variations are accounted for by the heliocentric distance dependence of the ejection velocity. The effect of the resonance will also change with true anomaly as a result of the

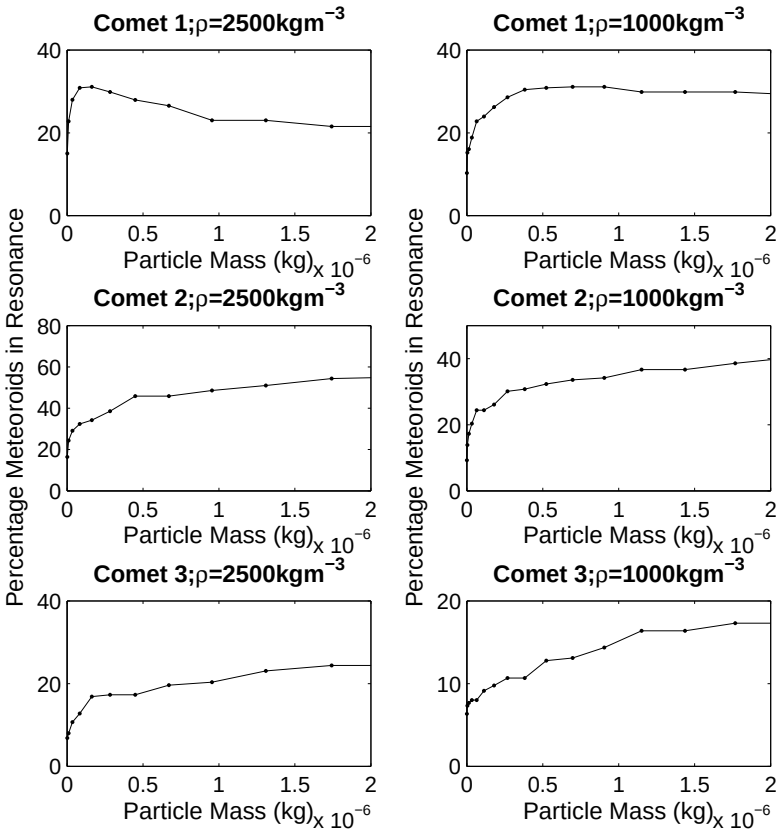

Figure 6.13: *The variation in the percentage of ejected meteoroids trapped in resonance as a function of particle mass, shown for all three comets, for two different particle densities.*

variation in the location of Jupiter. This effect, however, is removed by careful selection of the mean longitude of Jupiter at each point (see Section 6.5). For all three model comets the variation in the percentage of trapped particles is examined for (a) 100 μm radius particles of density 2500 kgm^{-3}; (b) 600 μm radius particles of density 2500 kgm^{-3}; and (c) 100 μm particles of density 1000 kgm^{-3}. A full range of true anomaly values 0 to 360° are tested, in steps of 20°. In general, however, we expect ejection of particles to occur only for heliocentric distances $r_h <\sim 3$ AU, this being the region within which sublimation of water ice can occur (though sublimation of other ices may produce a small effect beyond this point). This is further addressed in Section 6.11.2. The results are shown in Figures 6.15, 6.16 and 6.17.

The behaviour illustrated by these figures is as expected. For Comet 1 (a model Comet 2P/Encke) near perihelion ($\nu = 0$, $r_h = 0.3315$AU, $\lambda_P = 160.99°$) between 10% and 20% of particles are captured in resonance. As this comet is not within the resonance, these are particles that have sufficient ejection velocity to reach an orbit that is resonant.

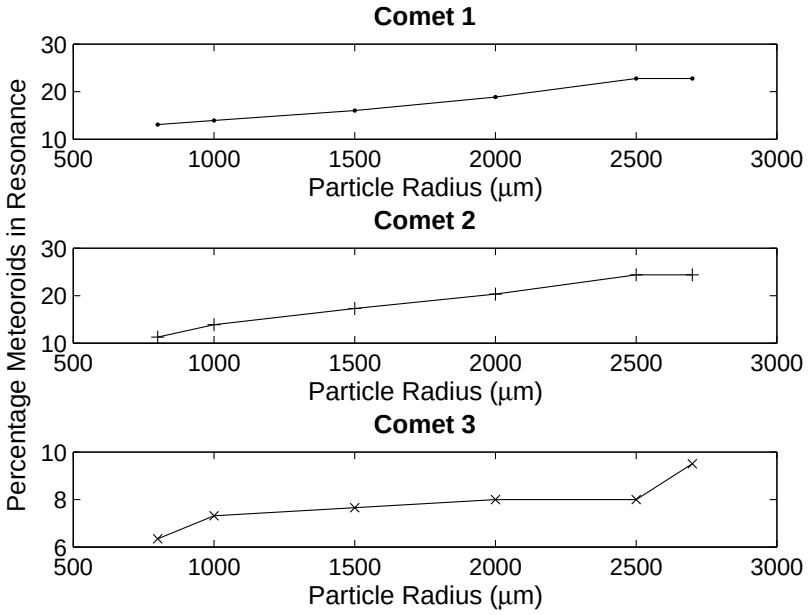

Figure 6.14: *The variation in the percentage of ejected meteoroids trapped in resonance as a function of particle density, for all three comets.*

As the comet moves beyond perihelion, a small increase in the capture percentage may be expected if there is a significant proportion at perihelion that reach orbits beyond the resonance: their velocities drop with increasing distance from the Sun, and they are eventually trapped in the resonance. Once the ejection velocity has dropped further (with increasing heliocentric distance), however, fewer particles are able to reach the resonant orbit, and the numbers trapped decline sharply to zero. We see, as expected, symmetrical behaviour as the comet re-approaches perihelion. Comet 1 is only able to inject particles into the resonance in the inner part of the orbit, within ~ 2 AU. The 600 μm particles have the lowest ejection velocities and therefore mostly have orbits close to the (non-resonant) Comet 2P/Encke, which cannot reach resonance: hence the lowest numbers of resonant particles are seen. For 100 μm particles, we expect those of density 1000 kgm^{-3} to have the highest velocities. Relatively low numbers of trapped particles are seen at perihelion, however, because of a significant number of particles reaching orbits beyond the resonance: that is, orbits with semi-major axes higher than the semi-major axis of the resonant centre. These numbers recover as the ejection velocity decreases with increasing heliocentric distance, and surpass the numbers for 2500 kgm^{-3} particles at around $\nu = 90°$.

Comets 2 and 3 display similar behaviour, except that particles from Comet 3 have higher ejection velocities (because of the higher comet mass) and therefore more

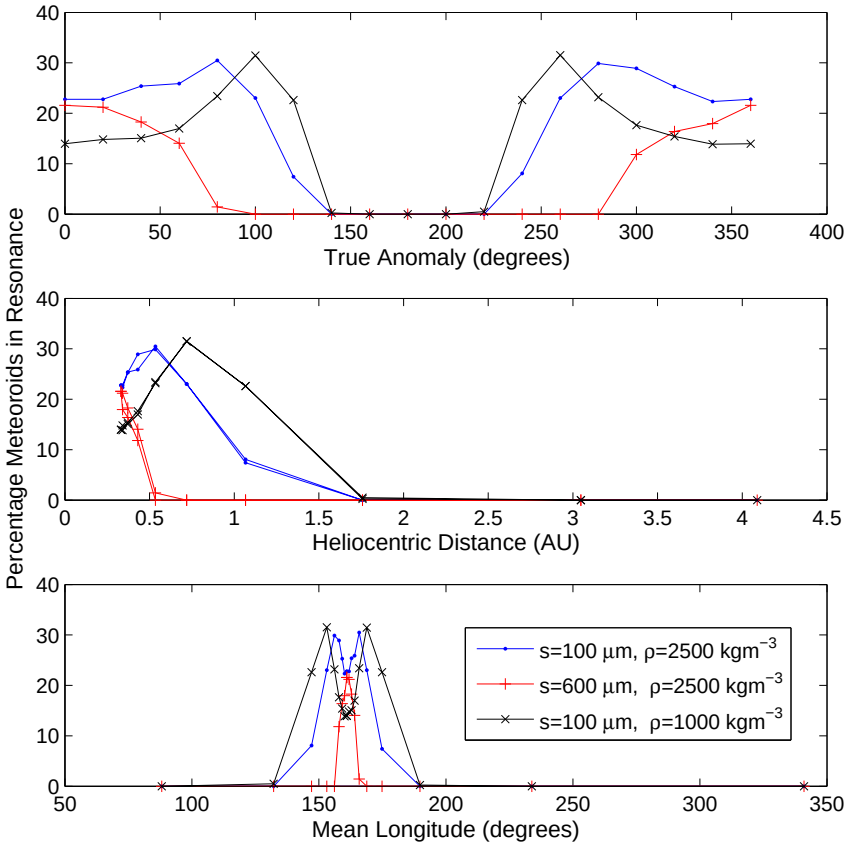

Figure 6.15: *Variation in the percentage of ejected meteoroids trapped in resonance for Comet* 1 *as a function of true anomaly, heliocentric distance and mean longitude (all of which are related measures of the position on the comet orbit).*

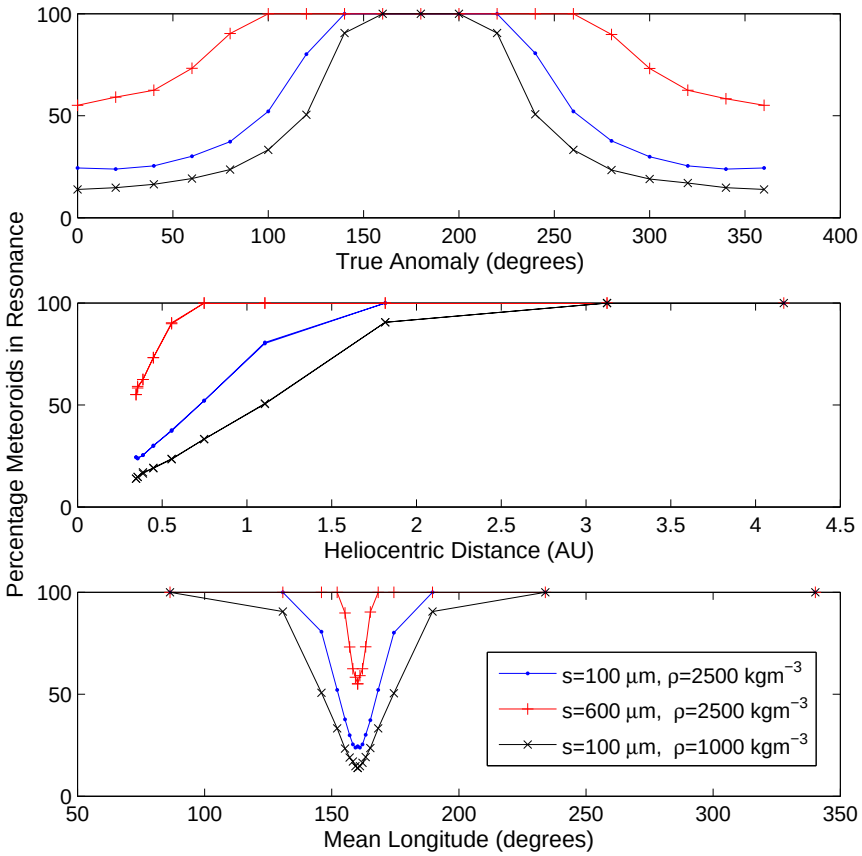

Figure 6.16: *The variation in the percentage of ejected meteoroids trapped in resonance for Comet 2 as a function of true anomaly, heliocentric distance and mean longitude (all of which are related measures of the position on the comet orbit).*

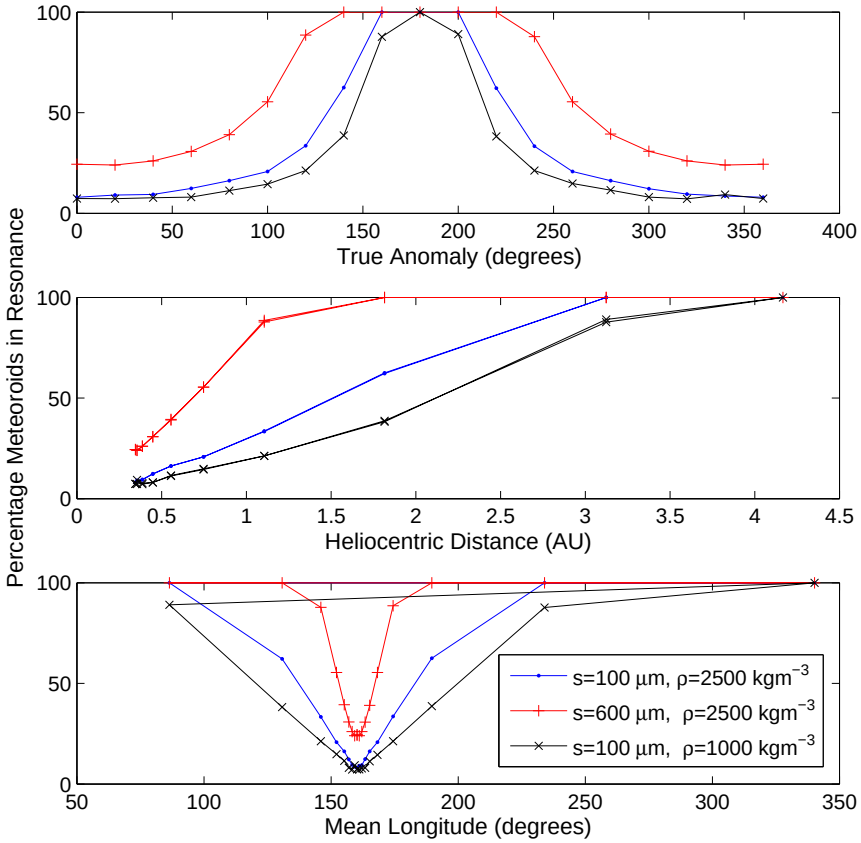

Figure 6.17: *The variation in the percentage of ejected meteoroids trapped in resonance for Comet* 3 *as a function of true anomaly, heliocentric distance and mean longitude (all of which are related measures of the position on the comet orbit).*

easily exit the resonance region near the comet. Trapped particle numbers are therefore lower for Comet 3 than for Comet 2. For both comets the number of trapped particles increases approaching aphelion, and decreases approaching perihelion. This is the result of decreasing ejection velocity with increasing heliocentric distance, which causes increasing numbers to be trapped in the near-comet resonance. All tests reach a point in the outer orbit where all ejected particles are trapped in the resonance. As expected, the slower 600 μm particles have higher capture percentages. The 1000 kgm^{-3} particles with 100 μm radii are faster as they are effectively lighter (though the density also affects the ejection velocity directly): thus these particles are less easily captured by the resonance. This is more important for Comet 2 (a 2P/Encke-sized comet) than for the larger proto-Encke Comet 3. As expected, capture of particles in a resonance is significantly easier for particles ejected from a resonant comet.

6.11 Details of Cometary Dust Ejection

Our model above assumes dust emission from the entire cometary surface, with uniform ejection of dust over the comet orbit. There are several reasons why this is a poor description of the behaviour of the ejected dust.

6.11.1 Ejection Areas on the Comet Surface

We first consider the ejection area of the cometary surface. There are two areas of interest here: whether ejection occurs only on the sunlit side of the comet, or on some fraction of the dark side also; and whether ejection occurs only from discrete regions of the comet, as 'jets' of activity.

Understanding whether ejection of dust is able to occur on the dark side of the comet depends on the temperature profile of the comet, which depends on the rotation speed of the comet nucleus and the thermal inertia of the comet surface. Light curves have been used to derive a variety of rotation periods for the nucleus of Comet 2P/Encke. Luu and Jewitt (1990) find 15.08 hours and Fernández et al. (2000) find 15.2 ± 0.3 hours for the rotation period of nucleus of Comet 2P/Encke; however, Fernández et al. (2005) find $P = 11.079 \pm 0.009$ hours (or $2P = 22.159 \pm 0.012$ hours). The thermal inertia Γ is not known for Comet Encke. Fernández et al. (2000) show that, using a rotation period of 15.2 hours, if Comet Encke has a thermal inertia similar to that of the moon ($\Gamma = 50$ JK^{-1}m^{-2}s$^{-1/2}$) it would be classed as a (moderately) slow rotator. However, if instead it has a thermal inertia similar to the surface of (3200) Phaethon (presumed to be an extinct comet) ($\Gamma = 320$) it would fall somewhere near the border between a fast and slow rotator. They thus conclude that a slow rotator thermal model that results in a

symmetrical temperature distribution centred on the subsolar point is a sufficient (but not perfect) model for Comet 2P/Encke. Further information on the thermal inertia of Comet Encke is required for a more satisfactory conclusion. For meteoroid stream modelling it is often assumed that only the sunlit side of the comet is able to eject significant numbers of particles (such as Vaubaillon et al. (2005)).

A complicating factor is that Comet Encke is thought to eject particles in discrete jets. Sekanina (1988) first proposed such a model, which also included the rotation of the nucleus, to explain the observed asymmetry in Comet Encke's outgassing. In this model the two jets were located at latitudes of $-75°$ and $+55°$, with a pole position of $RA = 206°$ and $Dec = +3°$. However, Reach (2000) were able to produce similar (an observationally supported) results using a model with only one jet at latitude $-15°$, with a pole position of $RA = 102.8°$ and $Dec = +32.6°$. Interestingly, this then creates a situation where the jet is on the dark side of the comet through perihelion. The jet is thus not able to eject particles through the inner part of the comet orbit, turning off ~ 30 days before perihelion, and turning on ~ 25 days after perihelion. In the model of Ferrín (2008), however, two jets - one near the south pole, the other near the north pole - are located such that one is active through perihelion, and the other near aphelion. This also assists in accounting for the significant level of activity that Comet Encke exhibits at aphelion (Ferrín, 2008) (Belton et al., 2005) (though they find the coma is observationally unresolvable).

In addition, it is expected that the active surface area of Comet Encke is small. A'Hearn et al. (1995) find an active surface area for Comet Encke of 0.72km^2: if we assume a comet radius of 2.4 km, we find that this is equivalent to the active area comprising $\sim 1\%$ of the comet surface area. Jenniskens (2006) quotes 5% of Comet Encke's surface being active.

Thus, we expect that only discrete areas of the comet, amounting to $\lesssim 5\%$ of the comet's surface, are able to eject particles. Unless comet Encke has a high thermal inertia, it is also unlikely that these 'jets' will eject significant amounts of dust unless they are on the sunlit side of the comet, at each point in its orbit. In our coordinate system, the sunward side is given by the angles $\theta = \nu + 90°$ to $\theta = \nu + 270°$, and $\phi = 0$ to $\phi = 180°$.

6.11.2 Variation in Dust Output with Heliocentric Distance

The variation in the dust output of Comet 2P/Encke with heliocentric distance is governed by the temperature decrease suffered by the comet with increasing heliocentric distance, and by the location and orientation of the jets with respect to the Sun.

General empirical expressions can be formulated to describe the dust release rates with heliocentric distance. These use H_2O release rates determined from observed visual

magnitudes of the comet. The assumption is that water vapour is the major component of the ice of Comet 2P/Encke: indeed, there is no present detection of CO or CO_2 associated with Comet Encke. Sanzovo et al. (2001) use water release rates for $r_h < 2.5$ AU to derive a relationship for the dust rate with heliocentric distance of $q_d \propto r^{-n}$ where n varies for each comet return for which data exist: $n = 3.94$ for 1977; $n = 3.0$ for 1980; $n = 2.3$ for 1984; $n = 2.9$ for 1990. We average these to obtain $q_d \propto r^{-3.0}$. This gives a dust production rate that drops to below 1% of the value at perihelion at $r_h = 1.57$AU (see Figure 6.18). Thus, such a model is not able to account for the observed aphelion outgassing. However, we expect the dust released at aphelion to represent only a small fraction of the total dust released (the secular light curve given in Ferrín (2008) supports this conclusion).

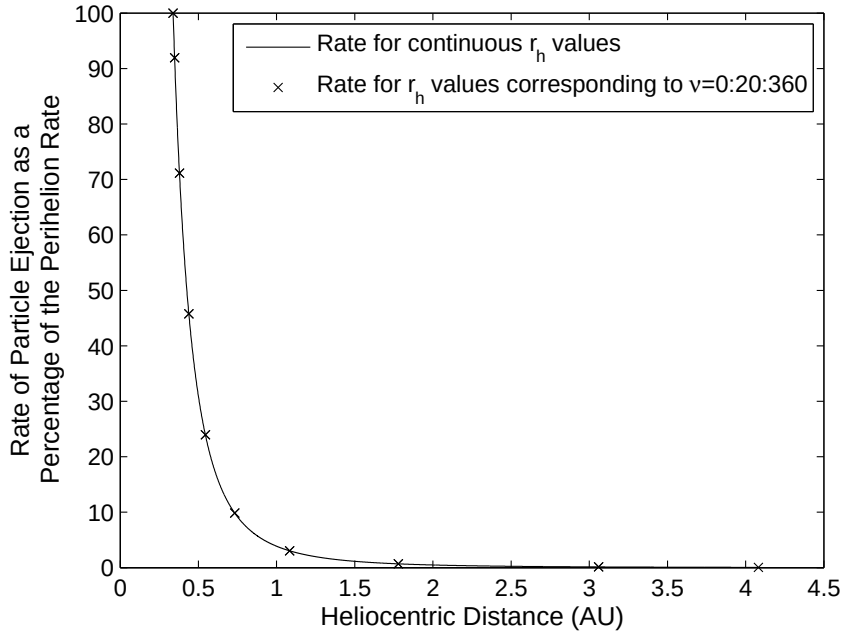

Figure 6.18: *The particle ejection rate for comet 2P/Encke, as derived from water production rate observations Sanzovo et al. (2001). The percentage ejection rates are relative to that at perihelion. Crosses demonstrate the ejection rates for particles at the true anomaly values tested in Section 6.10.*

In terms of the dust output, the majority of outgassing of Comet 2P/Encke occurs ~ 200 days around perihelion, with the majority of the dust ejected between 10 days before perihelion and 30 days after (equivalent to $\nu = 303.69°$ to $\nu = 102.99°$) (Jenniskens, 2006). However, Comet Encke also displays aphelion activity (Fernández et al., 2005). Ferrín (2008) finds that the first source is active from 87 ± 5 days before perihelion to 94 ± 15 days after perihelion ($\nu = 234°$ to $\nu = 138°$), and the second source is active from 160 ± 25 days after perihelion to 243 ± 15 days before perihelion ($\nu = 150°$ to $\nu = 201°$). Though

it is often assumed that water ice is not able to undergo significant sublimation beyond ~ 3 AU, this may not be the case. Meech and Svoren (2004) summarize research that suggests water ice sublimation processes are able to eject particles out to heliocentric distances of 5 to 6 AU. Given that the level of activity at aphelion is not well known, and should be significantly lower than that at perihelion, we proceed in the assumption that the relationship for the dust rate with heliocentric distance of $q_d \propto r^{-3.0}$ is sufficiently accurate. In our case this gives us ejection of particles from $\nu = 225°$ to $\nu = 135°$ (roughly equivalent to the outgassing region of the first source used by Ferrín (2008)).

6.11.3 Variation in Capture Percentages with the Relative Mean Longitude of Jupiter

The resulting capture percentages are maximum possible values, as they assume Jupiter is in an optimal mean longitude position. The true values at each comet location will vary with Jupiter's mean longitude approximately as a sine function, with a minimum of zero percent trapped particles. Accounting for this in a robust manner would involve integrating the comet orbit for many revolutions and ejecting particles at each location within the outgassing regions. This is beyond the scope of the present work.

6.12 Uncertainties

We here attempt to account for the variety of uncertainties that exist in the method. This is achieved by determining 'high' and 'low' values of the ejection velocity, and using these to determine minimum and maximum percentages of trapped particles. In order to determine these maximal ejection velocities, we must understand the uncertainties in each parameter in the ejection velocity equation (equation 6-1):

1. **The constant** 32.3**:** This constant encompasses information on various properties, including temperature. Values given in the literature fluctuate about ± 10 of this value. We use this as an approximate uncertainty in this constant.

2. **Comet Radius** R_c**:** The radius we use for Comet 2P/Encke, with the uncertainty as given by Fernández et al. (2000), is $R_c = 2.4 \pm 0.3$ km. This is dependent on the assumption that the Standard Thermal Model holds (essentially that the comet acts as a slow rotator). Furthermore, other studies have found a wide range of radius values. For example, Tancredi et al. (2006) find $1.95^{+1.96}_{-0.67}$ km while Luu and Jewitt (1990) find 3.28 ± 0.06 km. In the light of this we use an uncertainty ± 1 km. For Comet 3 (proto-Encke) 14.4 ± 5 km is used, to reflect the lack of knowledge on this proposed comet.

3. **Density ρ:** As discussed above, the density of Taurid/Encke stream particles is highly uncertain: we use 800 kgm^{-3} as a minimum and 2500 kgm^{-3} as a maximum.

4. **Heliocentric Distance Dependence r_h^{-x}:** There is some level of uncertainty as to the dependency of the ejection velocity on heliocentric distance. Simple models give $r_h^{-1.038}$, while some observations support $r_h^{-0.5}$: we will here compare results from both dependencies.

In addition, there will be uncertainty in the automatic selection of resonant captured particles. This is not dealt with in this section, but this error should not exceed ± 8 particles. As such, this error is small compared with other uncertainties.

Initially, a 'low velocity' and a 'high velocity' are created. For the low velocity we use $R_c = 1.4$ km, $r_h^{-0.5}$, $\rho = 2500$ kgm^{-3} and a constant of 22.3. For the high velocity we use $R_c = 3.4$ km, $r_h^{-1.038}$, $\rho = 800$ kgm^{-3} and a constant of 42.3. For Comet 3 (proto-Encke) we instead use 14.4 ± 5 km for the comet radius. 100 μm particles are ejected in 614 directions at perihelion ($\nu = 0$) at the low velocity and the high velocity, for all three comets. The results are presented in Table 6.4

Velocity	**Comet** 1	**Comet** 2	**Comet** 3
V_{high} ($\rho = 800$ kgm^{-3})	2%	7%	7%
V_{high} ($\rho = 2500$ kgm^{-3})	9%	8%	6%
V_{normal} ($\rho = 800$ kgm^{-3})	13%	11%	6%
V_{normal} ($\rho = 2500$ kgm^{-3})	23%	24%	8%
V_{low} ($\rho = 800$ kgm^{-3})	28%	46%	17%
V_{low} ($\rho = 2500$ kgm^{-3})	28%	46%	17%
Range	26%	39%	11%
Range ($\rho = 800$ **kgm**$^{-3}$)	22%	18%	17%
Range ($\rho = 2500$ **kgm**$^{-3}$)	19%	38%	36%
Result ($\rho = 800$ **kgm**$^{-3}$)	13^{+11}_{-11}%	11^{+13}_{-5}%	6^{+2}_{-1}%
Result ($\rho = 2500$ **kgm**$^{-3}$)	23^{+5}_{-14}%	24^{+13}_{-3}%	8^{+2}_{-1}%

Table 6.4: *Here we consider the uncertainties in the ejection velocity parameters: Here we present the variations in the capture percentages for particles ejected with maximum and minimum ejection velocities, found by analysing the uncertainties in each parameter in equation 6-1. Here 'V_{high} ($\rho = 800$)' refers to ejection using the highest velocity possible, with a density of $\rho = 800$ kgm^{-3}. Each column gives the percentage of captured ejected particles for the given comet and velocity condition. The 'Range' values give an idea of the spread of the results. The 'Result' values give the upper and lower bounds to the capture percentages determined for all three comets, for $\rho = 800$ kgm^{-3} and $\rho = 2500$ kgm^{-3}*

As given by the final three rows of Table 6.4, this method allows us to obtain uncertainty estimates for the capture percentages obtained. These uncertainty values

vary highly in magnitude. This is partially a result of the crude 10° resolution in the angles θ and ϕ, which may mean the number of particles captured do not vary smoothly with ejection velocity. Certain dynamical situations also have an impact. For instance, for Comet 1 the plateau of the number of particles captured for lower velocities represents the turning point of the capture percentage, as demonstrated in Figure 6.15. For these reasons, the resulting uncertainties are unique to each situation.

We use the above process to obtain uncertainties values for all comets at $\rho = 2500$ kgm^{-3} for true anomaly values 40°, 80° and 120°. These results are seen in Table 6.5. For Comet 1 the distribution of particles in resonance with true anomaly first increases then decreases, with a maximum at a capture percentage of $\sim 30.5\%$ of particles. In some situations it is thus more sensible to use 30.5% as the maximum percentage of captured particles to produce an upper uncertainty.

Velocity	**Comet** 1	**Comet** 2	**Comet** 3
Result at $\nu = 40°$	$25^{+5}_{-16}\%$	$25^{+23}_{-16}\%$	$9^{+10}_{-3}\%$
Result at $\nu = 80°$	$30^{+1}_{-13}\%$	$37^{+34}_{-20}\%$	$16^{+12}_{-8}\%$
Result at $\nu = 120°$	$7^{+16}_{-7}\%$	$80^{+20}_{-25}\%$	$34^{+27}_{-10}\%$

Table 6.5: *Uncertainty calculations for true anomalies* 40°, 80° *and* 120°. *Absolute uncertainties are given. Note that the uncertainties for Comet* 1 *for* $\nu = 40°$ *are based on a maximum number of resonant particles of* 167 *(*27.2%*)*

For Comets 2 and 3 that the percentage uncertainties vary between 13% and 118%. Percentage uncertainties in excess of 100% occur when the trapped percentage is less than 11% of the total number of ejected particles: that is, in cases where very few particles are trapped. In these cases the absolute variation is not in excess of 15%. For Comet 1, uncertainties are less than 85%, except in cases where less than 10% of particles are captured. We expect these approximate limits on uncertainties to hold for any density. As a result of these uncertainties, determination of the fraction of ejected particles captured in resonance is unlikely. However, we may still be able to draw conclusions on whether a trapped fraction is possible.

6.13 Accounting for Details of the Comet Ejection Process

6.13.1 Variations of Ejection with Heliocentric Distance

The distribution of particle ejections with semi-major axis is now applied to the resonance capture percentages. We assume that the relationship for the dust ejection rate with heliocentric distance is given by $q_d \propto r^{-3.0}$ (see Figure 6.18). This relation is used to produce a scaled distribution of capture percentages with true anomaly, with each capture

percentage scaled to the amount of dust expected to be ejected at that heliocentric distance (see Figure 6.19).

6.13.2 Particle Ejection from the Sunward Hemisphere of the Comet

Ejection of particles is not expected to occur over the whole comet surface. A more realistic situation is ejection from the sunlit hemisphere only. In reality, we expect that there will be some small component of ejection into the dark side of the comet (perhaps 20° to 30° into the dark side), but given the uncertainty of this we choose to assume that ejection occurs only on the sunlit hemisphere. The numbers of captured particle is therefore restricted to those ejected from angles $\theta = \nu + 90°$ to $\theta = \nu + 270°$, and $\phi = 0$ to $\phi = 180°$. These new capture percentages are shown in Figure 6.20. A further issue is the effect of ejection from a discrete jet (see Section 6.16).

6.14 Approximate Total Percentage of Particles Trapped in Resonance

For each model comet and set of particle parameters we now obtain the approximate total percentage of ejected particles that are trapped in the 7:2 resonance over the whole comet orbit. These percentages are calculated for the case of isotropic emission from the sunward side of the comet, and using the approximate heliocentric dust distribution of Comet 2P/Encke given in Figure 6.18. To accomplish this a test distribution is calculated in which all particles at all true anomalies are injected into the 7:2 resonance. This '100%' distribution is then scaled using the heliocentric dust distribution, and the resulting values at each true anomaly are summed. This gives the maximum sum of capture percentages possible. The sum of the scaled capture percentages produced by the model with particle ejection on the sunlit side only is divided by the maximum sum of the '100%' distribution. This provides the approximate total percentage of particles that are trapped in the resonance over the whole orbit of the comet (see Table 6.6).

In addition to those uncertainties discussed in Section 6.12, uncertainty in the ejection of particles with heliocentric distance and uncertainty in the regions of ejection on the comet surface will produce inaccuracies in these results. Total uncertainties in these values are expected to be well in excess of 50%. Rigorous uncertainty analysis is not justifiable, given that it is not expected to add significant information. We can thus only conclude that ejected particles from all three comets are capable of being trapped in the 7:2 resonance, even at the ~ 100 μm mass limit of the CMOR radar. Capture is usually more likely for heavier particles, except in the case of a comet that is displaced from the location of the resonance (such as Comet 1).

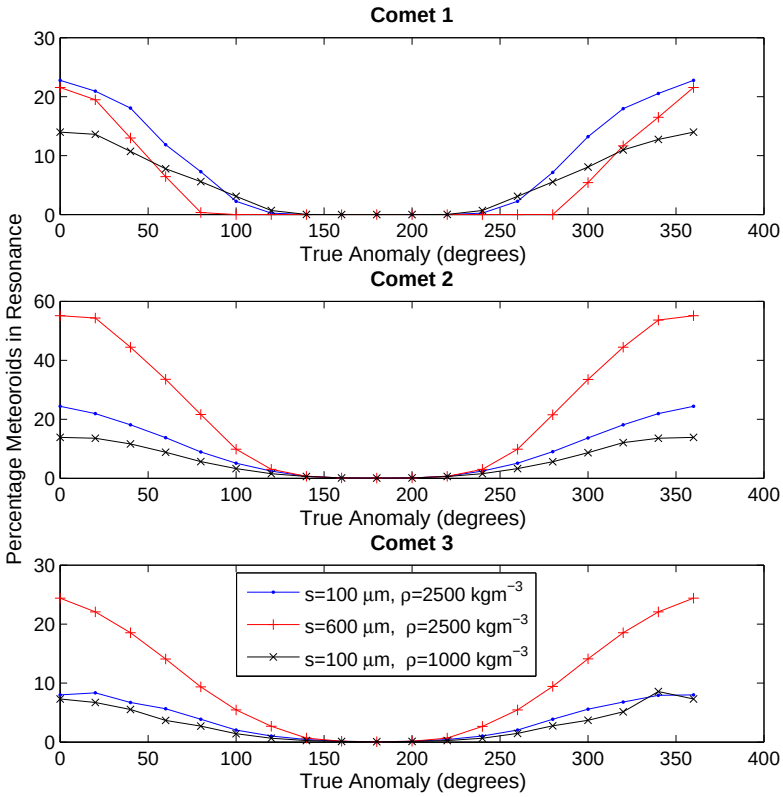

Figure 6.19: *The variation in the percentage of particles trapped in resonance, for all three comets, with values scaled by the particle ejection rates for comet 2P/Encke as given in Figure 6.18.*

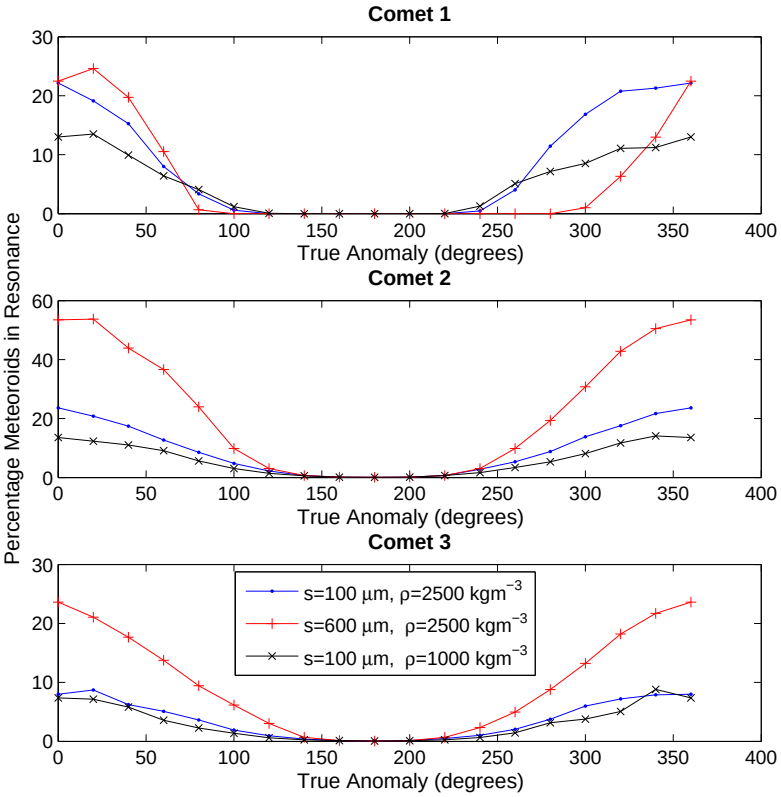

Figure 6.20: *The variation in the percentage of particles ejected from the sunward side of the comet that are trapped in resonance, for all three comets. Values are again scaled by the particle ejection rates for comet 2P/Encke as given in Figure 6.18.*

Comet	$s = 100$ μ**m;** $\rho = 2500$ **kgm**$^{-3}$	$s = 600$ μ**m;** $\rho = 2500$ **kgm**$^{-3}$	$s = 100$ μ**m;** $\rho = 1000$ **kgm**$^{-3}$
Comet 1	23%	17%	15%
Comet 2	27%	63%	17%
Comet 3	10%	27%	9%

Table 6.6: *Approximate total percentages of ejected particles trapped in the 7:2 resonance over the whole comet orbit.*

6.15 Variation of the Sunlit-Hemisphere Capture Percentages with Particle Mass

We are also interested in the difference between the capture percentages for visual and radar meteoroids. For this we extend the results of Section 6.8 to visual meteoroids of radii 2000 μm and 4000 μm, and determine the percentage of particles ejected from the sunlit hemisphere at perihelion that are captured in the 7:2 resonance (see Figure 6.21). We determine these approximate visual meteoroid radii limits by analysing the population index r (see Section 4.3.5) for Taurids. Dubietis and Arlt (2007) find this is an average of $r = 2.4$, with $r = 1.9$ for the 2005 swarm encounter year. The differential mass index is usually given by s: here it is denoted by s_{MI} to avoid confusion with the particle radius s. The differential mass index is related to the population index by:

$$s_{MI} = 2.5 \log(r) + 1$$

A number distribution can be derived from the differential mass index using:

$$N = Cm^{-(s_{MI}-1)}$$

where C is a constant, and N is cumulative the number of meteors down to a limiting mass m (Millman, 1973). The resulting distributions of N as a function of radius for $r = 2.4$ and $r = 1.9$ are given in Figure 6.22. A meteor density of 2500 kgm^{-3} is used. 1000 μm is used as the lower radius limit as it is approximately equivalent to a visual limiting magnitude of ~ 6 (for a velocity of about 30 kms^{-1}). This figure also indicates the 'perception function', which is a probability of visually observing a meteor of magnitude m (which is dependent on the experience and concentration of the observer). The values used are those derived by Koschack and Rendtel (2000), and are the same values used by Dubietis and Arlt (2007) to derive the population indices for Taurid meteors. We conclude from Figure 6.22 that most visual Taurids will be in the radius range 1000–4000 μm, with most meteors between 2000 and 3000 μm.

There are large differences between the results for different model comets (given in

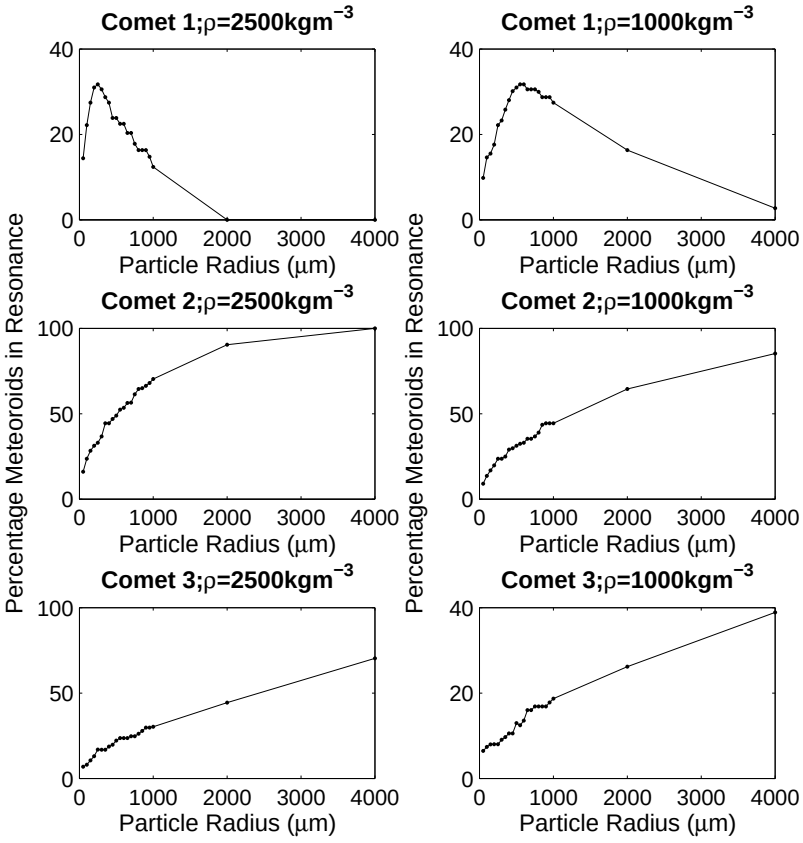

Figure 6.21: *The variation in the percentage of meteoroids ejected from the sunlit side that are trapped in resonance as a function of particle radius, shown for all three comets, for two different particle densities, and for radius values up to* 4000 μm.

Figure 6.21). Whether visual meteoroids ejected from Comet 2P/Encke (Comet 1) have resonant orbits is dependent on their density. Meteoroids with densities 2500 kgm^{-3} and radii greater than $\sim$ 2000 μm are not trapped in the resonance. However, about 16% of meteoroids with densities of 1000 kgm^{-3} and radius $\sim$ 2000 μm are captured. In both cases the proportion of radar meteoroids (100 to 1000 μm) captured is larger than the proportion of visual meteoroids (2000 to 4000 μm) captured.

However, for comets orbiting in the proposed orbit of proto-Encke (Comets 2 and 3) the percentage of visual meteoroids captured is greater than the percentage of radar meteoroids, as a result of the lower ejection velocities of visual meteoroids. Table 6.7 gives these values for approximate maximum, minimum and mean masses. For example, the radar rates for Comet 2 for 2500 kgm^{-3} particles are expected to be between 23% and 53% of the visual rates. The lowest radar rate is 23% of the visual rates (for Comet 2, 2500 kgm^{-3} particles). The uncertainties in these percentages should not be as significant

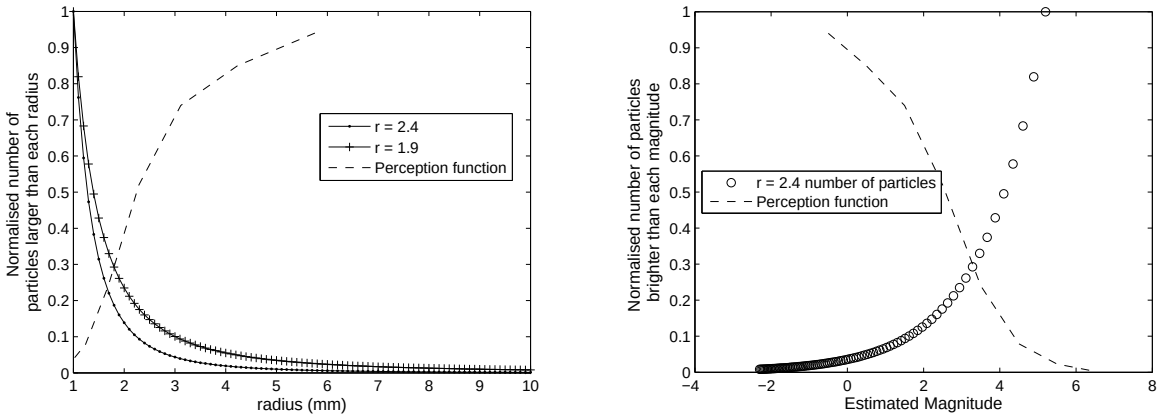

(a) (b)

Figure 6.22: *Radius and magnitude distribution graphs for visual Taurids. The two solid lines show the radius distribution (normalised to the number of particles of radius* 1000 *μm) for population indices $r = 1.9$ and $r = 2.4$. The dashed line is the approximate perception function.*

as the 50% uncertainties in individual capture percentages, as seen in Section 6.12.

In Section 4.10.3 we estimate that in a swarm year the proportion of visual Taurid meteoroids that are in the resonant swarm is about 20% to 40%, dependent on the swarm year. If we assume that the resonant Taurids are ejected from a resonant comet, this estimate can be combined with the rates given in Table 6.7 to determine approximate percentages of observed radar Taurids that are resonant. In consequence, the minimum proportion of observed radar Taurids that are expected to be resonant is approximately 4–5% (found using 23% of 20%). If the mean radar values are used it is found that a minimum of $\sim 5\%$ of Taurids are expected to be in the resonant swarm. In Chapter 4 it is also found that in order for the resonant swarm to be observable, we require a minimum of $\sim$ 5–6% of observed Taurids to be in the resonant swarm. Observation is then possible with a radar system with orbital uncertainties a factor of about one tenth of those of the CMOR data used here.

For a year of data from such a radar system, these results suggest that in years in which the swarm is weak there is a possibility that radar data may contain less than the $\sim$ 5–6% swarm particles required for observation. The mean values indicate that in most cases the resulting capture rate of radar Taurids may still allow detection of swarm in most cases. In stronger swarm years (such as 2005), detection chances are significantly higher. The radar proportions of captured particles as a percentage of the visual values are also lower for high density. This implies that we expect it to be more difficult to detect the swarm if the particle density is high.

If the visual meteor results given in Section 4.10.3 are accurate, then for strong

swarm years our results from the simulation of comet ejections produce a large enough proportion of resonant radar Taurids for detection of the swarm to be possible. In years in which the swarm only produces $\sim 20\%$ increase in the numbers of particles, the swarm may be on the edge of observability. A more complete cometary ejection model would include the distribution of the masses of particles ejected by the comet. This would provide more accurate estimates of the expected proportion of resonant Taurids of radar-detectable masses. At present, the above results can only be considered indicative.

	Minimum		**Maximum**		**Mean**	
	Comet 2	**Comet 3**	**Comet 2**	**Comet 3**	**Comet 2**	**Comet 3**
$\rho = 2500$ **kgm**$^{-3}$	23%	23%	53%	34%	44%	24%
$\rho = 1000$ **kgm**$^{-3}$	44%	42%	46%	43%	37%	33%

Table 6.7: *Approximate radar maximum, minimum and mean capture rates, as percentages of the visual maximum and minimum capture rates, for comets 2 and 3 at particle densities* $\rho = 2500$ *kgm*$^{-3}$ *and* $\rho = 1000$ *kgm*$^{-3}$*. The minimum and maximum are defined by particles of sizes* 100 *and* 600 μ*m for radar meteoroids of density* $\rho = 2500$ *kgm*$^{-3}$*;* 200 *and* 800 μ*m for radar meteoroids of density* $\rho = 1000$ *kgm*$^{-3}$*; and* 2000 *and* 4000 μ*m for visual meteoroids. The mean radar particle sizes are* 350 μ*m and* 500 μ*m for particle densities* $\rho = 2500$ *kgm*$^{-3}$ *and* $\rho = 1000$ *kgm*$^{-3}$ *respectively. These maximum, minimum and mean radar values are taken from Figure 6.11. The mean radar capture rates are percentages of the maximum visual capture rate.*

6.16 Ejection from a Discrete Jet on the Comet

In this section we consider the situation of ejection from a discrete jet comprising $\sim 4\%$ of the total comet surface, which is active around perihelion. This situation is an attempt to account for the discrete ejection from an area of the comet, as opposed to the previous assumption of even ejection from the whole sunlit hemisphere. We will make a number of assumptions that are speculation to some extent: though it is thought that Comet 2P/Encke has an active region at perihelion (and aphelion) the nature of this is highly uncertain (see Ferrín (2008); Reach (2000)). We therefore make several assumptions to provide an indicative model of the resonant status of particles ejected from a specific discrete jet.

It is assumed that the active area is centred on the sunward direction at perihelion: that is, its direction is defined by $\theta = 180^\circ$ and $\phi = 90^\circ$. We assume that this area is located at the southern rotational pole of the comet, which we assume to point towards the Sun at perihelion. We assume that the rotation axis of the comet is fixed in space, such that it remains in the orbital plane. It is expected that the point at which the southern pole faces the Sun is nearly coincident with perihelion: Ferrín (2008) calculates

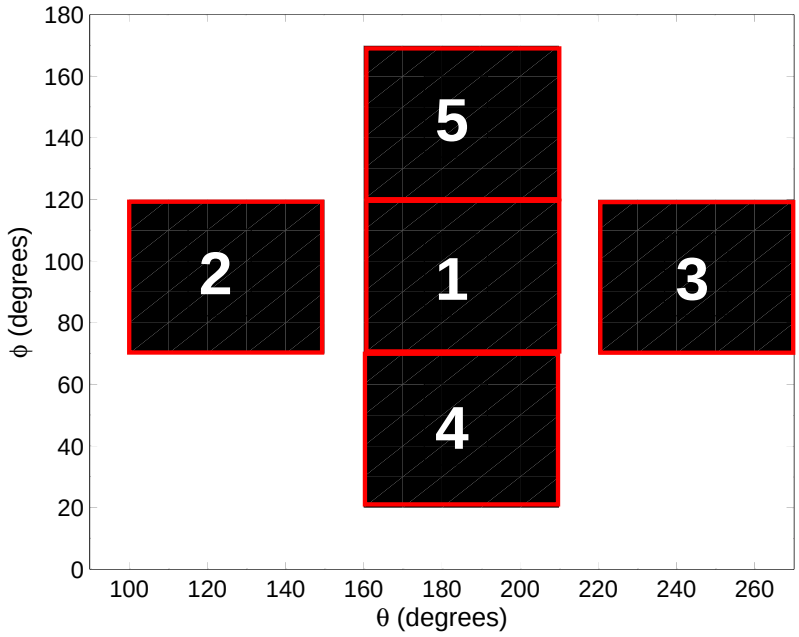

Figure 6.23: *The location of the five test jets on the comet surface.*

that this occurs 6 ± 1 day after perihelion (at $\nu = 26.7 \pm 4.5°$). We assume that ejection of particles occurs while this area is sunlit: between $\nu = 250°$ and $\nu = 110°$.

The jet region is approximated by selection $\sim 4\%$ of the direction angles used above. The region itself ranges from direction angles $\theta = 160°$ to $\theta = 200°$ and from $\phi = 70°$ to $\phi = 110°$ inclusive: that is it spans $50°$ in θ and ϕ. This comprises 4.07% of direction angles.

In order to test whether the location of the jet is crucial, we additionally test four alternative jets, positioned symmetrically either side of the south pole jet, such that they are all on the sunlit side when the comet is at perihelion. These jets are also of the same size in the angles θ and ϕ as the original jet. There will be a small difference in the size of the ejection areas encompassed by each jet due to the non-uniform spacing between ejection angles. This is not a major concern as we do not attempt to directly compare the results for each jet. Their locations on the sunlit side of the comet, using the coordinates θ and ϕ, are shown in Figure 6.23.

The percentages of jet particles captured in the 7:2 resonance are shown in Figure 6.24. What is apparent is that the capture percentages are highly variable with the comet, particle radius and density, and true anomaly. However, it is evident from this method that the capture of particles from a discrete jet in the southern hemisphere is possible: that is, such a capture mechanism is not excluded by this study.

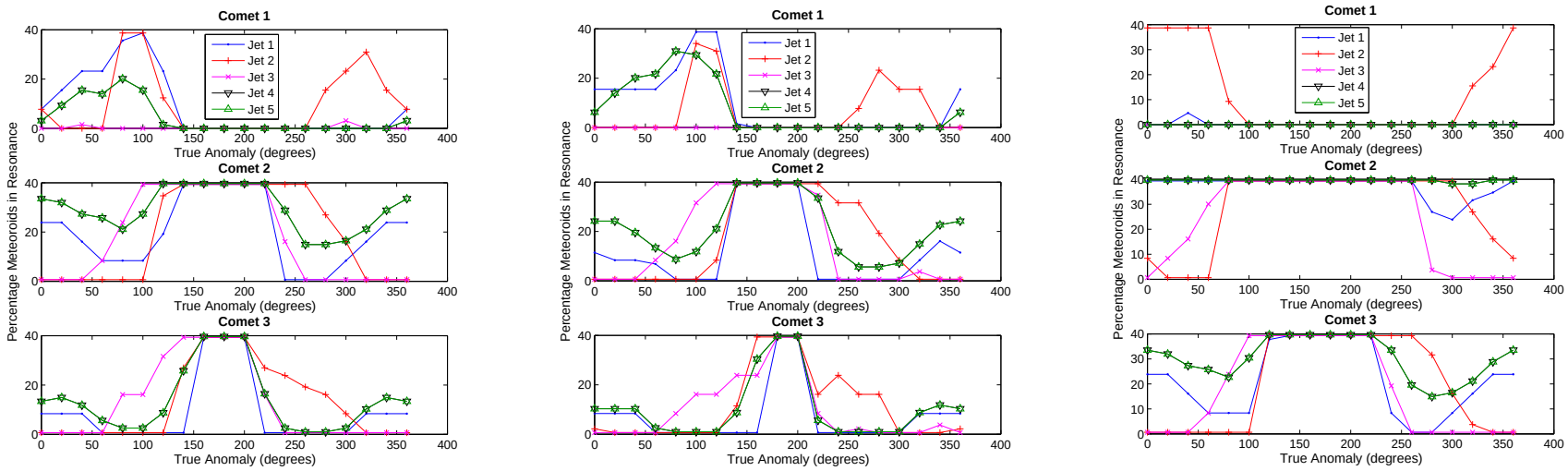

(a) (b) (c)

Figure 6.24: *Capture percentages for various jets (see Figure 6.23) for three comets. The capture percentages are out of the total number of ejection directions from the jet (25 in this model). Parameters used are (a) particle radius 100 μm, particle density 2500 kgm^{-3}; (b) particle radius 100 μm, particle density 1000 kgm^{-3}; (c)particle radius 600 μm, particle density 2500 kgm^{-3}. Note that a true anomaly of 480° is equivalent to a true anomaly of 120°. No correction for the variation in dust ejection with heliocentric distance is made here.*

6.17 Inclusion of Radiation Pressure

Since the above study does not include the effects of radiation forces, we now address whether radiation pressure will have a significant impact on the trapping of 100 μm particles in the 7:2 Jovian resonance.

We expect radiation forces to have both short and long term impacts on the motion of small meteoroid particles in the Solar System. Here we are only concerned with short term effects ($\lesssim$ a few years), including the instantaneous variation of orbital elements as a result of the variation in energy provided by radiation pressure. There will also be a shift in the location of the resonance.

An ejected particle immediately feels an increased radiation effect due to its apparent reduction in mass. As given in Section 2.3.5, the combined force on a particle subject to solar gravitational force and radiation pressure force is the vector sum $\mathbf{F} = \mathbf{F_g} + \mathbf{F_r}$:

$$\mathbf{F} = -\frac{GM_\odot m}{r_h^2}\hat{\mathbf{r_h}} + \frac{L_0 s^2 Q_{pr}}{4\pi r_h^2 c}\hat{\mathbf{r_h}}$$

Using $\beta = \frac{3L_0 Q_{pr}}{16\pi G M_\odot c\rho s}$ this reduces to

$$\mathbf{F} = -\frac{G(1-\beta)M_\odot m}{r_h^2}\hat{\mathbf{r_h}}.$$

From this is it is evident that the effect of radiation is to reduce the apparent gravitational effect of the Sun: that is, the particle appears to be orbiting a star of mass $M_\odot(1-\beta)$. With the expression for the heliocentric velocity of an object $V_h^2 = GM_\odot(\frac{2}{r_h} - \frac{1}{a})$, this can be used to derive expressions for the new orbital elements of a comet-ejected particle under radiation pressure (with the ejection velocity taken as negligible):

$$a' = a(\frac{1-\beta}{1-2a\beta/r_h}) \tag{6-7}$$

$$e' = |1 - \frac{(1-2a\beta a/r_h)(1-e^2)}{(1-\beta)^2}| \tag{6-8}$$

(These are also given in Moro-Martín and Malhotra (2002) and Kortenkamp and Dermott (1998)). From these, an expression for the true anomaly can be derived by taking the position of the particle on ejection to be constant: thus $r'_h = r_h = \frac{a(1-e^2)}{1+e\cos\nu}$. This produces:

$$\nu' = \arccos\left(\frac{e\cos\nu + \beta}{\sqrt{(1-\beta)^2 - (1-2\beta a/r_h)(1-e^2)}}\right)$$

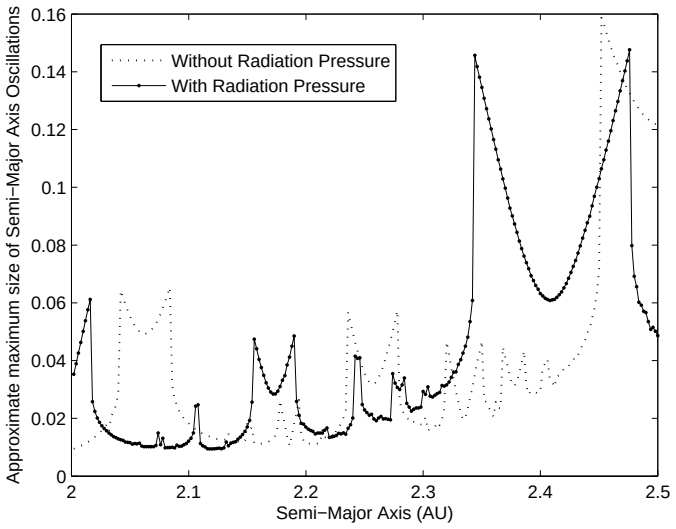

Figure 6.25: *The resonance shift experienced for 2 μm Taurid particles. Note that the 7:2 resonance is shifted from 2.256 AU to 2.173 AU (expected 2.1737 AU) and the 3:1 resonance is shifted from 2.5 AU to 2.408 AU (expected 2.4087 AU). This has also reduced the full resonant width (to a maximum of ~ 0.041)*

Additionally, $\varpi' = \varpi + \nu - \nu'$ is expected, again determined by assuming the position of the particle remains constant instantaneously. Because radiation pressure is radial it cannot affect the inclination and longitude of the ascending node.

The location of the resonance is also dependent on the β factor of the ejected particle. The location of a Jovian $p+q : p$ resonance is given by Weidenschilling and Jackson (1993) as:

$$a_{res} = a_{Jupiter} \times (1-\beta)^{1/3} \left[\frac{p}{p+q}\right]^{2/3}$$

or:

$$a_{res} = a_{res,\beta=0} \times (1-\beta)^{1/3}$$

For a 100 μm particle, this shift is only 0.00172 AU: such particles have $\beta = 0.00228$ assuming their density is $\rho = 2500$ kgm^{-3}. We thus demonstrate (in Figure 6.25) the shift for a 2 μm particle, with Taurid orbital elements and the semi-major axis stepping from 2 – 2.5 AU in 0.002 AU increments. This is not expected to produce a significant effect for radar-sized particles.

Inclusion of radiation pressure in the comet ejection model requires use of the HNDrag extension to HNBody. This requires a drag force input file which specifies the type of force (such as radiation pressure), the β fraction for the object, and the object on which the force is to act. We also need to consider the limits of the osculating

orbital elements used by HNDrag. Osculating orbital elements describe the orbit of an object in the absence of external perturbations, such as gravitational or radiation pressure perturbations. Thus, the osculating coordinates do not well describe an object's orbit when radiation pressure is added. This could be rectified by converting the osculating orbital elements to geometric elements. However, in order to avoid this conversion we here force the program to produce sensible orbital elements by avoiding the addition of radiation pressure directly to the ejected particles. The radiation pressure effect is simulated by altering the mass of the Sun to $(1-\beta)M_{\odot}$. This means that the level of radiation pressure experienced by the particle is now also applied to Jupiter and the model comet. We therefore apply a 'negative' radiation pressure to Jupiter and the comet, of magnitude $\beta' = \frac{\beta}{1-\beta}$. This is the correct β to apply in this situation due to the fact that this β is applied by a Sun of reduced mass $M_{\odot} \times (1-\beta)$. We also correct the Jupiter and comet orbital elements for the radiation pressure effect that they undergo in the scheme used here. We note that for a 100 μm particle from Comet 2 at perihelion this amounts to ejecting the particle from the comet at 2.318 AU instead of 2.256 AU. Note that the real situation is that the comet has a semi-major axis of 2.256 AU, but its ejected particles feel the radiation pressure effect instantaneously and embark on an orbit with semi-major axis 2.318 AU. Given that the resonant half width for the 7:2 Jovian resonance is ~ 0.024 AU, this will have a significant effect on the trapping of ejected particles in the resonance.

We demonstrate here the effect of radiation pressure on trapping for Comets 1 and 2 (100 μm particles of density 2500 kgm^{-3}) and Comet 2 (600 μm particles of density 2500 kgm^{-3}) (see Table 6.1). For efficiency a simple semi-major axis based resonance test is developed that evaluates whether each particle's semi-major axis places it within the resonance width of the 7:2 resonance. It is first verified that this gives comparable results to the resonant argument-based method in the case of no radiation pressure (as given above). It is found that for Comet 2 ejections of 100 μm particles of density 2500 kgm^{-3} the semi-major axis method produces capture percentages that are between 97.9% and 101.5% of the capture percentages determined using the resonant argument test.

We can then use a simple method to evaluate the capture percentages under radiation pressure. We begin with the starting semi-major axis values for the resultant ejected orbits of particles ejected without radiation pressure, and determine their corresponding values under radiation pressure, given by equation 6-7. We can then determine which particles are in resonance by using the simple semi-major axis test given above. We test this method specifically for a 100 μm particle of density 2500 kgm^{-3} ejected at perihelion from Comet 2 and inclusive of radiation pressure. In this case the simple semi-major axis method produced a capture percentage 90.3% of that given by numerically integrating the

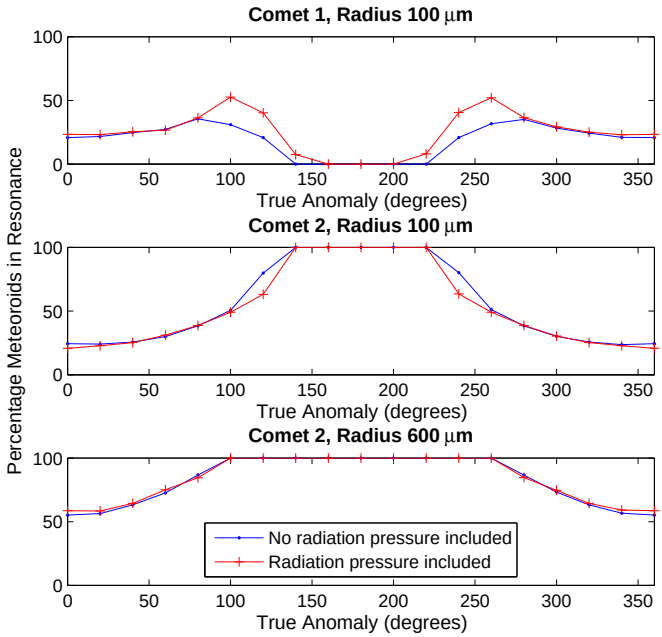

Figure 6.26: *Capture percentages (inclusive and exclusive of radiation pressure) for* 100 μm *and* 600 μm *particles of density* 2500 kgm^{-3} *ejected from comets 1 and 2 at a range of positions along the comet orbit. Variations between the rates inclusive and exclusive of radiation pressure can be large for* 100 μm *particles, but are low for* 600 μm *particles. No corrections for heliocentric distance or ejection only from the sunlit side are made at this point.*

orbits and using the resonant argument to determine whether they are resonant. This test is sufficient as the uncertainty it adds is small compared to that found in the uncertainty analysis above (Section 6.12).

We therefore see in Figure 6.26 the comparison between capture rates including and not including radiation pressure. It is evident that the error created by not including radiation pressure can be high for $s = 100$ μm particles:up to about 70% in isolated cases). However, the variations for $s = 600$ μm particles for Comet 2 do not exceed 7% at any point, as a consequence of the $\frac{1}{s}$ dependence of the β factor on heliocentric distance.

Several effects contribute to the differences between the percentage of particles captured with and without radiation pressure. One of the most important is the apparent ejection location of the comet: that is, the location that the particles appear to be ejected from. This is also equal to the semi-major axis of a particle ejected under radiation pressure with zero ejection velocity. Though the comet appears to be ejecting from a larger semi-major axis, only the particles are significantly affected by radiation pressure, due to the relatively large mass of the comet. Using equation 6-7 it can be seen that this

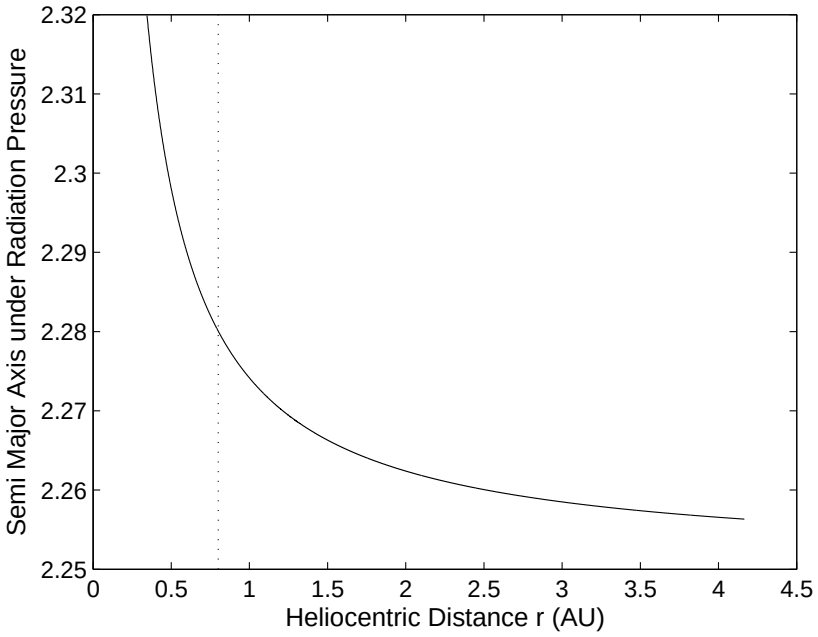

Figure 6.27: *Variation in the semi-major axis of* 100 μ*m particles (of density* 2500 kgm^{-3}*) ejected from Comet 2 and subject to radiation pressure, using equation 6-7. The largest variation in semi-major axis is experienced around perihelion, and the semi-major axis decreases thereafter, such that the semi-major axis of the particle is within the resonance further out than about* $r_h = 0.8$ *AU (indicated by the dotted line). For Comet 1 the particle is within the resonance if ejected within* 0.8 *AU.*

change in semi-major axis is dependent on the mass of the particles and the true anomaly of the comet at the ejection point.

The effect of this is different for comets 1 and 2, and for particles of different mass. Equation 6-7 can be used to demonstrate this. Comet 2 is orbiting within the resonance ($a_{C2} = 2.256\text{AU} \approx a_{res}$, where a_{C2} is the semi-major axis of Comet 2 and a_{res} is the semi-major axis of the 7:2 resonant centre). At perihelion and under radiation pressure it appears to eject 100 μm particles from a location exterior to the resonance ($a > a_{res}$). However, as Figure 6.27 demonstrates, for solar distances $r_h \sim 0.8$ AU ($\nu \approx 106°$) it appears to eject particles from a semi-major axis inside the resonance. This allows it to reach a point (near aphelion) at which all ejected particles are trapped in resonance, as is seen in the case with no radiation pressure. This is seen in Figure 6.26 to be the case between $\nu = 140°$ and $\nu = 220°$. 600 μm particles always appear to be ejected from within the resonance: equation 6-7 shows that a 600 μm particle ejected with zero ejection velocity at perihelion will have a resonant orbit.

Comet 1 is orbiting interior to the resonance with $a = 2.21$ AU. However, as a result

of radiation pressure, at perihelion it appears to be ejecting particles from within the resonance. As the heliocentric distance increases, the difference between the original semi-major axis and the apparent semi-major axis resulting from radiation pressure decreases. For heliocentric distances greater than $r_h \sim 0.8$ AU ($\nu \approx 104°$ for this comet) it is again outside the resonance.

The change in the apparent location of the ejecting comet will also affect the ejection directions that can produce resonant particles. This will to some extent influence the areas on the comet surface from which ejection results in resonant orbits, and could indicate that ejection is required from different areas on the comet surface for particles of different masses to become resonant. However, this would depend on the distribution of ejection angles of particles released from each point on the surface. This effect would only be important when ejection is in discrete jets, as is proposed for Comet 2P/Encke.

Figure 6.28 shows the ejection directions (in θ and ϕ) from the surface of Comet 2 that can produce resonant orbits in two different cases (ejection at $\nu = 0$ and $\nu = 120°$), and demonstrates the differences between the resonant and non-resonant cases. We briefly describe the behaviour represented in Figure 6.28 (a)–(d) as follows:

(a) Particles ejected at perihelion ($\nu = 0$); without radiation pressure: As Comet 2 starts in resonance, the ejected particles are ejected from approximately the centre of the resonance. Many particles have a total resulting velocity that is too high for them to retain resonant orbits. The highest-velocity particles are ejected in the comet forward direction ($\theta = 90°$) and in the opposite ($\theta = 270°$) direction.

(b) Particles ejected at perihelion ($\nu = 0$); with radiation pressure: The particles now appear to be ejected from outside the resonance ($a > a_{res}$). Most do not reach resonance. Particles ejected in the opposite direction to the comet's forward motion direction (with $\theta = 270°$) are slower than the apparent comet, and therefore can achieve orbits with lower semi-major axis values: they can thus reach resonant orbits). However, a number of particles ejected in this direction reach orbits on the opposite side of the resonance ($a < a_{res}$), creating a region of non-resonant particles centred on $\theta = 270°$.

(c) Particles ejected at a true anomaly $\nu = 120°$; without radiation pressure: These particles are ejected from approximately the centre of the resonance. Particles at $\nu = 120°$ are ejected with lower ejection speeds than those at perihelion, which results in a larger proportion of particles being captured in resonance, in comparison to (a). Those that are not captured are those that are ejected in the direction of the comet's motion ($\theta \approx 158°$), and in the directly opposite direction ($\theta \approx 338°$).

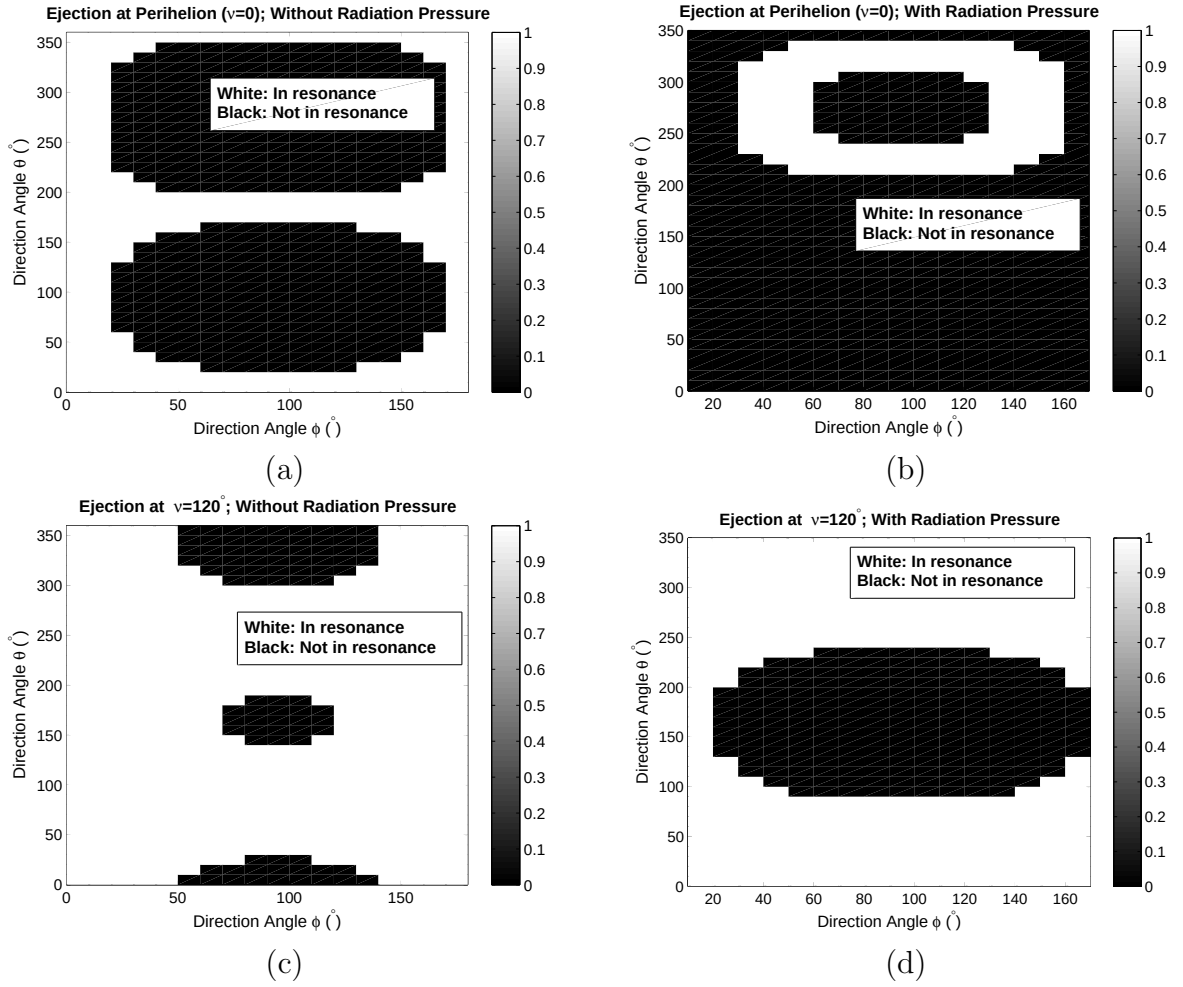

Figure 6.28: *Contour maps demonstrating the locations of ejected particles that have resonant orbits, and the variation that occurs when radiation pressure is added. In all cases $s = 100\ \mu m$, $\rho = 2500\ kgm^{-3}$ particles are ejected from Comet 2. (a) and (b) are ejected at perihelion; (c) and (d) are ejected at a true anomaly of $\nu = 100°$. (a) and (c) are exclusive of radiation pressure; (b) and (d) are inclusive of radiation pressure.*

(d) Particles ejected at a true anomaly $\nu = 120°$; with radiation pressure: Particles now appear to be ejected from within the resonance (compared to (b)). This ejection appears to occur near the edge of the resonance. This means particles ejected in the comet forward direction ($\theta \approx 158°$) can obtain velocities too high to remain in resonance, and therefore have orbits external to the resonance. All particles ejected in the opposite direction ($\theta \approx 338°$) remain within the resonance.

Thus, the percentage of captured particles for each case is affected by the variation in the apparent ejection location in semi-major axis (or the semi-major axis of a particle under radiation pressure and zero ejection velocity) and on the decreasing ejection velocity of the particles with heliocentric distance (or with true anomaly). The variation in the apparent ejection position affects the number of particles captured directly and also affects

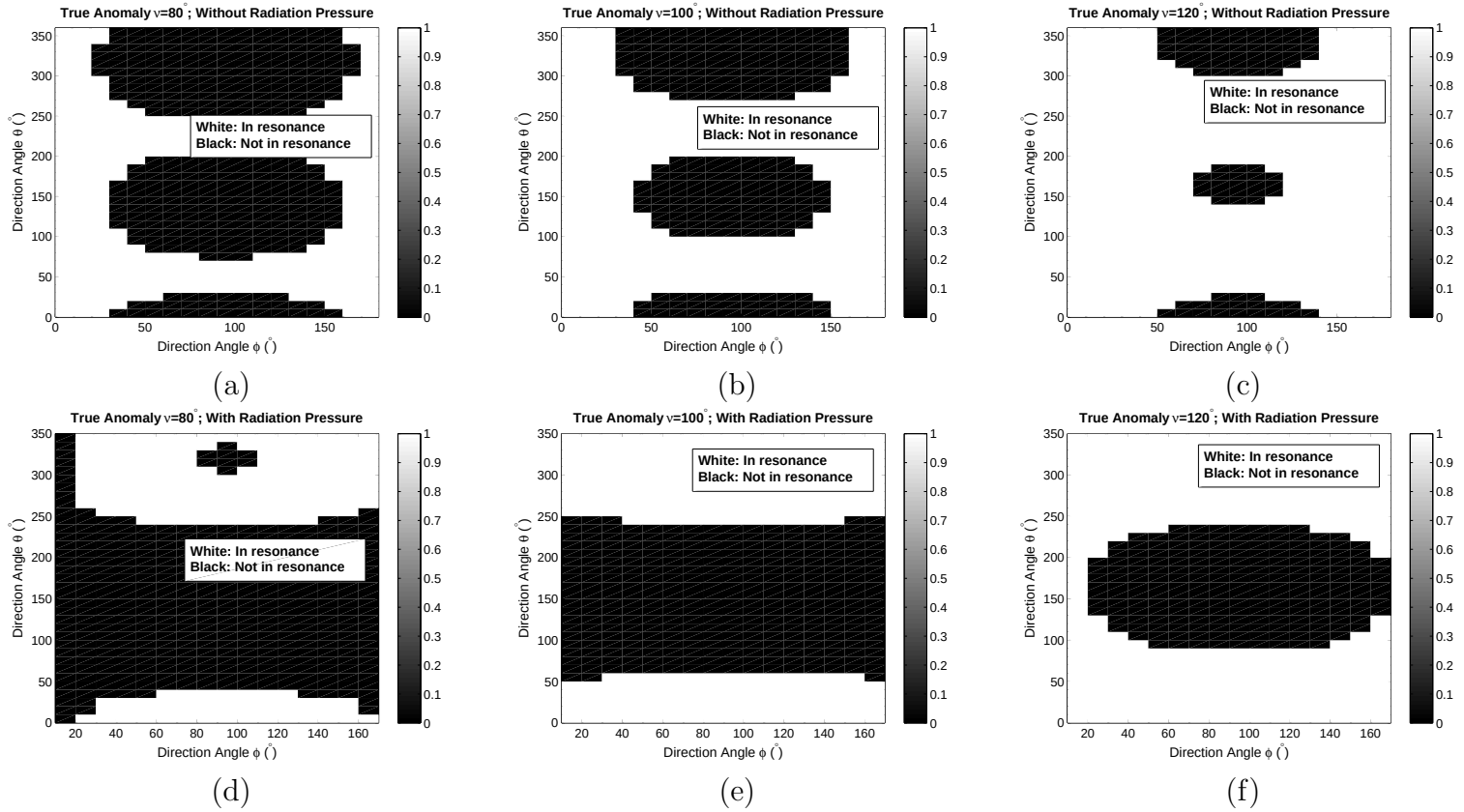

Figure 6.29: *Contour maps demonstrating the locations of ejected particles that have resonant orbits, and the variation that occurs when radiation pressure is added, for particles at true anomalies of* 80°, 100° *and* 120°. *In all cases* $s = 100\ \mu m$, $\rho = 2500\ kgm^{-3}s$ *particles are ejected from Comet 2. These figures demonstrate the change in the location of ejected particles for the radiation pressure case at* $\nu \sim 100°$ *(see Figure (e)).*

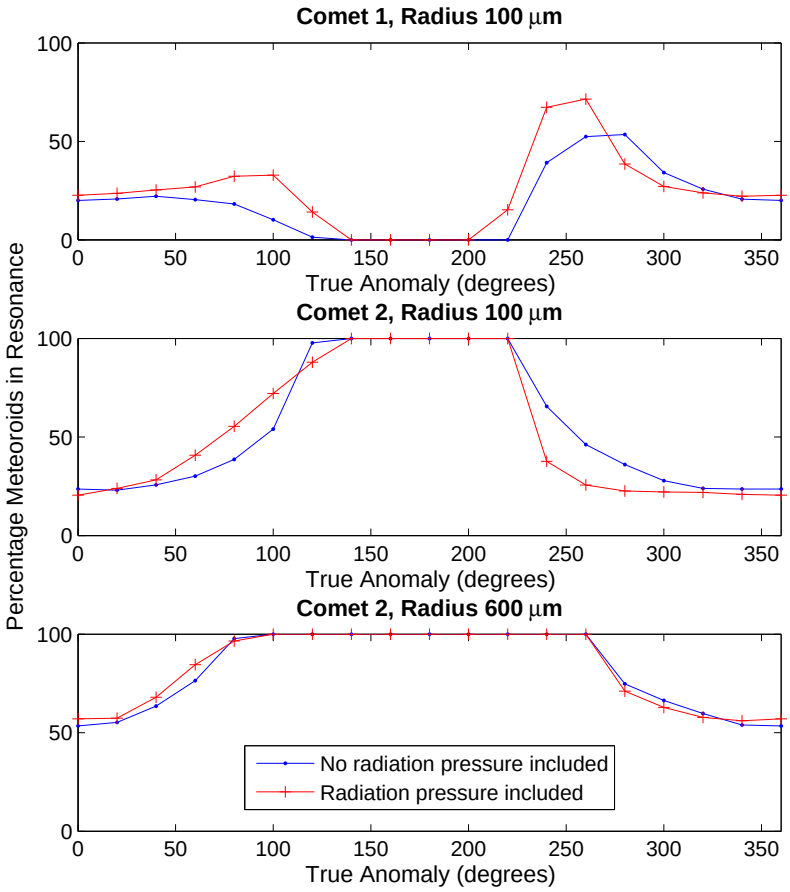

Figure 6.30: *Capture percentages (inclusive and exclusive of radiation pressure) for* 100 μm *and* 600 μm *particles of density* 2500 kgm^{-3} *ejected from comets 1 and 2 at a range of positions along the comet orbit.*

the ejection directions required. Because there are different effects contributing to the graphs in Figure 6.28, at any given point it is difficult to determine whether addition of radiation pressure will increase or decrease the captured percentage, or leave it unchanged. We observe that larger differences occur when the apparent ejection location of Comet 1 leaves the resonance, and when the apparent ejection location of Comet 2 enters the resonance (after approximately $\nu = 100°$ to $\nu = 120°$). In both cases this dynamical behaviour is a result of the change in ejection angles that can produce resonant orbits (see Figure 6.29). In the case of Comet 1, at perihelion particles appear to be ejected within the resonance. This should increase the number of particles captured. However, because the resonance width is small, the inclusion of ejection velocity causes a number of particles that are usually resonant (ejected in the comet forward direction) to achieve

orbits exterior to the resonance ($a > a_{res}$). This effect cancels out part of the benefit of the ejections occurring within the resonance, and capture percentages at perihelion are only $\sim 12\%$ different between the cases inclusive and exclusive of radiation pressure. This difference decreases with true anomaly as the difference between the apparent ejection location and the true location of Comet 1 decreases (as given by equation 6-7). Similarly, for Comet 2 particles appear to be ejected from an orbit exterior to the resonance, which should decrease the numbers captured. The variation in the ejection directions required for resonant capture again cancels partially with this effect. Thus, the capture percentages for Comet 2 at perihelion in the case without radiation pressure are $\sim 15\%$ different to those with radiation pressure.

Capture percentages are now generated for ejections from the sunlit hemisphere only (see Figure 6.30). Larger variations are seen between the radiation pressure and no radiation pressure cases, particularly for Comet 2. For Comet 2 the maximum variation between the radiation and no radiation pressure cases is $\sim 45\%$ for 100 μm particles and $\sim 11\%$ for 600% particles. Thus once the sunlit hemisphere correction is applied, which we expect to be necessary, there is a clear difference between the 600 μm and 100 μm cases.

The asymmetry in the capture percentages with true anomaly is due to the variation in the coincidence of the sunlit hemisphere and the hemisphere able to inject particles into the resonance. For example, for Comet 2 radiation pressure increases the semi-major axis of the ejected particles. The effect is such that only those that have an ejection velocity that produces a net decrease in the velocity of the particle will reach the resonance. These particles will be ejected backwards from the comet. We see particularly low rates of capture in the region $\nu = 240^\circ$ to 300° as in this region there is little coincidence between the sunlit hemisphere and the hemisphere ejecting particles backwards.

	Comet 1; $s = 100$ μ**m;** $\rho = 2500$ **kgm**$^{-3}$	**Comet 2;** $s = 100$ μ**m;** $\rho = 2500$ **kgm**$^{-3}$	**Comet 2;** $s = 600$ μ**m;** $\rho = 2500$ **kgm**$^{-3}$
Total %	26%	26%	64%
% of No-Radiation Pressure Values	109%	97%	103%

Table 6.8: Approximate total percentages of ejected particles trapped in the 7:2 resonance over the whole comet orbit, with the inclusion of radiation pressure

Finally, we add the heliocentric distance scaling (using the values given in Figure 6.18) and produce approximate total capture percentages for the whole comet orbit using the method given in Section 6.14(Table 6.8). This table also gives these resonant capture rates as percentages of the capture rates for the case of no radiation pressure. These give

an approximate idea of the error caused by the neglect of radiation pressure. In these cases this is not highly significant (less than $\sim 10\%$) because the largest errors from excluding radiation pressure occur at large heliocentric distances, at which Sun-comet distances the ejection rate of particle is low (see Figure 6.18).

6.18 Summary

Capture of particles into the 7:2 Jovian resonance is dependent on several parameters for which a high level of uncertainty exists. Cometary ejection processes for individual comets are not well understood. It is thus not possible to produce confident estimates of the percentages of particles that are likely to be trapped in a given resonance. However, a number of observations can be made:

- Ejection of cometary particles is possible from any of the three model comets proposed. Capture in the 7:2 resonance is easiest for Comet 2, which represents a small comet inside the resonance. Comet 1 (a model of Comet 2P/Encke) is displaced from the resonance, which hinders its ability to generate resonant particles. Comet 3 produces higher-velocity particles, which can more easily reach orbits beyond the resonance. Approximate capture percentages are determined (see Table 6.6), but are only considered indicative of the ability of these resonances to produce resonant particles, and of the variations between different particle mass and density combinations. Uncertainties are expected to be well in excess of 50%.

- The captured percentages of particles were found to be highly dependent on the mass (or radius) and density of ejected particles. The location of the comet in space with respect to the resonance dictates to some extent whether an increase in the particle mass lead to an increase in the captured percentage (see Figure 6.21). In particular, the variation between the capture percentages for photographic-sized and radar-sized meteoroids was evaluated. Capture of large, photographic-sized meteoroids is efficient for a librational comet such as model comets 2 and 3, but is less probable for a comet displaced from the resonant centre such as Comet 1. For librational comets (Comets 2 and 3), the capture percentages for radar-sized meteoroids are 23% to 53% of the capture radar of photographic-sized meteoroids. These are dependent on the comet, the particle density, and the exact mass limits.

- Ejection from a discrete jet (located such that it is active at perihelion) comprising only $\sim 4\%$ of the comet surface is not a barrier to trapping of radar-sized particles in the resonance. However, we note that our model is very limited in this case as it only accounts for strictly radial ejections, and includes several other assumptions.

- Radiation pressure may have a significant effect on the capture probabilities of particles at the lower end of the CMOR mass range (~ 100 μm) and at moderate heliocentric distances. As a result, different ejection angles are required for such particles to obtain resonant orbits. For particles of size ~ 600 μm, near the upper end of the CMOR mass range, such effects are small at all heliocentric distances. Without the heliocentric scaling, for sunlit hemisphere ejections from Comet 2 the maximum variation between the radiation and no radiation pressure cases is $\sim 45\%$ for 100 μm particles and $\sim 11\%$ for 600 μm particles. Overall, the effect of radiation pressure was small, with $\lesssim 10\%$ variations between the radiation pressure and non-radiation pressure cases for both Comet 1 and 2. This is partially a result of the fact that the largest variations between the two cases were found to exist at moderate-high heliocentric distances, where the relative dust output of the comet is expected to be low.

We also use the results regarding the capture percentages of visual and radar meteoroids to investigate how the proportion of visual Taurid particles that are in the 7:2 Taurid resonant swarm is likely to compare to the proportion of radar-sized particles. Along with estimates of the proportion of visual Taurids that are in the resonant swarm, this allows us to determine whether the proportion of radar Taurids in the resonant swarm is likely to be large enough to be detected using a CMOR type radar with measurement uncertainties improved by a factor of ten. With such a reduction in the measurement uncertainties we require approximately 5% to 6% of the total number of observed Taurids to be resonant in order for observation in one year of data to be possible. In strong swarm years, the size of the Taurid swarm should exceed this proportion. However, in weak swarm years we may expect only 4% to 5% of Taurids to be resonant, meaning the swarm would be on the edge of observability. Additionally, this is based on a gas-drag ejection model for cometary particles. The dependency of the ejection velocity on particle mass may vary for a fragmentation model: it is usually assumed that the ejection velocity is not a function of particle mass or radius (Tanigawa et al., 2010). Thus in such a case the proportion of radar particles captured may vary significantly from the results obtained here.

We thus conclude that the capture of a significant proportion of ejected Taurids in the 7:2 resonance is likely, but is highly dependent on the ejection velocities and ejection directions from the comet. An improved understanding of the exact ejection circumstances for a given comet is necessary to provide reliable capture percentages.

6.18.1 Survival of the Resonant Swarm

A final concern is the survival of particles in the swarm with time. It is not the intention in this chapter to address this question directly: we are concerned only with whether cometary ejection processes allow the swarm to be populated by particles of radar masses. An analysis of the population of particles within the swarm over time would require integration of the ejected particles for the approximate lifetime of the Taurid stream ($\sim 2\times10^4$ years) including gravitational effects of all planets and non-gravitational effects of radiation pressure, Poynting-Robertson effect and solar wind drag. This would also require accurate modelling of the expected orbits of Comet 2P/Encke and proto-Encke. Simple examples are used to study the approximate effects of such forces in the following section. The survival of particles is also limited by their collisional lifetime. However, the collisional lifetimes for Taurid particles of size 1 mm (calculated by Steel and Elford (1986)) are several times greater than the expected age of the Taurid stream (see Section 2.4). Thus, it is expected that collisions between meteoroids will not deplete the swarm in the timescale of interest.

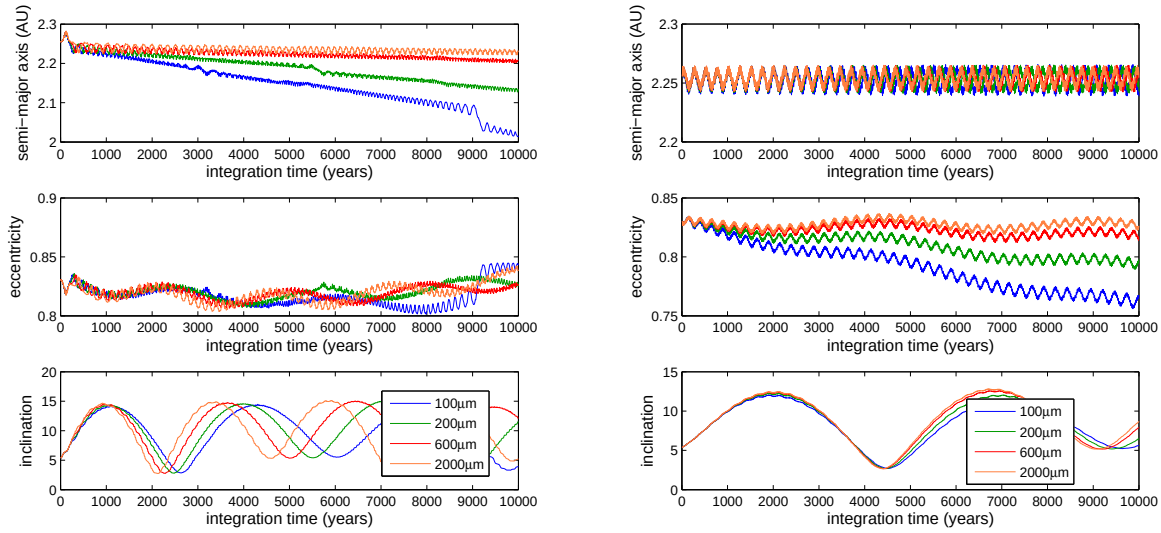

(a) (b)

Figure 6.31: *The effect of radiation pressure, Poynting-Robertson drag and solar wind drag over* 10^4 *years. (a) shows the result when the starting mean longitude places the particles very near the edge of the resonance; (b) demonstrates the behaviour when the starting mean longitude (relative to Jupiter) is optimised to place the particles in resonance. Particle sizes are* 100, 200, 600 *and* 2000 μ*m. Each figure provides the semi-major axis, eccentricity and inclination behaviour for each set of particles.*

We first study the effect of non-gravitational forces on particle of radii 100, 200, 600 and 2000 μm, and of density 2500 kgm^{-3}. Radiation pressure, Poynting-Robertson drag

and solar wind drag are applied using HNDrag, the latter as a component equal to 30% of the Poynting-Robertson drag (see Section 2.3.2). Integrations are run for 10^4 years (see Figure 6.31. Particles in Figure 6.31(a) are started at a mean longitude that places them at the edge of the resonance; particles in Figure 6.31(b) are placed at a mean longitude that optimises their location inside the resonance. It is clear that small particles at the resonance edge experience inspiralling that causes them to be lost from the Taurid region within 10^4 years. However, particles that are at an optimised resonant location are able to survive.

The action of planetary perturbations is expected to cause some particles to leave the resonance. This would allow them to inspiral under the Poynting-Robertson and solar wind drag forces. Thus, planetary perturbations (along with drag forces) will be a stronger loss mechanism for resonant particles than non-gravitational forces alone. To demonstrate this, the effect of planetary perturbations is shown for 200 μm particles. Particles are started at a semi-major axis of 2.256 AU, at ten evenly-spaced mean longitude values from 0 to 324°. Other orbital elements are mean values for the Taurid stream. All planetary bodies are included as HWPs, as well as Pluto and the asteroids Ceres, Pallas, Juno and Vesta. Non-gravitational forces are unchanged from those used above. The integrations are run for 10^4 and 10^5 years (see Figure 6.32). After 10^4 years, half of these evenly-spaced orbits suffer an orbital perturbation that causes them to leave the resonance and begin to inspiral. After 10^5 years, all particles have suffered such a perturbation, with the last particles leaving the resonance after $\sim 4 \times 10^4$ years.

Thus, radar-sized particles will be removed from the resonance on a timescale of approximately 1×10^4 to 3×10^4 years. This is approximately the expected age of the Taurid stream. We note that those that survive in the resonance longest tend to be those at optimal starting mean longitudes: in general we expect a resonant swarm to form at such mean longitude locations (with respect to Jupiter), and thus to have longer survival times. Given this, we conclude that it is possible for radar-sized particles to be trapped in the resonance swarm and to survive for $\sim 2 \times 10^4$ years. However, full stream modelling over the age of the Taurid stream would be required to confirm the magnitude of these loss mechanisms involving planetary perturbations. Such a study would require inclusion of all large planetary bodies, and as such the integration runtimes would be long. It is sufficient for our current study to have confirmed here that gravitational and non-gravitational effects do not exclude the possibility of radar-sized particles surviving in the swarm for such timescales.

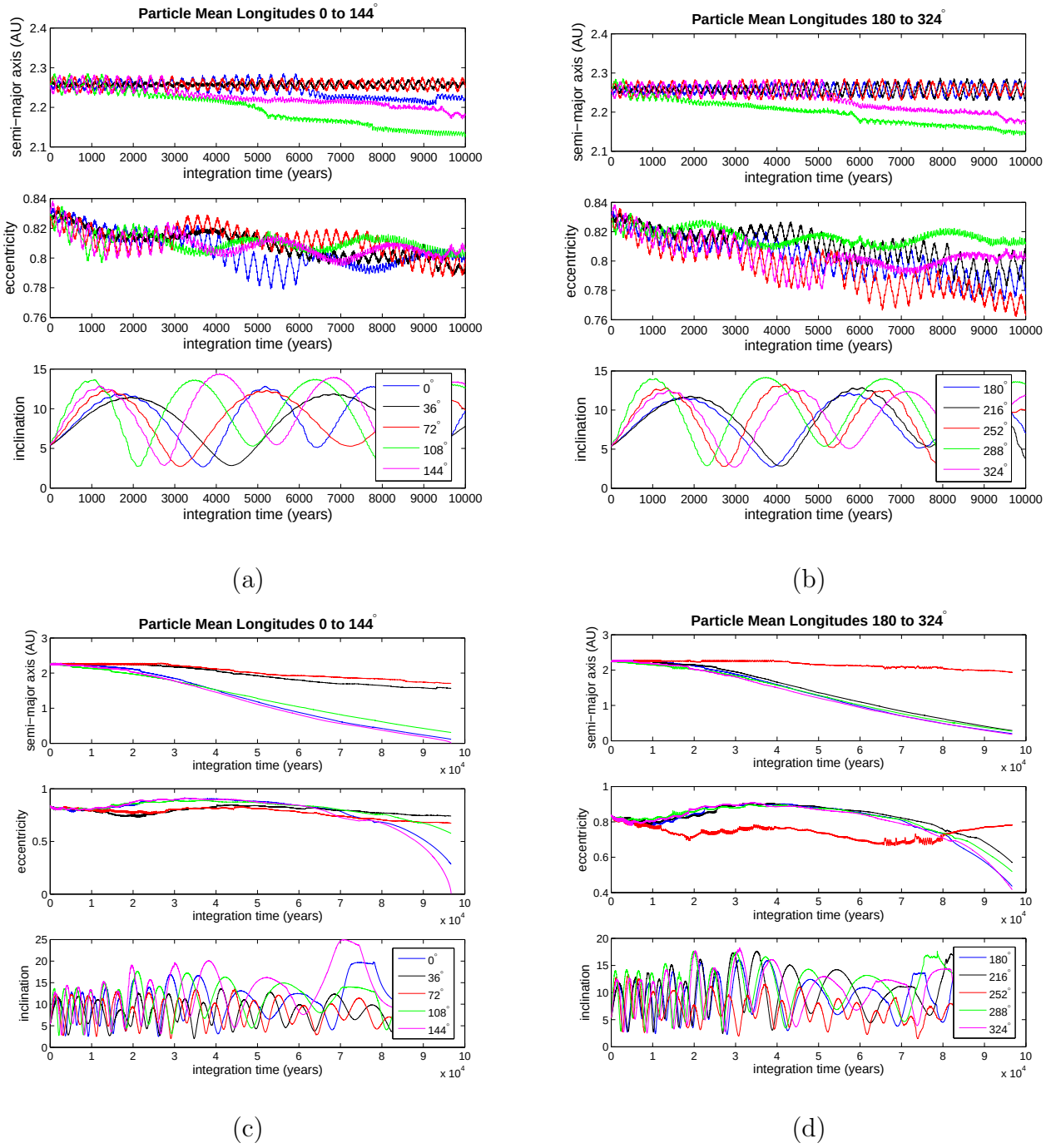

Figure 6.32: *The effect of gravitational perturbations and non-gravitational effects over* 10^4 *and* 10^5 *years. Non-gravitational effects included are radiation pressure, Poynting-Robertson drag and solar wind drag. (a) and (b) demonstrate integrations of length* 10^4 *years; (c) and (d) are extended integrations for* 10^5 *years. (a) and (c) demonstrate the behaviour are particles with starting mean longitudes of* 0 *to* $144°$*, while (b) and (d) demonstrate the behaviour of particles with starting mean longitudes of* $180°$ *to* $324°$*. Each figure provides the semi-major axis, eccentricity and inclination behaviour for each set of particles.*

Chapter 7

Conclusion

7.1 Summary and Conclusions

This thesis has analysed the observation of the 7:2 Taurid resonant swarm in meteor orbit radar data. Evidence for a number of resonant swarms is indicated in earlier works in photographic meteor orbit data: this study has investigated the ability of radar data to provide similar dynamical insights. Both data analysis and numerical integration of particle orbits are used to provide information on the observation of resonance structure using Canadian Meteor Orbit Radar (CMOR) data from the years 2002 to 2007.

A statistical study searched for the presence of the 7:2 swarm (expected to have a resonant centre at a semi-major axis of $\sim$ 2.25 AU) in this CMOR dataset. Two statistical tests were employed: a simple statistical test using the size of variations from a mean curve; and a Monte-Carlo test to determine the expected size of random variations in a dataset of this size. No evidence was found for a resonant feature at this location in the distribution of observed meteoroids with semi-major axis, in either the combined dataset for the years 2002 to 2007, or the dataset for the 2005 'swarm encounter' year (in which observation of the 7:2 resonance swarm was optimal for the 2002 to 2007 period). This must either be a consequence of the measurement uncertainties of the radar dataset; or of physical limitations of the swarm itself, such as a low proportion of radar-sized particles.

In order to address the former possibility, a numerical convolution method was developed. This method analysed the affect of the CMOR orbital uncertainties in broadening the Taurid semi-major axis distribution. It was found that the uncertainties of this CMOR data will broaden small scale resonant features such that they are unobservable. This method was used to determine the level of reduction of these radar meteor orbital uncertainties that is required for a swarm, of various sizes, to be observable. This was repeated for datasets of four different sizes to investigate the effect of dataset size on the size of random statistical fluctuations. The results of this are given by Figure 4.22. In summary, the results demonstrate that an improvement in the measurement uncertainties

of a factor of 5 to 10 is required for observation of a 7:2 resonant swarm, dependent on the size of the radar-sized proportion of the swarm (quantified by the proportion of the total number of Taurids detected).

In order to accomplish the statistical tests on the CMOR data and the numerical convolution method, it was necessary to know the approximate width of the resonant feature, in semi-major axis units. This provided the size of the feature for which evidence is sought in the radar data. Due to the high Taurid eccentricity of 0.83, the determination of a 'resonance' or libration width is not possible using an analytic method. This is because such methods are limited to the circular, planar restricted case. Thus, numerical integrations of particle orbits in and near the 7:2 resonance were used to calculate the resonant width. This required determination of the the region inside which the resonance can affect the dynamics of meteoroid particles. The HNBody program developed by Rauch and Hamilton (2002) was used to perform these numerical integrations. The resulting resonant width for particles with Taurid orbital elements was (0.047 ± 0.005) AU. At low eccentricities, this numerical method was compared to the analytic method (from Murray and Dermott (1999)) and the semi-analytic method developed by Gallardo (2006b). The latter required a conversion from resonant strengths to resonant widths: this was derived using the planar, circular form of the disturbing function given by Murray and Dermott (1999). Because different assumptions are inherent in the three methods, exact agreement is not expected. A good ($\lesssim 10\%$) agreement between the three method was achieved for orbits with eccentricities less than 0.4.

In the final chapter, the effect of meteoroid mass on resonant trapping efficiency was investigated. Evidence exists for the 7:2 Taurid resonant swarm in photographic meteor data. These photographic particles are larger than those detectable by radar (photographic particle have radii ~ 1000 μm to 4000 μm; radar particles have radii ~ 20 μm to 800 μm). If the mass distribution of swarm particles is weighted towards heavier particles, it may be that it is possible to observe the swarm at photographic sizes but not at radar sizes. Two possible mechanisms for producing such a mass distribution are: variations in the comet ejection velocities with particle radii; and variations in the effect of radiation pressure on orbital elements with particle sizes. Both areas were addressed using a simple model of particle ejections from a model comet using the HNBody numerical particle integrator and the HNDrag extension. The model comets used include one that resembles the current Comet 2P/Encke (Comet 1); one with the mass of Comet Encke but the orbital elements of an unconfirmed proto-Encke (Comet 2); and one with the mass and orbital elements of proto-Encke (Comet 3). These cover the comets expected to be capable of ejecting particles into the 7:2 Taurid resonant swarm. The aim was to determine the percentage of particles ejected in uniform directions that are injected into

resonant orbits. The mass dependency of the particle ejection speeds was determined using a Whipple-like ejection velocity model (Whipple, 1951), of the form given by Brown and Jones (1998).

Details of the particle ejection mechanism for individual comets remain highly uncertain, including with regard to the ejection regions on the comet surface, the density of ejected particles, and the distribution of particle ejections with heliocentric distance. This limits the ability for the model used here to provide accurate percentages of captured particles. In addition, the model makes assumptions on the locations of the model comets and Jupiter, which will affect the ability of the resonance to trap affected particles. In general, resonance capture of ejected cometary particles was found to be possible for all three model comets. The capture percentages are highly dependent on the masses and densities of the ejected particles. For comets 2 and 3, this effect is such that the capture percentages for radar-sized meteoroids are about 23% to 53% of those for photographic-sized meteoroids, dependent on the comet, the particle density, and the exact mass limits. Additionally, radiation pressure may have a significant effect for 100 μm particles, but will not for 600 μm particles. However, as the largest variations are not near perihelion where the majority of dust output occurs, the overall effect of radiation pressure on the total capture percentages over the orbit is found to be small. The variations between the radiation pressure and non-radiation pressure cases are $\lesssim$ 10% for both comet 1 and 2, for 100 μm and 600 μm particles.

Estimates were calculated for the expected proportion of radar-sized particles in the resonant swarm, compared to the total number of Taurids observed. This was achieved by comparing the capture percentages of visual and radar meteoroids with estimates of the proportion of visual Taurids that are in the resonant swarm. As given above, for detection of the swarm in one year of data to be possible using a radar with orbital uncertainties one tenth of those of the CMOR dataset used here, approximately 5% to 6% of the total number of observed Taurids must be resonant. In a weak swarm year, the total number of visual Taurids may increase by $\sim$ 20–40% (estimated using Taurid ZHR profiles given by Dubietis and Arlt (2007)). Calculations using the proportions of visual and radar meteoroids captured in the numerical integrations found that in the minimum 20% case only 4% to 5% of radar Taurids are expected to be resonant. Such a swarm would then be on the edge of observability. In strong swarm years, where a more optimal swarm geometry is present, the size of the Taurid swarm should exceed this proportion.

The parent object that has produced such a resonant swarm is expected to be either Comet 2P/Encke (modelled approximately by Comet 1), the currently unobserved proto-Encke object (Comet 3), or a small version of this proposed giant comet (Comet 2). The results of this study showed that there are vast differences in the resonance capture of

particles ejected from these comets. Capture of visual-sized meteoroids was found to be difficult for those that are ejected from a comet in the orbit of, and of approximate size to, Comet 2P/Encke. This is particularly true for dense particles, with density $\rho = 2500$ kgm^{-3}. Thus, the possibility of resonant capture of particles ejected from Comet Encke may depend on the density of such particles. As described in Section 6.3, this is not well constrained for Taurid meteoroids, but is expected to be slightly greater than that of other meteoroid stream particles. Thus, our study suggests that Taurid swarm particles need low densities in order for the current Comet 2P/Encke to be able to efficiently populate the 7:2 resonant swarm with visual-sized meteoroids.

7.2 Future Work

There is scope to improve the methods presented in this thesis. The numerical convolution method is an approximate approach to the effect of the radar uncertainties. In addition, it assumes a Gaussian form for the distribution of particles in the resonant swarm in semi-major axis. A future project should test the sensitivity of the results to resonant features with different distributions in semi-major axis: for example, a uniform distribution.

The ejection model problem would benefit from an improved treatment. By developing a model of streams from Comets 2P/Encke and proto-Encke, a more accurate description of the resonant trapping of such particles may be achieved. Such a model would include random ejections from the sunlit hemisphere, a mass distribution of particles, an improved water production rate (and thus dust production rate), an improved ejection velocity model (possibly using the Crifo model - which, notably, has the same mass dependency as the Whipple-type models), and the gravitational influence of more planets (here only Jupiter is included). Such a model would be computationally intensive but would remove the necessity to test individual mass, density and true anomaly cases, and would provide information on the behaviour of the whole stream. Further information on the ejection mechanisms of comet Encke would also reduce the uncertainties in the method.

Explicit modelling of a fragmentation model for stream formation, using a varied ejection velocity and ejection from all directions, would also be useful. This is important due to the expected role of fragmentation in the formation of Comet 2P/Encke and of a fraction of Taurid meteoroids. The results presented here on the proportion of radar Taurids expected to be resonant do not include such a fragmentation model, and as such these results can only be considered indicative. However, modelling this fragmentation situation would require the expected ejection velocities to be further constrained, particularly with regard to the variation of ejection velocity with mass.

These improvements, along with improved information on the increase in the observed numbers of visual Taurid particles caused by the presence of the resonant swarm, could provide a more exact value for the expected proportion of radar Taurids that are resonant. This would in turn improve the conclusions regarding the radar improvement required for the 7:2 resonant swarm to be detectable.

The results of this thesis imply that an improvement in the velocity uncertainties in radar orbital datasets is required to detect resonant features. The velocity measurement uncertainties in the CMOR dataset used in this thesis are $\sim 5\% - \sim 10\%$ (for the hybrid Fresnel method and the time-lag method respectively). The largest component to these uncertainties is the error in the determination of particle decelerations in the atmosphere. Reliable deceleration measurements are necessary to determine accurate pre-atmosphere speeds. In the 2002 to 2007 CMOR dataset, pre-atmospheric speeds are calculated using empirical expressions determined by comparing the radar-determined speeds and photographic speeds for major meteor showers. It is possible to determine acceleration values for individual meteoroids using a number of individual speed measurements. This requires several outlying stations in the radar system with interferometers capable of providing phase information. A new CMOR II radar is being developed with a total of five outlying stations (rather than the minimum of two): it is hoped that this configuration will be sufficient to obtain deceleration information (Brown et al., 2010).

If such methods are successful they provide what is probably the greatest chance of achieving the reductions in orbital measurement uncertainties required for studies of small-scale resonant features (including of resonant swarms) to be feasible with meteor radar data. Other methods of measuring the in-atmosphere speeds of detected meteoroids have the potential to provide velocity uncertainties 0.1 kms^{-1} (comparative to uncertainties of $\sim$ 3 kms^{-1} for Taurid meteoroids). However, such methods are dependent on clear meteoroid amplitude and phase profiles, which are only found for a small proportion of particles as a result of meteoroid fragmentation or atmospheric turbulence.

The methods outlined in this thesis are transferrable to the study of any other resonant features of interest, or small-scale dynamical features. An understanding of the level of radar orbital uncertainties necessary to detect such a feature is required. It would be necessary to determine the resonant width, or descriptive width of the feature of interest, in order to accomplish this. Depending on the situation, it may also be necessary to develop an understanding of the effect of particle mass on trapping of particles in this feature. From the results of Section 4.4 it is apparent that the Quadrantids are expected to be the next potential candidate for study in radar data. However, this section also demonstrates that the 7:2 Taurid resonant swarm is expected to be the most easily observable resonant feature in radar data. Thus, the results of this thesis indicate

that resonant features are not expected to be visible in meteor radar data until radar measurement uncertainties in velocity are improved by a factor of 5 to 10.

In such a manner, this study naturally leads to further study of such features by radar, and thus determination of the capabilities of a new radar system is preferable before further research is conducted. However, if the new generation of meteor orbit radar are found to be capable of probing dynamical resonant features, datasets from such radar could provide a powerful new tool for analysing the structure of resonances in the Solar System.

Appendix A

Details of Resonant Theory

Herein we include details and derivations of approximate resonant theory that help with the understanding of Chapter 5. These derivations are reduced content that appears in Murray and Dermott (1999).

A.1 Derivation of the Disturbing Function

The disturbing function arises considering relative motions of bodies in a three body system due to their gravitational forces. The following derivation is given in Murray and Dermott (1999) (Chapter 6). Consider three masses m_c (primary), and m_i and m_j (two secondary masses)) with position vectors relative to each other and to a central point as shown in Figure A.1. $\mathbf{R}_c$, $\mathbf{R}_i$, $\mathbf{R}_j$ are the position vectors for the three bodies from the fixed point O, and $\mathbf{r}_i$ and $\mathbf{r}_j$ are the position vectors of m_i and m_j from the primary. Using Newton's laws of motion and gravitation ($m\ddot{\mathbf{r}} = \mathcal{G}\frac{m_1 m_2}{r^3}\mathbf{r}$) we have:

$$m_c\ddot{\mathbf{R}}_c = \mathcal{G}m_c m_i\frac{\mathbf{r}_i}{r_i^3} + \mathcal{G}m_c m_j\frac{\mathbf{r}_j}{r_j^3}$$

$$m_i\ddot{\mathbf{R}}_i = \mathcal{G}m_i m_j\frac{(\mathbf{r}_j - \mathbf{r}_i)}{|r_j - r_i|^3} + \mathcal{G}m_i m_c\frac{\mathbf{r}_i}{r_i^3}$$

$$m_j\ddot{\mathbf{R}}_j = \mathcal{G}m_j m_i\frac{(\mathbf{r}_i - \mathbf{r}_j)}{|r_i - r_j|^3} + \mathcal{G}m_j m_c\frac{\mathbf{r}_j}{r_j^3}$$

The disturbing function describes the extra accelerations of the secondary masses due to the primary that are seen in the three body system. By expressing the (total) accelerations of the secondaries relative to the primaries, we will determine that they are composed of a two-body part, and a three-body correction: the disturbing function. These accelerations are given by

$$\ddot{\mathbf{r}}_i = \ddot{\mathbf{R}}_i - \ddot{\mathbf{R}}_c$$

$$\ddot{\mathbf{r}}_j = \ddot{\mathbf{R}}_j - \ddot{\mathbf{R}}_c$$

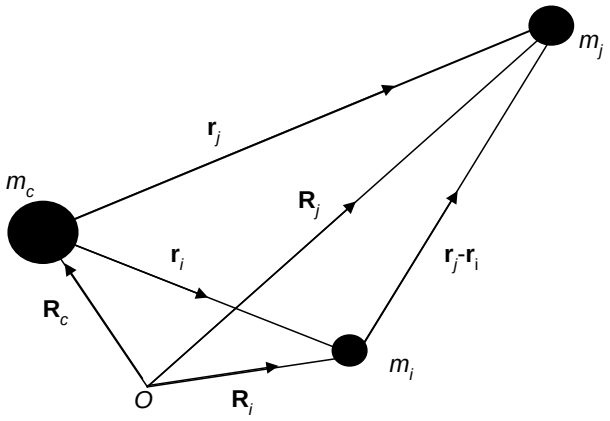

Figure A.1: *The Three-Body Problem: location of position vectors with respect to primary mass m_c and secondary masses m_i and m_j (After Murray and Dermott (1999), Chapter 6).*

Substituting previous expressions gives:

$$\ddot{\mathbf{r}}_i + \mathcal{G}(m_c + m_i)\frac{\mathbf{r}_i}{r_i^3} = \mathcal{G}m_j\left(\frac{(\mathbf{r}_j - \mathbf{r}_i)}{|r_j - r_i|^3} - \frac{\mathbf{r}_j}{r_j^3}\right)$$

$$\ddot{\mathbf{r}}_j + \mathcal{G}(m_c + m_j)\frac{\mathbf{r}_j}{r_j^3} = \mathcal{G}m_i\left(\frac{(\mathbf{r}_i - \mathbf{r}_j)}{|r_i - r_j|^3} - \frac{\mathbf{r}_i}{r_i^3}\right)$$

In order to obtain the primary and secondary components, we write these relative accelerations as gradients of scalar functions:

$$\ddot{\mathbf{r}}_i = \nabla_i(U_i + \mathcal{R}_i) = \left(\hat{\mathbf{i}}\frac{\partial}{\partial x_i} + \hat{\mathbf{j}}\frac{\partial}{\partial y_i} + \hat{\mathbf{k}}\frac{\partial}{\partial z_i}\right)(U_i + \mathcal{R}_i)$$

$$\ddot{\mathbf{r}}_j = \nabla_j(U_j + \mathcal{R}_j) = \left(\hat{\mathbf{i}}\frac{\partial}{\partial x_j} + \hat{\mathbf{j}}\frac{\partial}{\partial y_j} + \hat{\mathbf{k}}\frac{\partial}{\partial z_j}\right)(U_j + \mathcal{R}_j)$$

where $U_i = \mathcal{G}\frac{(m_c+m_i)}{r_i}$ and $U_j = \mathcal{G}\frac{(m_c+m_j)}{r_j}$, and $\mathcal{R}$ is the disturbing function. U_i and U_j represent the two-body part of the potential (pertaining to the effect of the central mass); thus $\mathcal{R}$ is the three-body/secondary mass part of the potential (as supported by the definition above). Considering that r_i is only a function of x_i, y_i and z_i (and similar for r_j) we have:

$$\mathcal{R}_i = \frac{\mathcal{G}m_j}{|\mathbf{r}_j - \mathbf{r}_i|} - \mathcal{G}m_j\frac{\mathbf{r}_i \cdot \mathbf{r}_j}{r_j^3}$$

$$\mathcal{R}_j = \frac{\mathcal{G}m_i}{|\mathbf{r}_i - \mathbf{r}_j|} - \mathcal{G}m_i \frac{\mathbf{r}_i \cdot \mathbf{r}_j}{r_i^3}$$

By generalising this to notation such that the inner secondary is given by m, $\mathbf{r}$ and $\mathcal{R}$, and the outer secondary by m', $\mathbf{r}'$ and $\mathcal{R}'$ we achieve final equations for the disturbing function of each of these objects:

$$\mathcal{R} = \frac{\mu'}{|\mathbf{r}' - \mathbf{r}|} - \mu' \frac{\mathbf{r} \cdot \mathbf{r}'}{r'^3}$$

$$\mathcal{R}' = \frac{\mu}{|\mathbf{r} - \mathbf{r}'|} - \mu \frac{\mathbf{r} \cdot \mathbf{r}'}{r^3}$$

where $\mu' = \mathcal{G}m'$ and $\mu = \mathcal{G}m$. The first term in these expressions is the direct term; the second is the indirect term produced by the choice of coordinate system. For the following sections, we note that we are primarily concerned with the inner secondary and will only discuss $\mathcal{R}$ in following sections.

A.2 A Circular Restricted Simplification

In order to reach a simple approximation to the resonant width, simplification to a planar circular problem assuming negligible mass for the inner perturbed body is necessary. Here this means zero inclinations for both bodies; and zero eccentricity for the perturbing body. Additionally, the use of a lowest order general form of the disturbing function means that low eccentricity of the interior (perturbed) body is also assumed. This is a standard practice for many Solar System applications: for example; for planetary resonant perturbations on an inner asteroid residing in the asteroid belt, the necessary conditions of small eccentricity and inclination of both bodies, and small mass ratio between the bodies, are usually upheld. For meteoroid applications, this is not generally the case, but we will see that this approximation still has useful functions for the problem at hand.

It can be shown that, to lowest order in eccentricity and inclination, the general term of the averaged expansion of the disturbing function is given by:

$$\langle \mathcal{R} \rangle = \frac{\mathcal{G}m'}{a'} [\mathcal{R}_D^{sec} + e^{|j_4|} e'^{|j_3|} s^{|j_6|} s'^{|j_5|} [f_d(\alpha) + f_e(\alpha)] \cos \varphi]$$

and similarly for $\langle \mathcal{R}' \rangle$. Here $s = \sin \frac{1}{2} I$ and $s' = \sin \frac{1}{2} I'$ and secular contributions are given by

$$\mathcal{R}_D^{sec} = (e^2 + e'^2) f_{s,1}(\alpha) + e e' f_{s,2}(\alpha) \cos(\varpi' - \varpi) + (s^2 + s'^2) f_{s,3}(\alpha) + s s' f_{s,4}(\alpha) \cos(\Omega' - \Omega)$$

In addition, $f_d(\alpha)$, $f_e(\alpha)$, $f_{s,i}(\alpha)$ refer to direct terms, indirect terms (for an external perturber) and secular terms in the expansion of the disturbing function.

For the circular, planar problem here, secular contributions are negligible, and the general term in the averaged expansion (for an internal resonance) is reduced to:

$$\langle \mathcal{R} \rangle = \frac{\mathcal{G}m'}{a'}[f_{s,1}(\alpha)e^2 + f_d(\alpha)e^{|j_4|}\cos\varphi]$$

where

$$\varphi = j_1\lambda' + j_2\lambda + j_4\varpi$$

The indirect terms are dependent on the mass of the inner body and thus are negligible when this mass is negligible; the circular orbit of the perturber ($e' = 0$) causes cancellation of many eccentricity terms; with both orbits are in the same reference plan the longitude of the ascending node terms are zero; an eccentricity of zero means that the argument of perihelion of the external (perturbing) body is zero also.

Lagrange's Planetary Equations are also required. These give the variations in orbital elements experienced by the perturbed body. A derivation is not given here; refer to Roy (1988).

$$\frac{\mathrm{d}a}{\mathrm{d}t} = \frac{2}{na}\frac{\partial \mathcal{R}}{\partial \epsilon}$$

$$\frac{\mathrm{d}e}{\mathrm{d}t} = -\frac{\sqrt{1-e^2}}{na^2e}(1-\sqrt{1-e^2})\frac{\partial \mathcal{R}}{\partial \epsilon} - \frac{\sqrt{1-e^2}}{na^2e}\frac{\partial \mathcal{R}}{\partial \varpi}$$

$$\frac{\mathrm{d}\epsilon}{\mathrm{d}t} = -\frac{2}{na}\frac{\partial \mathcal{R}}{\partial a} + \frac{\sqrt{1-e^2}(1-\sqrt{1-e^2})}{na^2e}\frac{\partial \mathcal{R}}{\partial e} + \frac{\tan\frac{1}{2}I}{na^2\sqrt{1-e^2}}\frac{\partial \mathcal{R}}{\partial I}$$

$$\frac{\mathrm{d}\Omega}{\mathrm{d}t} = \frac{1}{na^2\sqrt{1-e^2\sin I}}\frac{\partial \mathcal{R}}{\partial I}$$

$$\frac{\mathrm{d}\varpi}{\mathrm{d}t} = \frac{\sqrt{1-e^2}}{na^2e}\frac{\partial \mathcal{R}}{\partial e} + \frac{\tan\frac{1}{2}I}{na^2\sqrt{1-e^2}}\frac{\partial \mathcal{R}}{\partial I}$$

$$\frac{\mathrm{d}I}{\mathrm{d}t} = \frac{-\tan\frac{1}{2}I}{na^2\sqrt{1-e^2}}(\frac{\partial \mathcal{R}}{\partial \epsilon} + \frac{\partial \mathcal{R}}{\partial \varpi}) - \frac{1}{na^2\sqrt{1-e^2}\sin I}\frac{\partial \mathcal{R}}{\partial \Omega}$$

Here the angle ϵ is the mean longitude at epoch defined by $\lambda = nt + \epsilon$; and all other orbital elements are as defined in Chapter 2. We recognise that the inclination terms will not be important in the circular planar case: they are included for completeness. These can be simplified for the low-order (in eccentricity and inclination) problem addressed here:

$$\dot{n} = -\frac{3}{a^2}\frac{\partial \mathcal{R}}{\partial \lambda}$$

$$\dot{e} = -\frac{1}{na^2 e}\frac{\partial \mathcal{R}}{\partial \varpi}$$

$$\dot{I} = -\frac{1}{na^2 \sin I}\frac{\partial \mathcal{R}}{\partial \Omega}$$

$$\dot{\varpi} = \frac{1}{na^2 e}\frac{\partial \mathcal{R}}{\partial e} + \frac{\sin \frac{1}{2} I}{na^2}\frac{\partial \mathcal{R}}{\partial I}$$

$$\dot{\Omega} = \frac{1}{na^2 \sin I}\frac{\partial \mathcal{R}}{\partial I}$$

$$\dot{\epsilon} = \frac{e}{2na^2}\frac{\partial \mathcal{R}}{\partial e}$$

Note this also involves a conversion from $\dot{n}$ to $\dot{a}$, and from $\frac{\partial \mathcal{R}}{\partial \epsilon}$ to $\frac{\partial \mathcal{R}}{\partial \lambda}$.

These can be expanded for the circular restricted case, using $\langle \mathcal{R} \rangle = \frac{\mathcal{G}m'}{a'}[f_{s,1}(\alpha)e^2 + f_d(\alpha)e^{|j_4|}\cos\varphi]$ and the corresponding argument $\varphi = j_1\lambda' + j_2\lambda + j_4\varpi$ to determine the integrals:

$$\dot{n} = 3j_2\mathcal{C}_r n e^{|j_4|}\sin\varphi$$

$$\dot{e} = j_4\mathcal{C}_r e^{|j_4|-1}\sin\varphi$$

$$\dot{\varpi} = 2\mathcal{C}_s + |j_4|\mathcal{C}_r e^{|j_4|-2}\cos\varphi$$

$$\dot{\epsilon} = \mathcal{C}_s e^2 + \frac{1}{2}|j_4|\mathcal{C}_r e^{|j_4|}\cos\varphi$$

where:

$$\mathcal{C}_r = \frac{\mathcal{G}m'}{na^2 a'}f_d(\alpha) = (\frac{m'}{m_c})n\alpha f_d(\alpha)$$

$$\mathcal{C}_s = \frac{\mathcal{G}m'}{na^2 a'}f_{s,1}(\alpha) = (\frac{m'}{m_c})n\alpha f_{s,1}(\alpha)$$

These also use $\mathcal{G} = n^2a^3/m_c$, from Kepler's third law.

Finally, a conversion back from mean motion to semi-major axis is possible:

$$\dot{a} = -2j_2\mathcal{C}_r a e^{|j_4|}\sin\varphi$$

which can be used to give:

$$\frac{\mathrm{d}a}{\mathrm{d}e} = -2(j_2/j_4)ae$$

The variation in the argument is now:

$$\dot{\varphi} = j_1 n' + j_2(n + \dot{\epsilon}) + j_4\dot{\varpi}$$

using $\lambda = nt + \epsilon$.

A.3 A Pendulum Model and Libration Width

A simple way of obtaining an expression for the libration width is to determine the maximum oscillation energy that a particle can attain before it is lost from the resonance. This is illuminated by comparison to a pendulum model.

A simple pendulum has an equation of motion of the form:

$$\ddot{\theta} = -\omega_0^2 \sin\theta$$

where $\omega = \sqrt{\frac{g}{L}}$, g is the acceleration due to gravity and L is the length of the pendulum. An equation of motion for the resonance situation of an identical form can be derived, allowing a similar energy analysis to that of a simple pendulum.

The second time derivative of the argument of the general form of the disturbing function (and for the circular restricted problem) is:

$$\ddot{\varphi} = j_2\dot{n} + j_2\ddot{\epsilon} + j_4\ddot{\varpi}$$

Considering the equations of motion of the orbital elements ϵ and ϖ, we can rewrite these with $F(e) = \frac{1}{2}e^{|j_4|}$ and $G(e) = e^{|j_4|-2}$ giving:

$$\dot{\epsilon} = \mathcal{C}_s e^2 + |j_4|\mathcal{C}_r F(e)\cos\varphi$$

$$\dot{\varpi} = 2\mathcal{C}_s + |j_4|\mathcal{C}_r G(e)\cos\varphi$$

and these can be differentiated to give:

$$\ddot{\epsilon} = 2\mathcal{C}_s e\dot{e} + |j_4|\mathcal{C}_r\left(\frac{\mathrm{d}F(e)}{\mathrm{d}e}\dot{e}\cos\varphi - f(e)\dot{\varphi}\sin\varphi\right)$$

$$\ddot{\varpi} = |j_4|\mathcal{C}_r\left(\frac{\mathrm{d}G(e)}{\mathrm{d}e}\dot{e}\cos\varphi - G(e)\dot{\varphi}\sin\varphi\right)$$

It can be shown that these two contributions can be neglected in most circumstances, as the $\dot{e}$ and $\dot{\varphi}$ terms make them second order in m'/m_c: see Murray and Dermott (1999) for details and exceptions.

This simplifies the $\ddot{\varpi}$ expression to:

$$\ddot{\varphi} = 3j_2^2\mathcal{C}_r n e^{|j_4|}\sin\varphi$$

which can be rewritten as:

$$\ddot{\varphi} = -\omega_0^2\sin\varphi$$

where

$$\omega_0^2 = -2j_2^2\mathcal{C}_r n e^{|j_4|}$$

Here ω_0^2 is positive if only odd-order resonances are considered. In this case, the formula is identical to that given for a simple pendulum at the beginning of this section. For even order resonances, the formalism is the same, but with the subtlety that the stable equilibrium point occurs at $\varphi = \pi$ instead of $\varphi = 0$.

An expression for the total energy E, which can be given by the sum of the kinetic energy and the potential energy of the system,, is now achievable. Per unit mass we have kinetic energy $T = \frac{1}{2}\dot{\varphi}^2$ and potential energy $U = 2\omega_0^2 \sin\frac{1}{2}\varphi^2$, which gives:

$$E = T + U = \frac{1}{2}\dot{\varphi}^2 + 2\omega_0^2 \sin\frac{1}{2}\varphi^2$$

By considering the value of the total energy E compared with the maximum of the potential energy $U_{max} = 2\omega_0^2$, we can see that three cases of motion can result. For the case $E > U_{max}$, the angle φ is unbounded and the motion is described as circular. For $E < U_{max}$ we have bounded oscillatory motion in φ: this is known as libration of the resonant argument. The final case, $E = U_{max}$ is the location of the separatrix, that is the line at which motion changes from circulation to libration. This position, therefore, defines the maximum libration (or oscillation) in φ that can occur, before the object leaves libration and displays circulation. We define the libration width as the maximum energy a particle can attain, or maximum oscillation distance a particle can move, before it is no longer in the resonance. Thus, from this simple model, the maximum libration energy (at which point $\dot{\varphi} = 0$ and $\varphi = \pm\pi$) is at:

$$E_{max} = 2\omega_0^2 = -6j_2^2\mathcal{C}_r n e^{|j_4|}$$

By setting $E = E_{max}$ the variation in the argument can then be studied, and rearranging for φ gives:

$$\dot{\varphi} = \pm j_2(12|\mathcal{C}_r|ne^{|j_4|})^{\frac{1}{2}} \cos\frac{1}{2}\varphi$$

To describe the maximum width in semi-major axis, we must first convert to mean motion, using the equation of motion for n:

$$\mathrm{d}n = 3j_2\mathcal{C}_r n e^{|j_4|}\frac{\sin\varphi}{\dot{\varphi}}\mathrm{d}\varphi$$

which can be simplified using the expression for $\dot{\varphi}$ to:

$$\mathrm{d}n = \pm(3\mathcal{C}_r n e^{|j_4|})^{\frac{1}{2}} \sin\left(\frac{1}{2}\varphi\right)\mathrm{d}\varphi$$

Integrating produces:

$$n = n_0 \pm (12|\mathcal{C}_r| n e^{|j_4|})^{1/2} \cos\left(\frac{1}{2}\varphi\right)$$

with a maximum change in n given by the magnitude of the second term:

$$\delta n_{max} = \pm(12|\mathcal{C}_r| n e^{|j_4|})^{1/2}$$

Converting from mean motion n to semi-major axis a using Kepler's third law $T^2 = \frac{4\pi^2}{\mu}a^3$ and $n = \frac{2\pi}{T}$:

$$\delta a_{max} = \pm(\frac{16}{3}\frac{|\mathcal{C}_r|}{n}e^{|j_4|})^{1/2} a$$

which describes the maximum change in semi-major axis that can result for a particle in a given resonance (defined by $|j_4|$ and the semi-major axis value a).

For first order resonances ($|j_4| = 1$) there is an extra term in $\ddot{\varphi}$ that becomes non-negligible, leading to a more complicated equation for δa_{max}:

$$\frac{\delta a_{max}}{a} = \pm\left(\frac{16}{3}\frac{|\mathcal{C}_r|}{n}e\right)^{1/2}\left(1 + \frac{1}{27 j_2^2 e^3}\frac{|\mathcal{C}_r|}{n}\right)^{1/2} - \frac{2}{9 j_2 e}\frac{|\mathcal{C}_r|}{n}$$

A more complete Hamiltonian model for resonance behaviour is described in detail in Murray and Dermott (1999); it is not outlined further here. It does contain one result that is interesting for our purposes: namely, that (for first order resonances for which $j_4 = -1$ so $|j_4| = 1$) the resonant width as a result of the Hamiltonian formalism is similar to that from the simple pendulum model above:

$$\Delta a_{max} = \pm(\frac{16}{3}\frac{|\mathcal{C}_r|}{n}e_{res})^{1/2} a$$

This gives us confidence that the initial δa_{max} equation derived above gives an adequate approximation to the resonant width in semi-major axis.

References

M. F. A'Hearn et al. The ensemble properties of comets: Results from narrowband photometry of 85 comets. *Icarus*, 118:223–270, 1995.

N. Altobelli et al. Cassini/Cosmic Dust Analyzer in situ dust measurements between Jupiter and Saturn. *Journal of Geophysical Research*, 112, 2007.

E. V. Appleton and M. A. F. Barnett. On some direct evidence of downward atmospheric reflection of electric rays. *Proceedings of the Royal Society*, A109:621–641, 1925.

D. J. Asher, M. E. Bailey, and V. V. Emelyanenko. Resonant meteoroids from comet Tempel-Tuttle in 1333: the cause of the unexpected Leonid outburst in 1998. *Monthly Notices of the Royal Astronomical Society*, 304(4), 1999.

D. J. Asher and S. V. M. Clube. An extraterrestrial influence during the current glacial-interglacial. *Quarterly Journal of the Royal Astronomical Society*, 34:481–511, 1993.

D. J. Asher and S. V. M. Clube. Towards a dynamical history of 'Proto-Encke'. *Celestial Mechanics and Dynamical Astronomy*, 69:149–170, 1998.

D. J. Asher, S. V. M. Clube, and D. I. Steel. The Taurid complex asteroids. In *Meteoroids and their Parent Bodies*, 1993.

D. J. Asher and V. V. Emel'yanenko. The origin of the June Bootid outburst in 1998 and determination of cometary ejection velocities. *Monthly Notices of the Royal Astronomical Society*, 331:126–132, 2002.

D. J. Asher and K. Izumi. Meteor observations in Japan: new implications for a Taurid meteoroid swarm. *Monthly Notices of the Royal Astronomical Society*, 297:23–27, 1998.

W. J. Baggaley. Radar surveys of meteoroid orbits. *Earth, Moon and Planets*, 68:127–139, 1995.

W. J. Baggaley. The interstellar particle component measured by AMOR. In Baggaley W J and Porubčan V, editors, *Meteoroids 1998*, pages 265–273. Astronomical Institute of the Slovak Academy of Sciences, 1999.

W. J. Baggaley. The AMOR radar: an efficient tool for meteoroid research. *Advances in Space Research*, 28(9):1277–1282, 2001.

W. J. Baggaley. *Meteors in the Earth's Atmosphere*, chapter Radar Observations, pages 123–147. Cambridge University Press, 2002.

W. J. Baggaley. Interstellar dust in the Solar System. *Earth, Moon and Planets*, 95: 197–209, 2004.

W. J. Baggaley and J. Grant. Techniques for measuring radar meteor speeds. *Earth, Moon, and Planets*, 95:601–615, 2004.

M. Beech, M. Hargrove, and P. Brown. The running of the bulls: A review of Taurid fireball activity since 1962. *The Observatory*, 124:277–284, August 2004.

M. J. S. Belton et al. The excited spin state of comet 2P/Enkce. *Icarus*, 175:181–193, 2005.

O. E. Berg and E. Grün. Evidence of hyperbolic cosmic dust particles. *Space Research XIII*, 2:1047–1055, 1972.

N. M. Bone. Visual observations of the Taurid meteor shower 1981 - 1988. *Journal of the British Astronomical Association*, 101:145–152, 1991.

J. Borovička. Properties of meteoroids from different classes of parent bodies. In *Near Earth Objects, our Celestial Neighbours: Opportunity and Risk*. IAU Syposium no. 236, 2006.

G. Breit and M. A. Tuve. A test of the existence of the conducting layer. *Physical Review*, 28:554–573, 1926.

P. Brown and J. Jones. Simulation of the formation and evolution of the Perseid meteoroid stream. *Icarus*, 133:36–68, 1998.

P. Brown, J. Jones, R. J. Weryk, and M. D. Campbell-Brown. The velocity distribution of meteoroids at the Earth as measured by the Canadian Meteor Orbit Radar (CMOR). *Earth, Moon and Planets*, 95:617–626, 2004.

P. Brown, R. J. Weryk, D. K. Wong, and J. Jones. A meteoroid stream survey using the Canadian Meteor Orbit Radar I. methodology and radiant catalogue. *Icarus*, 195: 317–339, 2008.

P. Brown, D. K. Wong, R. J. Weryk, and P. Wiegert. A meteoroid stream survey using the Canadian Meteor Orbit Radar II: Identification of minor showers using a 3D wavelet transform. *Icarus*, 207(1):66–81, 2010.

J. A. Burns, P. L. Lamy, and S. Soter. Radiation forces on small particles in the Solar System. *Icarus*, 40:1–48, 1979.

H. Campins and T. D. Swindle. Expected charactersitics of cometary meteorites. *Meteoritics and Planetary Science*, 33:1201–1211, 1998.

T. K. Carey-Smith. The design of, construction and initial operation of the Canterbury ST radar. Master's thesis, University of Canterbury, 2003.

E. F. F. Chladni. Account of a remarkable firey meteor seen in Gascony on the 24th of July 1790. *Philosophical Magazine*, 2:225–231, 1798.

S. V. M. Clube and D. J. Asher. The evolution of Proto-Encke: Dust bands, close encounters and climatic modulations. In *Proceedings of Asteroids, Comets and Meteors III 1989*, pages 275–280, 1990.

S. V. M. Clube and W. M. Napier. The microstructure of the terrestrial catastophism. *Monthly Notices of the Royal Astronomical Society*, 211:953–968, 1984.

J. Crifo. A general physicochemical model of the inner coma pf active comets. I. Implications of spatially distributed gas and dust production. *The Astrophysical Journal*, 445: 470–488, 1995.

J. F. Crifo and A. V. Rodionov. The dependence of the circumnuclear coma structure on the properties of the nucleus I. comparison between a homogeneous and an inhomogeneous spherical nucleus, with application to P/Wirtanen. *Icarus*, 127:319–353, 1997.

J. G. Davies and J. C. Gill. Radio echo measurements of the orbits of faint sporadic meteors. *Monthly Notices of the Royal Astronomical Society*, 121:437–462, 1960.

W. F. Dennings. The Arietid and Taurid meteoric showers. *Journal of the British Astronomical Association*, 38:302–304, 1928.

J. S. Dohnanyi. *Cosmic Dust*, chapter Particle Dynamics. John Wiley and Sons, 1978.

J. Dorschner. Properties of interstellar dust. In B. Å. S. Gustafson and M. A. Hanner, editors, *Physics, Chemistry and Dynamics of Interplanetary Dust*. ASP Conference Series, 1996.

A. Dubietis and A. Arlt. Taurid resonant-swarm encounters from two decades of visual observations. *Monthly Notices of the Royal Astronomical Society*, 376:890–894, 2007.

W. G. Elford. Observations of the structure of meteor trails at radio wavelengths using fresnel holography. In *Proceedings of the Meteoroids 2001 Conference*, pages 405 – 411, 2001.

V. V. Emel'yanenko. Resonance structure of meteoroid streams. In *Proceedings of the Meteoroids 2001 Conference, Swedish Institute of Space Physics, Kirunda, Sweden, 6-10 August 2001*, pages 43–45, 2001a.

V. V. Emel'yanenko. Resonance structure of meteoroid streams. In *Proceedings of the Meteoroids 2001 Conference*. Sweedish Institute of Space Physics, 2001b.

G. H Stokes et al. Study to determine the feasibility of extending the search for NEOs to smaller limiting diameters: Report of a NASA science definition team. Technical report, National Aeronautics and Space Administration Office of Space Science - Solar System Exploration Division, 2003.

P. Farinella, A. Milani, A. M. Nobili, and G. B. Valsecchi. Tidal evolution and the Pluto-Charon system. *Moon and the Planets*, 20:415–421, 1979.

H. Fechtig et al. *Interplanetary Dust*, chapter Historical Perspectives, pages 1–55. Springer, 2001.

Y. R. Fernández et al. Physical properties of the nucleus of comet 2P/Encke. *Icarus*, 147: 145–160, 2000.

Y. R. Fernández et al. New near-aphelion light curves of comet 2P/Encke. *Icarus*, 175: 194–214, 2005.

I. Ferrín. Secular light curve of 2P/Enkce, a comet active at aphelion. *Icarus*, 197:169–182, 2008.

C. Froeschlé and A. Morbidelli. The secular resonances in the Solar System. In *Asteroids, Comets and Meteoroids 1993*. IAU Syposium no. 160, Kluwer Academic Publishers, 1994.

C. Froeschlé and H. Scholl. Gravitational splitting of Quadrantid-like meteor streams in resonance with Jupiter. *Astronomy and Astrophysics*, 158:259–265, 1986.

T. Gallardo. Atlas of mean motion resonances in the Solar System. `http://www.fisica.edu.uy/ gallardo/atlas/`, 2006a.

T. Gallardo. Atlas of the mean motion resonances in the Solar System. *Icarus*, 184:29–38, 2006b.

D. Galligan and W. J. Baggaley. The orbital distribution of radar-detected meteoroids of the Solar System dust cloud. *Monthly Notices of the Royal Astronomical Society*, 353: 422–446, 2004.

D. P. Galligan. *Structural Analysis of Radar Meteoroid Orbital Data*. PhD thesis, University of Canterbury, 2000.

G. Gartrell and W. G. Elford. Southern hemisphere meteoroid stream determinations. *Australian Journal of Physics*, 28:591–620, 1975.

C. Gockel and R. Jehn. Testing cometary ejection models to fit the 1999 Leonids and to predict future showers. *Monthly Notices of the Royal Astronomical Society*, 317:L1–L5, 2000.

R. Greenberg and H. Scholl. *Asteroids*, chapter Resonances in the Asteroid Belt, pages 310–333. The University of Arizona Press, 1979.

E. Grün. *The Century of Space Science*, chapter The Dusty Heliosphere, pages 1163–1189. Kluwer Academic Publishers, 2001.

E. Grün et al. *Interplanetary Dust*, chapter In Situ Measurements of Cosmic Dust. Springer, 2001.

E. Grün and M. Landgraf. Collisional consequences of big interstellar grains. *Journal of Geophysical Research*, 105:10291–10297, 2000.

E. Grün and H. A. Zook. Dynamics of micrometeoroids. In Halliday I and McIntosh B A, editors, *Solid Particles in the Solar System*, pages 293–298. IAU, 1980.

E. Grün, H. A. Zook, H. Fechtig, and R. H. Giese. Collisional balance of the meteoritic complex. *Icarus*, 62:244–272, 1985.

B. Å. S. Gustafson. Zodiacal dust. *Annual Review of Earth and Planetary Sciences*, 22: 553–595, 1994.

D. P. Hamilton, E. Grün, and M. Baguhl. Electromagnetic escape from the Solar System. In B. Å. S. Gustafson and M. S. Hanner, editors, *Physics, Chemistry, and Dynamics of Interplanetary Dust*, page 31. Astronomical Society of the Pacifics, 1996.

R. L. Hawkes. Television meteors. In J Stŏhl and I P Williams, editors, *Meteoroids and their Parent Bodies*, pages 227–234, 1993.

G. S. Hawkins. The harvard radio meteor project. *Smithsonian Contributions to Astrophysics*, 7:53, 1963.

J. Henrard, N. Watanabe, and M. Moons. A bridge between secondary and secular resonances inside the Hecuba Gap. *Icarus*, 115(2):336–346, 1995.

J. S. Hey and G. S. Stewart. Radar observations of meteors. *Proceedings of the Physical Society*, 59:858–883, 1947.

W. K. Hocking. Real-time meteor entrance speed determinations made with interferometric meteor radars. *Radio Science*, 35(5):1205–1220, 2000.

D. W. Hughes. Meteoroids - an overview. In J Stohl and I P Williams, editors, *Meteoroids and their Parent Bodies*, pages 15–28. Astronomical Institute of the Slovak Academy of Sciences, 1993.

D. W. Hughes. Mass and evolution of the Solar System dust cloud. *Quarterly Journal of the Royal Astronomical Society*, 37:593–604, 1996.

D. W. Hughes, I. P. Williams, and C. D. Murray. The orbital evolution of the Quadrantid meteor stream between ad 1830 and 2030. *Monthly Notices of the Royal Astronomical Society*, 189:493–500, 1979.

P. Jenniskens. *Meteor Showers and their Parent Comets*. Cambridge University Press, 2006.

P. Jenniskens and H. Betlem. Massive remnant of evolved cometary dust trail detected in the orbit of Halley-type comet 55/p Tempel-Tuttle. *The Astrophysical Journal*, 531: 1161–1167, March 2000.

P. Jenniskens et al. On the unusual activity of the Perseid meteor shower (1989-96) anhd the dust trail of comet 109p/swift-tuttle. *Monthly Notices of the Royal Astronomical Society*, 301:941–954, 1998.

P. Jenniskens et al. Leonids 2006 opbservations of the tail of trails: Where is the comet fluff? *Icarus*, 196:171–183, 2008.

P. Jenniskens and E. Lyytinen. Meteor showers from the debris of broken comets: D/1819 W1 (Blanpain), 2003 WY25, and the Phoenicids. *The Astronomical Journal*, 130:1286–1290, 2005.

P. Jenniskens and J. Vaubaillon. 3D/Biela and the Andromedids: Fragmenting versus sublimating comets. *The Astronomical Journal*, 134:1037–1045, 2007.

J. Jones. The effect of gravitational perturbations on the evolution of the taurid meteor stream complex. *Monthly Notices of the Royal Astronomical Society*, 221:257–267, 1986.

J. Jones. The ejection of meteoroids from comets. *Monthly Notices of the Royal Astronomical Society*, 275:773–780, 1995.

J. Jones et al. The Canadian Meteor Orbit Radar: system overview and preliminary results. *Planetary and Space Science*, 53:413–421, 2005.

J. Klačka and M. Kocifaj. Times of inspiralling for interplanetary grains. *Monthly Notices of the Royal Astronomical Society*, 390:1491–1495, 2008.

K. H. Knuth. Kevin H Knuth's code repository - optBINS. `http://knuthlab.rit.albany.edu/optBINS.html`, 2006a.

K. H. Knuth. Optimal data-based binning for histograms. http://arxiv.org/abs/physics/0605197, 2006b.

N. A. Konovalova. Interaction of large Taurid meteoroids with the Earth's atmosphere. *Astronomy and Astrophysics*, 404:1145–1152, 2003.

S. J. Kortenkamp and S. F. Dermott. Accretion of interplanetary dust particles by the Earth. *Icarus*, 135:469–495, 1998.

R. Koschack and J. Rendtel. Determination of spatial number density and mass index from visual meteor observations (II). *WGN, the Journal of the IMO*, 35(5):1205–1220, 2000.

L. Kresák and V. Porubčan. The dispersion of meteors in meteor streams. *Bulletin of the Astronomical Institute of Czechoslovakia*, 21(3):153–170, 1970.

A. V. Krivov. Physics of debris disks. In *Dust in Planetary Systems*. ESA SP-643, 2007.

H Krüger et al. Interstellar dust in the Solar System. *Space Science Review*, 130:401–408, 2007.

H. Krüger and E. Grün. Interstellar dust inside and outside the heliosphere. *Space Science Review*, 143:347–356, 2009.

P. Lee. Electrostatic levitation of fines on asteroids. *Meteoritics*, 30(5):535, 1995.

C. Leinert, S. Röser, and J. Buitrago. How to maintain the spatial distribution of interplanetary dust. *Astronomy and Astrophysics*, 118:345–357, 1983.

H. F. Levison and M. J. Duncan. The long term dynamical behvaior of long-period comets. *Icarus*, 108:18–36, 1994.

B. A. Lindblad. The distribution of 1/a in photographic meteor orbits. In Millman P M Hemenway C L and Cook A F, editors, *Evolutionary and Physical Properties of Meteoroids, Proceedings of IAU Colloq. 13*, page 175. National Aeronautics and Space Administration, 1973.

A. C. B. Lovell. *Meteor Astronomy*. Oxford University Press, 1954.

J. Luu and D. Jewitt. The nucleus of comet 2P/Encke. *Icarus*, 86:69–81, 1990.

I. Mann, A. Krivov, and H. Kimura. Dust cloud near the Sun. *Icarus*, 146:568–582, 2000.

D. W. R. McKinley. *Meteor Science and Engineering*. McGraw-Hill Book Company Inc, 1961.

K. J. Meech and J. Svoren. *Comets II*, chapter Using Cometary Activity to Trace the Physical and Chemcial Evolution of Cometary Nuclei. University of Arizona Press, 2004.

H. Meng. The relationship between the semi-major axis, mass index and age of the Leonid meteor shower. *Monthly Notices of the Royal Astronomical Society*, 359:1433–1436, 2005.

N. Meyer-Vernet. *Basics of Solar Wind*. Cambridge University Press, 2007.

P. M. Millman. The observational evidence for mass distribution in the meteoritic complex. *The Moon*, 8:228–240, 1973.

M. Moons. Review of the dynamics in the Kirkwood gaps. *Celestial Mechanics and Dynamical Astronomy*, 65:175–204, 1997.

M. Moons and A. Morbidelli. Secular resonances in mean motion commensurabilities - the 4/1, 3/1, 5/2, 7/3 cases. *Icarus*, 114:33–50, 1995.

A. Moro-Martín and R Malhotra. A strudy of the dynamics from the Kuiper Belt: Spatial distribution and spectral energy distribution. *The Astronomical Journal*, 124:2305–2321, 2002.

E. Murad and I. P. Williams, editors. *Meteors in the Earth's Atmosphere*. Cambridge University Press, 2002.

C. D. Murray. Nodal regression of the Quadrantid meteor stream: An analytic approach. *Icarus*, 49:125–134, 1982.

C. D. Murray. Real and imaginary Kirkwood gaps. *Monthly Notices of the Royal Astronomical Society*, 279:978–986, 1996.

C. D. Murray and S. F. Dermott. *Solar System Dynamics*. Cambridge University Press, 1999.

N. Murray and M. Holman. The role of chaotic resonances in the Solar System. *Nature*, 410:773–779, 2001.

H. Nagaoka. Possibility of disturbance of radio transmissions by meteoric showers. *Proceedings of the Imperial Academy, Tokyo*, 5, 1929.

V. Porubčan, L. Kornoš, and I. P. Williams. Associations between asteroids and meteoroid streams. In J. Stohl and I. P. Williams, editors, *Modern Meteor Science*, pages 697–711. Astronomical Institute of the Slovak Academy of Sciences, 2004.

K. P. Rauch and D. P. Hamilton. The HNBody package for symplectic integration of nearly-Keplerian systems. *Bulletin of the American Astronomical Society*, 34, 2002.

W. T. Reach. The formation of Encke meteoroids and dust trail. *Icarus*, 148:80–94, 2000.

J. Rendtel. The Orionid meteor shower observed over 70 years. *Earth, Moon and Planets*, 102:103–110, 2008.

R. E. Rinehart. *Radar for Meteorologists*. Rinehart Publications, 2004.

A. E. Roy. *Orbital Motion*. A. Hilger, 1988.

D. P. Rubincam. Radiative spin-up and spin-down of small asteroids. *Icarus*, 148:2–11, 2000.

S. Russell. The formation of the Solar System. *Journal of the Geological Society*, 164: 481–492, 2007.

G. O. Ryabova. Meteoroid streams: mathematical modelling and observations. In Ferraz Mello Lazzaro D and Fernández J A, editors, *Proceedings of Asteroids, Comets, Meteors, IAU Symposium No. 229*, pages 229–247, 2005.

G. C. Sanzovo et al. Mass-loss rates, dust particles sizes, nuclear active areas and minimum nuclear radii of target comets for missions STARDUST and CONTOUR. *Monthly Notices of the Royal Astronomical Society*, 326:852–868, 2001.

M. Sato and J. Watanabe. Origin of the 2006 Orionid outburst. *Publication of the Astronomical Society of Japan*, 59:L21–L24, 2007.

E. Schneider et al. Microcratering on Apollo 15 and 16 samples and corresponding cosmic dust fluxes. *Space Research XIII*, 2:1047–1055, 1973.

A. Sekanina. Outgassing asymmetry of comets 103P/Hartley 2 and 2P/Encke. *Astronomical Journal*, 96:1455–1475, 1988.

A. Sosa and J. A. Fernández. Cometary masses derived from non-gravitataional forces. *Monthly Notices of the Royal Astronomical Society*, 393:192–214, 2009.

P. Spurný and L. Shrbený. Exceptional fireball activity of Orionids in 2006. *Earth, Moon and Planets*, 102:141–150, 2008.

D. I. Steel and D. J. Asher. The orbital dispersion of the macroscopic Taurid objects. *Monthly Notices of the Royal Astronomical Society*, 280:806–822, 1996.

D. I. Steel, D. J. Asher, and S. V. M. Clube. The structure and evolution of the Taurid complex. *Monthly Notices of the Royal Astronomical Society*, 251:632–648, 1991.

D. I. Steel and W. G. Elford. Collisions in the solar system - III meteoroid survival times. *Monthly Notices of the Royal Astronomical Society*, 218:185–199, 1986.

J. Stohl and V. Porubčan. Meteor streams of asteroidal origin. In J. Stohl and I. P. Williams, editors, *Meteoroids and their Parent Bodies*, pages 41–47. Astronomical Institute of the Slovak Academy of Sciences, 1993.

J. Svoreň, Z. Kaňuchová, and M. Jakubík. Filaments within the Perseid meteoroid stream and their coincidence with the location of mean-motion resonances. *Icarus*, 183:115–121, 2006.

M. V. Sykes and R. G. Walker. Cometary dust trails I: Survey. *Icarus*, 95:180–210, 1992.

G. Tancredi, J. Fernández, H. Rickman, and J. Licandro. Nuclear magnitudes and the size distribution of jupiter family comets. *Icarus*, 182:527–549, 2006.

T. Tanigawa, S. Abe, M. Ishiguro, and T. Mukai. Models for the origin of the Quadrantids. *Earth, Moon and Planets*, 106:55–65, 2010.

A. D. Taylor, W. J. Baggaley, and D. I. Steel. Discovery of interstellar dust entering the earth's atmosphere. *Nature*, 380:323, 1996.

J. M. Trigo-Rodríguez et al. The 2006 Orionid outburst imaged by all-sky CCD cameras from Spain: meteoroid spatial fluxes and orbital elements. *Monthly Notices of the Royal Astronomical Society*, 380:126–132, 2007.

US Naval Observatory and The Royal Greenwich Observatory. *The Astronomical Almanac 2009*. HMSO, 2007.

G. B. Valsecchi et al. The dynamics of objects in orbits resembling that of P/Encke. *Icarus*, 118:169–180, 1995.

J. Vaubaillon, F. Colas, and L. Jorda. A new method to predict meteor shower I. Description of the model. *Astronomy and Astrophysics*, 439:751–760, 2005.

F. Verniani. An analysis of the physical parameters of 5759 faint radio meteors. *Journal of Geophysical Research*, 78(35), 1973.

A. Wehry, H. Kruger, and E. Grün. Analysis of Ulysses data: Radiation pressure effects on dust particles. *Astronomy and Astrophysics*, 419:1169–1174, 2004.

A. Wehry and I. Mann. Identification of β-meteoroids from measurements of the dust detector onboard the Ulysses spacecraft. *Astronomy and Astrophysics*, 341:296–303, 1999.

S. J. Weidenschilling and A. A. Jackson. Orbital resonance and Poynting-Robertson drag. *Icarus*, 104:244–254, 1993.

P. A. Weigert, P. G. Brown, J. Vaubaillon, and H. Schijns. The τ Herculid meteor shower and Comet 73P/Schwassmann-Wachmann 3. *Monthly Notices of the Royal Astronomical Society*, 361:638–644, 2005.

P. G. Welch. Matching cometary ejection processes to the Leonids 1998-2001 using a hybrid numerical model. *Monthly Notices of the Royal Astronomical Society*, 342:971–994, 2003.

F. L. Whipple. Photographic meteor studies III the Taurid shower. *Proceedings of the American Philosophical Society*, 83(5):711–744, 1940.

F. L. Whipple. A comet model. I The acceleration of comet encke. *The Astrophysical Journal*, 111:375–394, 1950.

F. L. Whipple. A comet model. II Physical relations for comets and meteors. *The Astrophysical Journal*, 113:464–479, 1951.

F. L. Whipple and S. E. Hamid. On the origins of the Taurid meteors. *The Astrophysical Journal*, 55:185–186, 1952.

P. Wiegert and P. Brown. The core of the Quadrantid meteoroid stream is two hundred years old. *Earth, Moon and Planets*, 95:81–88, 2004.

P. Wiegert and P. Brown. The Quadrantid meteoroid complex. *Icarus*, 179:139–157, 2005.

I. P. Williams and E. Murad. *Meteors in the Earth's Atmosphere*, chapter Introduction, pages 1–11. Cambridge University Press, 2002.

J. Wisdom. The origin of the Kirkwood gaps - a mapping for asteroidal motion near the 3/1 commensurability. *Astronomical Journal*, 87(3):577–593, 1982.

J. Wisdom. Chaotic behavior and the origin of the 3/1 Kirkwood gap. *Icarus*, 56(1): 51–74, 1983.

W. F. Wright and F. L. Whipple. The photographic taurid meteors. *Technical Report of the Harvard College Observatory*, 6, 1950.

Z. D. Wu and I. P. Williams. Gaps in the distribution of semimajor axes of the Perseid meteors. *Monthly Notices of the Royal Astronomical Society*, 276(3):1017–1023, 1995.

H A Zook and O E Berg. A source for hyperbolic cosmic dust particles. *Planetary and Space Science*, 23:183–203, 1975.